Gas Diffusion in Thin Porous Catalyst Layers of PEM Fuel Cells

by

Sina Salari

M.Sc., Sharif University of Technology, 2011

B.Sc., Amirkabir University of Technology, 2008

Thesis Submitted in Partial Fulfillment of the
Requirements for the Degree of
Doctor of Philosophy

in the
School of Mechatronic Systems Engineering

Faculty of Applied Sciences

SIMON FRASER UNIVERSITY

Fall 2018

Approval

Name:	**Sina Salari**
Degree:	**Doctor of Philosophy**
Title:	**Gas diffusion in thin porous catalyst layers of PEM fuel cells**
Examining Committee:	**Chair: Jiacheng (Jason) Wang** Assistant Professor
	Majid Bahrami Senior Supervisor Professor
	Byron Gates Supervisor Associate Professor
	Michael Eikerling Supervisor Professor
	Erik Kjeang Internal Examiner Associate Professor
	Xianguo Li External Examiner Professor Mechanical and Mechatronics Engineering University of Waterloo
Date Defended/Approved:	Oct 30th, 2018

Abstract

Oxygen molecules reach the reaction sites in the cathode catalyst layer (CL) of PEM fuel cells through diffusion, and the water vapor produced at the cathode leaves the reaction sites through diffusion. Therefore, the gas diffusivity of CL influences fuel cell performance. Uniform oxygen delivery to the Pt particles is one of the primary parameters ensuring high activity level of Pt particles and prolonging the CL lifetime. A sufficient supply of oxygen to the CL is required to achieve high current densities. Therefore, to reach high power outputs with low Pt loading, it is vital to understand the mechanism and improve the oxygen diffusion rate within CL and investigate the effects of different operating conditions on its performance.

To investigate the effect of different CL designs and operating conditions on gas diffusivity, a modified Loschmidt cell was used to measure the gas diffusivity of CL. Also, the pore size distribution of CL was measured with N_2 adsorption porosimetry. Moreover, the structure of CL was modeled through considering a packed-sphere model for carbon particles within agglomerates, and a network of overlapped spherical agglomerates forming the CL. The gas diffusion problem was solved analytically for the CL structure considering both Knudsen and molecular mechanisms.

The results show that decreasing the ionomer content of CL from an ionomer to carbon weight ratio of 1.5 to 0.5 increases the relative diffusivity by 400%. Dry milling the catalyst powders for 48 hours led to 50% drop in the relative diffusivities of CL. Drying the catalyst ink on the support substrate at elevated temperatures improved gas diffusivity in some cases.

The CL effective diffusivity is higher in higher operating temperature; however, its relative gas diffusivity is lower. High compressive loads (30 MPa or 50 MPa) reduces the CL diffusivity; however, in range of fuel cell operating condition (<5 MPa) the effect is negligible. The effect of gas relative humidity on the relative diffusivity of CL is negligible. On the other hand, liquid water reduces CL relative diffusivity. For example, a 25 wt. % water content in CL results in a 25% drop in relative diffusivity.

Keywords: fuel cell, modified Loschmidt cell, catalyst layer designs, gas diffusivity, operating conditions

To my beloved parents, Abdolkarim and Tooba,

my dear sisters, Mahsa and Golsa,

my awesome brothers, Reza and Ali

and the rest of my lovely family

Acknowledgements

This research was supported by funding from the Natural Sciences and Engineering Research Council of Canada (NSERC) Collaborative Research and Development (Grant No. M-CRDPJ453170) and Automotive Fuel Cell Corporation (AFCC). The research made use of facilities at Laboratory for Alternative Energy Conversion (LAEC), and SFU 4D LABS, as well as the facilities of the Automotive Fuel Cell Cooperation (AFCC) Structure, Properties and Performance Research Division.

I would like to express my sincere gratitude to my supervisor, Dr. Majid Bahrami, for the continuous support of my doctoral studies and related research, for his motivation, and immense knowledge. His guidance helped me throughout my research and the writing of this thesis.

I would also like to thank Dr. Byron Gates and Dr. Michael Eikerling, for agreeing to be in my supervisory committee, reviewing my candidacy report and thesis and providing useful feedback.

Also, I would like to express my appreciation to Dr. Claire McCague at LAEC, who helped me a lot with experimental data analysis and writing papers, and to Mr. Mickey Tam at AFCC for his support throughout LEAC-AFCC collaboration.

I was lucky enough to be a member of two research teams, LAEC and AFCC, where I was exposed to various research projects and could make good friends. I would like to thank my fellow labmates in both research teams for the stimulating discussions, for their support, and for all the fun we had in the last five years.

Last but not the least; I would like to thank my family who has always supported me in all stages of my life, and my best friends Amir and Mahsa who were always true friends and kept me going forward positively in life.

Table of Contents

Approval ii
Abstract iii
Dedication iv
Acknowledgements v
Table of Contents vi
List of Tables ix
List of Figures x
List of Acronyms xv
Nomenclature xvi
Executive Summary xviii
Research Milestones xix
Research Roadmap and Contributions xix

Chapter 1. Introduction 1
1.1. Polymer electrolyte membrane fuel cells (PEMFC) 1
1.2. Research motivation 3
1.3. Research objectives 4
1.4. Cathode catalyst layer 5
1.5. Gas diffusivity 6
1.6. Literature review 8
1.6.1. CL diffusivity measurement methods 8
1.6.2. CL diffusivity models 10
1.6.3. Comparison between CL diffusivity values measured/modeled in literature 12
1.6.4. CL pore size distribution (PSD) 15

Chapter 2. CL Samples Synthesis 21
2.1. Substrate and coating selection 21
2.2. Sample preparation procedure 27
2.3. Catalyst ink preparation 28
2.4. Chapter 2 acknowledgement 29

Chapter 3. CL Thickness, Porosity, and PSD 30
3.1. Thickness measurement 30
3.1.1. TUC-RUC thickness measurement 30
3.1.2. SEM imaging thickness measurement 31
3.1.3. Densitometer thickness measurement 32
3.1.4. Thickness measurement methods evaluation 33
3.2. Porosity and PSD measurements 34
3.2.1. Theoretical porosity based on thickness and Pt loading measurements 34
3.2.2. Densitometer porosity measurement 34

3.2.3. Mercury intrusion porosimetry....34
3.2.4. N_2 adsorption porosimetry....35
3.2.5. PSD testbeds evaluation....38
3.2.6. Porosity measurement/calculation evaluation....42
3.3. Chapter 3 acknowledgement....43

Chapter 4. Ex-situ Measurement of the PEMFC CL Diffusivity....44
4.1. Dry diffusivity testbed (DDT)....44
4.1.1. Testbed and measurement method....44
4.1.2. Dry diffusivity testbed uncertainty analysis....45
4.2. Modified Loschmidt cell (MLC)....46
4.2.1. Testbed and measurement method....46
4.2.2. MLC uncertainty analysis....50
4.3. MLC measurement parameters and sample configuration for CL....51
4.3.1. MLC measurement parameters....51
4.3.2. CL sample configuration....51
4.4. CL gas diffusivity measurement under different operating conditions with MLC....52
4.4.1. Operating temperature....52
4.4.2. Operating humidity....52
4.4.3. Operating compression....53
4.4.4. CL water content....55
4.5. Chapter 4 acknowledgement....57

Chapter 5. CL Structural and Gas Diffusivity Model....58
5.1. Catalyst structural model....58
5.1.1. Catalyst structure....58
5.1.2. Pore geometry within agglomerates....60
5.1.3. Geometry of the unit cells....61
Geometrical relationships in the unit cell....61
Volume ratios of the CL materials....64
Volume ratios of CL pores and ionomer coverage....64
C-Pt particles and agglomerate porosities in CL....66
Defining the CL structure based on the unit cell....67
5.1.4. Integration of compression load into the CL structural model....69
5.1.5. Integration of water content into the CL structural model....69
Ionomer swelling....70
Water pore filling....72
CL structural unit cells under saturated hydrophilic pores....74
CL structural unit cells for bellow saturated condition....74
5.2. CL diffusivity model....76
5.2.1. The diffusivity model within agglomerates....76
Numerical model for FCC arrangement....76
5.2.2. The diffusivity of the unit cell....78
5.2.3. The unit cell relative diffusivity model verification....82
5.2.4. The CL relative diffusivity model....84

Chapter 6. Effect of ink processing and composition on the CL pore structure, porosity, and relative diffusivity 85
6.1. Evaluation of the measurement and modeling methods for CL gas diffusivity used in this study 85
6.1.1. Gas diffusion testbed evaluation 85
6.1.2. Model Validation 89
6.2. Porosity and relative gas diffusivity 91
6.3. Dry milling time 94
6.4. Ionomer to carbon ratio 101
6.5. Drying temperature 105

Chapter 7. Effect of operating conditions on the CL pore structure, porosity, and relative diffusivity 110
7.1. Operating temperature 110
7.2. Operating compressive load 111
7.3. Operating humidity and water content 115
7.3.1. Operating humidity 115
7.3.2. Water content 118

Chapter 8. Conclusion and future work 120
8.1. Thesis Conclusion 120
8.1.1. Challenges 120
8.1.2. Conclusion 121
8.2. Future work 123

References 124

Appendix A. Measured experimental data 137

Appendix B. The developed code for CL structure and gas diffusion 159

List of Tables

Table 1.1 Different applications of fuel cell 2
Table 1.2 Differernt methods to measure CL gas diffusivity 10
Table 1.3 Available models for prediction of gas diffusivity in porous medium 10
Table 1.4 Relative diffusivity values in literature 14
Table 1.5 Studies evaluating the effect of composition and processing on CL structure 18
Table 2.1 Specification of Sigracet GDL 24BC, used as substrate, manufacturer data (except for porosity) 23
Table 2.2 The tested substrates for decal transfer. The substrates are all hydrophilic; porosities are chosen to be low to bear decal transfer condition 25
Table 2.3 Filter PTFE membranes and GDL-MPL 24BC specifications 26
Table 2.4 CL designs I/C, dry milling time, and drying temperature 29
Table 4.1 CL gas diffusion measurement with MLC specifications 51
Table 5.1 Unit cell modeled parameters 69
Table 6.1 CL thicknesses measured from SEM images of sample cross sections and measured CL effective length and relative diffusivity 85
Table 6.2 CL gas diffusivity investigations: the method, sample preparation, porosity, and operating conditions 88
Table 6.3 The inputs to the relative diffusivity model 89
Table 6.4 The results of the relative diffusivity model for CL design #4 (I/C= 1.1, Dm=0, and T_d=50 ˚C) 90

List of Figures

Figure 1.1 Schematic of a PEMFC 2
Figure 1.2 The research roadmap 5
Figure 1.3 SEM image of CL which shows the secondary and primary pores within CL 6
Figure 1.4 a) The gas diffusion resistance network for an in-situ CL. b) The gas diffusion resistance network for a CL ex-situ 8
Figure 1.5 AutoPore IV 9500 mercury intrusion porosimeter 16
Figure 1.6 Autosorb iQ-MP, Quantachrome N_2 adsorption porosimeter 16
Figure 2.1 Fujifilm Dimatix material printer DMP2800 22
Figure 2.2 MicroFAb Jetlab4 printer 23
Figure 2.3 SEM images of the cross-section of the CL coated on the MPL-GDL with two different printers (DMP2800 inkjet on the left side and Jetlab MicroFAb on the right side). This shows penetration of the CL into the substrate in both cases. 24
Figure 2.4 Decal transferring CL from coating substrate to the target one 24
Figure 2.5 Mayer bar coating 26
Figure 2.6 The SEM image of CL coating on GDL-MPL 24BC with the Mayer bar 27
Figure 2.7 SEM image of cross-section of CL coated with the Mayer bar on the Fluoropore FHUP04700 filter PTFE 27
Figure 2.8 The pattered surface of 150µm-thick filter PTFE substrate 27
Figure 2.9 Template support for the filter disk substrates to be catalyst-coated by the Mayer bar 28
Figure 3.1 TUC-RUC test setup 31
Figure 3.2 Sample holder for SEM thickness measurement 32
Figure 3.3 The comparison between the thicknesses obtained by SEM, densitometer, and TUC-RUC for five CL designs: #1: I/C=1.1, dry milling time=0 hr, drying temperature= 50 ˚C; #2: I/C=1.1, dry milling time=0 hr, drying temperature= 20 ˚C; #3: I/C=0.9, dry milling time=6 hr, drying temperature= 50 ˚C; #4: I/C=0.7, dry milling time=48 hr, drying temperature= 50 ˚C; and #5: I/C=0.7, dry milling time=24 hr, drying temperature= 50 ˚C. The error bars show the standard deviations for at least three measurement repetitions. 33
Figure 3.4 a) Measured PSDs with MIP, N_2 adsorption, and FIB-SEM methods for CL design #4 (Table 2.4). b) Sample image of the cross-section of the CL design #4 obtained by FIB. c) Measured PSDs with N_2 adsorption and FIB-SEM methods for the CL design #2. d) Sample image of the cross-section of the CL design #2 obtained by FIB. e) Measured PSDs with N_2 adsorption and FIB-SEM methods for the CL design #11. f) Sample image of the cross-section of the CL design #11 obtained by FIB. 41

Figure 3.5 The measured/calculated porosities for design #4 (Table 2.4) CL from different methods. The error bars shows the standard deviations of at least three measurements....42
Figure 4.1 Schematic of the dry diffusivity test bed....45
Figure 4.2 a) MLC testbed b) MLC testbed, open and clamped positions. b) The two tests the in the MLC procedure (test I and test II). d) The two tests done in the MLC to measure the CL gas diffusion resistance....49
Figure 4.3 The modeled error for effective length measurement of MLC with respect to sample diffusion effective length....50
Figure 4.4 Schematic of the MLC testbed used in this study....53
Figure 4.5 a)The sample holder for MLC tests under compression. b) Sample holders with the porous sample. c) Sample holder with a porous sample sandwiched between them. d) Screws used to tighten the sample holders and exert compressive load on the porous sample....54
Figure 5.1 a) Schematic of the unit cell used to model structure of the CL. b) Schematic of the network of unit cells used to model structure of the CL60
Figure 5.2 Schematic of the ionomer layer in the considered unit cell....63
Figure 5.3 The schematic of the CL PSD partially filled with water....75
Figure 5.4 a) FCC arrangement geometry. b) The geometry used in the numerical model for FCC arrangement....77
Figure 5.5 Mesh study for the numerical model of FCC arrangement toward relative diffusivity....78
Figure 5.6 a) Network of series resistances for the unit cell. b)Side view schematic of the angle identifying the diffusion resistance. c) Considered diffusion resistance element. d) The geometrical parameters of the gas diffusion resistance element. e) The schematice of the gas diffusion resistance element. f) The special location of the gas diffusion resistance element. g) The side view of the unit cell and angular location of the gas diffusion resistance element. h) The top view of the unit cell and the gas diffusion resistance element....80
Figure 5.7 Mesh study for numerical model of the unit cell toward relative diffusivity. For this unit cell, overlap was 1.2 and the ratio of agglomerate to secondary pore relative diffusivity was about 0.1....83
Figure 5.8 Comparison between the analytical, and the numerical relative diffusivities for different values of D^*_{agg}....83
Figure 6.1 Relative diffusivity values, D^*, for CLs with Pt loading from 140 to 290 μg/cm², measured by DDT (error bars are standard deviation of at least three measurements)....86
Figure 6.2 a) Relative diffusivity values, D^*, for stack of 10 CL (design #4) samples measured by MLC and repeated 10 times. b) The average of relative diffusivity values for 10 test repetitions, for 5 different stacks of 10 CL (design #4) samples measured by MLC....87
Figure 6.3 Comparison between ex-situ diffusivity measurements for CL design #4 and the results in the literature. Details for each data point are in Table 6.2....88

Figure 6.4 The measured PSD for CL design #4 with N_2 adsorption porosimetry applying BJH method, used as input to the relative diffusivity model 90

Figure 6.5 The measured relative diffusivity values by MLC versus calculated porosities based on thickness measurements. As the standard deviations of repeated measurements for the CL relative diffusivity were less than the calculated uncertainties based on thickness measurements (section 4.1.2), for both relative diffusivity and porosity, the error bars are calculated based on thickness measurements uncertainties. 92

Figure 6.6 a) The CL overlap angle and ionomer coverage versus porosity, keeping composition parameter and PSD constant. b) The CL and agglomerates relative diffusivities versus porosity, keeping composition parameters and PSD constant. The equation in the plot is a fit to the modeld relative diffusivity values at different porosities. 94

Figure 6.7 Isotherms obtained by N_2 adsorption of CL designs with, a) I/C=1.1, *dm*=0 hr, T_d=50˚C; b) I/C=1.1, *dm*=6 hrs , T_d=50˚C; and c) I/C=1.1, *dm*=48 hrs , T_d=50˚C 95

Figure 6.8 Isotherms obtained by N_2 adsorption of CL designs with, a) I/C=0.9, *dm*=6 hrs , T_d=50˚C; b) I/C=0.9, *dm*=24 hrs, T_d=50˚C; and c) I/C=0.9, *dm*=48 hrs, T_d=50˚C..... 96

Figure 6.9 Comparison of CL porosities calculated from densitometer for samples prepared with different dry milling times and a) I/C=1.1, T_d=50 ˚C, b) I/C=0.9, T_d=50 ˚C. The error bars shows the calculated standard deviation for 3 measurements 98

Figure 6.10 PSD obtained by N_2 adsorption porosimetry applying DFT and BJH methods of CL designs with: a) I/C=1.1, dm=0 hr, Td=50˚C; and b) I/C=1.1, dm=48 hrs. The error bars are calculated standard deviation for 3 repeating measurements of the same sample..... 98

Figure 6.11 PSD obtained by N2 adsorption porosimetry applying DFT and BJH methods of CL designs with: a) I/C=0.9, dm=6 hrs, Td=50˚C; and b) I/C=0.9, dm=48 hrs, Td=50˚C. The error bars are calculated standard deviation for 3 repeating measurements of the same sample..... 99

Figure 6.12 PSD obtained by N_2 adsorption porosimetry applying DFT and BJH methods of CL designs with: a) I/C=0.7, dm=24 hrs, T_d=50˚C; and b) I/C=0.7, dm=48 hrs, T_d=50˚C. The error bars are calculated standard deviation for 3 repeating measurements of the same sample..... 100

Figure 6.13 The measured and modeled relative diffusivity values comparison for CL design sets with different dry milling times. As the standard deviations of repeated measurements for CL relative diffusivity were less than the calculated uncertainties based on thickness measurements (section 4.1.2), the error bars are calculated based on thickness measurements uncertainties. 101

Figure 6.14 N_2 adsorption porositimetry for the CL designs with the same dry milling time of 48 hrs, drying temperature of 50˚C, and different I/Cs: 0.7, 0.9, and 1.1: a) Isotherms and porosities calculated based on SEM thicknesses; b) PSDs obtained applying BJH method; and c) PSDs obtained applying DFT method. The error bars shows calculated standard deviation for 3 repeating measurements of the same sample..... 103

Figure 6.15 BJH PSD for designs #1 (I/C=1.5) and 12 (I/C=0.5). The error bars shows calculated standard deviation for 3 repeating measurements of the same sample 104

Figure 6.16 The measured and modeled relative diffusivity values comparison for CL design sets with different I/C ratios. As the standard deviations of repeated measurements for the CL relative diffusivity were less than the calculated uncertainties based on thickness measurements (section 4.1.2), the error bars are calculated based on thickness measurements uncertainties. 104

Figure 6.17 Isotherms obtained by N_2 adsorption porositimetry for the CL designs with the same I/C=1.1, and: a) dm= 0 hr, T_d= 50˚C and 20˚C; and b) dm= 48 hrs, T_d= 50˚C and 20˚C. 106

Figure 6.18 Calculated porosities based on SEM thickness measurement for CL designs with the same I/C=1.1, and: a) dm= 0 hr, T_d= 50˚C and 20 ˚C; and b) dm= 48 hrs, T_d= 50˚C and 20 ˚C. The error bars shows calculated standard deviation for 3 repeating measurements of the same sample 107

Figure 6.19 PSDs obtained by N_2 adsorption porositimetry applying both BJH and DFT methods for CL designs with the same I/C=1.1 and: a) dm= 0 hr, T_d= 50˚C and 20 ˚C; and b) dm= 48 hrs, T_d= 50˚C and 20 ˚C. The error bars shows calculated standard deviation for 3 repeating measurements of the same sample..... 108

Figure 6.20 The measured and modeled relative diffusivity values comparison for the CL design sets with different drying temperatures. As the standard deviations of repeated measurements for the CL relative diffusivity were less than the calculated uncertainties based on thickness measurements (section 4.1.2), the error bars are calculated based on the thickness measurements uncertainties. 109

Figure 7.1 The relative diffusivity of CL design #4 (I/C=1.1, no dry milling, and T_d=50 ˚C)..... 110

Figure 7.2 Thickness and porosity measurements for stack of ten CL design #4 (I/C= 1.1, no dry milling, and T_d=50 ˚C) samples versus compressive load ranged from 0 to 50 MPa..... 112

Figure 7.3 The measured effective lengths for two stacks of ten filter PTFE samples and ten catalyst-coated filter PTFE samples (CL design #4), by MLC under 0, 30, and 50 MPa operating compressive loads. For each compressive load, the tests were repeated at least ten times..... 113

Figure 7.4 a) The relative diffusivity versus porosity for the CL design #4 (I/C= 1.1, no dry milling, and T_d=50 ˚C). The change in porosity was due to compressive load. b) The relative diffusivity of the CL design #4 (I/C= 1.1, no dry milling, and T_d=50 ˚C) versus compressive load. 114

Figure 7.5 Aquivion membrane water content form Ref. [131], ionomer thin film water content, and swell versus RH 116

Figure 7.6 Calculated secondary PSD of the CL design #4 (I/C= 1.1, no dry milling, and T_d=50 ˚C) under different RHs 117

Figure 7.7 The measured and modeled relative diffusivities for the CL design #4 (I/C= 1.1, no dry milling, and T_d=50 ˚C) under different operating RHs . 118

Figure 7.8 Measured and modeled relative diffusivity values of the CL design #4 (I/C= 1.1, no dry milling, and T_d=50 ˚C) containing different amount of liquid water.....119

List of Acronyms

AFCC	Automotive Fuel Cell Cooperation Corporation
BJH	Barrett-Joyner-Halenda
C/Pt	Carbon to Platinum
DDT	Dry Diffusivity Testbed
DFT	Density Function Theory
Dm	Dry milling
ETFE	Ethylene TetraFluoroEthylene
FCC	Faced-Centered Cubic
FIB	Focused Ion Beam
GDL	Gas Diffusion Layer
GSDFT	Solid Density Functional Theory
I/C	Ionomer to Carbon weight ratio
MIP	Mercury Intrusion Porosimetry
MLC	Modified Loschmidt Cell
MPL	Micro-Porous Layer
MSP	Method of Standard Porosimetry
NLDFT	Non-Local Density Function Theory
PSD	Pore Size Distribution
PTFE	PolyTetraFluoroEthylene
QSDFT	Quenched Solid Density Function Theory
RH	Relative humidity
SEM	Scan Electron Microscopy
TLD	Through the Lens Detector
TUC-RUC	Thickness Under Compression - Resistivity Under Compression

Nomenclature

English symbols

A	Area (m^2)
a	Unit cell dimension (m)
C	Concentration (mol/m^3)
D	Diffusivity (m^2/s)
d	Diameter (m)
D^*	Relative gas diffusivity
EW	Equivalent weight (g/mol)
g	Gravity (m/s^2)
h	Height (m)
l	Diffusion resistance length (m)
M	Molecular mass (kg/kmol)
N	Diffusion rate ($mol/s.m^3$)
P	Pressure (kPa)
R	Diffusion resistance (s/m^3)
r	Radius (m)
Sh	Sherwood number
st	strain
T	Temperature (°K)
t	Thickness (m)
V	Volume (m^3)
v	Volume ratio
W	Weight (kg)

Greek symbols

γ	Loading (kg/m2)
ε	Porosity
θ	Spatial angle (rad)
λ	Water content (mol/mol)
ξ	Overlap parameter
ρ	Density (kg/m^3)

σ	Surface tension (kg/s^2)
φ	Overlap angle (rad)
ω	Weight ratio
γ	Loading (kg/m2)
ε	Porosity

Executive Summary

Polymer electrolyte membrane fuel cells (PEMFCs) convert the reaction energy of hydrogen and oxygen to electricity with high efficiency, and the exhaust is mostly water which is green. Such features brought fuel cell technology to the attention of many green applications, e.g. fuel cell driven heavy and light duty cars and buses. Membrane electrode assembly (MEA) makes up the core of PEMFCs, which is constructed from multiple layers of microporous materials, and the associated interfaces, including a 7-20 μm thick cathode catalyst layer (CL) which contains Pt nanoparticles on electron conductive carbon support particles, where in vicinity the electro-chemical reaction occurs. Through flow channels and bipolar plates, oxygen and hydrogen are fed to the MEA. On the anode side, hydrogen molecules diffuse to the anode CL and split into electrons and protons. Electrons pass through the external circuit while protons transfer through the membrane to the cathode side. Oxygen molecules reach the reaction sites in the cathode CL, reduce and react with Ions. The products are water and heat which should be removed from the reaction sites for proper operation of the PEMFC. Therefore, the transport properties of the MEA layers are critical to the fuel cell performance. An insufficient supply of oxygen to the CL is a limiting factor to achieve high current densities. Also, the uniform oxygen delivery to the Pt particles is one of the primary parameters ensuring high activity level of Pt particles and prolonging the CL lifetime. Therefore, to reach high power outputs under low Pt loading (reducing the overall cost of the unit), it is vital to understand the mechanism and improve the oxygen diffusion rate within CL and investigate the effect(s) of different operating conditions on its performance. This can be achieved through experimental and theoretical investigation of the CL structure and gas diffusion. However, measuring the gas diffusivity of a several-micron thick porous layer is a challenging task, as is the selection of a suitable substrate and appropriate CL coating procedures (the support substrate and the coating method is one of the reasons to have a wide range of reported data for the CL gas diffusivity in the literature). It should be mentioned that CL does not exist as a stand-alone layer and should be fabricated on proper substrate. Moreover, existing gas diffusivity models for CL are either not accurate or computationally demanding which limit their use in performance prediction models; as to predict the PEMFC performance, several highly coupled governing equations including gas diffusion, thermal diffusion and convection,

electrical current, ion, water and water vapor transports should be solved. The change of transport properties of membrane electrolyte assembly (MEA) components due to the variation of design parameters or operating conditions makes the problem more complicated.

Research Objective: This research aims to address the gaps in the literature through: i) designing an reliable experimental procedure capable of measuring gas diffusivity of CL under different operating conditions, and for CLs with different designs; and ii) developing an accurate analytical low-demanding gas diffusion model to predict CL behavior under different operating conditions, and be used in PEMFC performance prediction models.

Research Milestones

To achieve the objectives, a systematic approach is adopted with the following milestones:

- Develop a procedure for catalyst layer sample fabrication, proper for ex-situ gas diffusion measurements.
- Establish easy-to-use characterization methods for CL structural parameters that affect its gas diffusivity.
- Develop and optimize an ex-situ gas diffusivity measurement procedure for CL.
- Develop a structural model for CL which could be used as a platform to calculate its gas diffusivity, and other transport properties.
- Develop an analytical gas diffusivity model based on the CL structural model.
- Investigate the effects of the different CL composition and production parameters on the catalyst layer gas diffusivity.
- Investigate the effect of operating conditions on the CL gas diffusivity.

Research Roadmap and Contributions

The research roadmap for accomplishing the milestones is shown in Figure **1**.

To achieve these objectives, the following methodology and steps had been conducted and reported as chapters in the thesis:

Chapter 1. Introduction

In this chapter the previous studies on the CL gas diffusivity measurement and modeling, as well as, the CL pore structure characterization are reviewed.

Chapter 2. Catalyst layer sample synthesis **[1]**

a. **Coating methods**: Various coating methods, including spraying, printing with Microfab and Fuji printers, Mayer bar (metering rod) coating, and decal transferring are thoroughly evaluated. As spraying and printing demand dilute inks to prevent nozzle clogging, these two methods result in high penetration of catalyst ink into the porous substrate needed for diffusion tests. Such penetration compromises accuracy of the measurement results and has not been deemed acceptable. While having no penetration, decal transfer methods ruin the porous support substrate used for our tests, as it demands transferring catalyst layer under high pressure and temperature (i.e. 15 bar and 150ºC). After a comprehensive investigation, Mayer bar coating has been chosen as sample fabrication choice as it could work with viscous ink (less penetration) and be applied to delicate porous substrates.
b. **Support substrates:** The substrate for catalyst layer diffusion tests is needed to be highly porous and thin (20-200 µm) such that its gas diffusion resistance remains comparable to that of the CL. The catalyst ink should not penetrate into the substrate while coating. Therefore, depending on the coating method, the substrate should be mechanically strong, hydrophobic (or hydrophilic), and have a specific pore size range (<500 nm). After testing 40 different combinations of substrate-and-coating, Fluoropore FHUP04700, EMD Millipore (filter PTFE) and Mayer bar coating have been selected to be used to produce catalyst test samples suitable for the gas diffusion tests.
c. **Sample preparation procedures:** To produce uniform catalyst layer thickness, a coating template and procedure are devised to handle thin filter PTFEs without causing in defects in the substrate or the coated CL.

d. **Prepared CL samples:** More than 300 CL samples with different composition and ink process are produced with different ionomer content, dry milling time of the catalyst powder, and drying temperature of catalyst.

Chapter 3. Catalyst layer thickness, porosity, and pore size distribution **[2]**

a. **Thickness measurement**: To measure thickness of the prepared CL samples are evaluated using custom-made TUC-RUC (Thickness Under Compression - Resistivity Under Compression) machine, scan electron microscopy (SEM) imaging, and densitometer methods. The results obtained by different techniques have shown good agreement. Therefore, since TUC-RUC is easier to perform, and is non-destructive to the CL samples, this method is chosen. Also, at least 3 thickness measurements with SEM imaging are done for each CL design to ensure TUC-RUC accuracy for different CL designs.

b. **Porosity measurement**: Porosity of CL samples are obtained by using theoretical relationship between the measured CL thicknesses, platinum loadings, and CL porosity, as well as, direct porosity measurement with densitometer kit, mercury intrusion, and N_2 adsorption porosimetry. The porosities have been obtained based on the theoretical relationships with measured thickness, and by densitometry kit included the volume of all pore ranges in CL into the porosity calculations unlike the other two methods which have a specific pore detection range. Here the porosity values including all pore sizes are in demand. The results of the porosities obtained from thickness measurements and the ones obtained by densitometer kit were in good agreement; however the first method was easier to perform. Therefore, it was chosen as the main method to calculate the CL sample porosities.

c. **Pore size distribution measurement:** To measure pore size distribution (PSD) of CL samples, method of standard porosimetry (MSP), mercury intrusion porosimetry (MIP), N_2 adsorption porosimetry, and studying reconstructed geometries from images obtained by focused ion beam scan electron microscopy (FIB-SEM), are evaluated. There are major challenges applying MSP on CL samples which eliminate using this method for the CL samples prepared in this study. MIP might change the CL porosity, and FIB-SEM method is very demanding method to perform.

The main concern about N_2 adsorption method is its limited pore detection range. However, MIP and FEB-SEM methods have shown almost the same pore diameter ranges for CL as N_2 adsorption porosimetry, and, as a result, N_2 adsorption porosimetry is chosen to measure the CL samples' PSDs. In N_2 adsorption porosimetry the quenched solid density functional theory (adsorption branch or equilibrium) method with slit/cylindrical or cylindrical pore shape had the least fitting error, and Barrett-Joyner-Halenda method resulted in the broadest pore detection range.

Chapter 4. Ex-situ measurement of PEM fuel cell catalyst layer diffusivity **[1,3]**

Two methods are evaluated to measure the CL relative gas diffusivity ex-situ including Wicke-Kallenbach cell (WKC) and modified Loschmidt cell (MLC) methods. The major problem with WKC method is involvement of the method with gas flows during the test which results in convective flows and measured artificially high relative diffusivities for the CL samples. MLC does not have the former problem. Besides, performing the tests under different operating conditions has less complexity. Also, the CL gas diffusivity results measured by this method are comparable with the existing ones obtained by other experimental and modeling methods including reconstructing geometry based on FIB-SEM imaging tomography. Therefore, MLC method is chosen as the main method to measure the CL relative gas diffusivity.

Chapter 5. Catalyst layer structural and gas diffusivity model **[3-7]**

The structure of CL is modeled in two scales: i) the structure within agglomerates, considering the carbon-platinum particles as spherical porous particles with orderly-packed arrangement and primary pores as gaps between them, and ii) the structure of the network of agglomerates, considering agglomerates as spherical porous units with overlap and secondary pores as the gaps between them. The inputs to the model are the porosity, PSD, ink composition, and material properties of CL. The size of carbon-platinum particles, size distribution of agglomerates and their overlap, ionomer thickness distribution and coverage are calculated for the effective medium assumed for the CL. The gas diffusion resistance of the structure is calculated analytically and validated with measured gas diffusivity values which ensured the accuracy of the model results.

Chapter 6. Effect of ink processing and composition on the CL pore structure, porosity, and relative gas diffusivity **[2,8]**

Twelve different CL designs are prepared, and the thickness, porosity, PSD, and gas diffusion measurements are done to evaluate the effects of the composition, and production procedure. The model is validated with the measurement results, and followings are concluded:

a. **Ionomer content:** Increasing ionomer content of the CL causes a drop in porosity, a shift of pore diameters toward smaller ones, and drop in relative diffusivity of CL.
b. **Dry milling the catalyst powder:** Dry milling the catalyst powder lead to drop in the porosity, shifts of pore diameters toward smaller ones, introducing narrower necks for pores, and drop in the relative diffusivity of CL.
c. Drying CL in elevated temperatures: Drying CL in elevated temperatures after coating lead to larger pore diameters and higher relative diffusivities.

Chapter 7. Effect of operating condition on the CL pore structure, porosity, and relative diffusivity **[3,8-9]**

The base line CL design relative diffusivity is measured under different operating conditions and followings are concluded:

a. Operating temperature: The CL effective diffusivity is higher in higher operating temperature; however, as the increase rate of the effective diffusivity is less than the one for binary diffusion, the CL relative diffusivity decreases in higher operating temperatures.
b. Operating compressive load: The CL porosity decreases under compressive load, and, as a result, the relative diffusivity drops as well. However, in the compression ranges for the fuel cell (<5 MPa) the changes are negligible.
c. Operating gas humidity: The gas humidity causes CL ionomer to swell. However, as the swell amount is not significant, changes in the relative diffusivity of CL are almost negligible.
d. **Liquid water content:** Unlike the gas humidity, the liquid water effect on the ionomer swell is detectable. The ionomer swell due to the liquid water

and the pore-filling effect of liquid water lead to a detectable drop in the relative diffusivity of CL.

Chapter 8. Conclusion and future work

The findings of the project are summarized in this chapter and followings are suggested for future work:

- The structural model is validated for the gas diffusivity of CL. However, if some aspects of the structural model could be validated, the structural model application will go beyond gas diffusivity. These aspects include:
    - Agglomerate size distribution, e.g. by comparison with a reconstructed geometry based on FIB-SEM for the CL samples prepared in the same way as in this study.
    - Ionomer thickness distribution, e.g. by comparison with a reconstructed geometry based on FIB-SEM for the CL samples prepared in the same way as in this study.
    - Ionomer coverage, e.g. through experimentally determination by double layer capacitance.
- The composition and production parameters are not limited to the ones evaluated here. Samples of different CL designs could be produced, and effects of more parameters could be assessed on the gas diffusivity of CL including:
    - Carbon support type
    - C/Pt ratio
    - Catalyst ink viscosity
    - Catalyst ink solvent parameters
    - Catalyst ink mixing time
- Adding the gas diffusion through water and ionomer to the model, the gas diffusivity value that delivers oxygen molecules to the reaction sites could be calculated. The result should be validated with the in-situ gas diffusivity measurements by limiting current method. Then, the model could be integrated into the performance prediction models of the fuel cell.

In summary, the contributions of this research have resulted in four peer reviewed journal papers, and five conference papers published/presented:

[1] Salari S, McCague C, Tam M, Saha MS, Stumper J, Bahrami M. Accurate ex-situ measurements of PEM fuel cells catalyst layer dry diffusivity. ECS Trans., vol. 69, 2015. doi:10.1149/06917.0419ecst.

[2] Salari S, McCague C, Jankovic J, Stumper J, Bahrami M. Structural characterization of PEM fuel cell catalyst layer using N2 adsorption porosimetry: effects of ink composition and ink processing. Eur. Hydrog. Energy Conf. 2018, Malaga: 2018.

[3] Salari S, Stumper J, Bahrami M. Direct measurement and modeling relative gas diffusivity of PEMFC catalyst layers: The effect of ionomer to carbon ratio, operating temperature, porosity, and pore size distribution. Int J Hydrogen Energy 2018.

[4] Salari S, McCague C, Stumper J, and Bahrami M. Measuring relative diffusivity of PEM fuel cell catalyst layer using modified Loschmidt cell: effects of ink composition, ink processing, and operating temperature and humidity. Eur. Hydrog. Energy Conf. 2018, Malaga: 2018.

[5] Salari S, Stumper J, and Bahrami M. Through Plane Gas Diffusion of Catalyst Layer of PEMFC: Bimodal Unit Cell Modeling. 27th Int Sympos Transp Phenom 2016, Honolulu 2016.

[6] Salari S, McCague C, Tam M, Stumper J, Bahrami M. Modeling Diffusivity in Catalyst Layer of a PEMFC Based on a Unit Cell Approach. 228th ECS., Phoenix 2015.

[7] Salari S, McCague C, Stumper J, Bahrami M. Modeling pore network in catalyst layer of a PEMFC to calculate through plane gas diffusion. IVth Int Sympos Innovat Mater Process Energ Syst 2016., Sicily 2016.

[8] Salari S, McCague C, Tam M, Stumper J, Bahrami M. In-situ versus ex-situ gas diffusivity of catalyst layer of PEM fuel cells with different ink designs. J Power Sources., **Under review**.

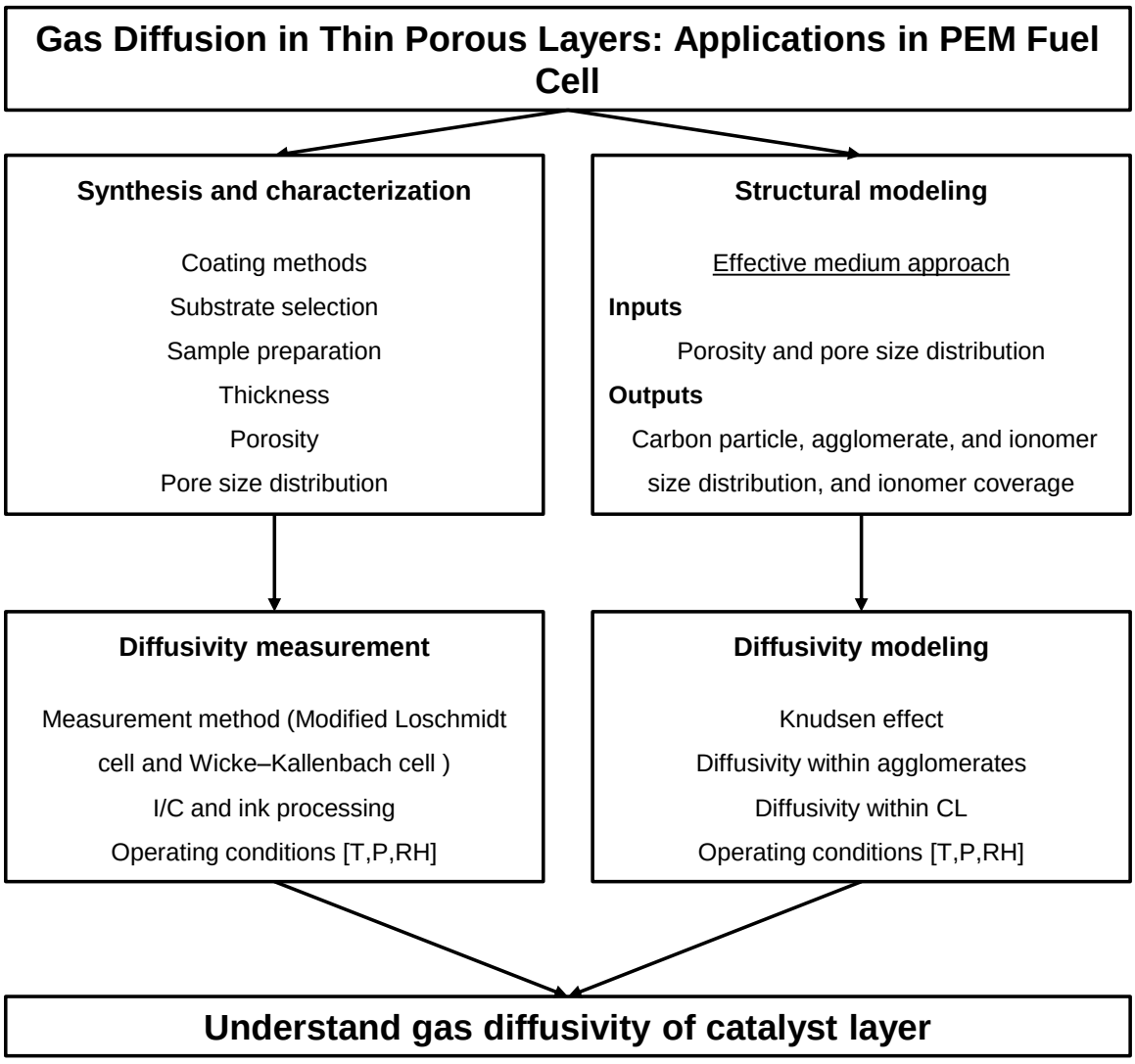

Figure 1 The research roadmap

Chapter 1.

Introduction

1.1. Polymer electrolyte membrane fuel cells (PEMFC)

PEMFC convert the reaction energy of hydrogen and air to electricity, water, and heat with higher efficiencies than internal combustion engines and without harmful emissions [2]. Such features brought fuel cell technology to the attention of many green applications [3] listed in Table 1.1.

PEMFC rely on a membrane-electrode assembly (MEA) constructed from multiple thin layers of microporous materials and their associated interfaces (Figure 1.1). The MEA includes a polymer electrolyte membrane (PEM) that conducts protons; a composite nanostructured catalyst layer (CL) which contains platinum (Pt) nanoparticles on an electron conducting carbon support; and a fibrous gas diffusion layer (GDL) that distributes reactant gases and collects current. Through flow channels and bipolar plates, oxygen and hydrogen are fed to the MEA. On the anode side, hydrogen molecules are split into electrons and protons. Electrons pass through the external circuit while protons transfer through the membrane to the cathode side. In reaction sites within CL, oxygen molecules reduce in vicinity of platinum particles. These reduced oxygen molecules and hydrogen ions will react where wet ionomer and Pt particles meet (triple points: Pt particles, ionomer, water). The products is water and heat is generated which should be removed from the reaction sites for proper operation of the PEMFC. Therefore, the gas diffusivity, thermal conductivity, and electrical conductivity of the MEA layers especially CL, which is a challenging layer to characterize structurally, are critical to the fuel cell performance. CL is also the most expensive layer to produce, in part due to the Pt particles that are the catalyst agent for the electrochemical reaction.

Table 1.1 Different applications of fuel cell

Portable power generation (5W-500kW)	✓ Military applications, i.e., portable soldier power ✓ Auxiliary power units, i.e., for the leisure and trucking industries ✓ Portable products, i.e., torches, vine trimmers ✓ Small personal electronics, i.e., mp3 players, cameras
Stationary power generation (0.5 kW – 5MW)	✓ Off-line short run-time systems for telecommunication base stations ✓ Off-line extended run-time systems for critical communication base stations ✓ Off-line extended run-time rack mountable systems for data centers
Power for transportation	✓ Two- and three-wheeler vehicles such as scooters ✓ Light duty vehicles, such as cars and vans ✓ Buses, trucks, forklift trucks, trains and trams ✓ Ferries and smaller boats, and unmanned undersea vehicles ✓ Manned and unmanned light aircraft

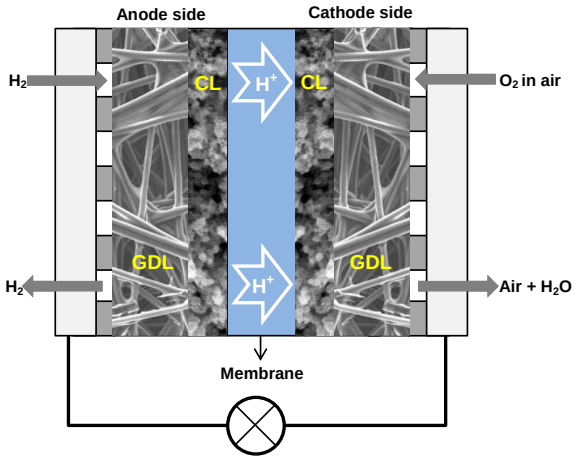

Figure 1.1 Schematic of a PEMFC

1.2. Research motivation

Several automotive companies such as Daimler, Ford, General Motors, Honda, Hyundai, Nissan, and Toyota, have plans for commercialization of their fuel cell vehicles in the near future [13]. Mercedes-Benz Fuel Cell Division has constructed the world's first large-scale production facility of PEMFC stacks for passenger vehicles in Burnaby, British Columbia (BC). This multimillion-dollar investment reflects the strength of the fuel cell research teams in BC and their value to the commercialization of fuel cell technology.

The production cost and limited durability of the Pt CL are among the main challenges for the commercialization of hydrogen fuel cells [4]. To reduce the cost, the utilization of Pt particles in CL should be maximized [2], which demands understanding/optimizing of the energy and reactant conversion mechanisms in the performance of the fuel cell. Specifically, the CL gas diffusivity affects the uniformity of the reaction within the CL, the lifetime of the CL, and the power density of the fuel cell [5]. Besides, an insufficient supply of oxygen to the CL is a limiting factor to achieve high current densities, and therefore, it is vital to improve the oxygen diffusion rate within CL [2].

To analyze/predict PEMFC's performance, several highly coupled governing equations including gas diffusion, thermal diffusion and convection, electrical current, and ion, water and water vapor transport should be solved [1]. The change of transport properties of the MEA components due to the variation of design parameters or operating conditions makes the problem more complicated. Therefore, accurate analytical models for each transport property significantly help to optimize MEA design parameters.

Significant progress has been made in understanding how cell design, materials [6], and operating parameters impact the transport [7–12], mechanical properties [12] and performance of the MEA components [13]. However, a critical gap remains due to the limited available, reliable data on the transport properties including gas diffusivity, water diffusivity, heat transfer coefficient, and electrical conductivity, testing protocols and low-cost models for CL. This research is focused on filling this gap for gas diffusivity of CL by introducing the reliable experimental method to measure diffusivity of CL, and developing low-cost model(s), which can be used to predict CL diffusivity and effects of operating conditions on gas diffusion within CL.

1.3. Research objectives

The present research aims to develop a reliable experimental procedure, and low-cost model, which could be used to investigate the effect of cathode catalyst composition, production process, and operating conditions, with acceptable uncertainty. Therefore, the primary milestones of this research are:

1. Develop a CL production procedure, proper for ex-situ gas diffusion measurements.
2. Establish easy-to-use characterization methods for the CL structural parameters that affect the gas diffusivity.
3. Develop and optimize an ex-situ gas diffusivity measurement method for the CL.
4. Develop an analytical structural model for CL which could be used as a platform to calculate the gas diffusivity (and other transport properties) of the CL.
5. Develop an analytical gas diffusivity model for the CL structural platform.
6. Investigate the effect of CL composition and production parameters on the catalyst layer gas diffusivity.
7. Investigate the effect of operating conditions on the CL gas diffusivity.

The research roadmap of this program is given in Figure 1.2.

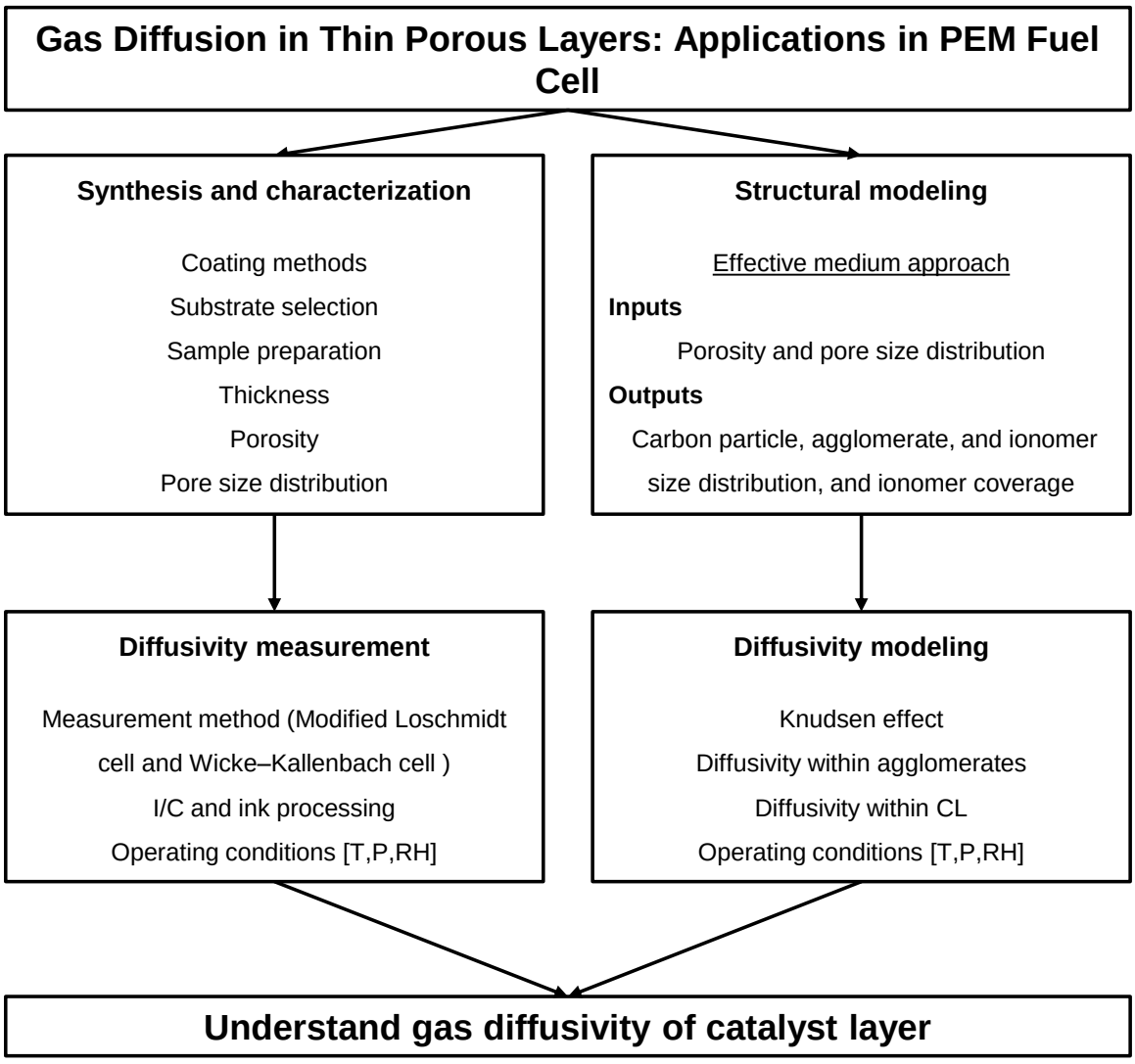

Figure 1.2 The research roadmap

1.4. Cathode catalyst layer

The CL is a micro/nanocomposite structure of these particles form agglomerates. The average number of carbon particles that form an agglomerate is reported to be 79 for Vulcan XC-72 carbon black in Ref. [14]; however, generally the characteristics of agglomerates, e.g., the number of carbon particles and size, depend on the material and production process [15].

The catalyst layer is a several-micron-thick micro/nano composite of carbon support agglomerates, primary and secondary pores, Pt particles supported on carbon particles, and ionomer (See Figure 1.3). CL does not exist as a standalone layer and has to be

coated on a substrate. Carbon black particles can be envisioned as spheres with 5 to 300 nm diameters [16] with an average diameter reported at 20-30 nm [14,17] depending on the production process. These carbon particles form agglomerates. Primary pores exist between the carbon support particles (with diameters less than 20 nm [18,19]) and secondary pores between agglomerates. Generally the characteristics of agglomerates e.g., number of carbon particles and size, depend on the material and also production process [15]. During formation of CL, ionomer works as a binder that keeps the carbon particles and the agglomerates together. It mostly fills the secondary pores in CL and does not penetrate into primary pores [20].

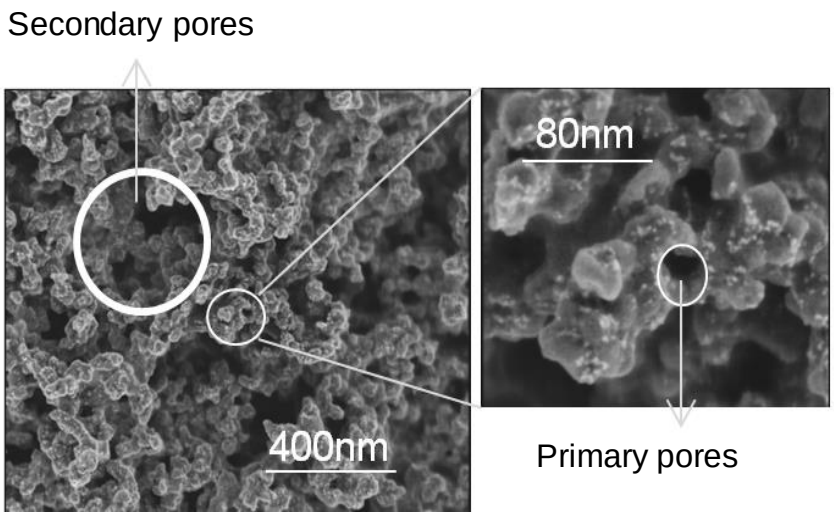

Figure 1.3 SEM image of CL which shows the secondary and primary pores within CL

The carbon support particles type, the way catalyst powder was prepared, the weight ratio of carbon and platinum ($\omega_{C/Pt}$), the ionomer type, the weight ratio of ionomer and carbon ($\omega_{I/C}$), type of solvents for ionomer and catalyst ink, and production processes are the main parameters that specify properties of a CL.

1.5. Gas diffusivity

Binary gas diffusivity D_{binary} is defined for a system of two gases in an open space with concentration gradient which forces them to diffuse in each other where Fick's law is valid Eq. 1. For oxygen-nitrogen pair D_{binary} is calculated from Eq. 2 [21].

$$N = D\frac{\partial C}{\partial x}$$

Eq. 1

$$D_{\text{binary}} = \frac{1.13 \times 10^{-9}}{P} T^{1.72}$$

Eq. 2

where P is the gas pressure (atm), T is the absolute temperature (K), and the unit for D_{binary} is m^2/s. $D_{\text{molecular}}$ is the molecular diffusivity due to the collision of gas molecules with each other unaffected by the walls of the system. Therefore, molecular and binary diffusivities of two gases in open space have the same values.

Unlike molecular diffusion, Knudsen diffusion is due to the collision of gas molecules with the confining pore, which is calculated from Eq. 3 [22].

$$D_{Kn} = \frac{8}{3} r_{channel} \sqrt{\frac{RT}{2\pi M}}$$

Eq. 3

where R is the gas constant 8.314 (J/mol.K), M is the molecular weight of the gas (kg/kmol), and r_{channel} is the characteristic radius of the channel (m). Knudsen number (Kn), i.e., ratio of the mean free path of gas molecules to the characteristic length of the medium (or space), is used to evaluate the diffusion regime in channels or within the pores for porous media. In case of porous media with pore sizes comparable to mean free path of gas molecules (e.g. CL), the gas experiences an effective diffusivity which is a combination of molecular and Knudsen diffusivities and can be calculated from Eq. 4 [23]:

$$D_{eff} = \left(\frac{1}{D_{\text{molecular}}} + \frac{1}{D_{Kn}} \right)^{-1}$$

Eq. 4

In this study, the effect of operating conditions, catalyst composition and processing parameters on relative gas diffusivity D^* is investigated, which is the non-dimensional effective diffusivity with respect to binary diffusivity Eq. 5:

$$D^* = \frac{D_{eff}}{D_{\text{binary}}}$$

Eq. 5

One of the most basic diffusivity models widely used for porous material is the Bruggemann model [24] which relates the relative diffusivity to porosity:

$$D^* = \varepsilon^{1.5}$$

Eq. 6

1.6. Literature review

1.6.1. CL diffusivity measurement methods

Different methods used to measure CL gas diffusivity are summarized in Table 1.2. As oxygen diffusivity within the CL directly affects the fuel cell output (See the gas diffusion resistance network for the CL in-situ operation and ex-situ in Figure 1.4), several studies deduced CL diffusivity indirectly by investigating polarization curves of PEMFC, see for example Ref. [25–30]. In this method, impedance spectra of the cell are measured for the same cell current but with different oxygen concentrations in the cathode channels. Based on the difference between the resistivity of the cell for different concentrations, oxygen diffusivity can be calculated. The accuracy of such diffusivity measurements is highly influenced by the model relating the impedance of the CL to its diffusivity [31]. Other studies determined oxygen diffusivity indirectly using ex-situ solid state electrochemistry [32–34]. According to Rashapov et al. [35], there are challenges with these methods which compromise accuracy. In case of electrochemistry, it demands a thick wet layer of about several millimeters. As for limiting currents, difficulties include the effect of uncontrollable liquid water production in the cell, some in-plane gas flows, the indistinguishable contribution of the CL in the current limitation, and the impact of Brinkman effect disturbing the boundary conditions (due to convection in the flow channel) [35].

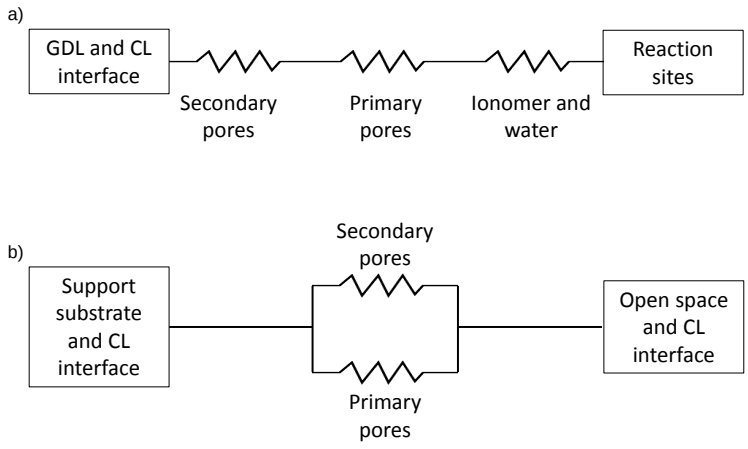

Figure 1.4 a) The gas diffusion resistance network for an in-situ CL. b) The gas diffusion resistance network for a CL ex-situ

Water vapor diffusion through GDL was measured ex-situ in Refs. [2,30,36]. They exposed one side of the GDL sample to water vapor saturated environment while dry gas flew on the other side. Based on humidity detected of the outlet of the gas side and the mass flow rate of gas, the effective diffusivity of the sample was determined.

The Wicke–Kallenbach cell (WKC) method was widely used in the literature to measure gas diffusivity of porous layers [37–42]. In the WKC two steady gas streams flow with different oxygen concentrations on the opposite sides of a porous sample [43], and counter diffusion of each gas in the other one is measured. The method is capable of measuring diffusivity of samples with pores smaller than 5 μm, such as the CL, if the pressure difference between sides of the sample is kept close to zero (pure diffusion problem) [43].

Rashapov et al. [35] targeted in-plane gas diffusivity of GDL using a transient approach. First, they flushed the sample with nitrogen, and, then, let oxygen to diffuse to the sample and monitored the concentration. Comparing the oxygen concentration with an analytical solution, the gas diffusivity could then be calculated.

Gas diffuses in CL mostly in the through-plane direction, but there are limited available data, measured directly, to prove this hypothesis, mostly due to the challenges involved in direct measurements of through-plane diffusivity in CL. The diffusion resistance of CL is small for through-plane direction as the CL is generally less than ~10 μm thick. Measuring diffusivity of thin layers demands a precise measurement procedure capable of detecting minor changes in gas concentration. Shen et al. [5] measured through-plane diffusivity of CL samples that were spray coated on alumina substrates using a modified Loschmidt cell (MLC) apparatus. MLC has two chambers filled by oxygen and nitrogen separated with a valve and the desired sample. Initially, the valve is opened, and oxygen diffuses through the sample to the other chamber, where the oxygen concentration is monitored. Comparing oxygen concentration-time plot to the analytical solution for the problem, the effective diffusivity of the sample is calculated. The major problem with MLC was its high uncertainty magnification factor (UMF) relating oxygen concentration measurements uncertainty to the diffusivity uncertainty, in the case of thin multilayers (< 200 μm) like CL [44]. UMF values for oxygen concentration is about ~30 in case of ordinary CLs. Such UMF leads to about ~30% uncertainty values for diffusivity using oxygen probes with 99% accuracy. MLC can be used for thicker porous layers than CL such as GDL [45,46] with higher accuracy.

Table 1.2 Differernt methods to measure CL gas diffusivity

Method	Basics	ref
In-situ	Investigating polarization curves of PEMFC	[25–30]
Ex-situ, water vapor diffusion	Exposing one side of the sample to water vapor saturated environment while dry gas flows on the other side	[2,30,36]
Ex-situ, Wicke–Kallenbach cell	Exposing each side of the sample to gas flows with different oxygen (or other gases) concentrations	[37–42]
Ex-situ, modified Loschmidt cell	Exposing each side of the sample to gas chambers with different oxygen (or other gases) concentrations	[5,45,46]

1.6.2. CL diffusivity models

There are several diffusivity modeling methods in the literature for porous materials presented in Table 1.3.

In effective medium models, the effective properties of the medium are calculated as a whole by especial averaging over constituents that directly make up the medium. The primary input for these models is the porosity. While these methods are generally applicable for any porous materials, they are not accurate enough for sensitive applications e.g. modeling CL gas diffusivity. Especially when the Knudsen diffusion is in effect, the accuracy of such models is highly in doubt [47].

Table 1.3 Available models for prediction of gas diffusivity in porous medium

Modeling Method	Advantages	Disadvantages	ref
Medium theory	Compact relation using only porosity as input	Highly overestimate diffusivity	[24,48]
Percolation theory	Compact relation	Inaccurate for large pores	[49,50]

Pore network	Considering some geometrical details about porous medium	High computational cost	[51–55]
Stochastic-based numerical models	Considering some geometrical details about porous medium	High computational cost	[56–60]
Geometry reconstruction based on imaging techniques	Potentially high accuracy Full details about geometry	High computational cost Expensive imaging techniques	[47,61–67]

A network of pore units connected with throats is developed in pore network models. Features of the network, e.g., shape of the pores and the neck diameter of the throat are specified based on the medium characteristics. The stochastic-based modeling targets the solid part of the medium. The solid part is constructed from arranging solid units, e.g. fibers or spheres partially randomly to keep both randomness of the geometry and some characteristics of the medium, e.g. porosity. The transport properties of CL can be modeled accurately using reconstructing the geometry based on focused ion beam electron microscopy (FIB-SEM) images or X-ray Nano-CT of the CL. Stochastic-based, pore network, and reconstructing methods all consider more details about the geometry than the effective medium theory. While potentially more accurate (especially reconstructing methods), the problem is being computationally demanding, making them difficult to use for the study of CL designs; also they require many input parameters (geometrical as well as material properties) which make their application challenging. Therefore, there is a vital necessity for a user-friendly, inexpensive, and timesaving model for gas diffusivity within MEA components. One approach to address this issue is to assume a simplified geometry for the porous cluster, which still preserves the main features like porosity, pore size distribution (PSD) and general shape. In this approach, an organized structure of small unit cells is assumed. The unit cell has all the main features of the CL and repeated through the geometry to form the CL. Transport properties of such unit cell are the same as ones for the CL. Because of the organized configuration, the unit cell approach is less computationally expensive. There are successful unit cell models for transport properties of GDL [68,69] and CL [70]. In the CL, the concept of spherical carbon particles with a small overlap, covered with ionomer was used in Ref. [71,72], and spherical agglomerates touching each other without any

overlap in Ref. [73–77]. However based on reconstructing numerical simulations using FIB-SEM, such unit cells consider a high active surface area for agglomerates in CL [78]. The unit cell model with spherical agglomerates overestimates the diffusivity of CL. Another problem with such models is that they cannot capture low porosity of CLs (~ 0.2-0.4).

1.6.3. Comparison between CL diffusivity values measured/modeled in literature

Table 1.4 shows the CL relative diffusivity values reported in the literature obtained using different methods. There is limited available data on CL diffusivity and none of the values listed in Table 1.4 is for CLs prepared by the same procedures or measured under the same conditions.

Shen et al. [5] measured through-plane gas diffusivity of samples prepared through spraying a CL ink over the hydrophilic alumina support substrate. Spraying demands dilute ink, which can penetrate into the support substrate especially when it is a hydrophilic one. To eliminate the effect of the interfacial resistance due to the catalyst penetration into the substrate, authors measured the gas diffusion resistance of CLs with different thicknesses.

Yu and Carter [42] measured in-plane diffusivity of CL. Lower values of CL diffusivity are expected for the in-plane direction compared with the through-plane one because of the cracks and large pores. In the through-plane direction, cracks of several-micron-long can create pathways for oxygen to diffuse through the CL. These cracks are not expected to affect the in-plane diffusivity as dramatically as the through-plane diffusivity. They showed that diffusivity decreased sharply by increasing I/C, but gradually with the relative humidity (RH). Diffusivity decreases 70% and 95% going from I/C=0.5 to 1 and 1.5 respectively, while 20% and 25% going from RH=0 to 100% for I/C=0.5 and 1, respectively. Because of ionomer swelling, RH decreased the diffusivity. In low I/C ratios there was lots of space to be filled with ionomer swelling, whereas in high I/C ratios such space did not exist. Thus the RH effect was less on higher I/C ratios.

Inoue et al. [40] measured CL diffusivity using WKC. They targeted different I/Cs and carbon support types including black pearls, Ketjenblack, and graphitized to obtain a range of porosities. The coating method was spraying. There is no information about the support substrate or even existence of a support substrate for CL in this study.

Data in the literature for diffusivity calculated from in-situ impedance spectra, e.g., in Ref. [25] are an order of magnitude lower than the ex-situ measured gas diffusivities. One possible explanation could be that in-situ methods target the diffusion mechanism that delivers oxygen to the Pt particles (reaction sites). Oxygen should pass through water ionomer and primary pores in the order of several nanometers within or on the surface of agglomerates to reach the reaction sites. While in ex-situ methods, oxygen diffuses mostly through large pores of CL (in order of several hundred nanometers). The existence of two diffusivities for macro-pore and micro-pore structures in CL was also mentioned in Ref. [79].

Siddique et al. [47] reconstructed the structure of CL numerically by mimicking experimental fabrication process of CL. First locations of centers of agglomerates were distributed randomly thorough the domain and then carbon particles, Pt particles, and ionomer were added. Gas transport problem was solved numerically in the domain and oxygen diffusivity was determined as a function of the porosity. They showed that there was an optimum number for agglomerates per unit of volume from transport properties point of view.

Litster et al. [80] calculated the CL diffusivity numerically in a reconstructed geometry of a CL from Nano scale X-ray tomography. Diffusivity was locally assigned for pores, which was a combination of Knudsen and molecular mechanisms. They deduced that the transition regime diffusivity was significantly more sensitive to porosity. The increase in the effective diffusion coefficient from the lowest porosity to the highest porosity was 41% for molecular diffusion, whereas for the transition regime it was 89%. They also found out that diffusivity ratio for through-plane to in-plane was about 1.17.

Lange et al. [71] modeled CL considering carbon spheres covered with ionomer with a uniform thickness, distributed randomly in the computational domain. Using the model, the effect of carbon particle size, ionomer thickness, and overlap degree of carbon particles were evaluated. They showed that larger carbon particles lead to higher oxygen diffusivity values, and considering a uniform value of pore diameter to calculate the Knudsen diffusivity leads to over-prediction of diffusivity to some extent.

Berson et al. [63] obtained diffusivity as a function of porosity by reconstructing the geometry of the CL using a Monte-Carlo method. Monte-Carlo methods are a broad class of computational algorithms that rely on repeated random sampling to obtain numerical results while preserving some distributed properties.

Table 1.4 Relative diffusivity values in literature[1]

J. Shen et al. [5]	Ex-situ, MLC	T=25 ºC, spraying on hydrophilic alumina		0.01
Z. Yu and R.N. Carter [42]	Ex-situ, WKC (in-plane)	T=80 ºC, I/C=0.5, 1, and 1.5, RH=0	I/C=0.5	0.09
			I/C=1	0.03
			I/C=1.5	3×10^{-3}
G. Inoue et al. [40]	Ex-situ, WKC	T=22 ºC, P=201 kPa, Pt/C=0.5, spraying	ε=0.41	0.01
			ε=0.52	0.05
			ε=0.61	0.1
			ε=0.73	0.18
K. Wippermann et al. [25]	In-situ, impedance spectra	T=30 ºC		~ 10^{-3}
Siddique and Liu [47]	Numerically mimicking fabrication process	T=75 ºC	ε=0.30	9×10^{-3}
			ε=0.45	0.05
			ε=0.60	0.07
S. Litster et al. [80]	Nano X-ray tomography, geometry reconstruction	I/C=0.65, T=330 ºK, ε =0.42, Pt loading=0.9 mg/cm^2, Hand printed	Molecular	0.21
			Molecular and Knudsen	0.08
Lange et al. [71]	Numerically, considering spherical carbon particles		$r_{carbon\ particle}$=40 nm, ε=0.30	~0.05
			$r_{carbon\ particle}$=40 nm, ε=0.40	~0.09
			$r_{carbon\ particle}$=40 nm, ε=0.50	~0.15

[1] For most of the references there are more data points available in the original papers

	covered with ionomer		
A. Berson et al. [63]	Monte-Carlo geometry reconstruction	ε=0.30	~0.18
		ε=0.40	~0.28
		ε=0.50	~0.45

1.6.4. CL pore size distribution (PSD)

The CL composition and structure define its transport properties. Therefore, the structural investigation of CL is a major topic of many studies in the fuel cell literature. As PSD and morphology have a crucial role in specifying the gas diffusivity of CL, here, initially, different methods to study the CL PSD are discussed, and then, part of the results obtained for the effect of catalyst processing and composition on its PSD in literature will be reviewed.

Different methods to characterize CL include visualizing CL structure [61,71,81,82], numerical modeling [47,79,83], and effective property measurements [20,84,85]. Each method has limitations. All numerical models first should be validated by experimental measurements to be considered reliable. Although the FIB-SEM technique is a powerful method used for visualization and determination of PSD, it is expensive and there are many challenges when it is applied to fuel cell CLs. FIB-SEM tomography samples only a small volume, selected during imaging. The gallium ion beam can damage the surface of the sample, causing a curtaining effect, affecting the quality of the images. Ionomer and carbon in the CL can be locally smeared under the beam, closing the small pores. Another challenge is image segmentation, specifically resolving the solid phase from the voids [82], using Feret maxima measurements, fitted sphere algorithms, or other similar methods.

Mercury intrusion porosimetry (MIP) (see Figure 1.5), and N_2 adsorption porosimetry (see Figure 1.6) are conventional techniques used to measure the PSD of CL. MIP applies compressive loads up to 30,000 psi, which might crush the CL samples. Another problem is the fact that, the contact angle of mercury is different for Pt particles and carbon particles and using a single contact angle limits accuracy of MIP [86].

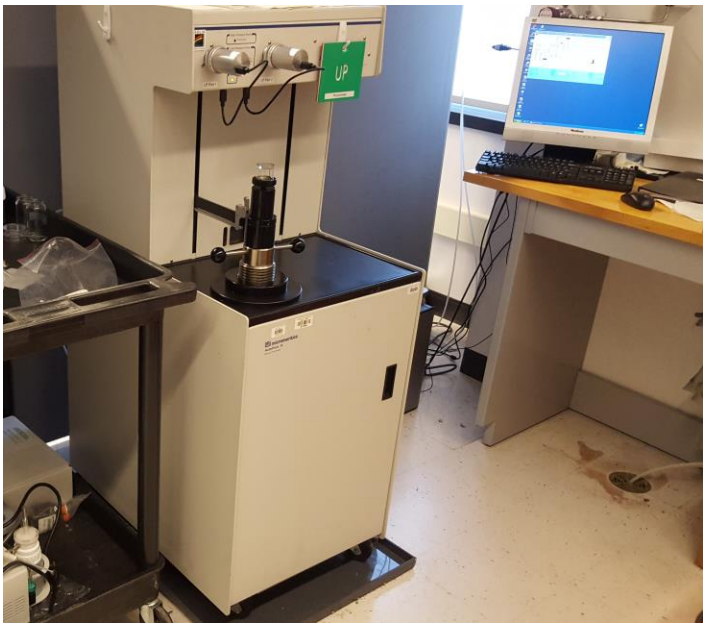

Figure 1.5 AutoPore IV 9500 mercury intrusion porosimeter

Figure 1.6 Autosorb iQ-MP, Quantachrome N_2 adsorption porosimeter

In the recent literature, CL isotherms obtained by N_2 adsorption porosimetry are commonly analyzed using the BJH method. The Barrett-Joyner-Halenda (BJH) approach predicts the equilibrium vapor pressure at which nitrogen condenses on the curved surface of pores of a given size. The desorption branch of isotherms traces equilibrium transitions, while the adsorption branch is metastable. However, delayed desorption

from large pores when there are significant networking effects, including pore blocking or cavitation, can create artifacts in the PSD obtained from the desorption branch. Morishige [87], and Morishige and Tarui [88] measured nitrogen adsorption isotherms for three samples of controlled pore glasses with mean pore diameters of 16.0, 24.4, and 37.8 nm. For isotherms that have cavitation, they showed that the use of the adsorption branch to calculate PSD is preferable.

BJH can detect pores smaller than 300 nm that covers the pore range of the CL. However, BJH analysis is known to underestimate pore size in comparison with X-ray data [89], particularly for narrow mesopores with diameters less than 10 nm, and it excludes micropores [90]. The accuracy of BJH results also decrease at the right bound of its detection range, 300 nm. De Lange et al. has established that the BJH method yields PSDs with a high degree of uncertainty [91]. Therefore, for quantitative investigations of the CL PSD, one should be cautious using BJH method. On the other hand, molecular level microscopic theories, such as non-local density function theory (NLDFT) or quenched solid density functional theory (QSDFT), provide a more accurate representation of the filling of narrow mesopores and micropores. They accurately account for the local fluid structure near curved solid walls and compute adsorption isotherms for model pores using the intermolecular potentials of fluid-fluid and solid-fluid interactions [92]. NLDFT considers pore wall as a perfect surface, while QSDFT accounts explicitly for the effects of the surface heterogeneity and characterize it by a single roughness parameter [93]. The isotherms obtained using such models can be compared with the experimentally obtained isotherms to attain a more accurate PSD than those yielded by macroscopic theories [94]. However, the pore detection range for these theories is limited, e.g. 0.4-35 nm for QSDFT [93].

Different deposition methods, such as inkjet, spray, and Mayer bar coating, create different pore structures. The I/C ratio, Pt/C weight ratio, carbon support type, ink viscosity, drying temperature, ink mixing (i.e., ionomer dispersion), ink solvent, and the substrate can also affect the structure. Using the mentioned methods, researchers investigated the effect of some of the mentioned parameters on PSD and pore structure of the CL (Table 1.5).

Table 1.5 Studies evaluating the effect of composition and processing on CL structure

Method	
FIB-SEM reconstruction	Airbrushed CL was found to have lower porosity and larger mean pore size than sprayed CL (44.9% vs 62.5%; and 233 nm vs 113 nm) [61].
MIP	The effect of high-boiling-point solvent in the catalyst ink on the CL microstructure was investigated. By choosing the anion CL with a designed PSD, the power output improved by 55% [95].
MIP	The effect of organic solvent on the structure of CLs with I/C of 0 and 0.3, before and after hot pressing, was investigated. Adding ionomer increased the peak pore diameter from 74 to 95 nm [96].
Water vapor sorption	The vapor sorption of CL prepared with Ketjen Black and Vulcan carbon with different I/C ratios was investigated. Operating under dry conditions requires higher ionomer content compared to humid conditions. Narrow PSD is preferable for cathode CL (where water removal is crucial), while a broader PSD is advantageous for anode CL [84].
N_2 adsorption (BJH)	The fraction of micropores in Ketjen Black was found to be about 25% of the total pore volume, while in Vulcan XC-72 the portion was 15% [20].
MIP	The effect of sulfonated polyetheretherketone (SPEEK) content on the performance of CL was studied. The particle size for catalyst inks containing SPEEK was smaller than the corresponding Nafion-catalyst. SPEEK CL was denser. The thickness of CL decreased from 14 to 4 μm when SPEEK content was increased from 10 to 40 wt% [97].
MIP	The larger I/C, the lower porosity, mean pore, and gas diffusivity. CLs made with Pt particles on amorphous carbon had a larger

N_2 adsorption (BJH)	mean pore, porosity and diffusivity compared with CLs made with Pt particles supported on graphitized carbon as measured with MIP and N_2 adsorption (BJH) porosimetry. The PSD in range of 3 to 20 nm in MIP is due to ETFE compression [85].
MIP	While the volume of primary pores was almost independent of I/C, the volume of secondary pores decreased with increasing I/C [18].
N_2 adsorption (BJH)	Pt content and pore structure gradient distribution were studied. Utilizing a two-layer CL, with Pt poor and rich sides, 11% power generation boost was achieved. Larger pores on the Pt poor side increased the gas diffusivity [98].
N_2 adsorption (BJH)	The effect of catalyst pore size (4.0 to 8.1 nm) on oxygen reduction was investigated for ordered mesoporous carbon FDU-15 supported platinum, and 6.4 nm pore size had the highest rate [99].
Stochastic reconstruction and MIP	CL structure was modeled based on a stochastic reconstruction method, and the PSD was validated with MIP data from Ref. [100]. The effect of agglomerate size (40 to 180 nm) on the PSD was investigated. The decrease in porosity and mean pore diameter of CL with increasing RH, because of ionomer swelling, was quantified [101].
N_2 adsorption, STEM observation	Carbon black, graphitized carbon black, and 30 wt% acetylene black (AB)-supported Pt catalysts were investigated. The presence of Pt particles in the interior structure of carbon support particles had a negative effect on the accessibility of Pt particles and electrochemical performance of the cathode CL. In (AB)-supported Pt, the catalyst particles were located on the exterior of the support particles, which improved the performance under high current densities when mass transport is a limiting factor [102].
MIP **N_2 adsorption**	Investigating twelve carbon support types with the different surface area, they concluded that improvement of PEMFC performance

(BJH)	was achieved by optimal carbon support with a larger pore volume able to distribute the perfluorosulfonated ionomer over Pt inside the agglomerate [103].
SEM imaging	The effect of electrospray (ES) parameters on CL coatings was investigated (e.g. nozzle diameter and applied voltage) to improve ionomer coverage, increase active surface area values, and create highly porous CLs with increased gas mass transport efficiency at current densities below 0.5 A cm^{-2} at 80–100% RH [104].
Method of standard porosimetry	The effect of different Pt loading and carbon to platinum weight ratio was investigated on the PSD and gas diffusion/permeation of the fuel cell electrode [105].

Chapter 2.

CL Samples Synthesis

2.1. Substrate and coating selection

There are two primary criteria to be considered when choosing a support substrate for the CL diffusivity tests: i) low diffusion resistance, and ii) low engagement with the CL. To measure diffusivity, the total resistance of the CL and the support substrate are measured together, and then, CL diffusivity resistance is de-convoluted from the resistance measured for the multilayer CL-substrate sample. Therefore, the support should have the lowest possible diffusion resistance relative to the CL, i.e., it should be highly porous and as thin as possible (CL is generally less than 10 µm thick). On the other hand, the support should have sufficient mechanical strength for coating and handling as well.

Beside the low resistance, the substrate should not adsorb CL during the coating procedure. As for diffusion tests, the substrate should be porous. Depositing CL on the substrate, some of it might penetrate into the substrate, which may introduce an interfacial resistance. Such resistance compromises the accuracy of the result for diffusivity of CL. Thus, the substrate alongside with the coating method should be appropriately chosen to minimize such penetration.

There are several coating methods for CL including spraying, printing, hand brushing, dipping, decal transferring, and Mayer bar using. As coating method might have an effect on CL structure and its properties, to produce CLs similar to the ones used in PEMFC, it is better to choose the same fabrication method as the one used in manufacturing the cell.

Two inkjet printers were used in this study. The first one was Fujifilm Dimatix Material Printer DMP2800 (Figure 2.1), an inkjet printer which utilized disposable piezoelectric inkjet cartridges to distribute fluids. The capacity of each cartridge was about 1.5 mL. The printer had a metal vacuum plate (20 x 28 cm) of which temperature can be controlled (<60 °C). The printing pad had an electronic pulse producer, which could design a proper droplet and a camera, which did the followings:

- Capturing images of printed patterns or droplets;
- Locating original starting positions to match initial substrate placement;
- Measuring distances between 2 points;
- Allowing substrate rotational alignment;

Figure 2.1 Fujifilm Dimatix material printer DMP2800

The printer head contained sixteen 20-μm nozzles with spacing about 254 μm. The preferred particle size and viscosity were about 200 nm and 12 cP, respectively. Droplet spacing and resolution could be controlled by changing the angle of the cartridge.

The second inkjet printer was MicroFAb Jetlab4 printer (Figure 2.2). The printer had an 80-μm nozzle. A pulse generator designed the droplet size, speed, shooting interval and angle with voltage up to few hundreds V and effective current over 100 mA. The stage could move in 3 directions and rotate in one direction. It also had a heater, which made it possible to set the stage temperature. The droplet frequency, size, and orientation were also controllable. The tool was equipped with a camera, which could be used to check the quality of the droplet.

Both of the mentioned printers were used, and the quality of CLs produced by each method was evaluated. Printing demanded dilute catalyst ink to prevent nozzle clogging. Dilute ink could easily penetrate into the porous substrate, especially if the surface was a hydrophilic one. As an attempt to evaluate printing, Sigracet GDL 24BC (Table 2.1) was used as a substrate to coat the CL on.

Figure 2.2 MicroFAb Jetlab4 printer

Table 2.1 Specification of Sigracet GDL 24BC, used as substrate, manufacturer data (except for porosity)

Substrate	Thickness	PTFE %	Areal weight	Porosity
GDL 24BC	235±9 µm	5	100 g/m^2	84%[8]

Figure 2.3 shows an SEM image of the cross-section of the CL coated on MPL-GDL substrate. The dilute ink penetrated into the pores of the substrate, which was not acceptable for diffusion tests. In attempts to use viscous ink, nozzle clogging happened that prevented a uniform CL coating. It should be mentioned spraying catalyst ink on the substrate, also demand a dilute ink, which found to be not desirable.

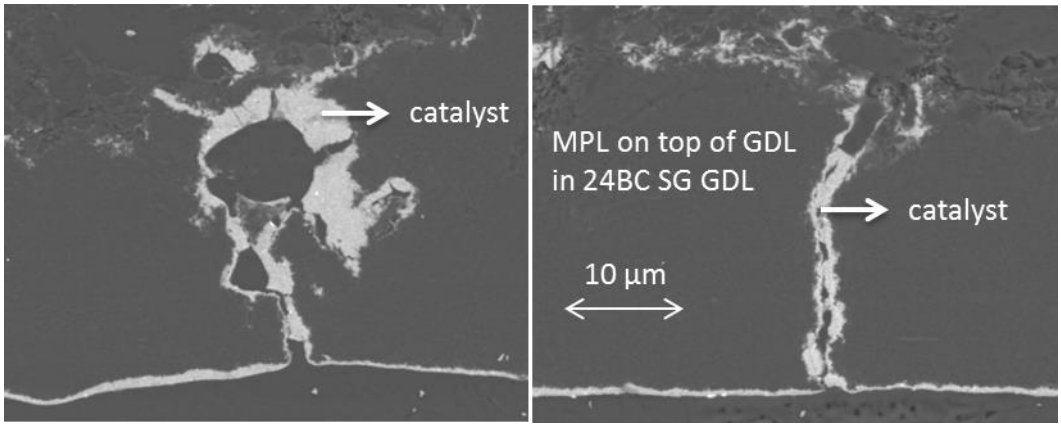

Figure 2.3 SEM images of the cross-section of the CL coated on the MPL-GDL with two different printers (DMP2800 inkjet on the left side and Jetlab MicroFAb on the right side). This shows penetration of the CL into the substrate in both cases.

To eliminate the CL penetration into the substrate in the next step, instead of printing, decal-transfer method was used. Decal-transfer is one of the conventional methods to transfer CL onto the membrane in fuel cell fabrication, wherein, the catalyst ink is coated on ETFE sheets using printing or in large scales using Mayer bar. Then the CL is sandwiched between target membrane and the ETFE sheet, and pressed under 15 bars and 150 ºC for several minutes. After that, hot-press ETFE sheets were peeled off from the sandwich and the CL stayed on the membrane (Figure 2.4).

Hot-press could transfer the CL on any substrate if the target substrate is less hydrophobic than the ETFE or original one. Because in this method there is no fluid ink, the least CL penetration onto the target substrate could be obtained. Using decal-transfer, CL was coated on the various substrates given in Table 2.2. In all cases, the transfer was successful; however, harsh conditions of hot-pressing ruined all the tested substrates. As the substrate should be a thin porous layer, none of the tried substrates could bear the hot-press condition, and all become rigid after the procedure.

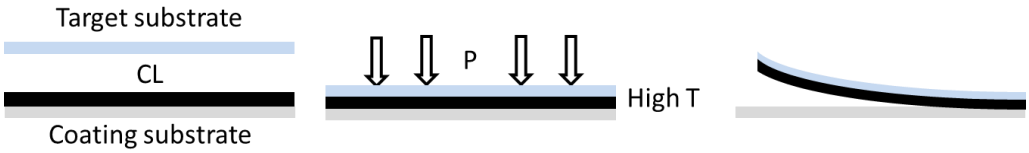

Figure 2.4 Decal transferring CL from coating substrate to the target one

Table 2.2 **The tested substrates for decal transfer. The substrates are all hydrophilic; porosities are chosen to be low to bear decal transfer condition.**

Supplier	Pore diameter nm	Thickness µm (supplier)	Thickness [2] ± 1 µm	Porosity %[3]	Porosity % (supplier)	Glass transition ºC (supplier)
Nuclepore	15	-	6	11	-	140
Nuclepore	10	-	10	8	-	140
Nuclepore	50	-	10	1	-	140
Sterlitech	100	8.3	6	3	-	140
Sterlitech	400	29.0	10	13	-	140
Sterlitech	1000	-	11	16	-	140
Sabeu	1000	22.0	22	16	17	150-160
Sabeu	500	22.0	22	17	16	150-160
Sabeu	200	23.0	22	9	12	150-160
Sabeu	100	-	-	-	50	150-160
Sabeu	300	-	-	-	60	150-160
Millipore	100	-	25	5	4	150
Millipore	220	37.0	25	19	14	150
Millipore	400	-	10	19	5-20	150
Millipore	600	27.0	28	11	5-20	150
Millipore	800	19.0	25	20	5-20	150
Millipore	200	170	-	-	70	150
Millipore	220	125	-	-	70	150

[2] Measured by custom made thickness measurement tool, Tuc Ruc at Automotive Fuel Cell Cooperation Corporation (AFCC)

[3] Measured by N_2 adsorption porosimetry at AFCC

Table 2.3 Filter PTFE membranes and GDL-MPL 24BC specifications

Supplier	Pore diameter nm (Supplier)	Thickness µm (Supplier)	Porosity % (Supplier)
Millipore	450	50	<85
Millipore	450	150	85
Sigracet	-	230	76

As decal transfer could not be used with porous substrates, in the next step, Mayer bar was tried. Mayer bar coating is widely used in industry for mass production of CL. Mayer bar coats catalyst ink onto a substrate by spreading the ink with a rolling bar at a specific distance from the surface (Figure 2.5). It can use a highly viscous ink, which prevents the ink penetration into the surface of the hydrophobic support. Two highly hydrophobic filter PTFE membranes and Sigracet GDL-MPL 24BC (specifications in Table 2.3), were chosen to be tested with the Mayer bar.

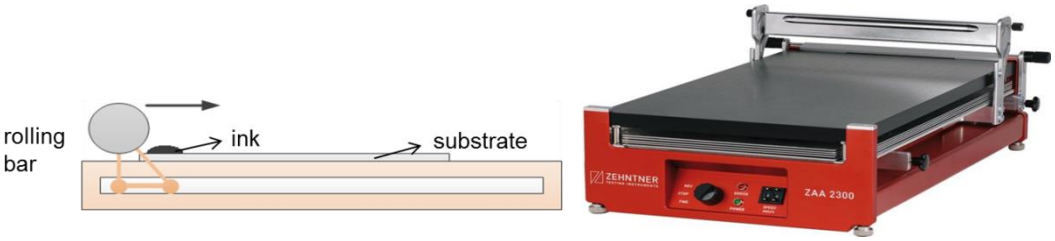

Figure 2.5 Mayer bar coating

The coating on GDL-MPL was not successful, as shown in Figure 2.6. However, the coatings on both PTFE filters were successful. Figure 2.7 shows an SEM image of the cross-section of the CL coated on the 50 µm-thick filter PTFE with Mayer bar. The CL was uniform with the low penetration into the filter. The thicker filter was supported by the PTFE, which made it more rigid and easier to handle. However, the pattern on the surface (Figure 2.8) made the CL thickness measurements challenging. On the other hand, the thin filter had no patterns on the surface, however, needed special handling. Aiming for the best measurement's accuracy, the 50 µm-thick filter PTFE membrane (Fluoropore FHUP04700, EMD Millipore) was selected as the final substrate with Mayer bar coating. A sample preparation procedure was devised to provide guidelines to handle the substrate.

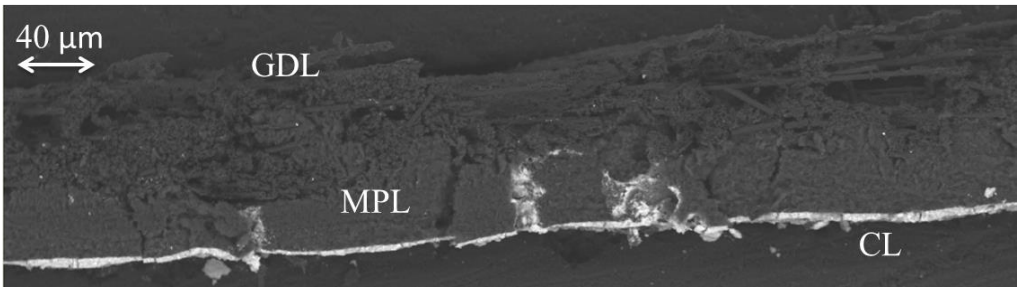

Figure 2.6 The SEM image of CL coating on GDL-MPL 24BC with the Mayer bar

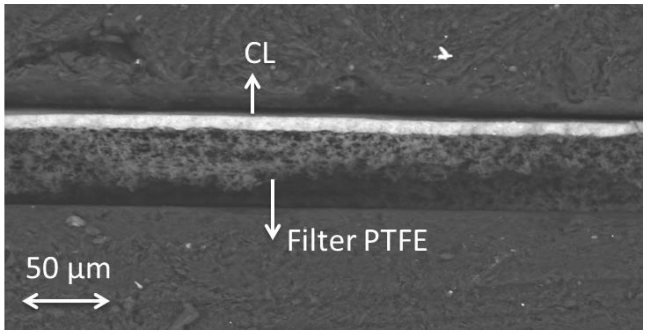

Figure 2.7 SEM image of cross-section of CL coated with the Mayer bar on the Fluoropore FHUP04700 filter PTFE

Figure 2.8 The pattered surface of 150µm-thick filter PTFE substrate

2.2. Sample preparation procedure

In Mayer bar coating, the distance between the rolling bar and the surface of the substrate determines the thickness of the coated CL. Any wrinkles on the surface of the substrate can highly compromise the uniformity of the CL. Therefore, particular sample preparation method should focus on minimizing coating imperfections. In the present study, the circular disc filter PTFEs were placed on the top of a solid hydrophobic backing layer (a solid PTFE substrate) with almost the same thickness as the substrate (50 µm). The two materials were punched out using a hole puncher with the diameter of

about 1.75”, slightly smaller than the filter PTFE samples. The filters were fitted into the holes in the backing layer template, and kept fixed with a suction surface. While under suction to prevent wrinkling, the edges of the filters were taped to the backside of the template, as shown in Figure 2.9. The template was fixed faced up on the coating pad of the Mayer bar to be coated by the rolling bar.

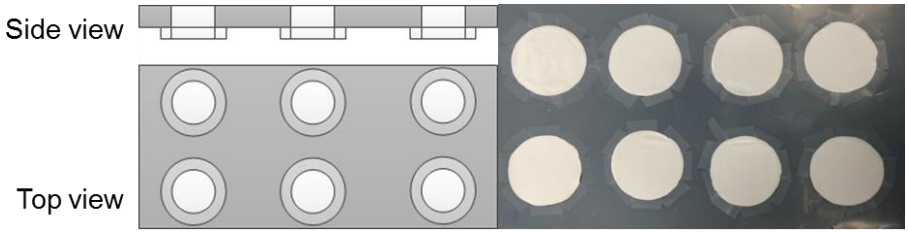

Figure 2.9 Template support for the filter disk substrates to be catalyst-coated by the Mayer bar

After coating and drying, the CL coated filter substrates were punched out of the template.

2.3. Catalyst ink preparation

The catalyst ink was prepared using catalyst powder consisting of Pt nanoparticles deposited on 10 to 50 nm partially graphitized carbon particles (50% weight, carbon particle mean diameter of 30 nm). The catalyst powder and zirconia balls were placed in a ceramic jar and rotated at 60 to 100 rpm with a jar mill (US Stoneware, model 755 RMW). The catalyst powder was milled for 0 to 48 hrs depending on the design. To prepare the catalyst ink, the powder was dispersed in the solvent (deionized water and alcohol). Then, aqueous ionomer dispersion (Aquivion® PFSA, Solvay) was added. Finally, the ink was placed in a ceramic jar containing zirconia balls and jar milled in the same proprietary way for all designs. The ink was coated by Mayer bar on ETFE and filter PTFE sheets. After drying on a hot plate at 50 ˚C (or 20 ˚C depending on the design), the CL samples coated on the filter PTFEs were used for gas diffusivity measurements. Also, the ones coated on the ETFE was decal transferred onto Nafion membrane (25 μm NRE211, Chemours) by hot pressing at 150˚C and 15 bar for 2.5 minutes for PSD measurements. In total, more than 500 samples were prepared to evaluate the CL composition and processing parameters. The parameters that were varied include ionomer content of the ink, the dry milling time of the catalyst powder, and the drying temperature of the coated ink, as summarized in Table 2.4.

Table 2.4 CL designs I/C, dry milling time, and drying temperature

Design number	**1**	**2**	**3**	**4**	**5**	**6**	**7**	**8**	**9**	**10**	**11**	**12**
I/C	1.5	1.1	1.1	1.1	1.1	1.1	0.9	0.9	0.9	0.7	0.7	0.5
Dry milling time, hr	0	48	6	0	0	48	48	24	6	48	24	0
Drying temperature, ˚C	50	50	50	50	20	20	50	50	50	50	50	50

2.4. Chapter 2 acknowledgement

The material and coating facilities for sample preparation were provided by Automotive Fuel Cell Corporation (AFCC). The AFCC Structure, Properties and Performance Research Division is acknowledged for their technical support.

Chapter 3.

CL Thickness, Porosity, and PSD

3.1. Thickness measurement

Three methods were used to measure the CL thickness: a custom-made thickness measurement tool called TUC-RUC machine (~1 µm accuracy); studying SEM images of the cross-sectioned CL coated substrates obtained by freeze and fracture procedure; and a densitometer set up.

3.1.1. TUC-RUC thickness measurement

The TUC-RUC (Thickness Under Compression - Resistivity Under Compression) machine is a custom-made machine designed by Automotive Fuel Cell Cooperation (AFCC) (Figure 3.1) to measure electrical resistivity and thickness at different compressions (up to 5 MPa). The accuracy of thickness measurement is 1 µm, and the testbed is programmable to measure the sample thickness at the given compression points by the user.

To measure the CL thickness with TUC-RUC, stacks of 10 layers were used, as the measurement accuracy for a single layer was not acceptable (1 µm divided by the CL thickness which was mostly less than 10 µm). Both the CL and the filter PTFE were porous layers which could be compressed easily. Therefore, no specific compression value could make the perfect contact between the CL or filter PTFE and the device probes, yet not compress the samples. As a result, instead of a single thickness measurement at no compression, for each stack, plots of thickness versus compression load was obtained, and the thickness of the stack at zero compression load was extrapolated from the obtained plot. After optimizing the procedure, to measure the stack thickness, the 2 MPa starting point was chosen, and the compression was increased with 500 kPa steps to 5 MPa. At each step, the dwelling time was three seconds to ensure reaching to steady state (more dwelling time may introduce creep to the results). Each stack was tested under compression for eight cycles to investigate the potential

hysteresis effects. The result of the first cycle was not used since the first cycle only closed the “gaps” between the layers in the stacks.

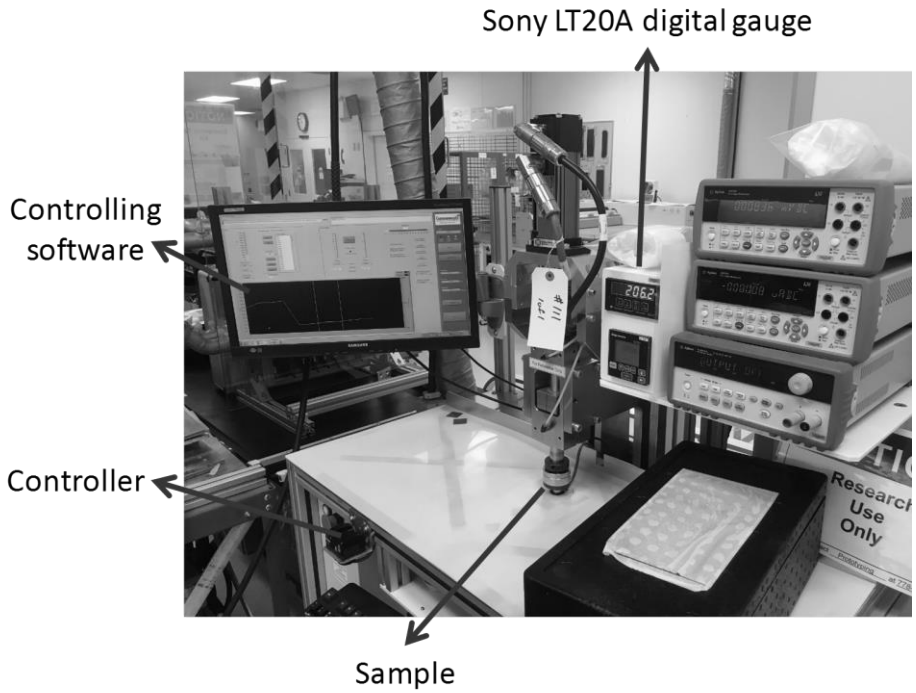

Figure 3.1 TUC-RUC test setup

To find the CL thickness in each stack, the measured thickness of the bare filter PTFE stack was subtracted from the measured thickness of the stack of catalyst-coated filter PTFE stack. The measurements were repeated at least three times. The average CL thickness for each sample was obtained by dividing the total CL thickness by the number of samples per stack.

3.1.2. SEM imaging thickness measurement

The thickness of the CL was also measured by studying the SEM images of cross-sectioned CL coated substrates obtained by freeze and fracture procedure. In this method, the CL samples were sandwiched between graphite plates in a sample holder shown in Figure 3.2. Then the whole sandwich was immersed in liquid nitrogen, and under low temperature, the cross-section was cut with a sharp lancet. Cutting under such low temperature caused minimal defects. Then the SEM images of the cross-section were obtained, and the thickness of the CL was measured using Image Pro

software and the magnification factor for the SEM image. Figure 2.7 shows one of the images used to measure the thickness of the CL. For each sample at least 3 cross-sections were prepared, and for each cross-section at least 3 different locations were examined. The length of each examined cross-section was in order of 100 µm.

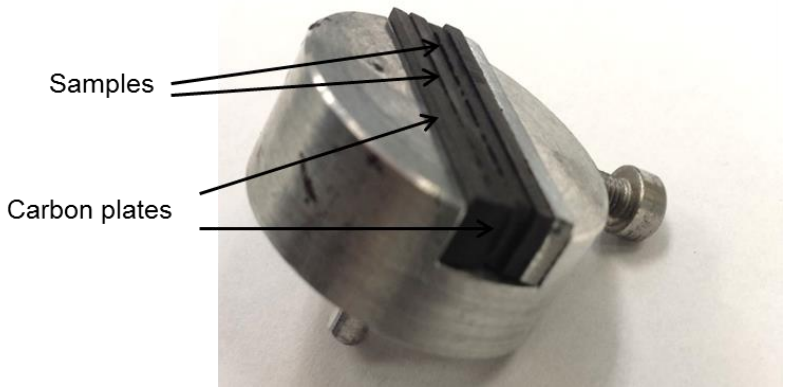

Figure 3.2 Sample holder for SEM thickness measurement

3.1.3. Densitometer thickness measurement

An analytical balance (Ohaus AX124, accuracy: ±0.1 mg) and a densitometer (Ohaus) were used to measure the thickness of the CL, using Archimedes' principle (buoyancy method). The weight of a body immersed in a liquid is decreased by the upward buoyancy force that is equal to the weight of the liquid displaced by the body. The difference between the weight of a body in the air (almost zero buoyancy force) and the weight in the liquid was used to calculate the volume of the displaced liquid:

$$V_{\text{liquid}} = (W_{\text{air}} - W_{\text{water}})/(g\rho_{\text{water}})$$

Eq. 7

As both of the filter PTFE and CL are extremely hydrophobic layers, which do not absorb water, the displaced volume of the water was equal to the bulk volume of the body:

$$V_{\text{bulk}} = (W_{\text{air}} - W_{\text{water}})/(g\rho_{\text{water}})$$

Eq. 8

To find the volume of the CL, the weight of catalyst-coated filter PTFE samples and bare filter PTFE samples were measured both in the water and air, and all of the bulk volumes were obtained using Eq. 8. The difference between volumes of the catalyst-coated filter PTFE and the bare filter PTFE was the CL volume. Dividing the CL volume by its area, the average thickness was obtained.

For each sample, measurements were repeated at least three times. The area of tested samples was 6 cm^2, and the CL weight in the sample was around 10-20 mg.

3.1.4. Thickness measurement methods evaluation

The CL thicknesses of different samples/designs were measured with all mentioned methods to evaluate the measurement results (See Figure 3.3).

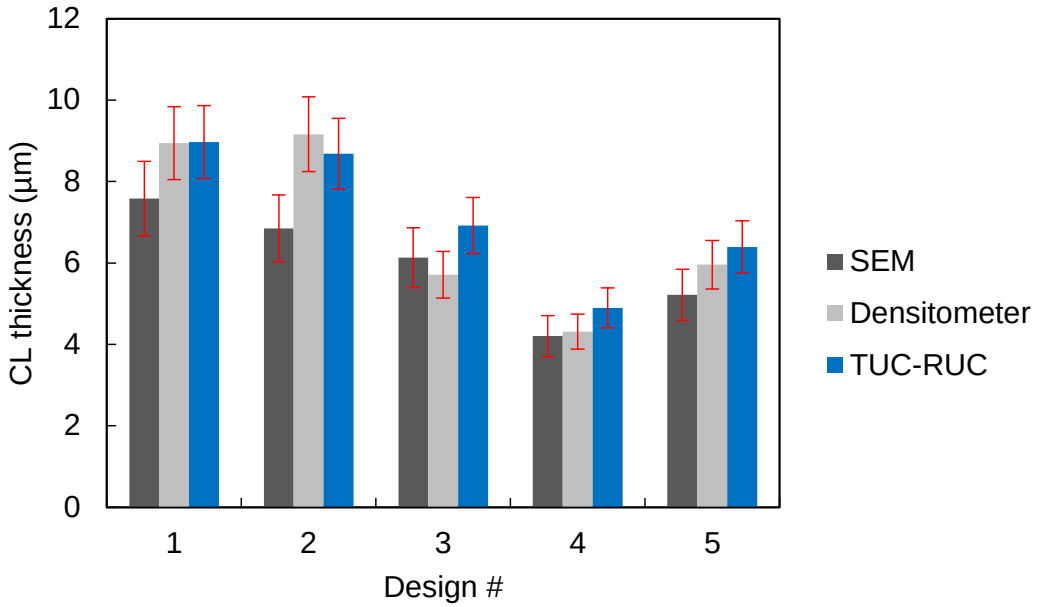

Figure 3.3 **The comparison between the thicknesses obtained by SEM, densitometer, and TUC-RUC for five CL designs: #1: I/C=1.1, dry milling time=0 hr, drying temperature= 50 ˚C; #2: I/C=1.1, dry milling time=0 hr, drying temperature= 20 ˚C; #3: I/C=0.9, dry milling time=6 hr, drying temperature= 50 ˚C; #4: I/C=0.7, dry milling time=48 hr, drying temperature= 50 ˚C; and #5: I/C=0.7, dry milling time=24 hr, drying temperature= 50 ˚C. The error bars show the standard deviations for at least three measurement repetitions.**

All methods resulted in almost the same measured values for different CL samples. Therefore, mostly TUC-RUC was used to measure the CL thicknesses, as it was easier to conduct compared to the other two methods, and was harmless to the CL samples.

3.2. Porosity and PSD measurements

3.2.1. Theoretical porosity based on thickness and Pt loading measurements

CL porosity could be calculated based on measured CL thickness, Pt loading, and the densities of CL components using Eq. 9:

$$\varepsilon = 1 - \left(\frac{\lambda_{Pt}}{t_{CL}}\right)\left(\frac{1}{\rho_{Pt}} + \omega_{C/Pt}\left(\frac{1}{\rho_C} + \omega_{I/C}\frac{1}{\rho_I}\right)\right)$$

Eq. 9

where λ_{Pt} is the measured Pt loading in kg/m^2 (by X-Ray scanning the CL samples), $\omega_{C/Pt}$ is the carbon to platinum weight ratio, $\omega_{I/C}$ is the ionomer to carbon weight ratio, and t_{CL} is the CL thickness (m). The used density values were ρ_{Pt}=21.5 g/cm^3 for Pt [106], ρ_C=2 g/cm^3 for carbon black particles [107], and ρ_I=1.9 g/cm^3 for ionomer [108].

3.2.2. Densitometer porosity measurement

The CL bulk volume and thickness measurements with densitometer were explained in section 3.1.3. To find the porosity of the CL, the solid part of the volume should be determined. It was done by measuring the weight of the CL in octane. Octane has a very low surface tension and penetrates almost into all open pores of a CL sample. Therefore, the solid volume of the porous sample was calculated from the weight difference in air and octane:

$$V_{\text{solid}} = (W_{\text{air}} - W_{\text{octane}})/(g\rho_{\text{octane}})$$

Eq. 10

The porosity of the sample was calculated from the ratio of the solid volume to the bulk volume:

$$\varepsilon = 1 - V_{\text{solid}}/V_{\text{bulk}}$$

Eq. 11

3.2.3. Mercury intrusion porosimetry

The capillary law for penetration of liquids into small pores is the basis of mercury intrusion porosimetry (MIP). In the case of non-wetting liquids and cylindrical pores, this

law relates the pressure of intrusion, to the contact angle, pore diameter, and the liquid surface tension (details can be found in Ref [109].

In MIP, following steps are done to measure porosity and PSD:

1. The test sample undergoes vacuum condition.
2. The test sample is filled with mercury under varying pressure from low to high values.
3. At each pressure step, the volume of mercury injected into the sample is monitored.
4. Based on the mercury properties, the injection pressure values are related to the pore diameter they fill, and the volume of injected mercury into the pore volume. The sample PSD is obtained plotting these volumes versus pore diameters.
5. The total injected mercury volume shows the total pore volume of the sample. Dividing this volume by the sample total volume results in the porosity of the sample.

AutoPore IV 9500 instrument (Figure 1.5) available in the 4D LABS of Simon Fraser University was used to measure PSD of the CL samples. This instrument has low and high injection pressure ranges, which covers 1.5 to 30000 psi. For CL materials, such pressure range leads to theoretical detection of pore diameter from 10^{-9} to 10^{-4} m that completely covers the pore size in the CL. For each test, at least 300 mg of CL was used. Advancing and receding Hg contact angles about 130 ° was considered. The set values for evacuating pressure (step 1 of the measurement), evacuation time (step 1 of the measurement), and the equilibration time (to reach steady state at each pressure step) were 60 µmHg, 300 sec, and 10 sec, respectively. For each chosen CL design, at least three samples were tested. For each test, a total of 53 data points were collected.

3.2.4. N_2 adsorption porosimetry

N_2 adsorption porosimetry is another way to measure the CL PSD. The PSD and pore volume of the subject material is found based on the obtained isotherms of nitrogen (adsorption/desorption) for the sample at the saturation temperature of nitrogen at the atmospheric pressure. To obtain the isotherms, following steps were followed:

1. The sample was outgassed under vacuum of elevated temperature (50°C).

2. The under vacuum sample cell with the sample was immersed in liquid nitrogen (saturation temperature of nitrogen at atmospheric pressure).
3. The nitrogen gas was introduced to the sample (initially under vacuum) to change the partial pressure of gas incrementally from 0 (vacuum) to partial pressure 1. At each step, the amount of gas adsorbed by the sample was monitored (adsorption curve).
4. Decreasing the partial pressure of nitrogen from 1 to 0, desorption curve was obtained.

Based on different theories, the amount of gas adsorbed and desorbed at each partial pressure (isotherm) could be analyzed to obtain the PSD and total pore volume.

In this work, a volumetric nitrogen physisorption porosimeter (Autosorb iQ-MP, Quantachrome Instruments, Figure 1.6) was used to measure the isotherms of the CL samples. The CL samples were dried under vacuum for about 10 hrs at 50˚C. A 9 mm sample cell with bulb and filler rod was loaded with at least 300 mg of catalyst-coated membrane for each test. A total of 200 data points were collected for each of the isotherms, and each test was repeated at least three times.

There are different theories that can be used to find the PSD of the test sample from the isotherms. The Barrett-Joyner-Halenda (BJH) method [110] is commonly used to find the PSD of the CL in literature. De Lange et al. has shown that the BJH method yields PSDs with high degree of uncertainty [91]. BJH misrepresents the filling of micropores and narrow mesopores, thereby underestimating the pore sizes [90]. Normally desorption branch of the isotherms are closer to equilibrium state and should be chosen to analyze the PSD [91], however if the tensile strength effect (TSE) (details can be found in Ref [91]) is detected in the desorption branch, adsorption branch should be used, as TSE can result in artificial PSDs.

Molecular level microscopic theories, such as density function theory (DFT), provide a more accurate representation of the filling of narrow mesopores and micropores by accurately accounting for the local fluid structure near curved solid walls, and computing adsorption isotherms for model pores using the intermolecular potentials of fluid-fluid and solid-fluid interactions [92]. The isotherms obtained using such models can be compared with the experimentally obtained isotherm to attain a more accurate PSD than those yielded by macroscopic theories such as BJH which have high uncertainties [94]. However they have limited pore detection range (0-35 nm) [90].

The non-local DFT (NLDFT) method (model detail can be found in Ref. [111]) considers pore wall as a perfect surface, while quenched solid DFT (QSDFT) (model detail can be found in Ref. [93]) accounts explicitly for the effects of surface heterogeneity and characterize it by a single roughness parameter.

To obtain the best possible PSD from the measured isotherms of the CL, a post processing code was developed in MATALB which was linked to the device software. The code did the following tasks:

1. It checked the isotherm set partial pressure points. If the changes in adsorbed/desorbed gas was too high/low between two pressure points, it modified the set points to make equal adsorbed/desorbed gas amounts between each two consequent points, i.e., more pressure points when there was a sharp change in the isotherm and less pressure points when the isotherm was flat.
2. It calculated BJH PSD based on the desorption curves, unless it detected TSE in the curve where it switched to the adsorption curve.
3. Based on the device specifications and equations presented in Ref. [91], the uncertainty of the obtained PSD was calculated.
4. DFT models can be used with different pore shapes. As CL pores are random and do not have a specific shape, the code ran all the DFT models including NLDFT equilibrium transition, NLDFT adsorption branch, QSDFT equilibrium transition, and QSDFT adsorption branch, applying all possible pore shapes for carbon-based materials. These shapes included cylindrical, cylindrical/spherical, slit, slit/cylindrical, and slit/cylindrical/spherical. The method with the least fitting error was chosen, and the PSD was obtained applying the chosen method.
5. It translated the obtained PSDs to histogram PSDs (pore range vs volume percentage), with the pore ranges set by the user. For each pore range, the average pore diameter was presented as well.

In this study, the QSDFT (equilibrium or adsorption branch) with slit/cylindrical or cylindrical pores had the least fitting errors, less than 2% for all of the CL samples except design #5, where the fitting error was less than 3%.

3.2.5. PSD testbeds evaluation[4]

There are challenges for each mentioned method to measure the PSD of the CL. As pores are rarely cylindrical, the MIP method presents a model rather than actual pore diameter. The mercury intrusion pressure changes from 3,000 psi to 30,000 psi to identify pores smaller than 60 nm for the CL. At high pressures, the CL structure is crushed, which makes the results unreliable. However, as large pores in the medium fill at low pressures, the larger the pores, the more reliable the results become. Another challenge with the MIP method is the fact that the contact angle of mercury is different for Pt particles and carbon particles, therefore, using a single contact angle limits the accuracy [86].

While N_2 adsorption method does not have the problems of the former method (except for cylindrical pore assumption in some cases), it might not be capable of detecting the whole pore range of the CL.

To evaluate the mentioned methods, PSDs of several CL designs were measured with MIP and N_2 adsorption porosimetry. Moreover, the samples were sent to Dr. Li Lab in Waterloo University to be tested by the method of standard porosimetry. They were also sent to AFCC to be analyzed using FIB-SEM imaging and reconstructing the geometry.

The MSP (the method details can be found in [112]) was applied to several samples, however, due to the experimental challenges, no acceptable results were obtained. As the CL samples were ~10 µm thick, MSP required a precise weighing method and a standard sample of the same thickness for comparison. Characterizing thin standard samples was challenging and expensive. Therefore, a stack of CL samples with holes in the stack (to allow liquid to access the middle CL samples), were used and compared to a thicker standard sample. However, the in-plane diffusion resistance of the CL was too high to let the liquid access the CL bulk volume. The results for tests on three samples of the same design were not reproducible and included pores larger than the CL thickness, because the gaps between the layers in the stack were measured as pores; therefore,

[4] The measurements with method of standard porosimetry were done at Fuel Cell and Green Energy Lab at Waterloo University, and FIB-SEM analysis was done by AFCC.

they are not reported here. Although MSP could not be used for CL samples here, it could be used successfully for the whole electrode in PEMFC (details in Ref. [105])

The FIB-SEM (FEI Helios NanoLab 650) dual beam system milled the CL surface with a 30 keV accelerating voltage Ga+ ion beam gun. The CL decals were mounted on a pin stub sample holder using adhesive carbon tabs, and electrical contact was ensured by connecting the sample and the holder with copper tape. During the milling procedure, the sample surface was tilted 52˚ from the vertical electron beam direction, to be perpendicular to the milling ion beam. A protective layer of ~ 500 nm thick Pt was deposited on the surface in the region of interest using 83 pA ion current and 200 ns dwell time. A set of line markers were milled using 83 pA ion beam current to help with image registration. The FIB location was prepared by milling the trenches in the catalyst layer surrounding the area and leaving only the area of interest. Automatic slicing with 10 nm slice thickness was performed using a 24 pA ion beam current. High-resolution secondary electron (HRSEM) images with 4096 x 3536 pixel resolution were recorded after each slice using a through-the-lens detector (TLD), 2 keV electron beam energy, immersion lens operating mode, and 50 pA electron beam current. The total number of images collected was ~400 for each sample to reconstruct a 3D volume of the CL (e.g., 10×5×10 μm^3). Internally developed algorithms for registration, tilt correction, segmentation, and PSD using sphere-fitting approach were applied to process the images, reconstruct the CL volume, and extract the PSD.

The CL design #4 (Table 2.4) was chosen for the MIP measurements as it had a high average pore diameter relative to the other designs. Three samples of this design were measured by the MIP (Figure 3.4a). FIB-SEM tomography was also performed for this design (Figure 3.4a and b). The obtained PSDs from reconstructed geometries of the CL designs, the N_2 adsorption porosimetry, and MIP are compared in Figure 3.4a. The PSDs obtained varied due to the different pore shapes assumed by each method (cylindrical for N_2 adsorption and MIP methods and spherical for FIB-SEM method); however, the diameter range was the same for all methods (applying BJH for N_2 adsorption method). The PSD obtained by MIP was shifted toward the smaller pores in comparison with the one measured by N_2 adsorption BJH method. This shift could be due to the high pressure applied by mercury on the sample during the PSD measurement (3,000 psi to 30,000 psi to measure pores smaller than 60 nm) that could crush the CL structure. In N_2 adsorption porosimetry, BJH theory can be used for mesopores smaller than 300 nm; however, BJH is a qualitative method with high

uncertainty [91]. The pore volume percentages obtained by DFT are reliable for pore diameters ranging from 0.4 to 35 nm [93]. Comparing MIP and N_2 adsorption result for design #4, we could use N_2 adsorption method to measure the PSD of the CL as the pore range detected for the CL was the same for both methods. To ensure that the CL pore size was in the detection range of N_2 adsorption method, the CL PSD was measured for designs #2 (containing large pores) and #11 (containing large pores) using the FIB-SEM and reconstructing geometry (Figure 3.4c-f). Both FIB-SEM and N_2 adsorption methods showed the same pore size range for the tested CLs. As a result, considering all the accuracies, limitations, and challenges for each method, in this study N_2 adsorption applying both BJH and DFT theories was chosen to study the CL PSD.

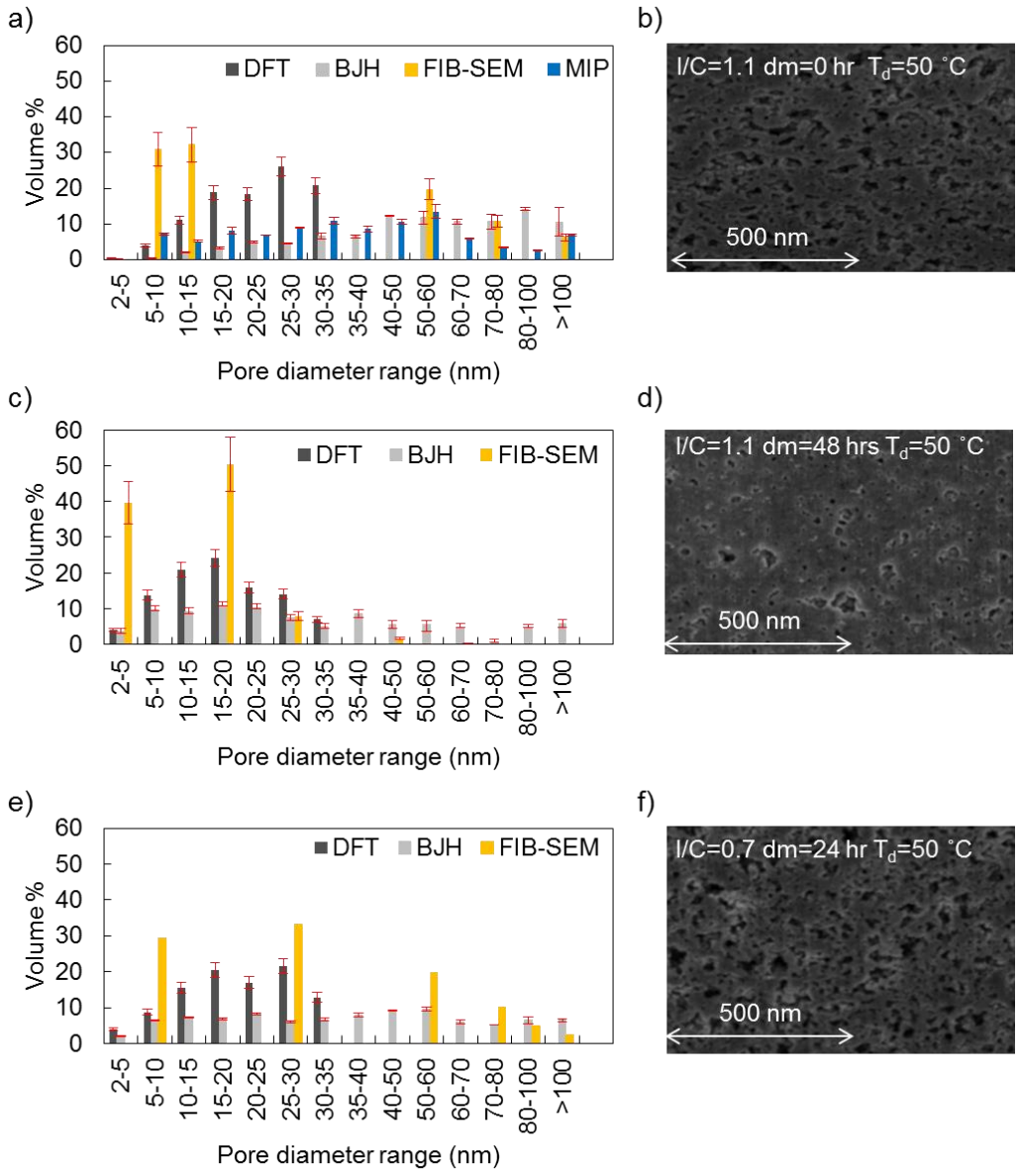

Figure 3.4 **a) Measured PSDs with MIP, N_2 adsorption, and FIB-SEM methods for CL design #4 (Table 2.4). b) Sample image of the cross-section of the CL design #4 obtained by FIB. c) Measured PSDs with N_2 adsorption and FIB-SEM methods for the CL design #2. d) Sample image of the cross-section of the CL design #2 obtained by FIB. e) Measured PSDs with N_2 adsorption and FIB-SEM methods for the CL design #11. f) Sample image of the cross-section of the CL design #11 obtained by FIB.**

3.2.6. Porosity measurement/calculation evaluation

Porosity values of the CL design #4 (Table 2.4), calculated from SEM and densitometer thicknesses (Eq. 9), densitometer, N_2 adsorption porosimetry, MIP, and FIB-SEM reconstructed geometry are presented in Figure 3.5.

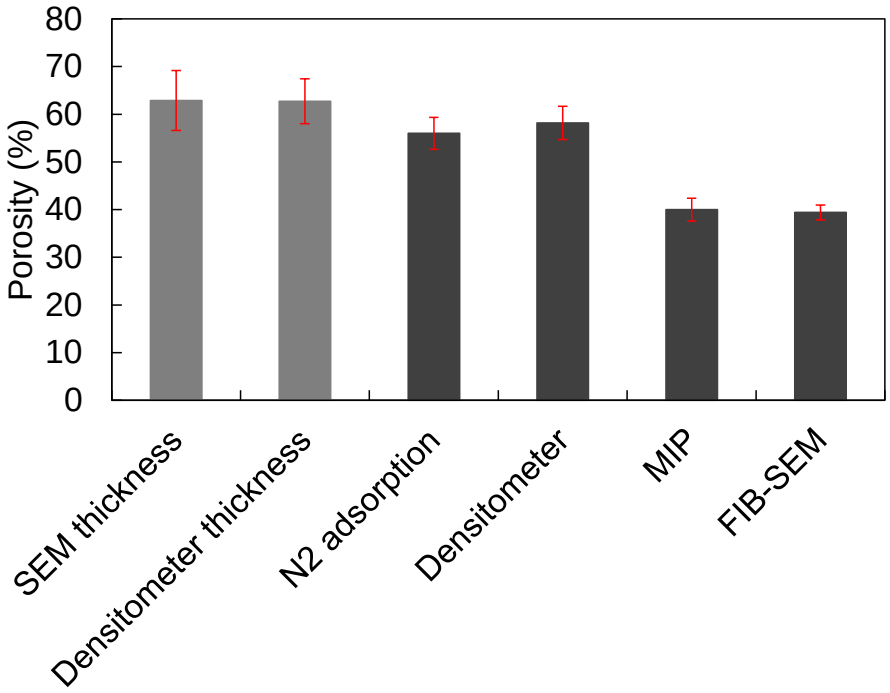

Figure 3.5 The measured/calculated porosities for design #4 (Table 2.4) CL from different methods. The error bars shows the standard deviations of at least three measurements

There are pores in different scales in the CL, including pores of the carbon particles, pores between carbon particles within the agglomerates, and pores between agglomerates. Moreover, these pores could be categorized to the blind ones and the accessible ones. The porosity value of the CL depends on which group of pores are considered as the void space within the CL. The CL thicknesses measured by SEM and densitometer included all pore scales, regardless of being blind or accessible. In N_2 adsorption, MIP, and FIB-SEM methods, the reported porosity values were including just part of the pores in the CL. N_2 adsorption and MIP methods ignored blind pores. MIP method probably ignored also part of the small pores, which demanded high intrusion pressures, or the pores, which became blind under deformed CL structure under high

intrusion pressures. Some of the CL pores were out of the FIB-SEM resolution range to be captured.

While all of these methods showed reliable porosities related to the specific pore ranges, for the modeling purposes, the total porosity including blind and accessible pores in all scales was needed (will be explained later). As a result, for the structural model input, the porosities calculated from thickness measurement were used. The accuracy of these porosities was dependent on the accuracy of thickness measurements, and density values used in Eq. 9.

3.3. Chapter 3 acknowledgement.

The densitometer facilities and FIB-SEM imaging analysis for this chapter were provided by AFCC. Also, the mercury intrusion porosimetry of SFU 4D lab were used for this study. The AFCC Structure, Properties and Performance Research Division and SFU 4D lab are acknowledged for their support.

Chapter 4.

Ex-situ Measurement of the PEMFC CL Diffusivity

4.1. Dry diffusivity testbed (DDT)

4.1.1. Testbed and measurement method

Dry diffusivity testbed (DDT) is an apparatus designed based on the Wicke–Kallenbach cell (WKC) [37]. There are two flow channels separated by a porous sample, as shown schematically in Figure 4.1. In one channel, nitrogen flows at a specific rate, temperature, and pressure, and in the other channel, air flows at the same conditions. Oxygen passes through the porous sample due to the oxygen concentration gradient as well as convective flows between the two sides of the sample, from one side to the other. After reaching steady state, the oxygen concentration at the outlet of the nitrogen channel becomes fixed. The gas diffusion resistance of the sample can be calculated based on the channels and sample geometries, thermodynamic conditions, and the oxygen concentration measured at the outlet of the nitrogen channel.

Following Ref. [113], the gas diffusion effective length of the sample was calculated considering both diffusion and convective mechanisms:

$$l_{eff} = D_{\text{binary}} \left(\frac{89.28 A_s RT}{p\dot{V}\, ln\left(\frac{C_o^{in}}{C_o^{in} - 89.28 x_o^{out}}\right)} - \frac{4h}{ShD_{\text{binary}}} \right)$$

Eq. 12

where l_{eff} is the effective length of the sample (m), A_s is the sample area (m^2), $\dot{V}$ is volumetric flow rate (m^3/s), C_o^{in} is oxygen concentration at the inlet of the oxygen-rich channel (mol/m^3), x_o^{out} is the measured oxygen volume percentage at nitrogen channel outlet, h is the depth of the channels in DDT (m), and Sh is Sherwood number. The effective diffusivity, D_{eff}, and relative diffusivity, D^* of the sample (Eq. 5) were calculated from the measured sample thickness, the calculated binary diffusivity, and the measured effective length of the sample. Sherwood number is a dimensionless number

proportional to the ratio of convective to the diffusion, mass flow rates. This number was calibrated in AFCC for the test condition and the testbed design.

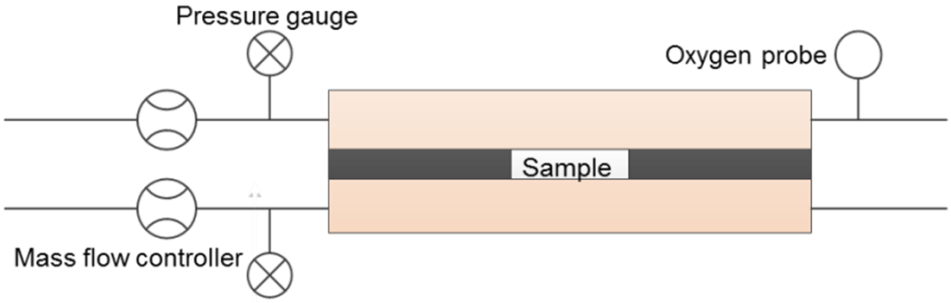

Figure 4.1 Schematic of the dry diffusivity test bed

To measure the diffusivity of CL coated on the filter PTFE, two tests had to be done. The first test was just for the bare filter PTFE, and the second one was for the catalyst-coated filter. The difference between the measured resistances for each test was equal to the resistance of the CL and the interfacial resistance. Although in this study, the coating procedure was designed to make weak penetration of the CL into the substrate and minimal interfacial resistance, the existence of the interfacial resistance was evaluated, studying gas diffusion resistance of the CLs with the same designs but different thicknesses. The y-intersection of R vs thickness plot for different CL designs (which showed the interfacial resistance) were almost zero (2 orders of magnitude less than CL resistances) for all of the designs. As a result, the difference between the gas diffusion resistances of the filter PTFEs (the support substrate) and the coated filter PTFEs were CL resistances.

4.1.2. Dry diffusivity testbed uncertainty analysis

The uncertainty of the measured effective length in Eq. 12 is a function of the uncertainty of the measured oxygen concentration, the thermodynamic conditions, the geometry parameters, and the uncertainty of the measured volume flow rate. To find the relation of the total uncertainty with each parameter uncertainty, the effective diffusivity from Eq. 12 should be differentiated with respect to each parameter (Eq. 13):

$$\left|\frac{d(l_{eff})}{l_{eff}}\right| = \sqrt{\left(\frac{C_o^{out} D_{binary}}{l_{eff}} \frac{-\left(\frac{A_{sample} RT 7.97E4}{p\dot{V}(C_o^{in} - 89.28 x_o^{out})}\right)}{\left(\ln\left(\frac{C_o^{in}}{C_o^{in} - 89.28 x_o^{out}}\right)\right)^2} \frac{dx_o^{out}}{x_o^{out}}\right)^2 + \left(\frac{d\dot{V}}{\dot{V}}\right)^2}$$

Eq. 13

4.2. Modified Loschmidt cell (MLC)

4.2.1. Testbed and measurement method

The Loschmidt cell (LC) method is a well-known technique for measuring the binary diffusion of two gases [114]. The LC method is based on a 1D diffusion problem. There are two large gas-filled chambers at the same pressure connected by a closed valve. At time zero, each chamber contains one type of gas, and then opening the valve, the gases diffuse into each other, and the concentration of each one changes with respect to time at any specific location. The analytical solution for this 1D diffusion problem is explained in Ref [5]. Comparing the monitored concentrations with the analytical solution, the binary diffusivity coefficient is determined.

The modified Loschmidt cell (MLC) method also works on the same basis; however, the gases have to pass through a porous sample from one chamber to the other. Because of the sample in between the chambers, the gas diffusion resistance increases. The difference between resistance with and without the sample is due to the porous sample. Then the gas diffusivity of the sample is calculated based on the thickness of the sample and its resistance.

In the MLC testbed of this study (Figure 4.2a), a sliding gate with slots for porous samples is mounted between the chambers (Figure 4.2b). The gate acts as both the sample holder and the valve when the chambers are clamped to the stage (Figure 4.2b). The measurement procedure consists of the following steps:

1. Purge I: At the beginning of the test, the metal part of the stage is between the chambers, isolating them from each other. The upper and lower chambers are flushed with nitrogen and oxygen, respectively.
2. Test I: The stage rotates to an empty sample slot to directly connect the chambers, allowing the gases to diffuse into each other as the oxygen concentration is monitored over time.
3. Purge II: The stage isolates the chambers again to flush and fill each of them with pure nitrogen or oxygen.
4. Test II: The sample holder rotates to the slot with the porous sample, and gases diffuse through the sample.

For each test, the oxygen concentration versus time plots for oxygen probe locations are stored. Using a MATLAB code (developed by Waterloo Technical Instrument INC), the gas diffusion resistances between the probes in the nitrogen chamber, and the top of the other chamber are calculated, comparing the monitored concentrations with the analytical solution (the detailed theoretical explanation of the code can be find in Ref. [115]). Considering Figure 4.2c, the relation between the diffusion resistances in the two tests is as follows:

$$R_{II} - R_I = \left(R_{\text{gap 2}} + R_s\right) - R_{\text{gap 1}}$$

Eq. 14

where R_I and R_{II} are the total gas diffusion resistances between the oxygen probe and the top of the oxygen chamber in the tests I and II, respectively; $R_{\text{gap 1}}$ and $R_{\text{gap 2}}$ are the resistances of the gas gap in tests I and II, respectively; and R_s is half of the resistance of the porous sample (half of the sample is in the nitrogen chamber, and the other half is in the oxygen chamber).

In terms of measured effective lengths, the Eq. 14 can be rewritten as follows:

$$\frac{l_{II}}{D_{\text{binary}}A} - \frac{l_I}{D_{\text{binary}}A} = \left(\frac{l_p - 1/2t_s}{D_{\text{binary}}A} + \frac{1/2t_s}{D_{eff}A}\right) - \frac{l_p}{D_{\text{binary}}A}$$

Eq. 15

where, t_s is the sample thickness, and l_p is the probe distance from the middle of the cell. The porous sample diffusivity can be calculated from Eq. 16:

$$t_s/D_{eff} = \frac{2(l_{II} - l_I) + t_s}{D_{\text{binary}}}$$

Eq. 16

and the relative diffusivity is:

$$D^* = \frac{t_s}{2(l_{II} - l_I) + t_s}$$

Eq. 17

To measure the diffusivity of the CL coated on a porous substrate, a similar procedure was followed; however, test I was performed with the filter PTFE mounted between the chambers, and test II had the CL coated filter between the two chambers as shown in Figure 4.2d. The relative diffusivity equation can be calculated and was the same as Eq. 17; however, l_I and l_{II} were obtained for different tests:

$$D^*_{CL} = \frac{t_{CL}}{2(l_{II} - l_I) + t_{CL}}$$

Eq. 18

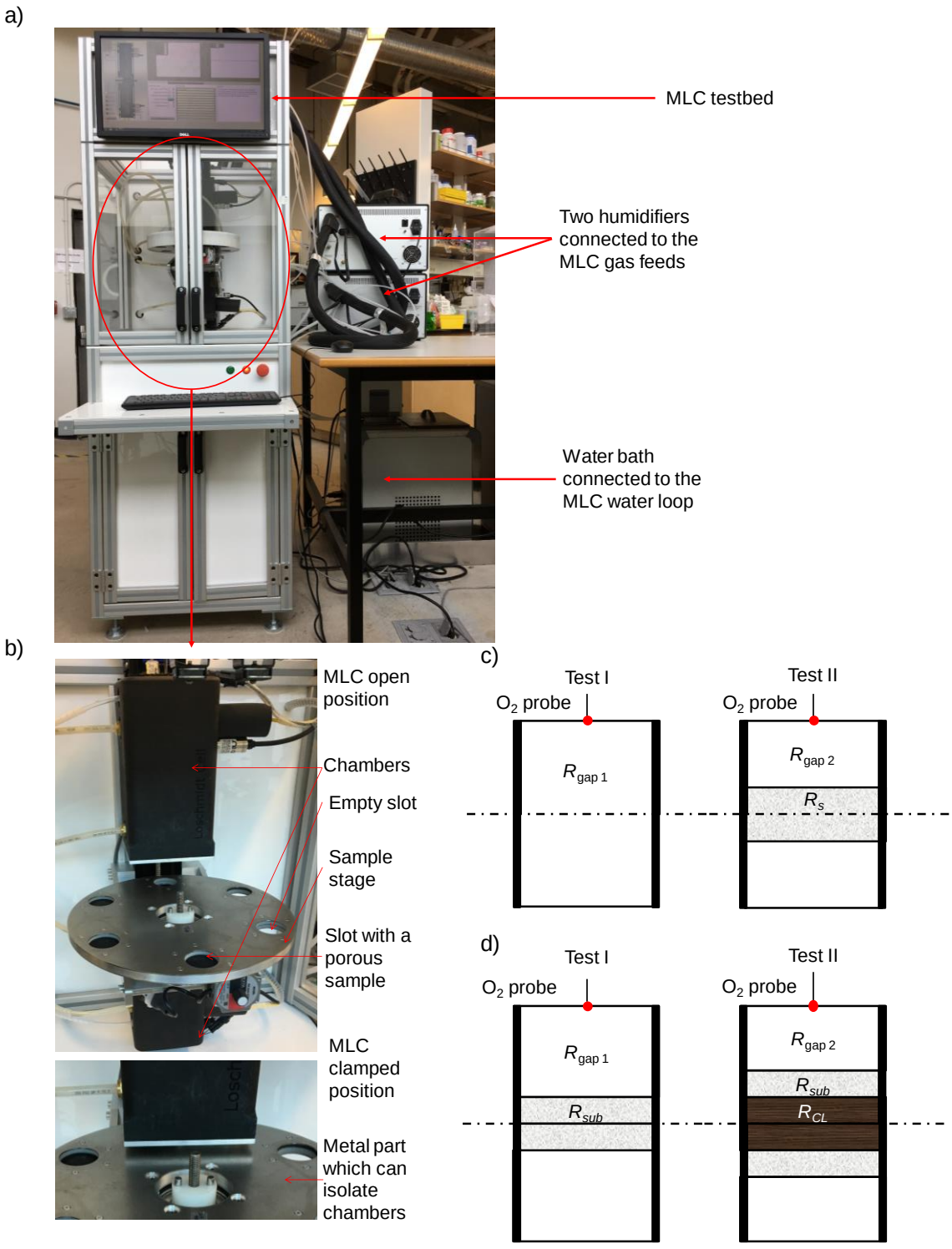

Figure 4.2 **a) MLC testbed b) MLC testbed, open and clamped positions. b) The two tests the in the MLC procedure (test I and test II). d) The two tests done in the MLC to measure the CL gas diffusion resistance**

4.2.2. MLC uncertainty analysis[5]

In this study, the standard measurement error of the MLC was estimated using a numerical simulation of the diffusion process. The error introduced by the physical measurement system, such as random probe noise, was simulated by randomly perturbing the input data using samples drawn from a normal distribution. The error was applied to the simulated data 1,000 times, and the sample diffusivity was calculated in each case. The real relative diffusivity of the sample was 0.1. The oxygen probe error was heteroscedastic, as the variance increased with increasing oxygen concentration. The binary gas diffusivity was cited from the experimental measurements in the literature and is available for many binary gas systems with the accuracy of about 2% [116].

A parametric study investigating the standard error for various sample thicknesses and diffusivity was conducted using the numerical simulation of the MLC described above.

The results of the parametric study are presented in Figure 4.3 as the standard error versus the sample diffusion effective length for a probe physically located 5 mm from the surface of the sample. Note that the error will increase if the probe is located further away from the sample.

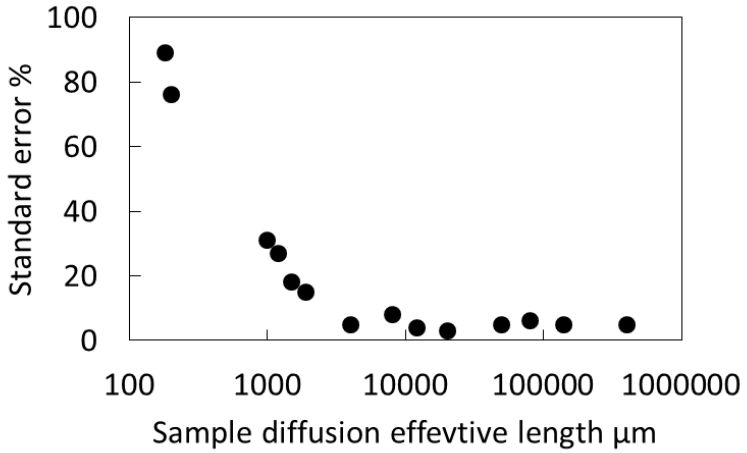

Figure 4.3 The modeled error for effective length measurement of MLC with respect to sample diffusion effective length

[5] The entire uncertainty analysis was done at Waterloo University as part of the MLC evaluation.

The uncertainty of the CL relative diffusivity was calculated based on the uncertainty of the measured CL thickness and effective lengths:

$$\frac{d(D^*_{CL})}{D^*_{CL}} = \sqrt{\left(\frac{\partial(D^*_{CL})}{\partial t_{CL}}\frac{d(t_{CL})}{t_{CL}}\right)^2 + \left(\frac{\partial(D^*_{CL})}{\partial l_I}\frac{d(l_I)}{l_I}\right)^2 + \left(\frac{\partial(D^*_{CL})}{\partial l_{II}}\frac{d(l_{II})}{l_{II}}\right)^2}$$

Eq. 19

4.3. MLC measurement parameters and sample configuration for CL

4.3.1. MLC measurement parameters

The MLC measurement parameters should be optimized based on the testbed dimensions and the subject sample. The followings are the measurement parameters used to measure CL gas diffusivity:

Table 4.1 CL gas diffusion measurement with MLC specifications

O_2 probe calibration duration	40 (min)	Oxygen probe manual
Test purge duration	10 (min)	Ensure oxygen probe reading in nitrogen chamber become less than 0.5%
Transient O_2 diffusion duration	3 (min)	Ensure no change detected in oxygen concentration of nitrogen chamber (reaching steady state)
Oxygen sampling frequency	2 (s^{-1})	There was no difference between the obtained results using higher frequencies

4.3.2. CL sample configuration

The gas diffusion resistance of the test subject affects the accuracy of MLC measurements based on Figure 4.3. As the gas diffusion of one filter PTFE is about 150 µm (measured by MLC), based on Figure 4.3 the expected uncertainty would be about 80% which is not acceptable.

To avoid low resistance of the test subject instead of one filter PTFE, a stack of 10 filters sandwiched between two layers of Sigracet GDL 24 BC was used in the all bare

substrate tests (test I). Then the stacks of 10 catalyst-coated filter PTFEs sandwiched between GDL papers were used to measure CL diffusivity (test II). The gas diffusion of the filter PTFE stack was around 2.1 mm (resulted in less than 20% uncertainty), and the catalyst-coated stack had gas diffusion resistances more than 4 mm that result in less than 10% uncertainty.

4.4. CL gas diffusivity measurement under different operating conditions with MLC

4.4.1. Operating temperature

The testbed was equipped with a water coil, which was connected to a water bath circulator (Polystat Cole-Parmer) (Figure 4.2a and Figure 4.4). The coil surrounded both gas chambers, gas fittings, and the entire sample holder. The water bath provided water with temperature ranging from 10 to 80 ˚C. The testbed pipeline for the feeding gases was also equipped with an electrical heater jacket with an adjustable temperature. For tests under elevated temperatures, the water and heater jackets were set on for several hours before the experiments. To ensure measurements under the desired condition, the temperature was monitored during the entire operation for feeding gases and both gas chambers.

4.4.2. Operating humidity

The feeding gas pipelines were connected to two gas Cellkraft P-series humidifiers (Figure 4.2a and Figure 4.4). The humidifiers could change the humidity and temperature of the gas from 0 to 95% and 10 to 80 ˚C, respectively. The humidity was also monitored in the gas chambers to ensure operation under the set humidity. It should be mentioned the binary gas diffusion laws can be used for humid gases as well as the concentration of water vapor will be low in comparison with the main test gases i.e. oxygen and nitrogen [117].

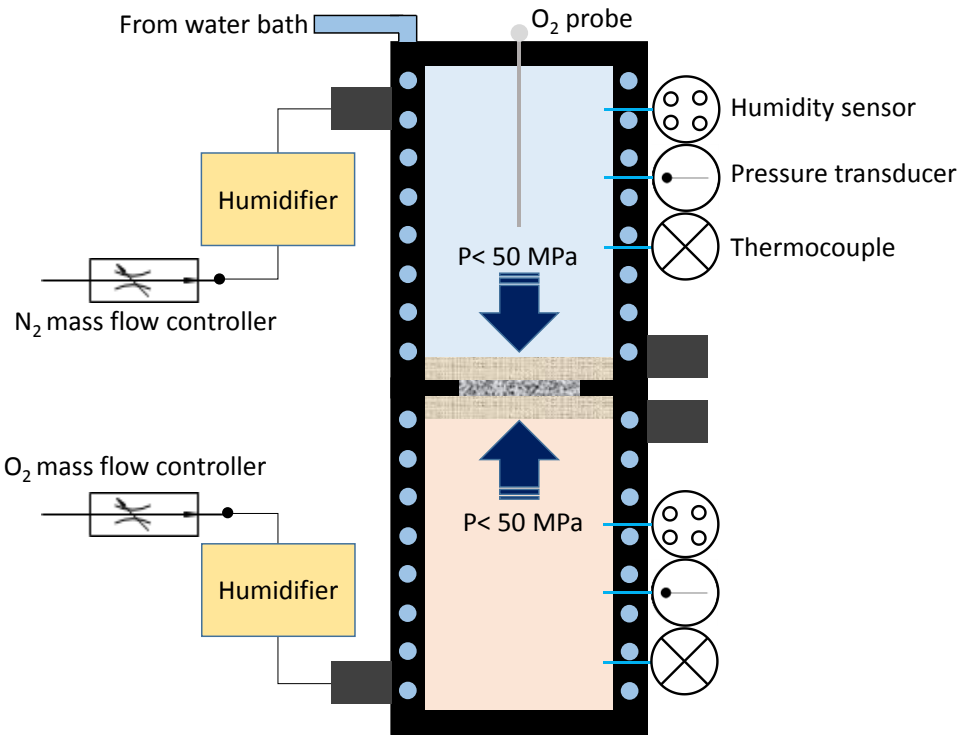

Figure 4.4 Schematic of the MLC testbed used in this study

4.4.3. Operating compression

To test the samples under compression, a particular sample jacket was used (Figure 4.5). The sample jacket consisted of two metal meshes that could screw together and sandwich the porous samples in between. The jacket could lock the porous samples under up to 50 MPa.

To measure the CL gas diffusion resistance under a specific compression, the following steps were followed:

1. The pressure versus thickness plots for the stack of filter PTFEs and GDL papers were obtained using TUC-RUC.
2. The compressive load versus thickness curve for the stack of catalyst-coated filter PTFEs and GDL papers was obtained using TUC-RUC.
3. The stacks thicknesses for the desired compressions were calculated based on the obtained curves from the previous steps.
4. The gas diffusion resistance of the stack of the filter PTFEs and GDL papers was obtained at the desired compression.

5. The gas diffusion resistance of the stack of the catalyst-coated filter PTFEs and GDL papers was obtained at the desired compression.
6. Based on the gas resistance difference obtained in step 4 and 5, the gas resistance of the compressed CL was obtained.

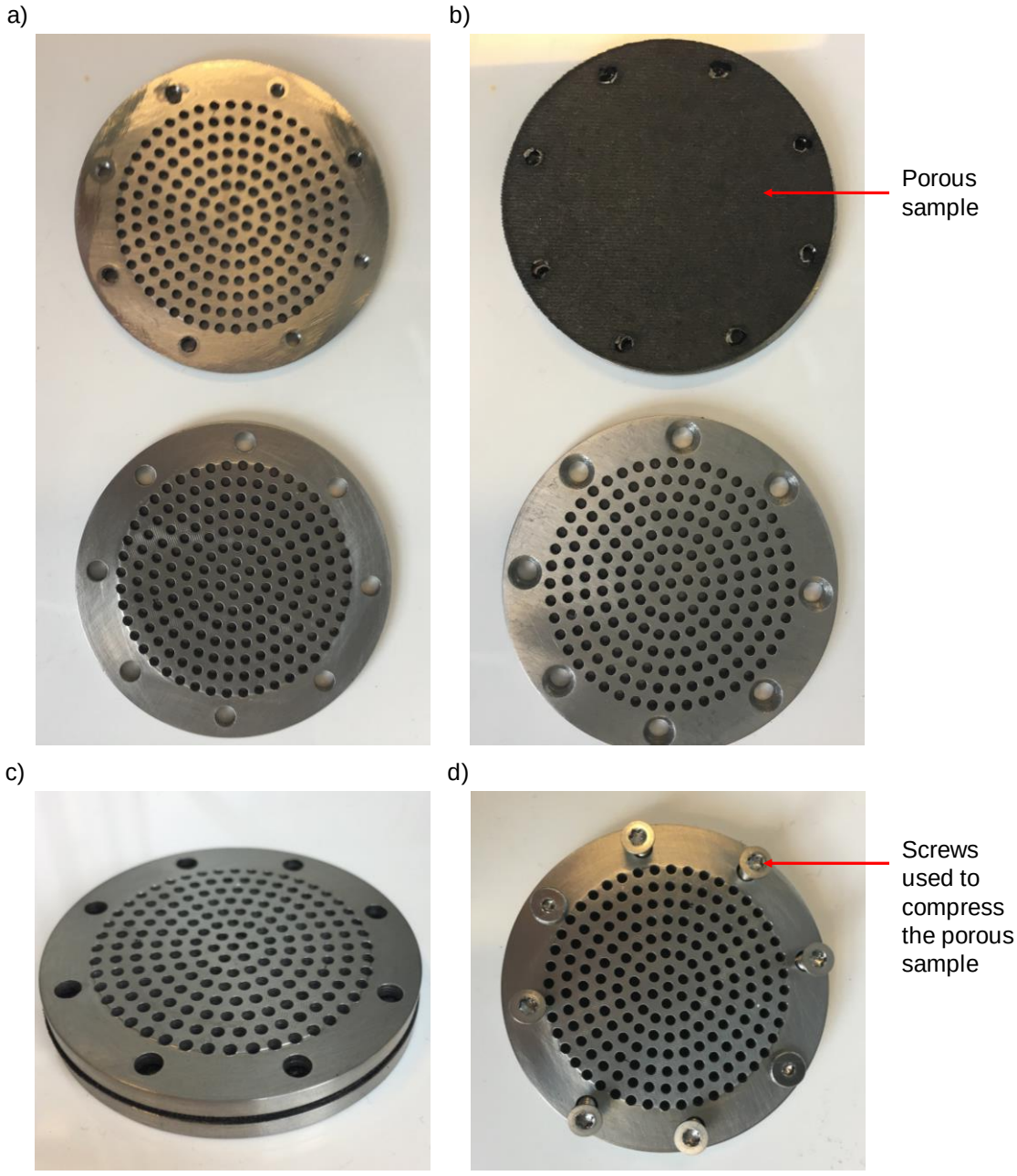

Figure 4.5 a)The sample holder for MLC tests under compression. b) Sample holders with the porous sample. c) Sample holder with a porous sample sandwiched between them. d) Screws used to tighten the sample holders and exert compressive load on the porous sample

4.4.4. CL water content

The last parameter that was studied is the CL water content. During the fuel cell operation, water is produced inside the CL due to the reaction of oxygen and hydrogen. To ease the water removal from reaction sites inside the CL, manufacturers make the CL hydrophobic. Introducing water to the CL ex-situ was a challenging task. Several methods were used to put water inside the CL. To ensure that there was water inside the CL, and measuring its amount, the weight of the CL samples were measured before and after introducing the water.

The first method was dipping the catalyst-coated filter PTFE samples into the water for several hours. The weight measurements for 400 mg of catalyst-coated filter PTFE sample showed no sign of weight increase due to the water adsorption.

In the next step same procedure was followed with hot water (80 ˚C). Again, no water content could be detected.

Then the catalyst-coated filters were vacuumed using a vacuum pump, and then suddenly water was added to the chamber containing the samples. Again, no water adsorption was observed.

To force water passing through the coated filters, in the next try, a vacuum pump was connected to a chamber with a port covered with the catalyst coated filter. Water was poured onto the CL and drawn through the filter and chamber by the vacuum pump for several minutes. The weight measurement showed there was some water inside the stack. The same test was done for the stack of filter PTFEs (not catalyst-coated ones) several times, and no water gain was detected, as the filters were extremely hydrophobic. Therefore, it was concluded that all of the water content belonged to the CL part of the stack. After several seconds of vacuum pump operation, the water content of the stack was independent of the duration of the experiment. The volume percentage of water content was calculated based on the water and CL weights, porosity, and density as follows:

$$v_{\mathrm{water}}(\%) = \frac{W_{\mathrm{water}}}{W_{\mathrm{CL}}} \times \frac{\rho_{\mathrm{CL}}}{\varepsilon_{\mathrm{CL}} \rho_{\mathrm{water}}}$$

Eq. 20

Exposing to air at the temperature of 20 ˚C and RH of 20%, the water content of the CL stack (10 layers) vanished in about 7 minutes based on the weight measurements. To delay the evaporation, all the tests for the CLs with water content were done under

almost 100% humidity. The weights of the stacks were also measured under 100% humid condition and plots of water content versus time were obtained for the CL stacks under humid condition. The total evaporation took around an hour depending on the design.

To measure the gas diffusion resistance of the CL with water content, following steps were followed:

1. The weight of the filter PTFE stack and the catalyst-coated stack were measured (dry weight).
2. Water forced to pass through the catalyst-coated filter PTFE stack.
3. The weight of the stack was monitored under 100% humid condition to obtain the water content versus time plot for the stack.
4. Water was forced to pass through the filter PTFE stack.
5. The weight of the filter PTFE stack was measured (to make sure it was the same as the dry weight).
6. The filter PTFE stack was tested with MLC 10 times in a row under 100% humid condition (test duration 3 min followed by 3 min purge duration that led to an hour total experiment time).
7. Water was forced to pass through the catalyst stack (catalyst-coated filter PTFE stack).
8. The weight of the catalyst stack was measured (to find out the water content).
9. Time was monitored as soon as the weight measurement was done.
10. The catalyst stack was tested with MLC 10 times in a row under 100% RH (test duration of 3 min followed by 3 min purge duration that led to an hour total experiment time).
11. The difference between the measured resistances for catalyst stack and filter PTFE stack was obtained (the CL diffusion resistance).
12. The water content for each test was calculated comparing monitored time with the obtained water content versus time plots.
13. Relating the CL resistances to the water contents, the plots of resistance versus water content were obtained.

4.5. Chapter 4 acknowledgement

The wicke-Kallenbach cell was provided by AFCC. Also, the Modified Loschmidt cell was built by Waterloo Technical Instrument Inc. The AFCC Structure, Properties and Performance Research Division and Waterloo Technical Instrument Inc. are acknowledged for their support.

Chapter 5.

CL Structural and Gas Diffusivity Model

5.1. Catalyst structural model

5.1.1. Catalyst structure

Measuring the size of agglomerates, and their shape characteristics is a challenging task involving different SEM techniques, assumptions, and uncertainties. The agglomerate definition itself includes many question marks, e.g., where does an agglomerate start and where does it end. On the other hand, while there exist some of the same lack of clarities about pore concept as well (e.g., pore diameter for pores with random shapes), it is more established in the literature, and there are different experimental methods to measure characteristics of pores of a porous medium with not as complicated as the imaging techniques. Also, gas diffusion happens through pores mostly. Therefore, the structural model here was developed based on the pore characteristics inputs rather than the characteristics of the solid part of the CL, including agglomerates, ionomer, and carbon-platinum particles. The complex geometry of CL was simplified based on the following assumptions:

1. Primary pores were envisioned as gaps between spherical porous carbon-platinum particles (the spherical porous particle assumption for carbon-platinum particles is an accepted theory in the literature [16]).
2. The carbon-platinum particles were orderly arranged into spherical aggregates with overlap.
3. Ionomer covered the aggregates on the surface to form agglomerates. The coverage was not 100%. However, it blocked some of the primary pores inside the agglomerates.
4. The secondary pores with different diameters were gaps between the agglomerates.
5. The arrangement of agglomerates in the CL was known.

Based on these assumptions, the CL was modeled through unit cells representing the CL structure. The unit cell included one agglomerate and one secondary pore surrounding the agglomerate (see Figure 1.3 and Figure 5.1a). Ionomer partially covered the agglomerate, and the structure inside it included primary pores (uniform size), and carbon-platinum particles (see Figure 5.1a). As the defined unit cell included a pair of an identical-size primary pore and an identical-size secondary pore, the CL PSD had to be translated into a system of bi-modal PSD including an effective primary pore and an effective secondary pore diameter. As will be explained later, a linear function of diameter was the dominant part of the gas diffusivity within the primary pores. Therefore, the weighted linear average, based on the volume percentage over all primary pores was calculated for the effective primary pores, Eq. 21:

$$d_{pp\ eff} = \frac{\sum_i v_{pp}(i) \times d_{pp}(i)}{\sum_i v_{pp}(i)}$$

Eq. 21

where $d_{pp}(i)$ $v_{pp}(i)$ are the pore diameter and volume ratio of the i^{th} primary pore in the CL PSD, respectively.

In case of the secondary pores, the diffusivity was a complex function of the diameter. As a result, instead of an effective secondary pore, for each secondary pore size, a unit cell was defined, and the structure modeled through considering a system of unit cells with different sizes and volume ratios same as the secondary pore volume ratio (in the PSD) they represent. The secondary pore number in PSD, *i*, was the identifier of the unit cell and the number of the unit cell sizes was the same as the number of the secondary pores in the input PSD. Most of the calculations were the same for the unit cells with different sizes. As a result, to avoid complexity, the identifier was eliminated in part of the future calculations. However, wherever the parameters became specific to a unit cell size, the identifier *i* was included.

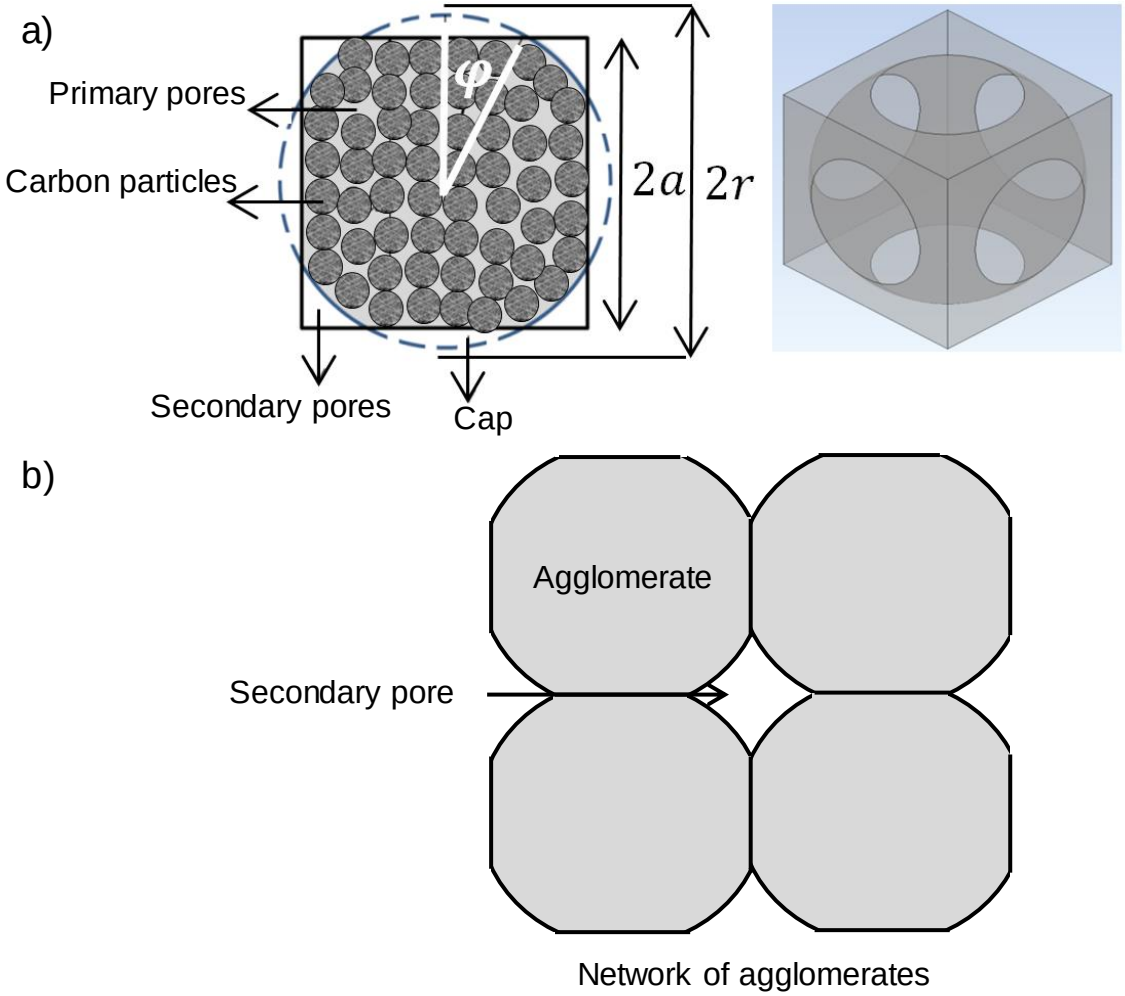

Figure 5.1 **a) Schematic of the unit cell used to model structure of the CL. b) Schematic of the network of unit cells used to model structure of the CL**

5.1.2. Pore geometry within agglomerates

To define the pore geometry within agglomerates, three parameters should be specified: pore size, pore shape, and pore connectivity. The size of the pores within the agglomerates was calculated based on Eq. 21 and the input PSD. The pore shapes and connectivity were modeled by considering pores as gaps between equally sized spheres (carbon-platinum particles) with orderly packing. Spherical carbon particles are shown to be reasonable according to experimental images [118] and this assumption is widely adopted [79,119]. For the arrangement, face-centered cubic (FCC) was chosen (details of FCC arrangement can be found in Ref. [120]). Other arrangements were also tried,

however, as FCC porosity (=0.26) was the closest one to the randomly packed spheres porosity [121], this arrangement was chosen.

5.1.3. Geometry of the unit cells

Geometrical relationships in the unit cell

To model agglomerates, the concept of spherical porous agglomerates touching without overlap in Refs. [49,122–125] was used. However, compared to the reconstructed CL geometry from FIB-SEM images [78], CL structure modeled with spherical agglomerates without overlap have overestimated active surface area and gas diffusivity [78]. Therefore, in this study, spherical agglomerates with overlap were considered (schematically shown in Figure 5.1b), to produce a realistic surface area with a lower active area. Ionomer partially covered the agglomerates and blocked portion of the primary pores. The overlap parameter, ξ, was defined as the ratio of the radius of the agglomerate, r, to the cell dimension, a, or as the angle of overlap, $\varphi=\cos^{-1}(1/\xi)$ (Figure 5.1a) that assumed to be the same for all unit cells. It will be proven that this assumption is correct if the CL porosity is homogenous, which was the case for CLs studied here based on the FIB-SEM reconstructed geometry analysis done by Sabharwal et al. [82]. The gaps between the agglomerates, which represented the secondary pores, did not have a perfect spherical shape. As a result, its equivalent radius was calculated using the square root of the area, following Bahrami et al. [126], at the middle cross-section (neck), which resulted in the narrowest passage. Considering Figure 5.1a, the secondary pore radius, r_{sp}, could be related to the overlap parameter, ξ, and angle, φ, as follows:

$$A_{sp}(i) = 4a(i)^2 - A_{agg}(i)$$

Eq. 22

$$A_{agg}(i) = \pi r_{agg}(i)^2 - 4A_{\mathrm{cap}}(\mathrm{i})$$

Eq. 23

$$A_{\mathrm{cap}}(i) = \varphi r_{agg}(i)^2 - a(i)^2 \tan\varphi = a(i)^2(\varphi\xi^2 - \tan\varphi)$$

Eq. 24

where A, a, and agg stand for cross-section area, unit cell dimension, and agglomerate respectively. Substituting Eq. 24 into Eq. 23:

$$A_{agg}(i) = \pi r_{agg}(i)^2 - 4a(i)^2(\varphi\xi^2 - \tan\varphi) = a(i)^2(\pi\xi^2 - 4\varphi\xi^2 + 4\tan\varphi)$$

Eq. 25

Then the secondary pore area, A_{sp}, and radius, r_{sp}, could be calculated:

$$A_{sp} = 4a(i)^2 - a(i)^2(\pi\xi^2 - 4\varphi\xi^2 + 4\tan\varphi) = 4a(i)^2\left(1 + \left(\varphi - \frac{\pi}{4}\right)\xi^2 - \tan\varphi\right)$$

Eq. 26

$$r_{sp}(i) = \frac{\sqrt{A_{sp}(i)}}{2} = a(i)\sqrt{1 + \left(\varphi - \frac{\pi}{4}\right)\xi^2 - \tan\varphi}$$

Eq. 27

The secondary pore diameter was an input to the model (from PSD). As a result, the size of the unit cell and agglomerate radius were calculated from the overlap parameter and the secondary pore diameter, manipulating Eq. 27. This procedure was repeated for all of the secondary pores, and different unit cell dimensions were obtained:

$$a(i) = \frac{r_{sp}(i)}{\sqrt{1 + \left(\varphi - \frac{\pi}{4}\right)\xi^2 - \tan\varphi}}$$

Eq. 28

$$r_{agg}(i) = \xi a(i) = \frac{\xi r_{sp}(i)}{\sqrt{1 + \left(\varphi - \frac{\pi}{4}\right)\xi^2 - \tan\varphi}}$$

Eq. 29

where *i* shows the i^{th} secondary pore diameter in the PSD.

Considering the geometry of an agglomerate, the volume of the agglomerate, V_{agg}, was obtained by subtracting the volume of caps from the volume of a sphere (with agglomerate radius):

$$V_{agg}(i) = V_{\text{sphere}} - 6V_{\text{cap}} = \frac{4\pi r_{agg}(i)^3}{3} - 6V_{\text{cap}} = \frac{4\pi a(i)^3\xi^3}{3} - 6V_{\text{cap}}$$

Eq. 30

$$V_{\text{cap}} = \frac{\pi\left(r_{agg}(i) - a(i)\right)\left(3\left(r_{agg}(i)^2 - a^2\right) + \left(r_{agg}(i) - a(i)\right)^2\right)}{6}$$

Eq. 31

$$V_{\text{cap}} = \frac{\pi a(i)^3(\xi - 1)(3(\xi^2 - 1) + (\xi - 1)^2)}{6} = \frac{\pi a(i)^3}{6}(4\xi^3 - 6\xi^2 + 2)$$

Eq. 32

Substituting Eq. 32 into Eq. 30:

$$V_{agg}(i) = \frac{4\pi a(i)^3\xi^3}{3} - 6\left(\frac{\pi a(i)^3}{6}(4\xi^3 - 6\xi^2 + 2)\right) = \frac{4\pi a(i)^3}{3}(4.5\xi^2 - 2\xi^3 - 1.5)$$

Eq. 33

Considering Figure 5.2, the average thickness of ionomer was calculated based on the volume of a spherical shell with overlap and the volume of the ionomer in the CL.

Considering Eq. 33, for the volume of a spherical agglomerate with overlap, the volume of the ionomer (spherical) shell in the unit cell was:

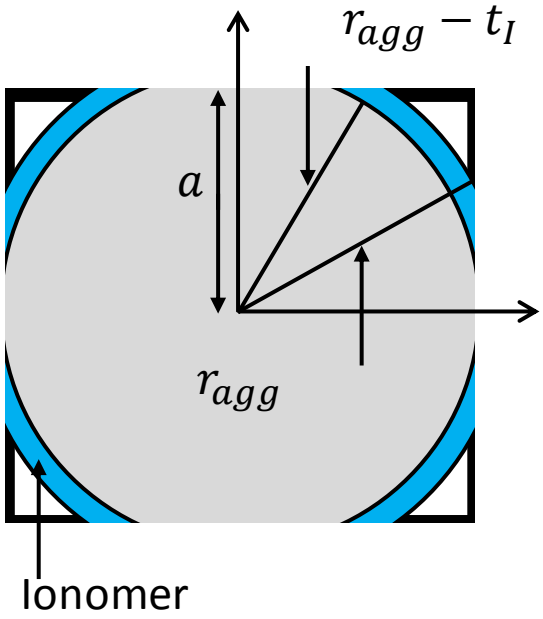

Figure 5.2 Schematic of the ionomer layer in the considered unit cell

$$V_{I\,shell}(i) = \frac{4\pi a(i)^3}{3}\left[(4.5\xi^2 - 2\xi^3 - 1.5) - \left(4.5\xi_{aggr}(i)^2 - 2\xi_{aggr}(i)^3 - 1.5\right)\right]$$

Eq. 34

where ξ_{aggr} is the overlapping parameter for the aggregate of carbon-platinum particles (agglomerate without ionomer thickness), calculated as follows:

$$\xi_{aggr}(i) = \frac{r_{agg}(i) - t_I(i)}{a(i)}$$

Eq. 35

where t_I is the ionomer thickness. The aggregate overlap parameter was dependent on the unit cell size, and as a result, the identifier *i* was included.

The Eq. 35 was obtained assuming that if one subtract the ionomer thickness from the radius of agglomerate, the resulted value is still greater than the unit cell size, *a*. If the calculated thickness proved otherwise, the ionomer shell on the agglomerate (blue area in Figure 5.2) was not a spherical one anymore and had to be calculated as follows:

$$V_{I\,shell} = \frac{4\pi a(i)^3}{3}(4.5\xi^2 - 2\xi^3 - 1.5) - \frac{4\pi\left(r_{agg}(i) - t_I(i)\right)^3}{3}$$

Eq. 36

$$V_{I\,shell} = \frac{4\pi a(i)^3}{3}\left(4.5\xi^2 - 2\xi^3 - 1.5 - \xi_{aggr}(i)^3\right)$$

Eq. 37

Eq. 34 or 37 will be used later to find the ionomer thickness in each unit cell. However, first, the unit cell dimension and overlap parameter should be caluclated. That was done here using ink composition, material properties, and porosity of the CL in the next section.

Volume ratios of the CL materials

The carbon-platinum particles were considered as porous spherical particles that were called *C-Pt* particles in this study. The volume of the *C-Pt* particles $V_{C\text{-}PT}$ was calculated based on the volume of the carbon particles as follows:

$$V_{C-Pt} = V_C + V_{Pt} = V_C + \frac{(V_C\rho_C)\omega_{Pt/C}}{\rho_{Pt}} = V_C\left(1 + \frac{\rho_C\omega_{Pt/C}}{\rho_{Pt}}\right)$$

Eq. 38

Ionomer volume was related to the carbon particles volume through I/C weight ratio, $\omega_{I/C}$:

$$V_I = \frac{(V_C\rho_C)\omega_{I/C}}{\rho_I}$$

Eq. 39

Eq. 38 was used to relate the ionomer volume to the volume of C-Pt particles:

$$V_I = \frac{\rho_{Pt}V_{C-Pt}}{\rho_{Pt} + \rho_C\omega_{Pt/C}} \times \frac{\rho_C\omega_{I/C}}{\rho_I} = \frac{\rho_{Pt}\rho_C\omega_{I/C}V_{C-Pt}}{\rho_I\left(\rho_{Pt} + \rho_C\omega_{Pt/C}\right)}$$

Eq. 40

Volume ratios of CL pores and ionomer coverage

Here, pores in the CL were divided into three groups: the secondary pores (all accessible by gas), V_{sp}, the accessible primary pores (including pores inside C-Pt particles and gaps between C-Pt particles) that could be reached by gas, V_{app}, and the blind primary pores that could not be reached by gas, V_{bpp}. The input porosity to the model was based on the theoretical calculations and SEM imaging. Therefore, the input porosity considered all primary pores, including both blind and accessible ones. As a result, the total pore volume, V_p, in CL was:

$$V_p = V_{sp} + V_{bpp} + V_{app} = \varepsilon_{CL} V_{CL}$$

Eq. 41

As the main reason to have blind pores was due to being covered by the ionomer, the ionomer coverage was defined as the volume ratio of the blind primary pores to all primary pores and calculated as follows:

$$\text{Ionomer coverage} = I_{\text{coverage}} = \frac{V_{bpp}}{V_{bpp} + V_{app}}$$

Eq. 42

$$v_{bpp/app} = \frac{V_{bpp}}{V_{app}} \rightarrow I_{\text{coverage}} = \frac{v_{bpp/app}}{1 + v_{bpp/app}}$$

Eq. 43

To find the ionomer coverage, the blocked to accessible primary pore ratio $v_{bpp/app}$ should be found. The input PSD was determined by N_2 adsorption porosimetry which only measured the accessible primary pores, V_{pp}, and all secondary pores, V_{sp} (as ionomer covered agglomerates on the surface, it was assumed that there were no blind secondary pores). The volume of all accessible pores including primary and secondary ones was called V_{ap}. The volume ratio of secondary pores to accessible primary pores $v_{sp/app}$ could be read from the input N_2 adsorption PSD:

$$v_{sp/app} = \frac{V_{sp}}{V_{app}} \text{ (known from PSD)}$$

Eq. 44

The volume of the primary pores V_{pp} is the pore volume inside agglomerates:

$$V_{pp} = V_{bpp} + V_{app} = \varepsilon_{agg} V_{agg}$$

Eq. 45

The volume ratio of all primary pores, to all pores, $v_{pp/p}$, obtained by dividing Eq. 45 by Eq. 41:

$$v_{pp/p} = \frac{V_{bpp} + V_{app}}{V_{sp} + V_{bpp} + V_{app}} = \frac{v_{bpp/app} + 1}{v_{sp/app} + v_{bpp/app} + 1} = \frac{\varepsilon_{agg} V_{agg}}{V_{CL} \varepsilon_{CL}} = \frac{V_{agg}}{V_{CL}} \times \frac{\varepsilon_{agg}}{\varepsilon_{CL}}$$

Eq. 46

The solid volume of agglomerates and CL was the same, therefore:

$$V_{agg}(1 - \varepsilon_{agg}) = V_{CL}(1 - \varepsilon_{CL}) \rightarrow \frac{V_{agg}}{V_{CL}} = \frac{1 - \varepsilon_{CL}}{1 - \varepsilon_{agg}}$$

Eq. 47

Substituting Eq. 47 into Eq. 46:

$$v_{pp/p} = \frac{v_{bpp/app} + 1}{v_{sp/app} + v_{bpp/app} + 1} = \frac{(1 - \varepsilon_{CL})\varepsilon_{agg}}{\varepsilon_{CL}(1 - \varepsilon_{agg})}$$

Eq. 48

Manipulating Eq. 48:

$$v_{bpp/app} = \frac{v_{pp/p}(v_{sp/app} + 1) - 1}{1 - v_{pp/p}} = \frac{(1 - \varepsilon_{CL})\varepsilon_{agg} v_{sp/app} + \varepsilon_{agg} - \varepsilon_{CL}}{\varepsilon_{CL} - \varepsilon_{agg}}$$

Eq. 49

or in terms of ionomer coverage:

$$I_{\text{coverage}} = \frac{(1 - \varepsilon_{CL})\varepsilon_{agg} v_{sp/app} + \varepsilon_{agg} - \varepsilon_{CL}}{(1 - \varepsilon_{CL})\varepsilon_{agg} v_{sp/app}}$$

Eq. 50

C-Pt particles and agglomerate porosities in CL

Assuming zero porosity for Pt particles and known porosity of carbon support particle, the porosity of the C-Pt particles $\varepsilon_{C\text{-}PT}$ were calculated based on the volume of C-Pt particles (Eq. 38) and porosity of the carbon particles as follows:

$$\varepsilon_{C-Pt} = \frac{V_C \varepsilon_C}{V_{C-Pt}} = \frac{V_C \varepsilon_C}{V_C\left(1 + \frac{\rho_C \omega_{Pt/C}}{\rho_{Pt}}\right)} = \frac{\varepsilon_C}{1 + \frac{\rho_C \omega_{Pt/C}}{\rho_{Pt}}} = \varepsilon_C \frac{\rho_{Pt}}{\rho_{Pt} + \rho_C \omega_{Pt/C}}$$

Eq. 51

where $\omega_{PT/C}$ is the weight ratio of the Pt to the carbon, known from the ink composition (input), and ρ is the density.

The porosity of agglomerates was obtained by finding its pore volume and its volume. The pore volume of the agglomerates was volume of primary pores, V_{pp} that had two components: the pore volume inside the *C-Pt* particles, $V_{C\text{-}Pt\ p}$, and the gap volume between them, $V_{C\text{-}Pt\ gp}$. The pore volume inside the agglomerates was calculated as follows:

$$V_{pp} = V_{C-Pt}\varepsilon_{C-Pt} + V_{C-Pt\ gp}$$

Eq. 52

The volume of agglomerates could also be calculated based on C-Pt particles' volume, considering that volume of the agglomerate is the summation of the volume of the C-Pt particles, $V_{C\text{-}Pt}$, volume of primary pores, V_{pp}, and the volume of ionomer around the C-Pt aggregate, V_I:

$$V_{agg} = V_{C-Pt} + V_{C-Pt\,gp} + V_I$$

Eq. 53

Substituting Eq. 40 (volume of ionomer) into Eq. 53, the volume of agglomerates was obtained based on the volume of C-Pt particles:

$$V_{agg} = V_{C-Pt}\left(1 + \frac{V_{C-Pt\,gp}}{V_{C-Pt}} + \frac{\rho_{Pt}\rho_C\omega_{I/C}}{\rho_I\left(\rho_{Pt} + \rho_C\omega_{Pt/C}\right)}\right)$$

Eq. 54

Combining Eq. 52 and Eq. 54, porosity of agglomerates was obtained:

$$\varepsilon_{agg} = \frac{V_{C-Pt}\left(\varepsilon_{C-Pt} + \frac{V_{C-Pt\,gp}}{V_{C-Pt}}\right)}{V_{C-Pt}\left(1 + \frac{V_{C-Pt\,gp}}{V_{C-Pt}} + \frac{\rho_{Pt}\rho_C\omega_{I/C}}{\rho_I\left(\rho_{Pt} + \rho_C\omega_{Pt/C}\right)}\right)} = \frac{\varepsilon_{C-Pt} + \frac{V_{C-Pt\,gp}}{V_{C-Pt}}}{1 + \frac{V_{C-Pt\,gp}}{V_{C-Pt}} + \frac{\rho_{Pt}\rho_C\omega_{I/C}}{\rho_I\left(\rho_{Pt} + \rho_C\omega_{Pt/C}\right)}}$$

Eq. 55

Defining the CL structure based on the unit cell

To define the CL structural unit cell, the agglomerate porosity, ε_{agg}, unit cells' dimension, *a(i)*, overlap parameters, ξ_{aggr} and ξ, and ionomer thicknesses, $t_l(i)$, should be calculated.

To solve Eq. 55 for agglomerate porosity, the ratio of the primary pore volume to the volume of C-Pt particles should be specified. As FCC arrangement was considered for the C-Pt particles inside the agglomerate, the volume of the aggregate of C-Pt particles, V_{aggr} was:

$$V_{aggr} = \frac{V_{C-Pt}}{1 - \varepsilon_{\mathrm{FCC}}}$$

Eq. 56

The pore volume of gaps between C-Pt particles, $V_{C\text{-}Pt\,gp}$, was:

$$V_{C-Pt\,gp} = \varepsilon_{\mathrm{FCC}}V_{aggr} = \frac{\varepsilon_{\mathrm{FCC}}V_{C-Pt}}{1 - \varepsilon_{\mathrm{FCC}}}$$

Eq. 57

$$\frac{V_{C-Pt\,gp}}{V_{C-Pt}} = \frac{\varepsilon_{\mathrm{FCC}}}{1 - \varepsilon_{\mathrm{FCC}}}$$

Eq. 58

Substituting Eq. 58 in Eq. 52, 54, and 55:

$$V_{pp} = V_{C-Pt}\varepsilon_{C-Pt} + \frac{\varepsilon_{\mathrm{FCC}} V_{C-Pt}}{1-\varepsilon_{\mathrm{FCC}}} = V_{C-Pt}\left(\varepsilon_{C-Pt} + \frac{\varepsilon_{\mathrm{FCC}}}{1-\varepsilon_{\mathrm{FCC}}}\right)$$

Eq. 59

$$V_{agg} = V_{C-Pt}\left(1 + \frac{\varepsilon_{\mathrm{FCC}}}{1-\varepsilon_{\mathrm{FCC}}} + \frac{\rho_{Pt}\rho_C\omega_{I/C}}{\rho_I\left(\rho_{Pt} + \rho_C\omega_{Pt/C}\right)}\right)$$

Eq. 60

$$\varepsilon_{agg} = \frac{\varepsilon_{C-Pt} + \frac{\varepsilon_{\mathrm{FCC}}}{1-\varepsilon_{\mathrm{FCC}}}}{1 + \frac{\varepsilon_{\mathrm{FCC}}}{1-\varepsilon_{\mathrm{FCC}}} + \frac{\rho_{Pt}\rho_C\omega_{I/C}}{\rho_I\left(\rho_{Pt} + \rho_C\omega_{Pt/C}\right)}} = \frac{\rho_{Pt}\rho_I\varepsilon_C(1-\varepsilon_{\mathrm{FCC}}) + \rho_I(\rho_{Pt} + \rho_C\omega_{Pt/C})\varepsilon_{\mathrm{FCC}}}{\rho_I\left(\rho_{Pt} + \rho_C\omega_{Pt/C}\right) + \rho_{Pt}\rho_C\omega_{I/C}(1-\varepsilon_{\mathrm{FCC}})}$$

Eq. 61

Eq. 61 defines the agglomerate porosity based on the model inputs (material properties and ink composition). The CL porosity relates to agglomerate porosity considering the fact that the non-porous volume of the agglomerate is the same as the non-porous volume of the CL:

$$\varepsilon_{CL} = 1 - \frac{V_{agg}\left(1-\varepsilon_{agg}\right)}{V_{CL}}$$

Eq. 62

The volume of the agglomerate in the unit cell could be replaced by Eq. 33 and the CL volume is the volume of the unit cell:

$$\varepsilon_{CL} = 1 - \frac{\frac{4\pi a(i)^3(4.5\xi^2 - 2\xi^3 - 1.5)}{3}\left(1 - \frac{\rho_{Pt}\rho_I\varepsilon_C(1-\varepsilon_{FCC}) + \rho_I(\rho_{Pt} + \rho_C\omega_{Pt/C})\varepsilon_{FCC}}{\rho_I\left(\rho_{Pt} + \rho_C\omega_{Pt/C}\right) + \rho_{Pt}\rho_C\omega_{I/C}(1-\varepsilon_{FCC})}\right)}{8a(i)^3}$$

Eq. 63

$$\varepsilon_{CL} = 1 - \frac{\pi(4.5\xi^2 - 2\xi^3 - 1.5)}{6}\left(1 - \frac{\rho_{Pt}\rho_I\varepsilon_C(1-\varepsilon_{FCC}) + \rho_I(\rho_{Pt} + \rho_C\omega_{Pt/C})\varepsilon_{FCC}}{\rho_I\left(\rho_{Pt} + \rho_C\omega_{Pt/C}\right) + \rho_{Pt}\rho_C\omega_{I/C}(1-\varepsilon_{FCC})}\right)$$

Eq. 64

Eq. 64 relates the catalyst porosity (input to the model) to the overlap parameter, material densities (inputs to the model), catalyst material composition (inputs to the model), and porosities of carbon support particles and the packed bed (inputs to the model). Through this equation, the overlap parameter was calculated.

The overlap parameter and ionomer coverage (Eq. 50) were the same for all of the unit cells regardless of the unit cell size. The calculations for other parameters specific to the unit cell is brought in Table 5.1:

Table 5.1 Unit cell modeled parameters

Parameter	Inputs	Equation or reference
Unit cell size, *a(i)*	ξ, ϕ, $r_{sp}(i)$ (PSD)	Eq. 28
Unit cell volume percentage, *v(i)*	$v_{sp}(i)$ (PSD)	
Agglomerate size, $r_{agg}(i)$	ξ, ϕ, $r_{sp}(i)$ (PSD)	Eq. 29
Agglomerate volume $V_{agg}(i)$	ξ, $a(i)$	Eq. 33
Volume of C-Pt particles $V_{C\text{-}Pt}(i)$	$V_{agg}(i)$, ρ_C, ρ_{Pt}, ρ_I,$\omega_{I/C}$, $\omega_{Pt/C}$, ε_{FCC}	Eq. 60
Ionomer volume in the unit cell $V_I(i)$	$V_{C\text{-}Pt}(i)$, ρ_C, ρ_{Pt}, ρ_I,$\omega_{I/C}$, $\omega_{Pt/C}$	Eq. 40
Aggregate overlap, $\xi_{aggr}(i)$	$V_I(i)$, $a(i)$, ξ	Eq. 34 or 37
Ionomer average thickness in the unit cell, $t_I(i)$	$a(i)$, $r_{agg}(i)$, $\xi_{aggr}(i)$	Eq. 35

5.1.4. Integration of compression load into the CL structural model

Compressive load could change the CL porosity and PSD. Here it was assumed that the compressed thickness and PSD of the CL is known (The thickness and PSD change under compressive load was modeled in Ref. [127]). The compressed porosity of CL was obtained assuming that under compression, only volume of the pores changes and the CL solid volume change is negligible, i.e.:

$$\frac{t_{\text{compressed}}}{t_{\text{not compressed}}} = \frac{1-\varepsilon_{\text{not compressed}}}{1-\varepsilon_{\text{compressed}}}$$

Eq. 65

The effect of the compression on the PSD of CL demanded complicated analytical calculations on the CL structure, which was done in another work. To consider the effect of compression in the structural model, the input porosity and PSD were changed to the ones under compression.

5.1.5. Integration of water content into the CL structural model

When water is added to the CL, it is partially absorbed by ionomer, causing ionomer to swell and partially occupies a portion of the pore space. Both ionomer and pore water-absorption change the gas-filled porosity and PSD of the CL that will be evaluated here.

Ionomer swelling

In the literature, the amount of water absorbed by ionomer is quantified for different conditions in different ways [128]. The unanimously accepted method is using the water content λ (mol of water per mol of SO_3^- in ionomer), following Ref. [129]. It is calculated based on the macroscopic water uptake [128]:

$$\lambda = \frac{\left[\Delta M_{H_2O}/M_I\right]EW}{\bar{M}_{H_2O}}$$

Eq. 66

where *EW* is the equivalent weight of the polymer (850 for Aquivion ionomer in this study g/mol [130]), and $\bar{M}_{H2O}$ is the molecular mass of water. Eq. 66 could be rearranged into Eq. 67 to relate water gain of ionomer to water content:

$$\Delta M_{H_2O} = \frac{\bar{M}_{H_2O} M_I \lambda}{EW}$$

Eq. 67

Zhao and Benziger [131] investigated the water content of Aquivion ionomer and its relationship to ionomer swell. They used and validated the following equation:

$$\lambda = \frac{[(1+st_I)^3 - 1]EW}{\rho_I \bar{V}_{H_2O}}$$

Eq. 68

where st_I is the ionomer strain, ρ_I is the ionomer density (=1.9 g/cm^3 [108]), and $\bar{V}_{H2O}$ is the molar volume of water (18 cm^3/mol).

When ionomer absorbs water, it swells volumetrically, i.e., not only its thickness will change, its area changes as well. Here, two possible scenarios were considered:

I. After ionomer swelled, ionomer coverage was not 100%; therefore, st_I is the same in all directions.

II. Ionomer swelling caused full ionomer coverage, therefore, after reaching full coverage, only thickness of ionomer changed.

Assuming small changes of ionomer thickness in comparison with agglomerate diameter, in the first scenario, the ionomer thickness and ionomer coverage were calculated as follows:

$$t_{I\,swelled}(i) = t_I(i)(1+st_I)$$

Eq. 69

$$I_{\text{coverage swelled}} = I_{\text{coverage}}(1+st_I)^2$$

Eq. 70

In the second scenario, the ionomer coverage would be 1, and the new thickness could be found based on the volume of the swelled ionomer:

$$V_{I\ swelled}(i) = V_I(i)(1 + st_I)^3$$

Eq. 71

$$A_{I\ swelled} t_{I\ swelled}(i) = A_I t_I(i)(1 + st_I)^3$$

Eq. 72

$$t_{I\ swelled}(i) = \frac{A_I}{A_{I\ swelled}} t_I(i)(1 + st_I)^3 = I_{\text{coverage}} t_I(i)(1 + st_I)^3$$

Eq. 73

The new overlap parameter was calculated as follows:

$$\xi_{\text{swelled}}(i) = \frac{r_{\text{swelled}}(i)}{a(i)} = \frac{\left(r_{agg}(i) + t_{I\ swelled}(i) - t_I(i)\right)}{a(i)} = \xi + \frac{(t_{I\ swelled}(i) - t_I(i))}{a(i)}$$

Eq. 74

Substituing the new overlap parameter in Eq. 27, the new secondary pore diameter could be calculated. This procedure was repeated for all of the unit cells to obtain the new secondary pore diameters when ionomer swelled.

$$d_{sp\ swelled}\ (i) = \ 2a(i)\sqrt{1 + \left(\varphi_{\text{swelled}}(i) - \frac{\pi}{4}\right)\xi_{\text{swelled}}(i)^2 - \tan\varphi_{\text{swelled}}(i)}$$

Eq. 75

$$\varphi_{\text{swelled}}(i) = \cos^{-1}\left(\frac{1}{\xi_{\text{swelled}}(i)}\right)$$

Eq. 76

To find the new volume percentage for the i^{th} secondary pore, the ratio of the secondary pore, before and after ionomer swell in each unit cell, was calculated:

$$\frac{V_{sp\ swelled}\ (i)}{V_{sp}(i)} = \frac{8a(i)^3 - V_{agg\ swelled}\ (i)}{8a(i)^3 - V_{agg}\ (i)}$$

Eq. 77

The volume of agglomerates before and after ionomer swell was calculated based on Eq. 33, and the overlap parameters before the swell from Eq. 64 and after the swell from Eq. 74. The effective primary pore diameter remained unchanged after the ionomer swell.

The new porosity of the CL was obtained based on the ratio of the swelled volume of Ionomer to the original volume of ionomer (Eq. 71) and assuming that the CL volume remained the same (the unit cell size remained the same):

$$\varepsilon_{CL\,swelled} = \varepsilon_{CL}\left(1 - \frac{V_{I\,swelled}(i) - V_I(i)}{8a(i)^3}\right) = \varepsilon_{CL}\left(1 - \frac{[(1+st_I)^3 - 1]V_I(i)}{8a(i)^3}\right)$$

Eq. 78

Combining Eq. 40 and Eq. 54, the volume ratio of ionomer to agglomerate was calculated:

$$V_I = \frac{\rho_{Pt}\rho_C\omega_{I/C}}{\rho_I(\rho_{Pt} + \rho_C\omega_{Pt/C})}\frac{V_{agg}}{\left(\frac{1}{1-\varepsilon_{\mathrm{FCC}}} + \frac{\rho_{Pt}\rho_C\omega_{I/C}}{\rho_I(\rho_{Pt} + \rho_C\omega_{Pt/C})}\right)}$$

Eq. 79

Considering Eq. 33 for the volume of agglomerate in the unit cell, Eq. 79 for the ionomer volume and Eq. 78 for CL porosity with swelled ionomer:

$$\varepsilon_{CL\,swelled} = \varepsilon_{CL}\left(1 - \frac{\pi(4.5\xi^2 - 2\xi^3 - 1.5)((1+st_I)^3 - 1)}{6\left(\frac{\rho_I(\rho_{Pt} + \rho_C\omega_{Pt/C})}{(1-\varepsilon_{\mathrm{FCC}})\rho_{Pt}\rho_C\omega_{I/C}} + 1\right)}\right)$$

Eq. 80

Water pore filling

In ex-situ gas diffusivity measurements, as mentioned in section 4.4.4, water was forced into the CL. To model the pore occupancy effect of water, the following assumptions were made:

- All hydrophilic pores of the CL were filled with water in the beginning.
- All agglomerates' pores are hydrophilic (following [70]).
- The percentage of the hydrophilic to total pore volume is the same for all of the secondary pore diameters.
- The ionomer thin film absorbs some of the water filled in the secondary pores, and primary pores remain occupied with water.

It was assumed that right after the ex-situ water introduction procedure, all of the hydrophilic pores of the CL were filled with water. The volume percentage of the secondary pores filled with water at this state (saturated hydrophilic secondary pores) $v_{fsp/sp}(sat)$, was calculated based on the weight gain of the CL, ionomer and primary pores:

$$v_{fsp/sp}(sat) = \frac{w_{CL\ water\ gain} - w_{I\ water\ gain} - w_{app\ water\ gain}}{V_{CL}\varepsilon_{CL\ swelled}v_{sp/p\ swelled}\rho_w}$$

Eq. 81

Here the CL water gain was input from the measurements explained in section 4.4.4. The ionomer water gain was calculated based on the mass of ionomer in the CL and Eq. 67. The volume of the CL was input from the densitometer measurements explained in section 3.1.3. The CL porosity with swelled ionomer was calculated in Eq. 80, and the volume ratio of the secondary pores to all pores $v_{sp/p\ swelled}$ was calculated as follows:

$$v_{sp/p\ swelled} = \frac{V_{sp\ swelled}}{V_{sp\ swelled} + V_{pp\ swelled}}$$

Eq. 82

The volume of primary pores remained the same after ionomer swell, as a result:

$$v_{sp/p\ swelled} = \frac{V_{sp\ swelled}}{V_{sp\ swelled} + V_{pp}}$$

Eq. 83

$$v_{sp/p\ swelled} = \frac{V_P\left(v_{sp/p} - \left(1 - \frac{\varepsilon_{CL\ swelled}}{\varepsilon_{CL}}\right)\right)}{V_P\left(v_{sp/p} - \left(1 - \frac{\varepsilon_{CL\ swelled}}{\varepsilon_{CL}}\right)\right) + V_p v_{pp/p}}$$

Eq. 84

$$v_{sp/p\ swelled} = \frac{v_{sp/p} + \frac{\varepsilon_{CL\ swelled}}{\varepsilon_{CL}} - 1}{v_{sp/p} + \frac{\varepsilon_{CL\ swelled}}{\varepsilon_{CL}} - 1 + v_{pp/p}}$$

Eq. 85

$$v_{sp/p\ swelled} = \frac{v_{sp/p} + \frac{\varepsilon_{CL\ swelled}}{\varepsilon_{CL}} - 1}{\frac{\varepsilon_{CL\ swelled}}{\varepsilon_{CL}}} = \frac{\varepsilon_{CL}v_{sp/p} + \varepsilon_{CL\ swelled} - \varepsilon_{CL}}{\varepsilon_{CL\ swelled}}$$

Eq. 86

So far, the water gain in ionomer and the denominator term of Eq. 81 was defined. To specify water gain weight in primary pores, it was assumed that the water first fills the accessible primary pores and then the ionomer coverage changes. For this reason, the water weight gain in primary pores was calculated based on the volume of accessible primary pores before ionomer swell:

$$w_{app\ water\ gain} = V_{CL}\varepsilon_{CL}v_{app/p}\rho_w$$

Eq. 87

where $v_{app/p}$ is the volume ratio of accessible primary pores to all pores. This ratio was calculated based on the volume ratio of primary pores to all pores (Eq. 46) and the volume ratio of the blind primary pores to accessible primary pores (Eq. 42):

$$v_{app/p} = v_{pp/p} v_{app/pp} = v_{pp/p} \times (1 - I_{\text{coverage}})$$

Eq. 88

where $v_{app/pp}$ is the volume ratio of accessible primary pores to all primary pores of the CL.

CL structural unit cells under saturated hydrophilic pores

As in fuel cell operation, the MEA is locked under compression load; it is assumed that the CL thickness remains constant when it absorbs water. As a result, the unit cell dimension remained the same for the CL with water. However, the ionomer thickness, CL porosity, overlap parameter, the secondary pore diameter, and gas-filled volume of the secondary pores changed. These parameters were calculated according to the driven equations:

1. Section 5.1.3: The dry unit cell set overlap parameter, ionomer coverage, unit cells' dimensions *a(i)*, unit cells' ionomer thickness $t_i(i)$
2. Eq. 87: Water weight gain in primary pores
3. Eq. 67: Water weight gain in ionomer
4. Eq. 70: Swelled ionomer coverage
5. Eq. 69 or 73: Swelled ionomer thicknesses $t_{i\ swelled}(i)$
6. Eq. 74: Swelled overlap parameter
7. Eq. 80: Swelled CL porosity
8. Eq. 75 and 77: Swelled PSD
9. Eq. 81: Volume percentage of the secondary pores filled with water

CL structural unit cells for bellow saturated condition

In fuel cell operation, the pore filling happens locally and controlled by capillary pressure [49]:

$$p_{\text{capillary}} = p_{\text{gas}} - p_{\text{liquid}} = \frac{2\sigma \cos\theta}{r_{\text{capillary}}}$$

Eq. 89

where σ is the surface tension, and θ is the contact angle. At any capillary pressure, all pores with a radius smaller than the capillary radius are filled with water. Eq. 89 suggest that water evaporates first from larger pores. To include water removal from the CL in the model, the weight of water content in the CL, $W_{H2O}(\tau)$, was assumed to be known. Following the procedure in section 4.4.4, it was assumed that all hydrophilic pores of the CL were saturated right after the water introduction into the CL. Therefore, the amount of water in the CL at the saturated condition, $W_w(sat)$, was calculated based on the CL water gain weight measurement right after the water introduction:

$$W_w(sat) = W_{CL\ water\ gain} - W_{I\ water\ gain} - W_{app\ water\ gain}$$

Eq. 90

The volume ratio evaporated from the CL, $v_{we}(\tau)$, was calculated based on the CL water content weight:

$$v_{we}(\tau) = 1 - \frac{W_w(\tau)}{W_w(sat)}$$

Eq. 91

Starting from the largest secondary pore in PSD, water was removed from the secondary pores based on this ratio .

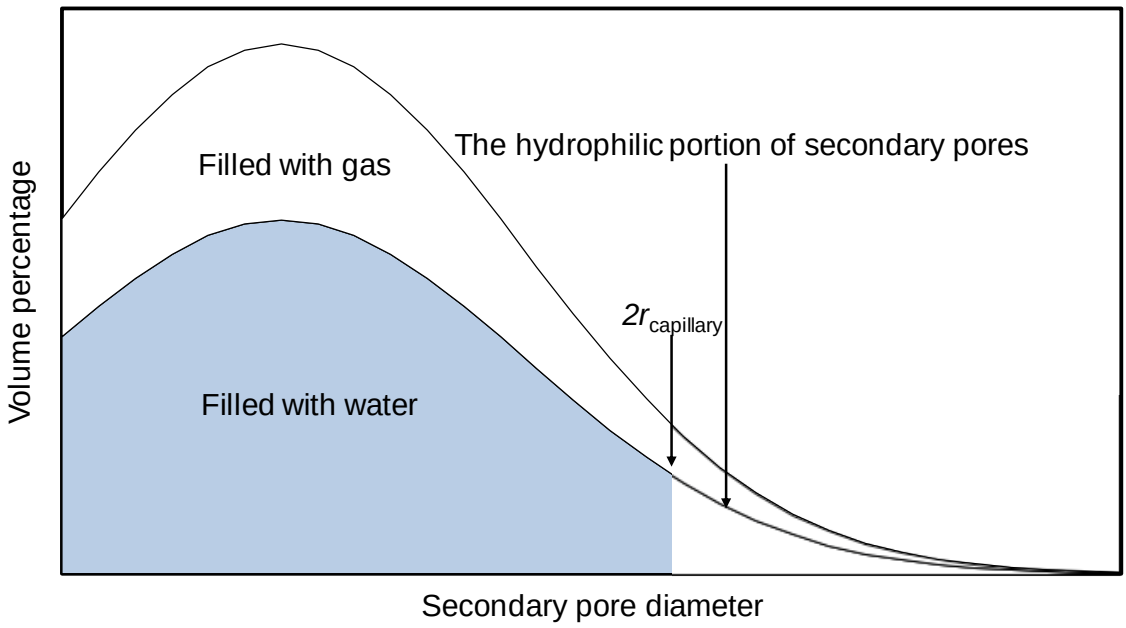

Figure 5.3 The schematic of the CL PSD partially filled with water

5.2. CL diffusivity model

Following the structural model, the gas diffusivity was modeled also in two scales: the diffusivity within agglomerates, and the diffusivity of the unit cell.

5.2.1. The diffusivity model within agglomerates

Considering a network of series molecular and Knudsen diffusion resistances following Ref. [23], the relative diffusivity was calculated from Eq. 92:

$$D^* = \left(D_{\text{binary}}/D_{\text{molecular}} + D_{\text{binary}}/D_{Kn}\right)^{-1}$$

Eq. 92

and Kn diffusivity was calculated from Eq. 93 [22]:

$$D_{Kn} = (4/3)d_{\text{pore}}\sqrt{RT/2\pi M}$$

Eq. 93

where R is the gas constant, 8.314 (J·mol-1·K-1), M is the molecular weight of the gas (kg/mol), and d_{pore} is the radius of the pore (m). Primary pores are less than 20 nm [18,19] in diameter and the mean free path of oxygen at room temperature and atmospheric pressure is 63 nm [132]; thus, Knudsen diffusion is dominant for primary pores, which is a linear function of pore radius. Therefore, an effective primary pore radius based on linear averaging on all primary pores could be used for diffusivity calculations (Eq. 21).

In Eq. 92, the Knudsen to binary ratio was calculated through Eq. 93 and the literature values for binary diffusion. The molecular ratio represents the effect of the pore shape and the connectivity of pores in the porous medium in comparison with open space, which is solely a function of geometry shape and not pore size or thermodynamic conditions. To this end, a numerical model for FCC arrangement of carbon particles in the CL was developed to find the unique value of the relative diffusivity, without the Knudsen effect. Pure diffusion was solved using commercial numerical software ANSYS Fluent 14.5 [133].

Numerical model for FCC arrangement

In the FCC arrangement, shown in Figure 5.4a, spheres are arranged in corners of equilateral triangles in a plane. In the upper row, each sphere sits on the three adjacent spheres form the lower row. To model the geometry of FCC without singular points with

zero size where spheres touch, an overlapping of about ~ 5% of diameter was considered between the adjacent spheres (Figure 5.4b). The diffusion coefficient within C-Pt particles (solid part of the FCC arrangement) was assumed to be zero in compare to the gas diffusion in the pore part (= 1). Boundary conditions were set as different concentrations on each end, and insulation on lateral surfaces. Pure diffusion was solved within the gaps between particles numerically. It should be mentioned that numerical modeling was capable of capturing pure diffusion problems if a fine mesh network was used. Independency of the model to mesh element size was verified by performing a mesh indecency study (Figure 5.5) toward relative diffusivity, Eq. 94 and 95:

$$N = \frac{D_{eff}}{D_{\text{binary}}} \frac{AD_{\text{binary}}\Delta C}{L}$$

Eq. 94

$$D^* = \frac{NL}{D_{\text{binary}} A \Delta C}$$

Eq. 95

where *L* is the diffusion path length, *C* is the gas concentration, and *N* is the diffusion rate, respectively.

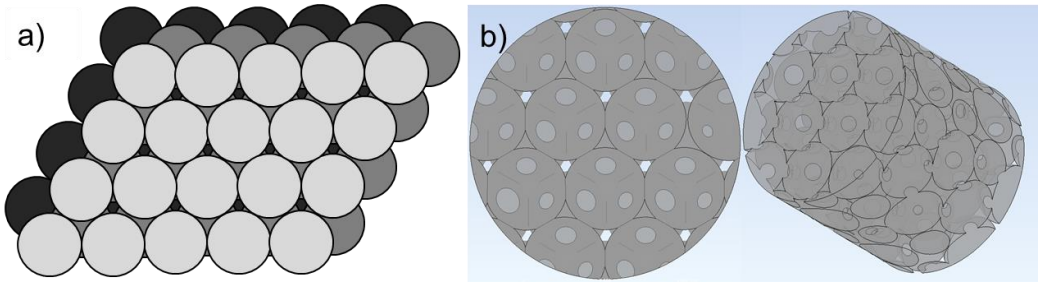

Figure 5.4 a) FCC arrangement geometry. b) The geometry used in the numerical model for FCC arrangement

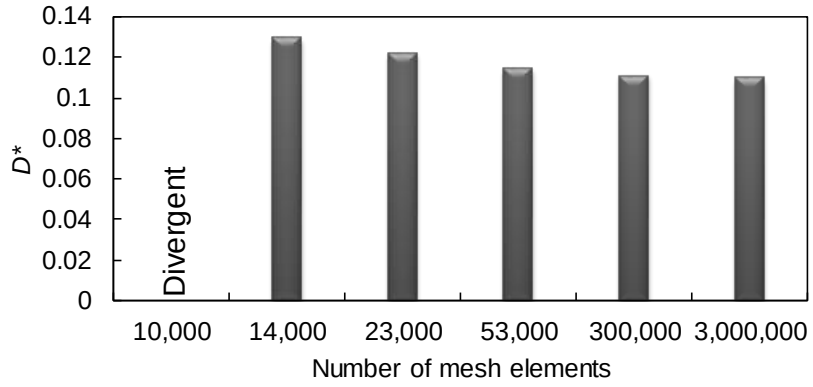

Figure 5.5 Mesh study for the numerical model of FCC arrangement toward relative diffusivity

As relative diffusivity results were almost the same using meshes with 300,000 and 3,000,000 elements, the one with 300,000 elements (the average size of the mesh elements were 3 orders of magnitude smaller than the unit cell dimensions) was identified to be proper for the numerical model.

Based on the numerical model, the relative diffusivity of FCC arrangement without Knudsen effect was about 0.11.

The diffusivity of the C-Pt particles packed-bed was calculated by substituting the FCC arrangement diffusivity and Knudsen diffusivity (Eq. 93) into Eq. 92:

$$D_{C-Pt\ aggr} = \left(9.09/D_{\text{binary}} + 0.19 d_{pp\ eff}\sqrt{M/RT}\right)^{-1}$$

Eq. 96

To find out the diffusivity of agglomerates, it was assumed that ionomer diffusivity is zero in comparison with diffusivity of the C-Pt particles aggregate. The overall diffusivity of agglomerates was calculated based on a parallel network of resistance for accessible (diffusivity calculated in Eq. 96) and blind (D=0) part of aggregates:

$$D_{agg} = \left(1 - I_{\text{coverage}}\right) D_{C-Pt\ aggr}$$

Eq. 97

$$D_{agg} = (1 - I_{\text{coverage}})\left(9.09/D_{\text{binary}} + 0.19 d_{pp\ eff}\sqrt{M/RT}\right)^{-1}$$

Eq. 98

5.2.2. The diffusivity of the unit cell

There was no exact analytical solution for gas diffusion within the defined unit cell in the literature as it was a complex geometry. However, assuming a 1-D simplification, a

network of infinitesimal series resistances was used to calculate the relative diffusivity of the unit cell (see Figure 5.6a). The unit cell was split into two regions (see Figure 5.6b). In the first region, the location of each element was specified with an angle θ (see Figure 5.6b), and its shape is showed in Figure 5.6d. Each element had two parts: agglomerate part and a secondary pore part. The elemental agglomerate radius, r_e, and the overlap angle, φ_e, were defined, as shown in Figure 5.6d. The element thickness, t_e, is showed in Figure 5.6e. Considering Figure 5.6c-f, the elemental geometry parameters calculated as follows:

$$r_e = \sqrt{r^2 - a^2\, tan^2\, \theta} = a\sqrt{\xi^2 - tan^2\, \theta}$$

Eq. 99

$$\xi_e = \frac{r_e}{a} = \sqrt{\xi^2 - tan^2\, \theta}$$

Eq. 100

$$\varphi_e = cos^{-1}\left(\frac{1}{\xi_e}\right)$$

Eq. 101

$$t_e = ad(tan\theta)$$

Eq. 102

$$A_{e\ agg} = 4a^2\left[\left(\frac{\pi}{4} - \varphi_e\right){\xi_e}^2 + tan(\varphi_e)\right]$$

Eq. 103

$$A_{e\ sp} = 4a^2\left[1 - tan\,\varphi_e + \left(\varphi_e - \frac{\pi}{4}\right){\xi_e}^2\right]$$

Eq. 104

where $A_{e\ sp}$ and $A_{e\ agg}$ are the cross-sectional area for secondary pore and agglomerate parts of the element respectively.

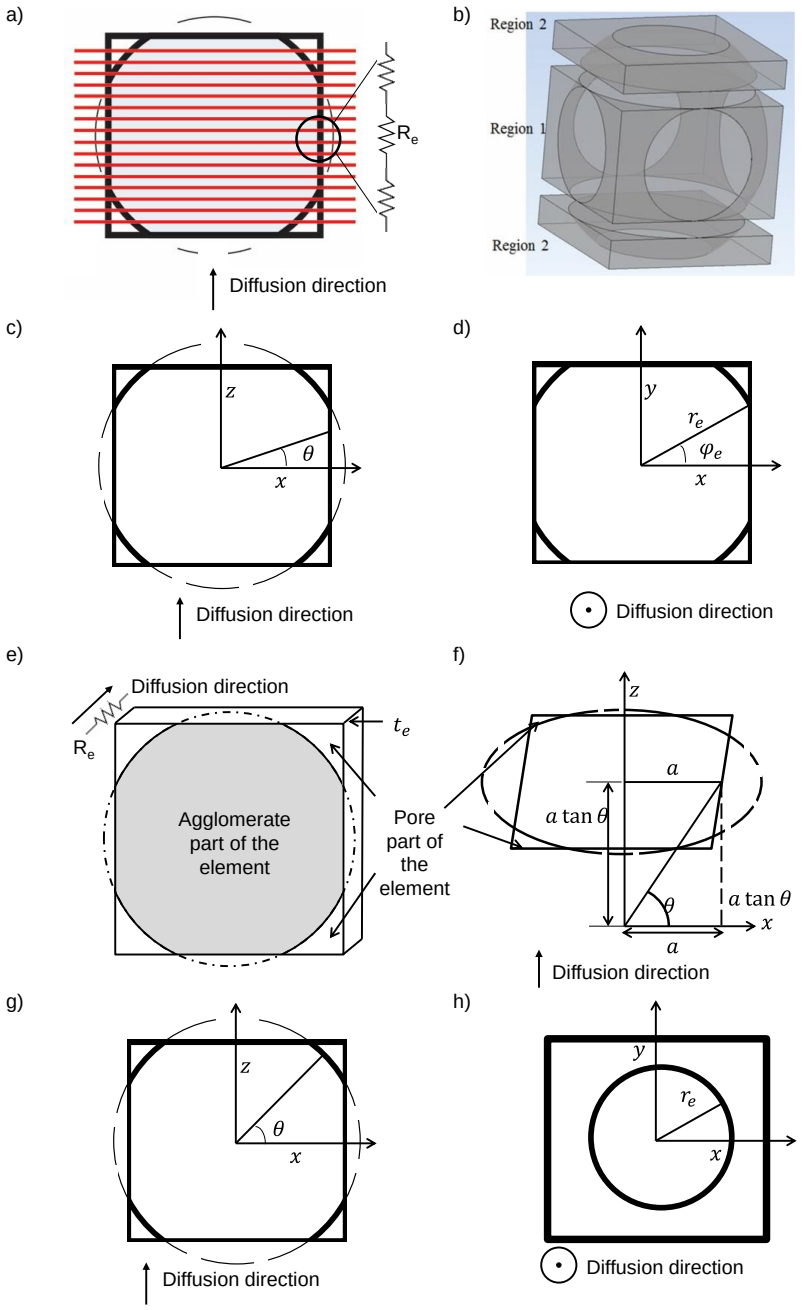

Figure 5.6 **a) Network of series resistances for the unit cell. b)Side view schematic of the angle identifying the diffusion resistance. c) Considered diffusion resistance element. d) The geometrical parameters of the gas diffusion resistance element. e) The schematice of the gas diffusion resistance element. f) The special location of the gas diffusion resistance element. g) The side view of the unit cell and angular location of the gas diffusion resistance element. h) The top view of the unit cell and the gas diffusion resistance element**

The resistance of each element consisted of two resistors related to the secondary pore and agglomerate parts that were calculated as follows:

$$R_e = \left(\frac{A_{e\,agg} D_{agg}}{t_e} + \frac{A_{e\,sp} D_{sp}}{t_e}\right)^{-1} = \frac{t_e}{A_{e\,agg} D_{agg} + A_{e\,sp} D_{sp}}$$

Eq. 105

$$R_e = \frac{1}{aD_{sp}} \frac{d(\tan\theta)}{\frac{D_{agg}}{D_{sp}} 4\left[\left(\frac{\pi}{4} - \varphi_e\right)\xi_e{}^2 + tan(\varphi_e)\right] + 4\left[1 - tan\,\varphi_e + \left(\varphi_e - \frac{\pi}{4}\right)\xi_e{}^2\right]}$$

Eq. 106

The total resistance of region 1 was calculated by integrating elemental resistance:

$$R_1 = \frac{1}{2aD_{sp}} \int_0^{\cos^{-1}\left(\frac{1}{\xi}\right)} \frac{d(\tan\theta)}{1 + \left(\frac{D_{agg}}{D_{sp}} - 1\right)\left(\tan(\varphi_e) + \xi_e{}^2\left(\frac{\pi}{4} - \varphi_e\right)\right)}$$

Eq. 107

In Eq. 107 D_{agg} was calculated based on Eq. 98, D_{sp} was calculated using Eq. 92 and 93, and the diameter of the unit cell secondary pore was calculated from:

$$D_{sp} = D_{\text{binary}}\left(1 + \frac{3D_{\text{binary}}\sqrt{2\pi M}}{4d_{sp}\sqrt{RT}}\right)^{-1}$$

Eq. 108

The procedure to calculate the second region resistance (Figure 5.6b) was the same. However, in this region, the angle specifying the location of the cell was redefined (See Figure 5.6g) to make the calculation easier. The geometry parameters for the new resistance elements were calculated as follows, considering Figure 5.6h:

$$r_e = r\cos\theta$$

Eq. 109

$$t_e = rd(\sin\theta) = a\xi d(\sin\theta)$$

Eq. 110

$$A_{e\,agg} = \pi r_e{}^2 = \pi r^2 \cos\theta^2 = \pi a^2 \xi^2 \cos\theta^2$$

Eq. 111

$$A_{e\,sp} = 4a^2 - \pi r^2 \cos\theta^2 = a^2(4 - \pi\xi^2 \cos\theta^2)$$

Eq. 112

Elemental resistance for this region also consisted of two parallel parts:

$$R_e = \frac{a\xi d(\sin\theta)}{D_{agg}\pi a^2 \xi^2 \cos\theta^2 + D_{sp} a^2(4 - \pi\xi^2 \cos\theta^2)}$$

Eq. 113

$$R_e = \frac{1}{aD_{sp}} \frac{\xi d(\sin\theta)}{\frac{D_{agg}}{D_{sp}} \pi \xi^2 \cos\theta^2 + 4 - \pi \xi^2 \cos\theta^2}$$

Eq. 114

The second region resistance was calculated through integrating the elemental resistances:

$$R_2 = \frac{2}{aD_{sp}} \int_{\cos^{-1}\left(\frac{1}{\xi}\right)}^{\frac{\pi}{2}-\cos^{-1}\left(\frac{1}{\xi}\right)} \frac{\xi d(\sin\theta)}{4 - \left(1 - \frac{D_{agg}}{D_{sp}}\right) \pi \xi^2 \cos\theta^2}$$

Eq. 115

Finally, the total resistance was calculated:

$$R_{tot} = R_1 + R_2$$

Eq. 116

Relating resistance to diffusivity, the relative diffusivity of the unit cell was calculated:

$$D^* = \frac{1}{2aD_{\text{binary}} R_{tot}}$$

Eq. 117

5.2.3. The unit cell relative diffusivity model verification

A numerical model was developed for the unit cell (shown in Figure 5.1c). The considered overlap parameter was 1.2. Different O_2 concentrations were set at the inlet and outlet boundaries. The relative diffusivity of the secondary pores was set to 1, and the relative diffusivity of agglomerate part was varied from 0.1 to 0.9. Velocity was set to zero in the domain; therefore, the only mechanism for mass to transport was through pure diffusion.

The analysis was performed in ANSYS Fluent 14.5. The independency of the model to mesh element size was verified by performing a mesh study (Figure 5.7) toward relative diffusivity (Eq. 95).

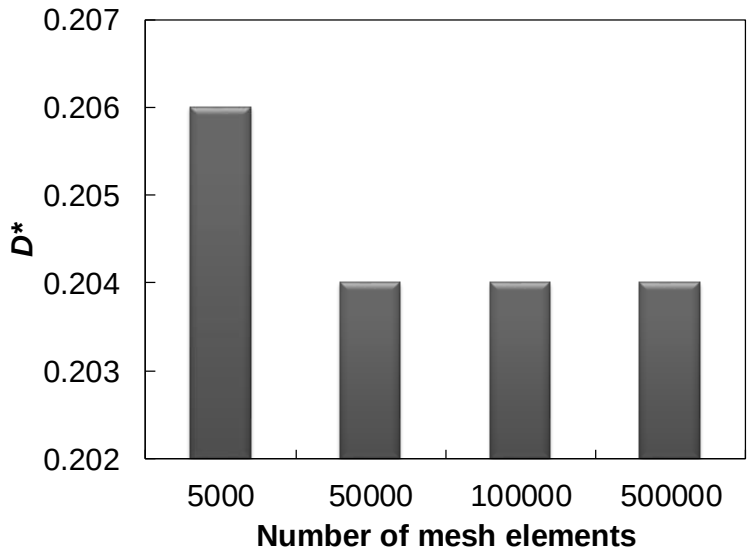

Figure 5.7 Mesh study for numerical model of the unit cell toward relative diffusivity. For this unit cell, overlap was 1.2 and the ratio of agglomerate to secondary pore relative diffusivity was about 0.1

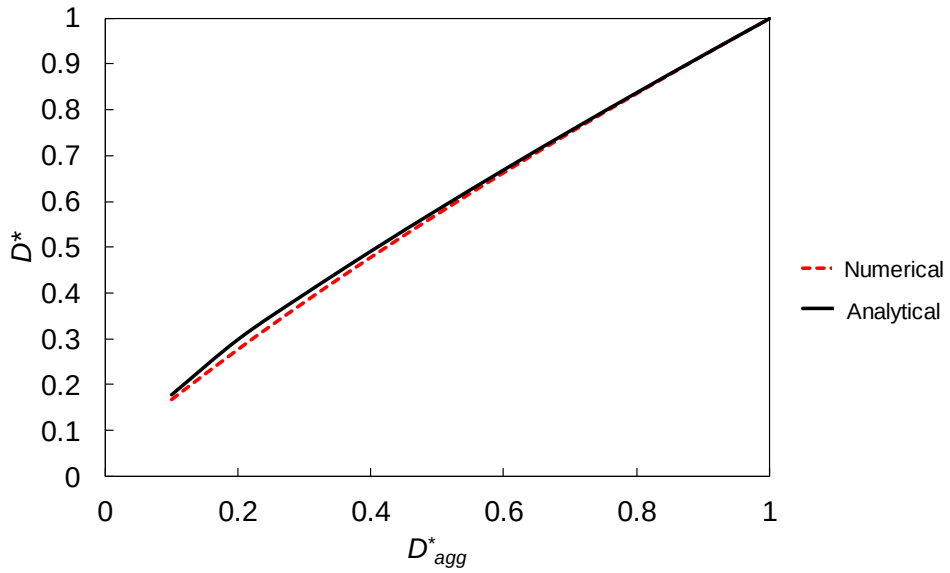

Figure 5.8 Comparison between the analytical, and the numerical relative diffusivities for different values of D^*_{agg}

Setting the relative diffusivity of secondary pores to 1, and changing the relative diffusivity of agglomerate part from 0.1 to 0.9, the relative diffusivities for the unit cell were numerically modeled, and compared to values calculated by the analytical solution

developed (Figure 5.8). The difference between relative diffusivity values were less than 1% for all agglomerates relative diffusivity values.

5.2.4. The CL relative diffusivity model

For each pair of the effective primary pore and a secondary pore from the input PSD, a unit cell was defined and its relative diffusivity was calculated. Then, the effective diffusivity of the CL was calculated through volume-ratio weighted average over the calculated diffusivities for each pair of the secondary pore and the effective primary pore:

$$D^*_{CL} = \frac{\sum_i v(i) \times D^*(i)}{\sum_i v(i)}$$

Eq. 118

where D^*_{CL} is the CL relative diffusivity, $D^*(j)$ is the relative diffusivity of the unit cell for the pair of the effective primary pore (Eq. 21) and the i^{th} secondary pore in the PSD, and $v(i)$ is the volume-ratio of i^{th} secondary pore in the PSD.

The proposed diffusivity model considers effect of different operating temperatures (through binary and Kn diffusivities) and compression loads (through input structural model). However, volume ratios, $v(j)$ in Eq. 118 should be changed to gas-filled volume ratios, $v_{gf}(i)$, for the CL containing water (the structural changes due to water was already considered through the structural model). $v_{gf}(j)$ was calculated using Eq. 81 and the ratio of weight of water inside the CL at time τ, $W_w(\tau)$, to the weight of water in saturated state $W_w(sat)$:

$$v_{gf}(i) = \left(1 - v_{fsp/sp}(sat)\frac{W_w(\tau)}{W_w(sat)}\right) v(i)$$

Eq. 119

As gas diffusivity of the water-filled unit cells was negligible in comparison with the gas-filled ones, to calculate diffusivity of the CL, Eq. 118 became:

$$D^*_{CL} = \frac{\sum_j v_{gf}(j) \times D^*(j)}{\sum_j v(j)}$$

Eq. 120

Chapter 6.

Effect of ink processing and composition on the CL pore structure, porosity, and relative diffusivity

6.1. Evaluation of the measurement and modeling methods for CL gas diffusivity used in this study

6.1.1. Gas diffusion testbed evaluation

Design #4 (I/C=1.1, dm=0, T_d=50 ˚C) was chosen to be tested by DDT and MLC. Tests were performed on eight CL samples with thicknesses ranging from 5 to 10 μm and Pt loadings from 140 to 280 μg/cm^2 (measured with X-Ray). The Pt loadings and CL thicknesses of the samples are summarized in Table 6.1. Diffusivity tests are performed at room temperature (~20˚C), atmospheric pressure, and relative humidity of 0%.

Table 6.1 CL thicknesses measured from SEM images of sample cross sections and measured CL effective length and relative diffusivity

Sample	1	2	3	4	5	6	7	8
Pt loading (μg/cm^2)	144±10	144±10	209±17	209±17	247±20	250±20	250±20	280±22
t (μm)	5.4±0.5	6.5±0.6	8.4±0.8	9.0±0.9	8.6±0.9	9.0±0.9	9.5±1.0	10.4±1.0
L_{eff} (μm)	43±5	49±5	72±8	60±7	74±8	72±8	80±9	74±8
D^*±.02	0.12	0.13	0.12	0.15	0.12	0.12	0.12	0.14

Figure 6.1 shows the measured relative diffusivities of CL with DDT as a function of Pt loadings. Considering the random porous structure of CL, the relative diffusivity values are highly consistent (~ 0.12), and all values agree within measurement uncertainty. The uncertainty of calculated relative diffusivities (obtained by Eq. 13) was about 15%.

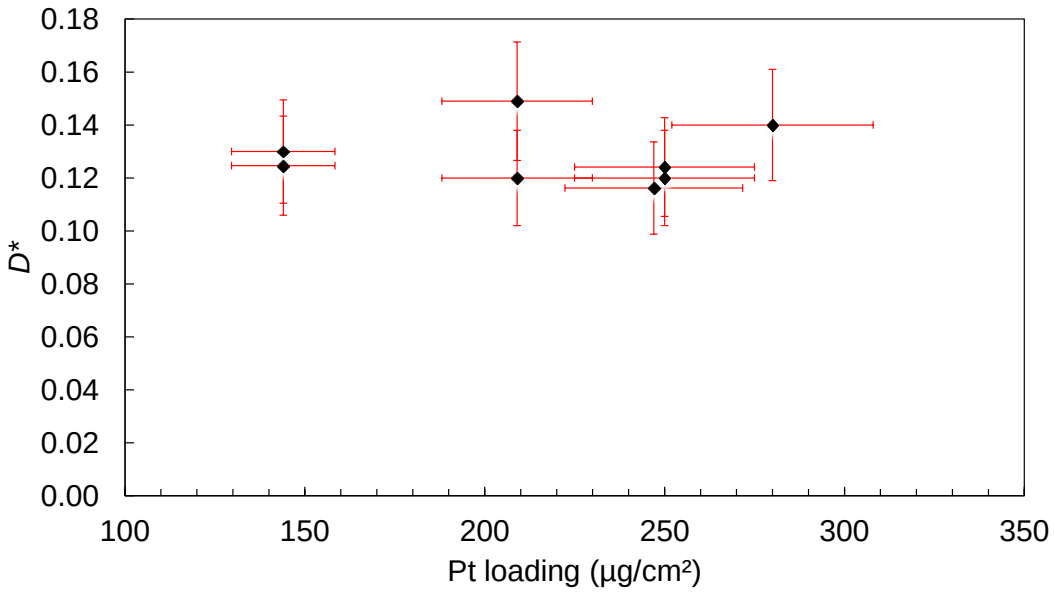

Figure 6.1 Relative diffusivity values, *D, for CLs with Pt loading from 140 to 290 µg/cm², measured by DDT (error bars are standard deviation of at least three measurements)**

Same samples were measured together as a stack with MLC as well. The main reason to use the stack of samples instead of separate tests for each one was to increase the test subject resistance. For samples with higher resistance, the measurement signal is stronger, and, as a result, the uncertainty will be lower. The test was repeated for the same stack ten times, and the measured relative diffusivities are brought in Figure 6.2a. This procedure was repeated for different stacks with the same design and the results (average of 10 test repetitions) are brought in Figure 6.2b.

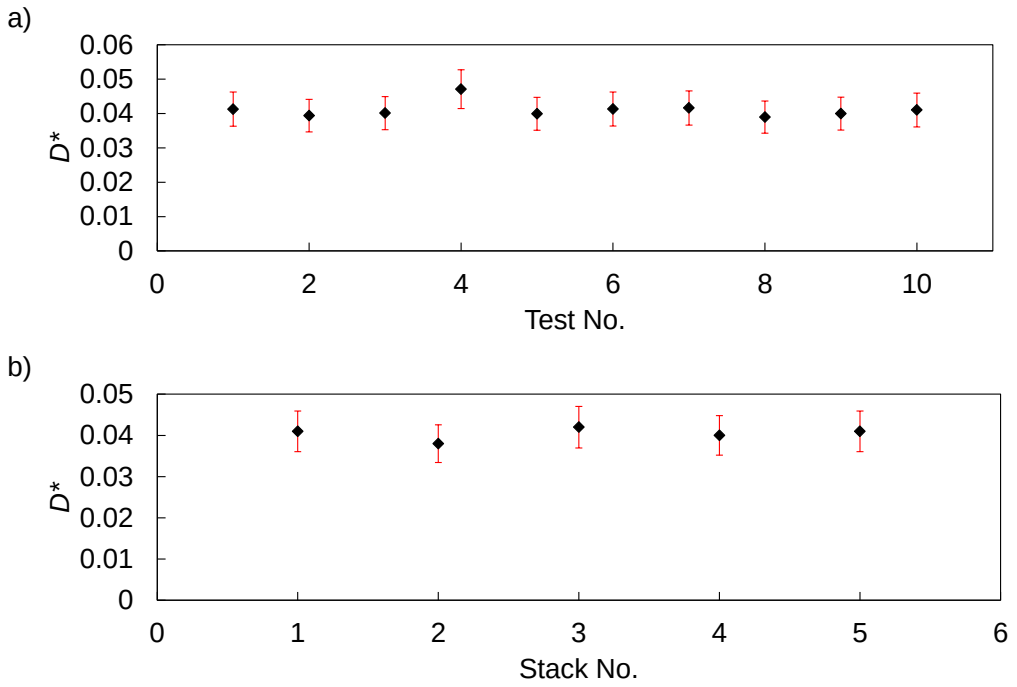

Figure 6.2 **a) Relative diffusivity values, *D**, for stack of 10 CL (design #4) samples measured by MLC and repeated 10 times. b) The average of relative diffusivity values for 10 test repetitions, for 5 different stacks of 10 CL (design #4) samples measured by MLC.**

Diffusivity values reported in the literature for CL are presented in Figure 6.3 and Table 6.2. The CL preparation method and composition affect its diffusivity. In Figure 6.3, CLs with porosity of ~0.5 are chosen for comparison (close to the porosity of the CL design #4 in this study).

Because of the gas flows in DDT, there was an uncontrollable pressure difference across the sample during tests (~30 Pa), which could lead to a convective flow and artificially increase the measured diffusivity. As a result, DDT showed diffusivities higher than MLC or the reported values in the literature. By comparison, there was no pressure difference across the sample in the MLC tests (closed chambers). Also, there was a good agreement between MLC result and the literature data.

Beside the mentioned superior accuracy of the MLC over DDT, the MLC used in this study had the capability of measuring the gas diffusion coefficient under different operating conditions (will be explained later). As a result, MLC was chosen as the primary measurement tool, and discussions are focused on the result of this testbed onward.

To measure gas diffusivity of each CL design and each operating condition, the oxygen concentration vs time measurements were done mostly for three different stacks of the CL samples of the same design, with at least ten repetitions of the test per stack. In this study, twelve different designs, three different operating temperatures, five different operating RH values, three different operating compressive loads, and six different operating water contents were evaluated. The unprocessed results can be found in Appendix A, and here the processed results are presented.

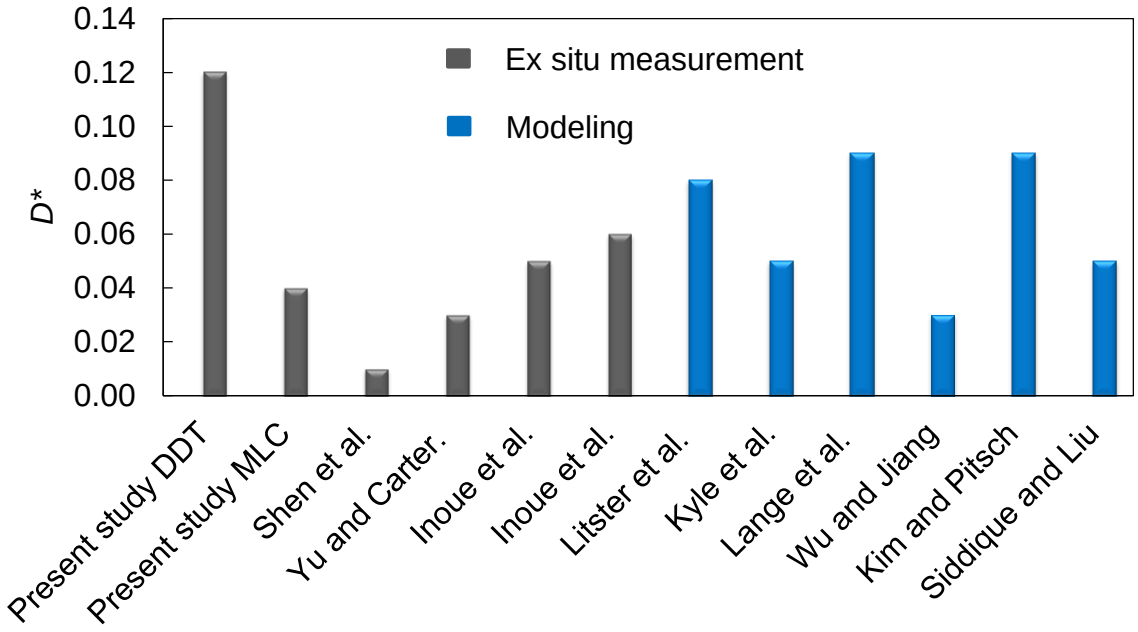

Figure 6.3 **Comparison between ex-situ diffusivity measurements for CL design #4 and the results in the literature. Details for each data point are in Table 6.2**

Table 6.2 **CL gas diffusivity investigations: the method, sample preparation, porosity, and operating conditions**

	Method	Sample preparation method	ε	Operating conditions
Present study	MLC-WKC (DDT)	Mayer bar coating on filter PTFE	0.58	T=20 ˚C, RH=0
Shen et al. [5]	MLC	Spraying on Alumina	-	T=25 ˚C
Yu and Carter. [42]	WKC in-plane	-	-	T=80 ˚C, RH=0
Inoue et al. [40]	WKC	Spraying	0.53	T=22 ˚C
Inoue et al. [40]	FIB-SEM	Spraying	0.57	T=22 ˚C
Litster et al. [80]	X-Ray CT	-	0.42	T=57 ˚C
Lange et al. [71]	FIB-SEM	Spraying	-	-
Wu and Jiang [134]	Stochastic microstructure	-	0.35	-

	reconstruction (lattice Boltzmann)			
Kim and Pitsch [100]	Stochastic microstructure reconstruction (lattice Boltzmann)	-	0.50	-
Siddique and Liu [47]	Numerically mimicking fabrication process	-	0.45	T=75 ˚C

6.1.2. Model Validation[6]

The CL design #4 (I/C= 1.1, Dm=0, and T_d=50 ˚C) was chosen to validate the relative diffusivity model. The inputs to the model are given in Table 6.3 and Figure 6.4.

Table 6.3 The inputs to the relative diffusivity model

Parameter	Value	Method/Reference
CL porosity	58%	In-house thickness measurements and Eq. 9
CL PSD	Figure 6.4	In-house N_2 adsorption measurement (BJH)
Carbon support particle porosity	28.7%	[135]
Carbon support particle density	2 g/cm^3	[107]
Ionomer density	1.9 g/cm^3	[108]
Platinum density	21.4 g/cm^3	[106]
FCC packed bed porosity	26%	[120]

[6] The model code is brought in Appendix B.

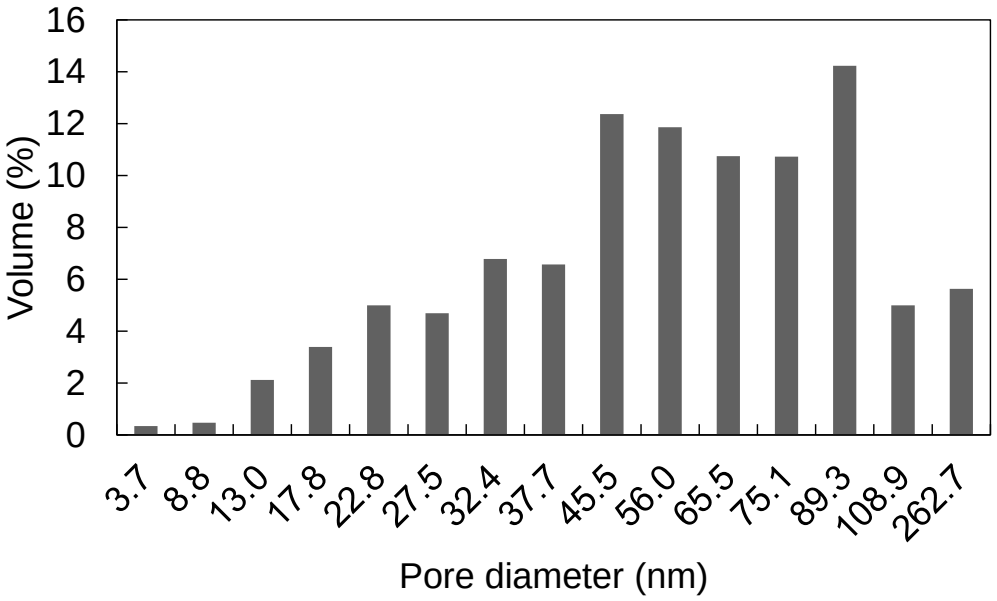

Figure 6.4 The measured PSD for CL design #4 with N_2 adsorption porosimetry applying BJH method, used as input to the relative diffusivity model

The results of the model are given in Table 6.4.

Table 6.4 The results of the relative diffusivity model for CL design #4 (I/C= 1.1, Dm=0, and T_d=50 ˚C)

Modeled parameters	Modeled result values
CL relative diffusivity without Knudsen effect	0.4206
CL relative diffusivity with Knudsen effect	0.0385
Relative diffusivity within agglomerates	0.0027
Ionomer coverage	0.61
Ionomer mean film thickness	14 nm
Agglomerates overlap angle	13 ˚

The measured relative diffusivity of CL was 0.04. The relative diffusivity value considering the Knudsen effect predicted the CL relative diffusivity accurately. However, the value without the Knudsen effect was an order of magnitude higher, which insists on the importance of considering the pore diameter in modeling relative diffusivity (Knudsen diffusion is a function of pore diameter).

The calculated relative diffusivity of agglomerates was an order of magnitude less than the CL relative diffusivity. As in fuel cell operation, oxygen molecules should reach the reaction sites within agglomerates, this parameter could be a critical parameter in

modeling the diffusion process that delivers oxygen molecules to the reaction sites. The gas diffusivity within agglomerates was still an order of magnitude higher than the reported values for in-situ gas diffusivity values (e.g., 4E-4 at T=30 ˚C in Ref. [25]). As for in-situ gas diffusivity, diffusion through water and ionomer is part of the gas path as well.

To compare the modeled parameters here with available data for other CLs, the Ishikawa et al. [136] work was considered. They modeled the CL structure by mimicking the actual shapes of Pt particles and carbon aggregates, as well as the ionomer adhesion in real CLs. They reported ionomer coverage over Pt particles of ≈0.74 for the CL with I/C=1, Pt/C=1, and ε=0.48, which is close to the calculated values here. The Ishikawa CL had 10% less ionomer than the CL design #4, which logically should lead to a less ionomer coverage. However, their CL porosity was about 20% less compared to the CL design #4, which result in higher ionomer coverage, and somehow cancel the former effect out.

Ishikawa also reported mean ionomer thickness of about 10 nm, which is less than the calculated value here (14 nm). As the ionomer content for their CL was 10% less than the ionomer content of the design #4, the lower ionomer thickness was expected.

6.2. Porosity and relative gas diffusivity

Figure 6.5 shows the measured relative gas diffusivities versus the CL porosities, regardless of the production process. While the general upward dependency of relative diffusivity to porosity is apparent, there is no simple mathematical function relating porosity to relative diffusivity. Different production procedures resulted in different PSDs, pore connectivities, and even pore structures (will be discussed later). As a result, porosity alone could not specify the relative diffusivity values. Such behavior might seem obvious; however, it is common in the literature to consider the gas diffusivity (and other transport properties) as a function of solely porosity in the porous field (e.g., power function [24]). In such models, based on the general structure of a material (e.g., a network of cylindrical fibers, agglomerate-type) or experimental data, different constants were fitted for the property function of a material. Figure 6.5 shows the shortcoming of such functions for the CL. Although all the samples were agglomerate-based porous structure, the fitted power function for relative gas diffusivity was not an accurate indication of the property. Moreover, the traditional Bruggeman model [24] overestimates

the CL relative diffusivity by an order of magnitude in comparison with the measured values for relative diffusivity.

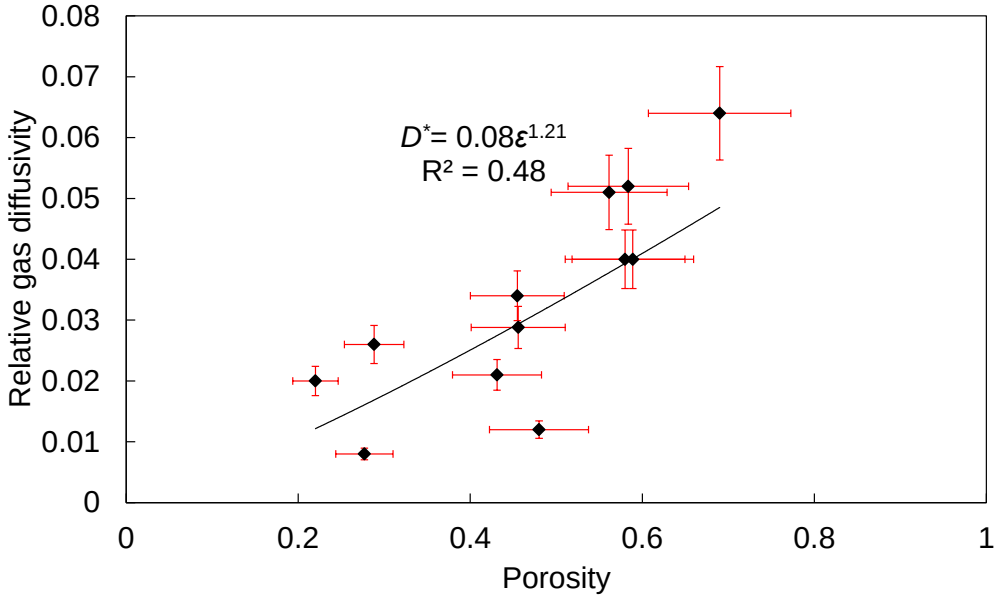

Figure 6.5 **The measured relative diffusivity values by MLC versus calculated porosities based on thickness measurements. As the standard deviations of repeated measurements for the CL relative diffusivity were less than the calculated uncertainties based on thickness measurements (section 4.1.2), for both relative diffusivity and porosity, the error bars are calculated based on thickness measurements uncertainties.**

As in different CL designs, both porosity and PSD changes, and the dependency of relative gas diffusivity to the porosity could not be specified. However, in the model porosity could be changed while other parameters were kept constant. To this end, design #4 was chosen to study the effect of porosity on the relative diffusivity of CL. Figure 6.6a shows that changing porosity from 32% to 62% decreased overlap angle from 40 ˚ to 5 ˚. Reducing the porosity from its original value (58%) will affect mostly the geometry in the agglomerate scale, as in sub-agglomerate scale, the structure was a compact one. The agglomerate scale porosity related directly to the overlap angle. Higher porosities resulted in the larger gaps and smaller overlap angles. Therefore, each agglomerate had more available surface area for ionomer to cover, and the ionomer coverage decreased (Figure 6.6a).

There were two resistive mechanisms in series in the way of the gas diffusion through the CL: the molecular resistance and the Knudsen resistance. Increasing the porosity had a direct effect on the molecular mechanism and reduced the molecular resistance (Figure 6.6b); however, it did not affect the Knudsen diffusion resistance. If there were no Knudsen effect, the relative diffusivity had to be unity at porosity equal to 1. However, as it can be seen in Figure 6.6b, due to Knudsen effect this scenario was not the case here. Of course, in the real situation, when the porosity approaches one, the pore diameter becomes infinity, which has no Knudsen resistance. As a result, for the real case, when porosity is equal to one, the relative diffusivity is also one.

Changing the CL porosity while I/C was kept constant, did not change the agglomerate porosity (Eq. 61). However, as mentioned, it changed the ionomer coverage, and that affected the relative diffusivity within agglomerates (Figure 6.6b). Some ionomer coverage is necessary for fuel cell proper performance as it is the pathway for ions. As a result, the optimum coverage should be found considering the ion conductivity, primary pore accessibility (to provide Pt particles with oxygen), and the overall CL gas diffusivity (to provide the CL with oxygen). This analysis brings some insight into the relationship between the ionomer coverage, CL relative diffusivity, and agglomerates relative diffusivity.

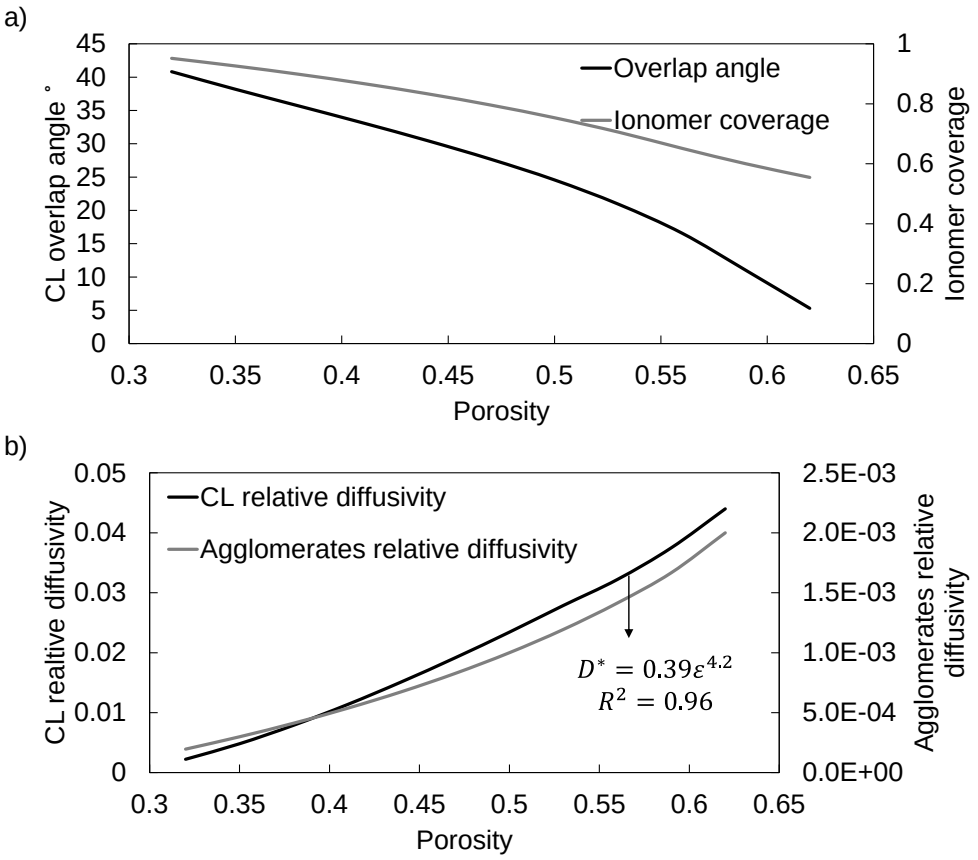

Figure 6.6 **a) The CL overlap angle and ionomer coverage versus porosity, keeping composition parameter and PSD constant. b) The CL and agglomerates relative diffusivities versus porosity, keeping composition parameters and PSD constant. The equation in the plot is a fit to the modeld relative diffusivity values at different porosities.**

6.3. Dry milling time

Figure 6.7 and Figure 6.8 shows the isotherms obtained for the CL designs with different dry milling times.

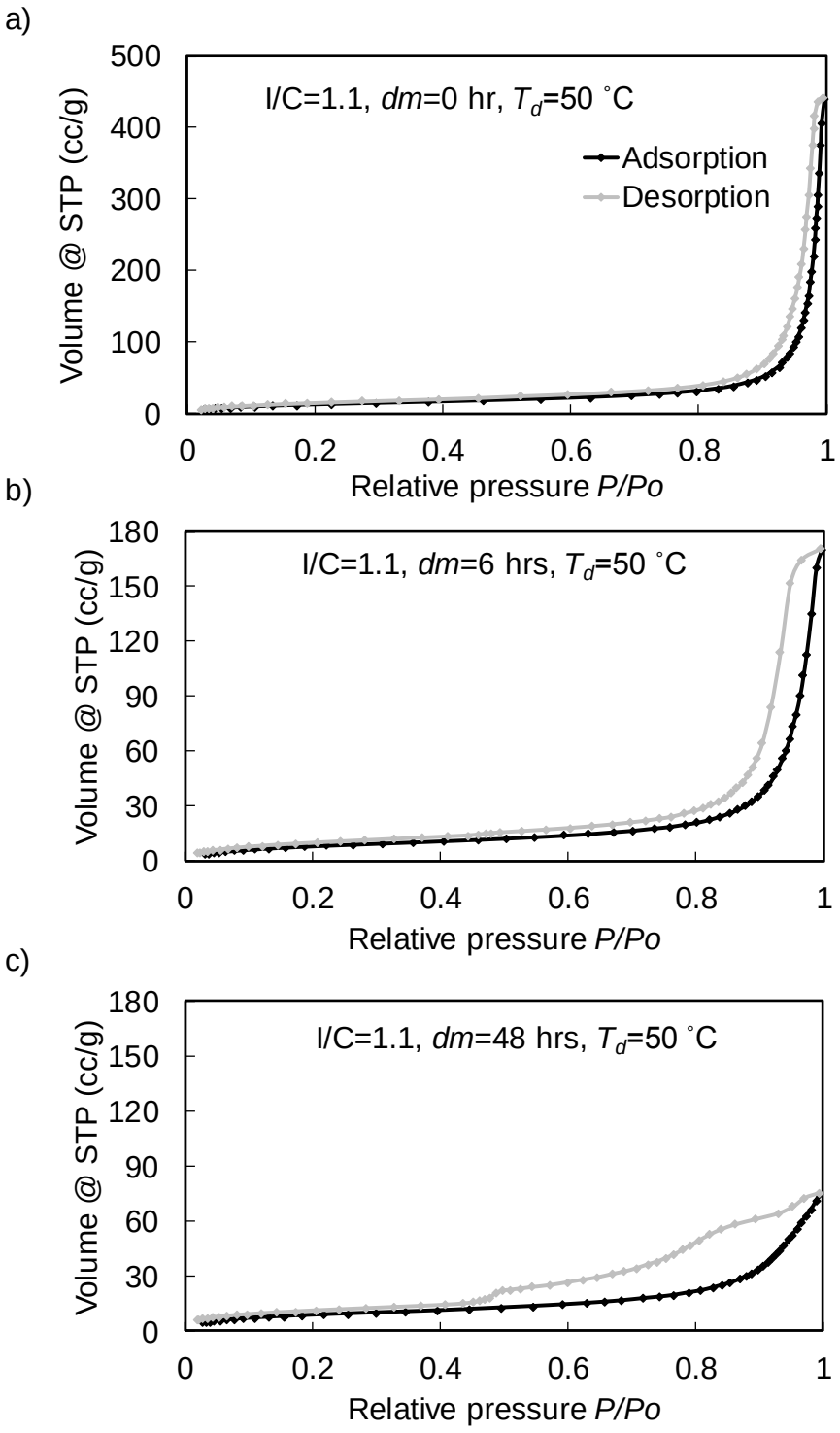

Figure 6.7 Isotherms obtained by N_2 adsorption of CL designs with, a) I/C=1.1, *dm*=0 hr, T_d=50˚C; b) I/C=1.1, *dm*=6 hrs , T_d=50˚C; and c) I/C=1.1, *dm*=48 hrs , T_d=50˚C

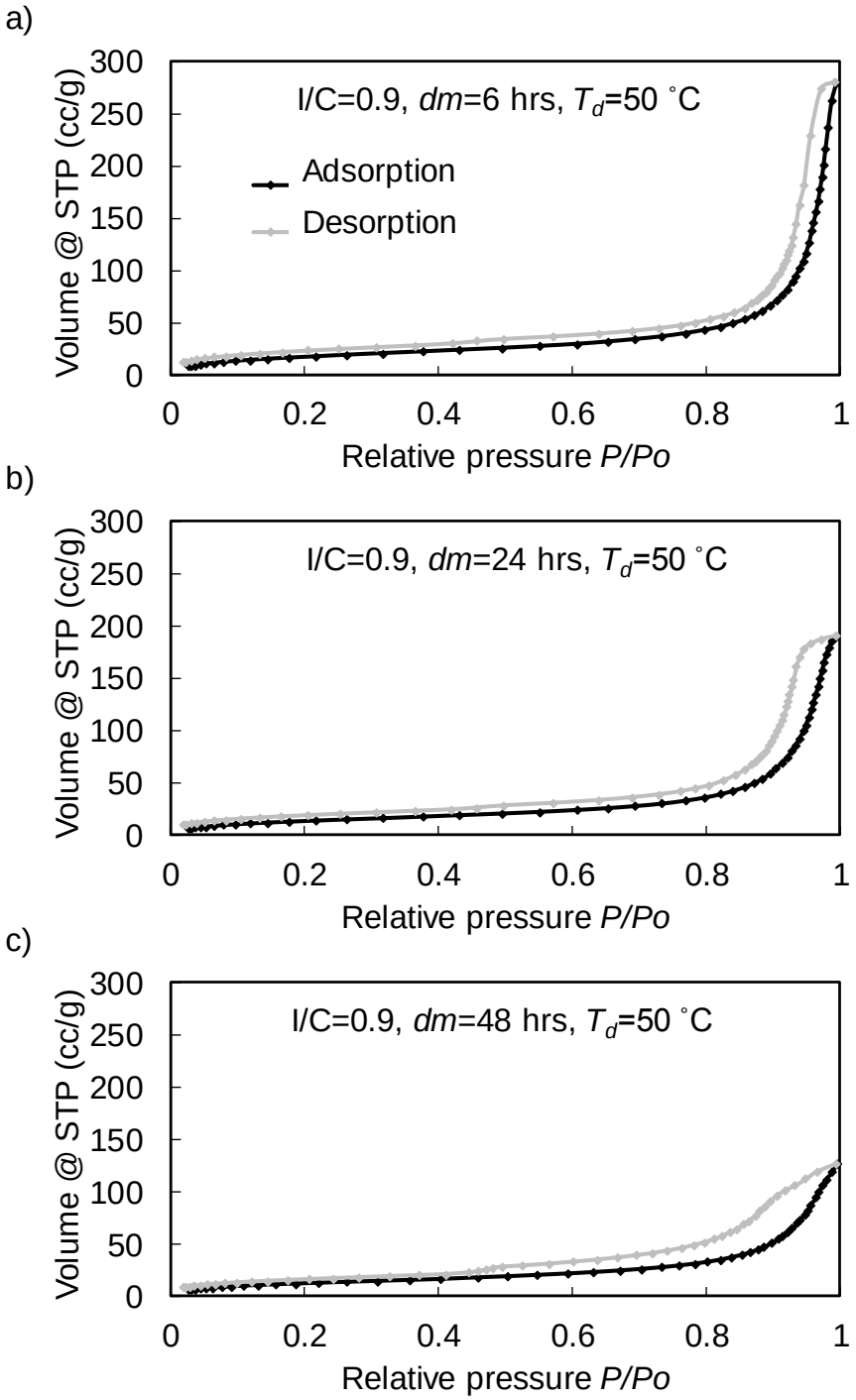

Figure 6.8 Isotherms obtained by N_2 adsorption of CL designs with, a) I/C=0.9, *dm*=6 hrs , T_d=50˚C; b) I/C=0.9, *dm*=24 hrs, T_d=50˚C; and c) I/C=0.9, *dm*=48 hrs, T_d=50˚C

Considering the shape of the isotherm for the CL design #4 (I/C=1.1, dm=0 hr, T_d=50) in Figure 6.7a, the isotherm and hysteresis loops were type IV and H1,

respectively, based on the IUPAC classification of isotherms [38]. Type IV isotherms indicate the filling and emptying of mesopores by capillary condensation and evaporation, respectively [39], and H1 hysteresis is associated with narrow, uniform pore distribution with open-ended cylindrical shapes. As shown in Figure 6.7b and c, dry milling the CL powder changed the isotherm shape drastically especially for the sample with 48 hrs of dry milling (Figure 6.7c). The hysteresis type of this design was H2, indicating a network of disordered interconnected pores of progressive sizes. The wide hysteresis loop is due to the pore blocking effects associated with the ink-bottle pores [39]. However, the sudden change at P/P_o=0.48 is an indication of the cavitation phenomena. Rasmussen et al. [27] showed that for nitrogen isotherms at 77.4 K, cavitation happens when the pore neck diameter is less than 5 nm. In their investigation, the adsorption curves of pores of two well-characterized types of mesoporous silicas (ordered mesoporous crystals (SBA-16), and hierarchically structured materials (KLE, KLE/IL and SLN-326)), the sharp change in hysteresis loop was also observed at P/P_o=0.48. Comparison of the porosimetry results for the CL samples with I/C=0.9 that were dry milled for 6, 24, and 48 hours showed a similar transformation in isotherm shape (Figure 6.8a-c). Such a transition was likely due to the over-smoothing of the catalyst powder. While it is unlikely that the dry milling could break the C-Pt particles into smaller pieces, it can break the weakly-bounded agglomerates of C-Pt particles (there is no binder between the particles) into smaller ones. The smaller C-Pt agglomerates in the catalyst powder for the dry-milled designs likely led to the smaller C-Pt and ionomer agglomerates, which resulted in reducing the size of gaps between agglomerates (secondary pores), and the more packed and tortuous structure. The presence of the cavitation effect is an indication of the gaps with narrow necks between agglomerates. Moreover, the reduction in the amount of nitrogen adsorbed by the dry-milled designs (note the vertical axis have different maximum values) confirms the less pore volume for the range of pore sizes detectable by N_2 adsorption. Figure 6.9 shows the same trend for the porosities of CLs with different amount of dry milling, which include all pores of the CL (See section 3.2.6). Besides, in Figure 6.10 and Figure 6.11, the shift of the PSD peaks to smaller pores and a reduction of the mean pore diameter for dry-milled designs is apparent. However, considering Figure 6.12a and b, there is a limit to the effect of dry milling and after 24 hrs of drying milling, the change in PSD for CL with I/C=0.7 became negligible.

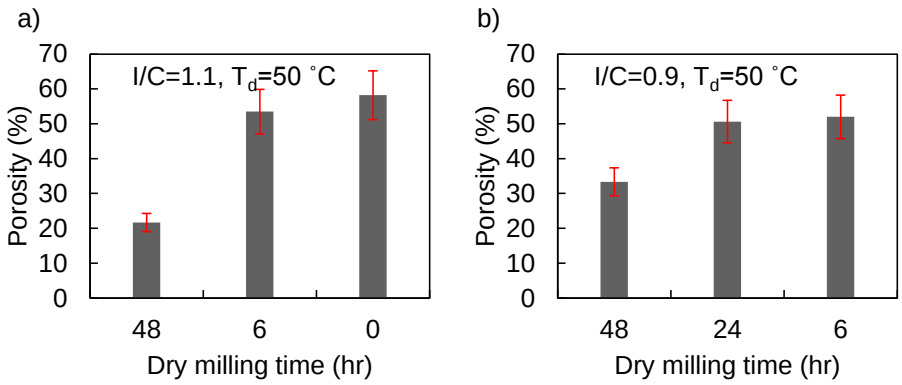

Figure 6.9 **Comparison of CL porosities calculated from densitometer for samples prepared with different dry milling times and a) I/C=1.1, T_d=50 ˚C, b) I/C=0.9, T_d=50 ˚C. The error bars shows the calculated standard deviation for 3 measurements**

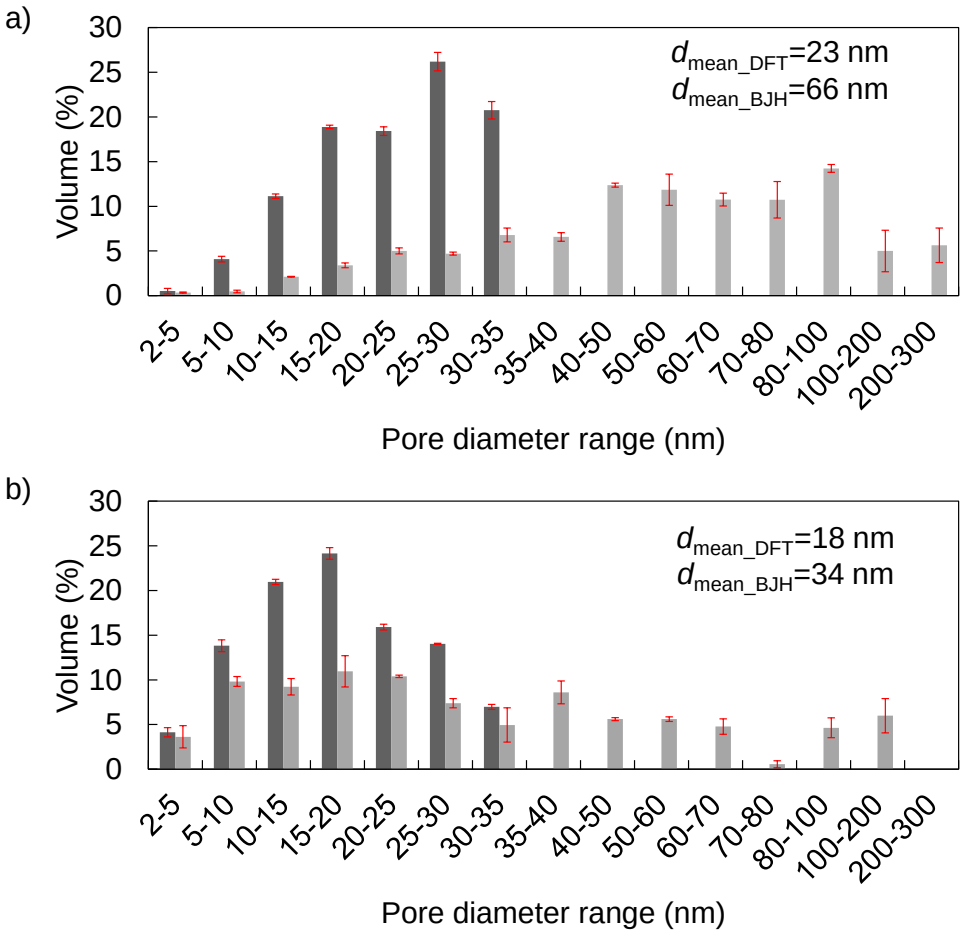

Figure 6.10 **PSD obtained by N_2 adsorption porosimetry applying DFT and BJH methods of CL designs with: a) I/C=1.1, dm=0 hr, Td=50˚C; and b) I/C=1.1, dm=48 hrs. The error bars are calculated standard deviation for 3 repeating measurements of the same sample**

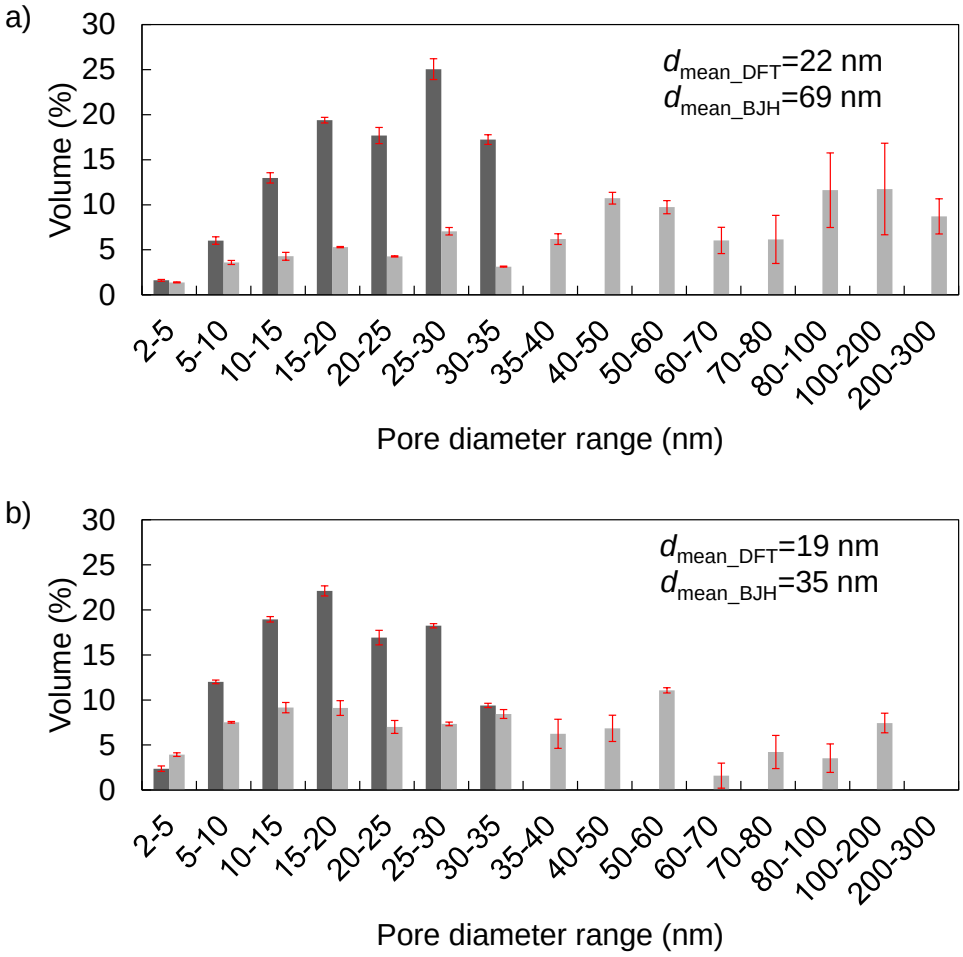

Figure 6.11 **PSD obtained by N2 adsorption porosimetry applying DFT and BJH methods of CL designs with: a) I/C=0.9, dm=6 hrs, Td=50˚C; and b) I/C=0.9, dm=48 hrs, Td=50˚C. The error bars are calculated standard deviation for 3 repeating measurements of the same sample**

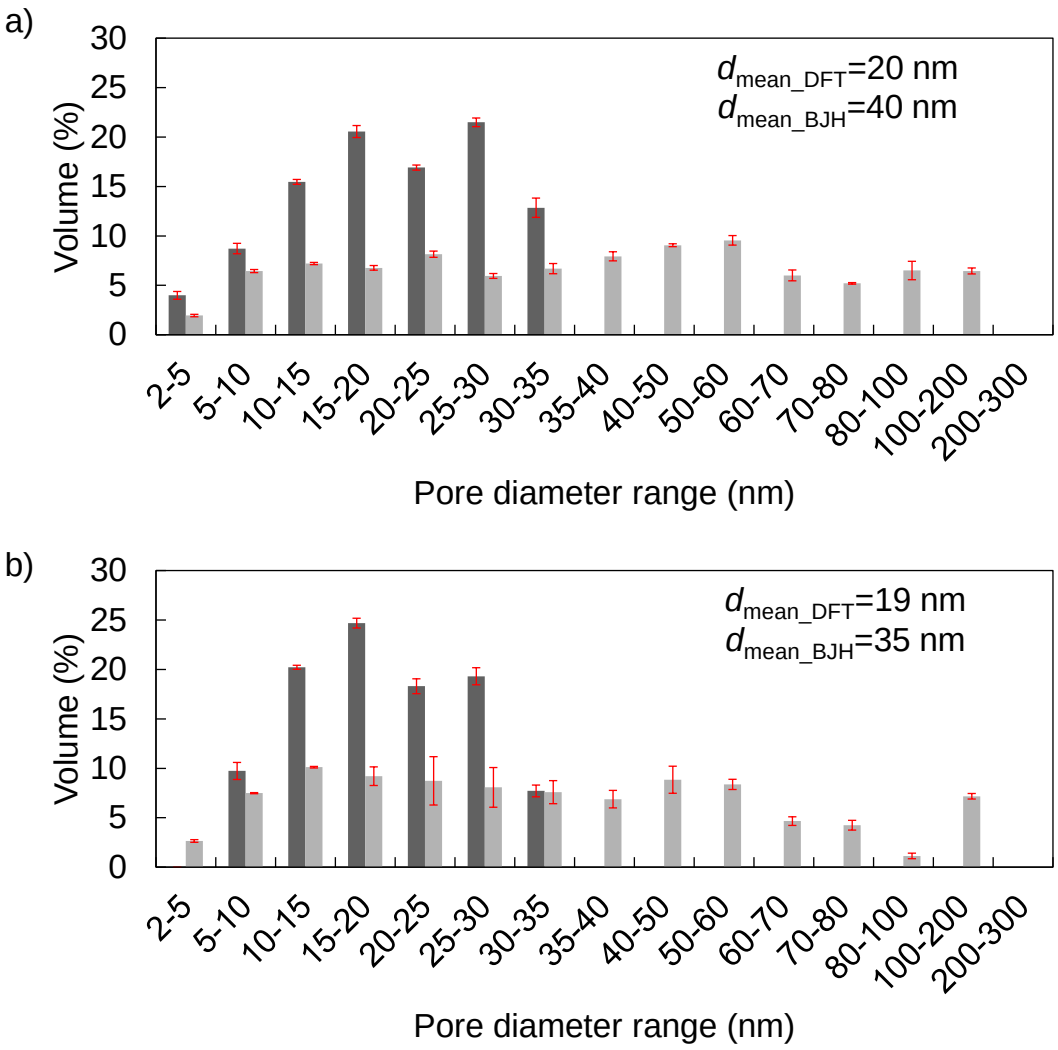

Figure 6.12 PSD obtained by N_2 adsorption porosimetry applying DFT and BJH methods of CL designs with: a) I/C=0.7, dm=24 hrs, T_d=50˚C; and b) I/C=0.7, dm=48 hrs, T_d=50˚C. The error bars are calculated standard deviation for 3 repeating measurements of the same sample

The sharp drops (around 50%) of the relative diffusivities for design sets showed in Figure 6.13 going from low dry-milled samples to high dry-milled ones show the negative effect of dry milling on the relative diffusivity of CL due to lowering the porosity and the pore diameters of CLs. Besides, isotherms for highly dry-milled samples (Figure 6.7c and Figure 6.8c) suggest that the gas path is more tortuous in comparison with the low dry-milled ones. It should be mentioned that for the assumption of overlapped spherical agglomerates in the model to be correct, CL porosity cannot be less than 31%. As for the CL design #6 (I/C=1.1, *dm*=48 hrs, T_d=20 ˚C), porosity was lower than the mentioned value (ε=22%), it was out of the model porosity range and could not be modeled.

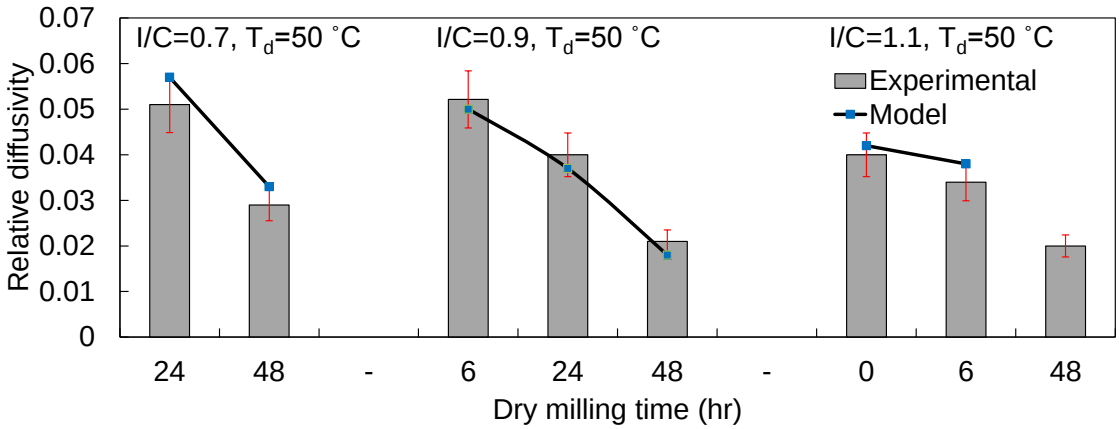

Figure 6.13 The measured and modeled relative diffusivity values comparison for CL design sets with different dry milling times. As the standard deviations of repeated measurements for CL relative diffusivity were less than the calculated uncertainties based on thickness measurements (section 4.1.2), the error bars are calculated based on thickness measurements uncertainties.

6.4. Ionomer to carbon ratio

Figure 6.14a shows isotherms for the CL designs with the same dry milling time of 48 hrs, and drying temperature of 50 ˚C, however, different I/Cs. The observed cavitation effect decreased with decreasing I/C. For the sample with I/C=0.7 and 48 hours of dry milling, there was almost no detectable cavitation effect, while a weak drop in P/P_o could be detected for the CL with I/C=0.9, and it became stronger for the CL with I/C=1.1. The volume of adsorbed nitrogen by the samples increased with decreasing I/C for CL samples with I/C of 1.1 to 0.9 and 0.7 that shows the increase in porosity of the CL. The comparison between the porosities of the CL designs with different I/Cs in Figure 6.14a also shows the same trend.

Logically such behavior is a result of ionomer acting as a binder. Ionomer mostly fills the secondary pores in the CL and does not penetrate into the primary pores [20], therefore, increasing the ionomer content of the CL from 0.7 to 1.1 should reduce the portion of secondary pores, and result in narrower pore necks (higher cavitation effect). On the other hand, increasing ionomer content of the CL also leads to the blockage of primary pores accessible by nitrogen. As a result, the shape of PSDs measured based on both BJH (Figure 6.14b) and DFT (Figure 6.14c) did not change. It should be mentioned that in these measurements the volume of pores smaller than 2 nm (pores within carbon particles) was ignored.

The secondary pore filling effect of ionomer was more in CL designs with the higher porosities, e.g., not dry-milled designs. Figure 6.15 shows the BJH PSD for designs #1, and 12 (no dry milling and T_d=50 ˚C). For these set of samples, the ionomer content difference was more than the previously discussed set (I/C= 0.5-1.5 vs 0.7-1.1), and porosities were higher. The large pores were entirely filled with ionomer in design #1 (I/C=1.5) and the PSD was shifted toward the small pores.

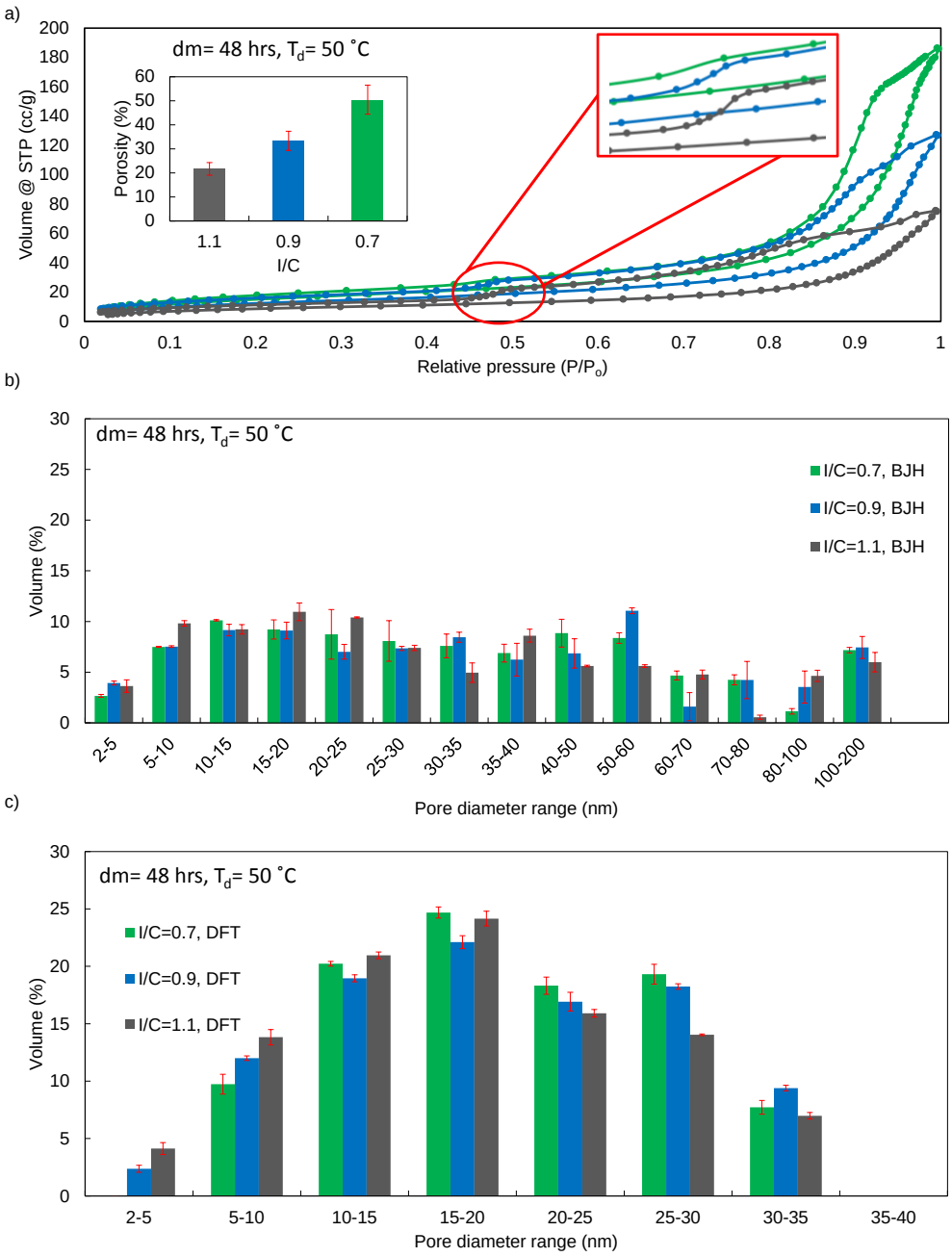

Figure 6.14 **N_2 adsorption porositimetry for the CL designs with the same dry milling time of 48 hrs, drying temperature of 50˚C, and different I/Cs: 0.7, 0.9, and 1.1: a) Isotherms and porosities calculated based on SEM thicknesses; b) PSDs obtained applying BJH method; and c) PSDs obtained applying DFT method. The error bars shows calculated standard deviation for 3 repeating measurements of the same sample**

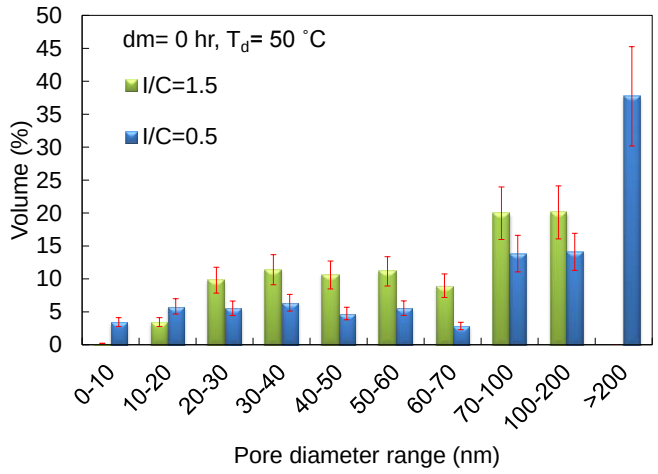

Figure 6.15 BJH PSD for designs #1 (I/C=1.5) and 12 (I/C=0.5). The error bars shows calculated standard deviation for 3 repeating measurements of the same sample

The comparison of measured and modeled relative diffusivity values for design sets with different I/Cs (Figure 6.16) was in-line with the calculated porosities and measured PSDs. The effect of ionomer content was highest for not dry-milled designs, and adding ionomer led to a sharp relative diffusivity drop. As mentioned, for theses designs, adding ionomer changed both porosity and PSD. However, the effect of ionomer for the highly dry-milled samples was relatively the least. Although porosity dropped by adding the ionomer, the PSD remained almost the same, i.e., only molecular diffusivity changed and Knudsen diffusion coefficients were the same for these designs.

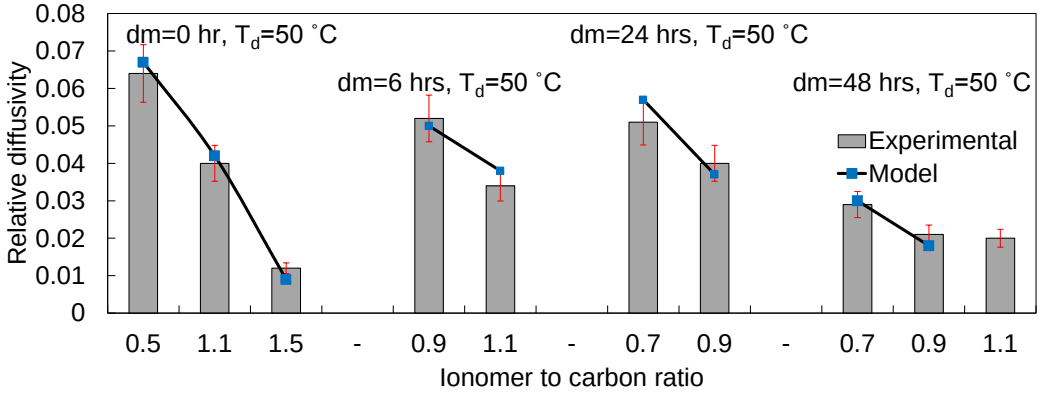

Figure 6.16 The measured and modeled relative diffusivity values comparison for CL design sets with different I/C ratios. As the standard deviations of repeated measurements for the CL relative diffusivity were less than the calculated uncertainties based on thickness measurements (section 4.1.2), the error bars are calculated based on thickness measurements uncertainties.

6.5. Drying temperature

The isotherms and porosities of the CL design #4 and 5 with I/C=1.1, no dry milling, and dried at 50 ˚C and 20 ˚C, are brought in Figure 6.17a and Figure 6.18a respectively. Drying the CL in the lower temperature slows down the drying process and lets the CL ink to settle and become more compact (mostly due to capillary forces). Therefore, the volume of the adsorbed nitrogen and the porosity was lower for the CL dried at 20 ˚C. Besides, there was a small shift in PSD (Figure 6.19a) toward the smaller pores for the CL design dried at 20 ˚C. However, the changes were not much to affect the relative diffusivity values (Figure 6.20). As the pore structured was disordered for the CL design dried at 20 ˚C, the deviation of model prediction from the measured value for relative diffusivity was high.

Figure 6.17b and Figure 6.18b show the obtained isotherms and porosities for the CL design #2 and 6 with I/C=1.1, 48 hrs of dry milling, and dried at 50 ˚C and 20 ˚C, respectively. Here as the porosities of the designs were low, changes were negligible for the porosity. However, more intense cavitation effects happened for the CL design dried at 20 ˚C. Also, the shape of the isotherms suggests that drying the CL in low temperature, resulted in a more disordered structure, probably because of different drying speeds at different depths of the CL. Comparison between the PSDs of the CLs (Figure 6.19b) also showed that lower drying temperature shifts the pore sizes toward the smaller diameters. Moreover, lower relative diffusivity was measured for the design dried at 20 ˚C (Figure 6.20).

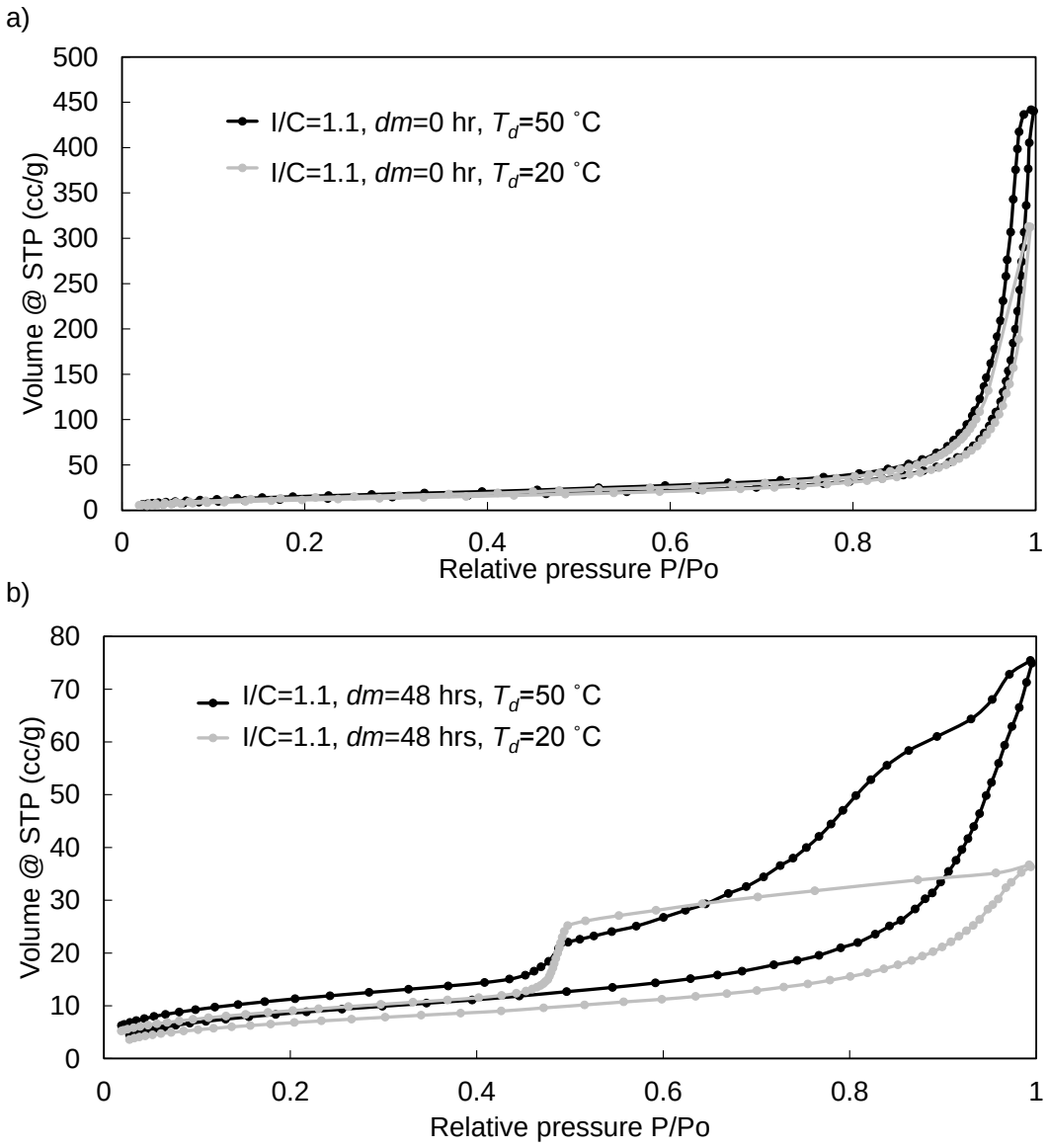

Figure 6.17 Isotherms obtained by N_2 adsorption porositimetry for the CL designs with the same I/C=1.1, and: a) dm= 0 hr, T_d= 50˚C and 20˚C; and b) dm= 48 hrs, T_d= 50˚C and 20˚C.

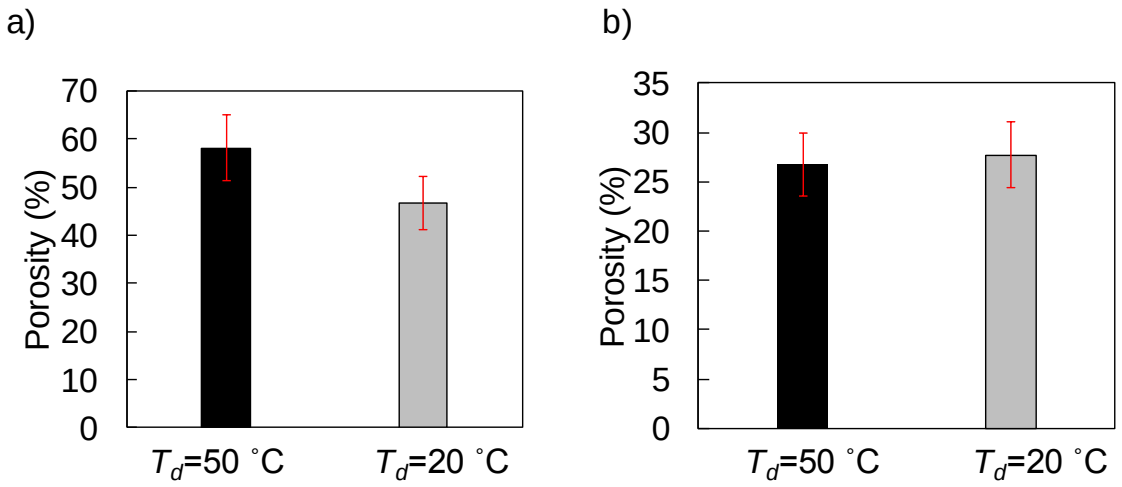

Figure 6.18 **Calculated porosities based on SEM thickness measurement for CL designs with the same I/C=1.1, and: a) dm= 0 hr, T_d= 50˚C and 20 ˚C; and b) dm= 48 hrs, T_d= 50˚C and 20 ˚C. The error bars shows calculated standard deviation for 3 repeating measurements of the same sample**

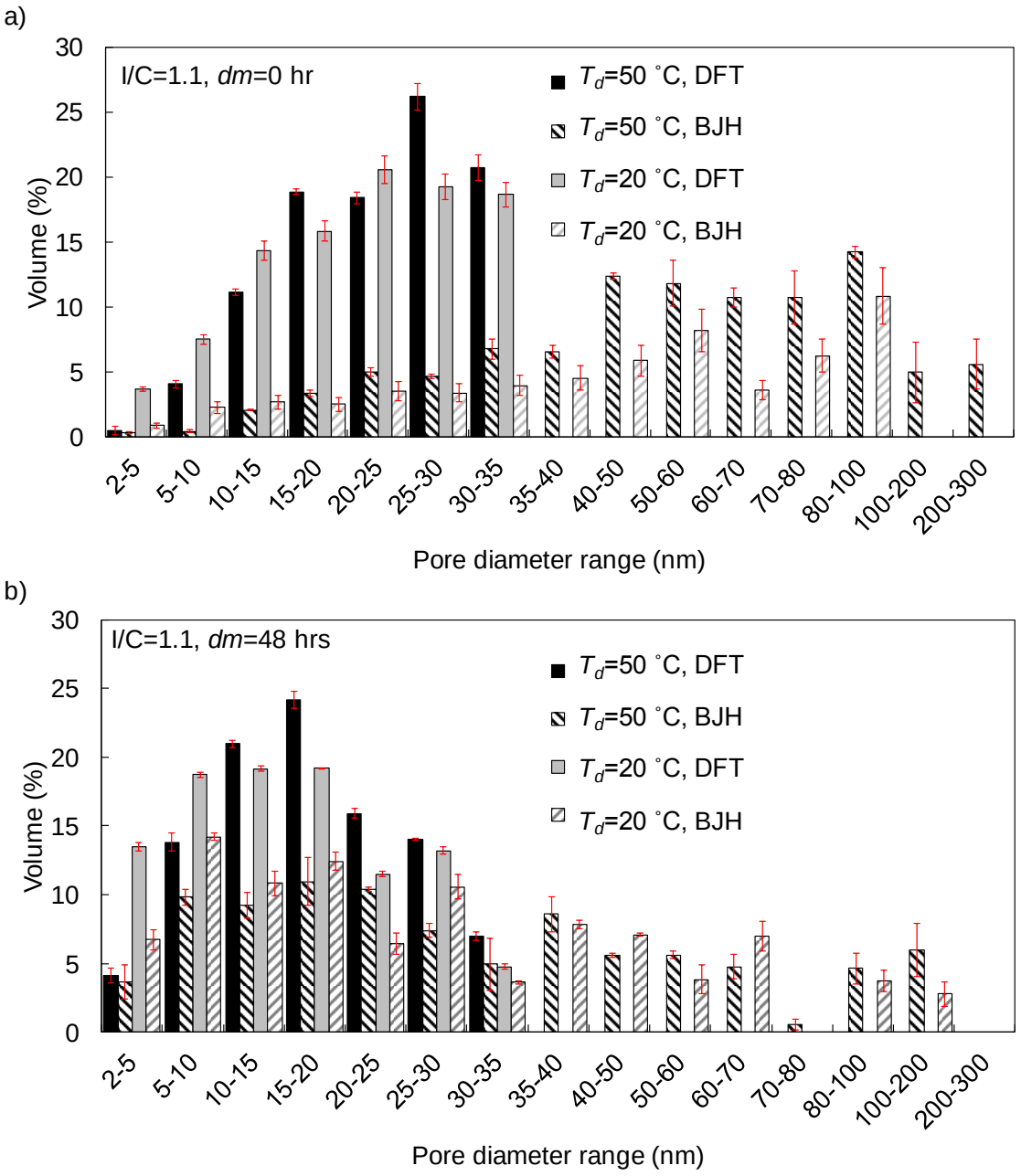

Figure 6.19 **PSDs obtained by N_2 adsorption porositimetry applying both BJH and DFT methods for CL designs with the same I/C=1.1 and: a) dm= 0 hr, T_d= 50˚C and 20 ˚C; and b) dm= 48 hrs, T_d= 50˚C and 20 ˚C. The error bars shows calculated standard deviation for 3 repeating measurements of the same sample**

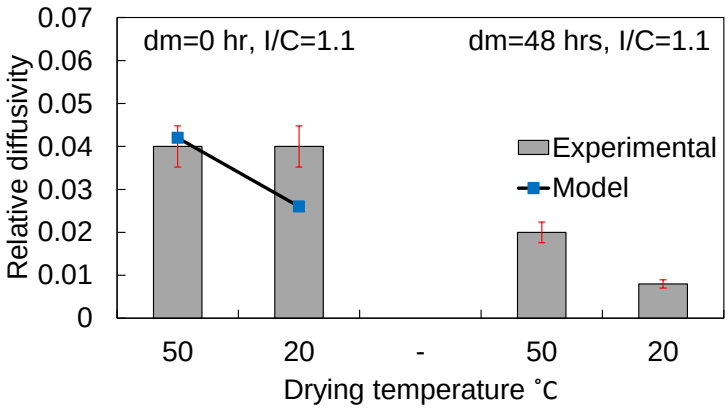

Figure 6.20 **The measured and modeled relative diffusivity values comparison for the CL design sets with different drying temperatures. As the standard deviations of repeated measurements for the CL relative diffusivity were less than the calculated uncertainties based on thickness measurements (section 4.1.2), the error bars are calculated based on the thickness measurements uncertainties.**

Chapter 7.

Effect of operating conditions on the CL pore structure, porosity, and relative diffusivity

7.1. Operating temperature

Figure 7.1 shows the measured and modeled relative diffusivity values for the CL design #4 (I/C=1.1, *Dm*=0 hr, and T_d=50 ˚C) at operating temperatures ranging from 293 to 342 K. The modeled relative diffusivity values matched the experimental values and the difference was less than 10%.

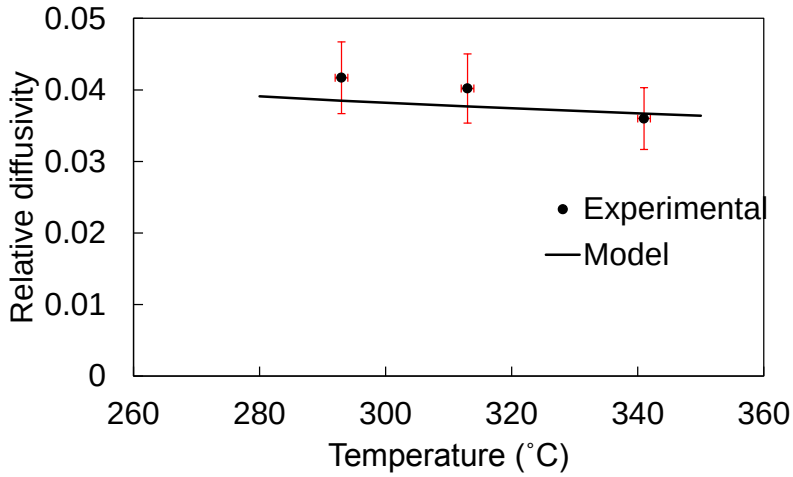

Figure 7.1 The relative diffusivity of CL design #4 (I/C=1.1, no dry milling, and T_d=50 ˚C)

The relative diffusivity of CL slightly decreased in higher operating temperatures. To explain such behavior, the different dependencies of binary and Knudsen diffusivities to temperature should be considered. Binary diffusion is proportional to the absolute temperature to the power of 1.72 [21] (Eq. 121), while, the Kn diffusivity is a function of absolute temperature to the power of 0.5 (Eq. 93). Therefore, when Knudsen diffusion is in effect, the relative diffusivity should change with temperature:

$$D_{\text{binary}} = 1.13 \times 10^{-9} T^{1.724}/p$$

Eq. 121

$$D^* = \frac{D_{eff}}{D_{\text{binary}}} = \frac{\left(\frac{1}{D_{Kn}} + \frac{1}{D_{\text{molecular}}}\right)^{-1}}{D_{\text{binary}}} = \frac{\frac{D_{\text{molecular}}}{D_{\text{binary}}}}{\left(1 + \frac{D_{\text{molecular}}}{D_{Kn}}\right)}$$

Eq. 122

$$D_{\text{molecular}} \gg D_{Kn} \xrightarrow{yields} D^* \propto T^{-1.22}$$

Eq. 123

Considering Eq. 122, increasing the temperature from 273 K to 340 K should decrease the relative diffusivity ~15% for the case where $D_{\text{molecular}} \cong 15 D_{Kn}$ (which was the case here based on the modeling results for the CL design #4) if all pores experience Knudsen diffusion.

The experiment results showed a decreasing trend for the relative diffusivity versus temperature almost the same as the model prediction. It should be mentioned that, although the relative diffusivity was decreasing with respect to temperature, the effective diffusivity of the CL was increasing, but at a lower rate in comparison with the binary diffusion.

7.2. Operating compressive load

CL in PEMFC operation will not experience compressive loads more than 2-5 MPa. However, detecting changes under such low compression, for thicknesses in the range of CL stack thickness (<200 μm) is very hard and demanding. To this end, much higher compressive loads were applied on the CL stacks. As explained in section 4.4.3, first the plots for CL thickness and porosity versus compressive load were obtained. The results for CL design #4 (I/C= 1.1, *Dm*=0 hr, and T_d=50 ˚C) are brought in Figure 7.2.

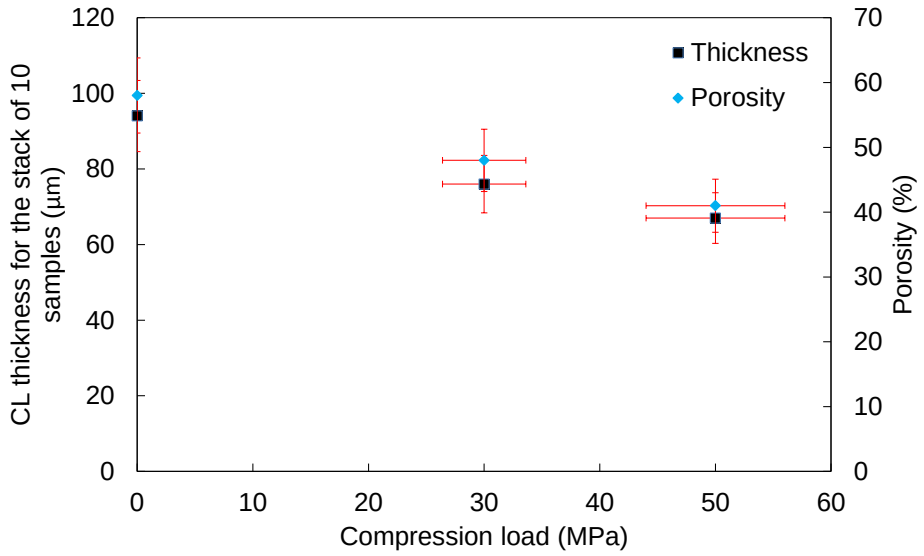

Figure 7.2 Thickness and porosity measurements for stack of ten CL design #4 (I/C= 1.1, no dry milling, and T_d=50 ˚C) samples versus compressive load ranged from 0 to 50 MPa.

The porosity decreased from 58% at zero compression to 40% at 50 MPa almost linearly. However, the changes in the fuel cell operation range (<5 MPa) were negligible.

Figure 7.3 shows the measured effective lengths for two stacks of ten filter PTFE samples and ten catalyst-coated filter PTFE samples, by MLC under 0, 30, and 50 MPa operating compressive loads. For each compressive load, the tests were repeated at least ten times. Gas diffusion effective lengths of both filter PTFE and catalyst-coated filter PTFE stacks increased under compressive load, as well as, the differences between the effective lengths, which showed that the CL effective length also increased under compression.

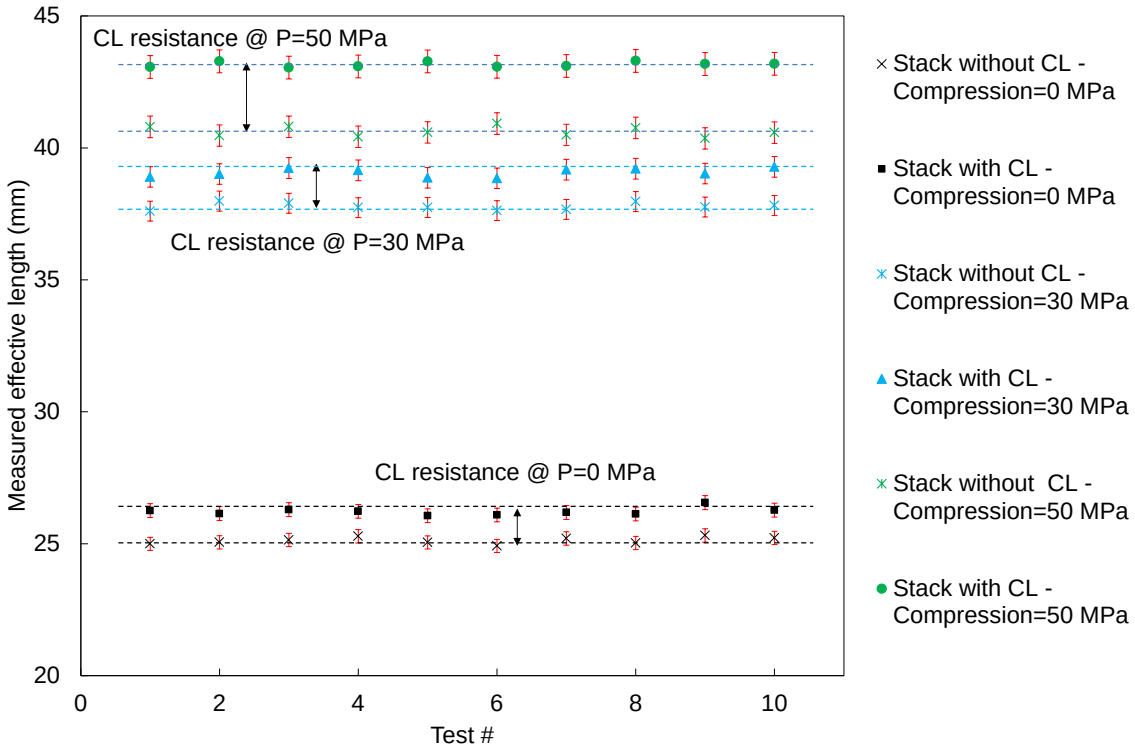

Figure 7.3 The measured effective lengths for two stacks of ten filter PTFE samples and ten catalyst-coated filter PTFE samples (CL design #4), by MLC under 0, 30, and 50 MPa operating compressive loads. For each compressive load, the tests were repeated at least ten times.

Figure 7.4 shows the relative diffusivity values of the CL versus porosity (part a) and compressive load (part b). While, the results show that the 50 MPa compression load affected the CL relative diffusivity drastically (more than 70% drop), in the working range of fuel cell (<5 MPa), the changes in relative diffusivity were negligible.

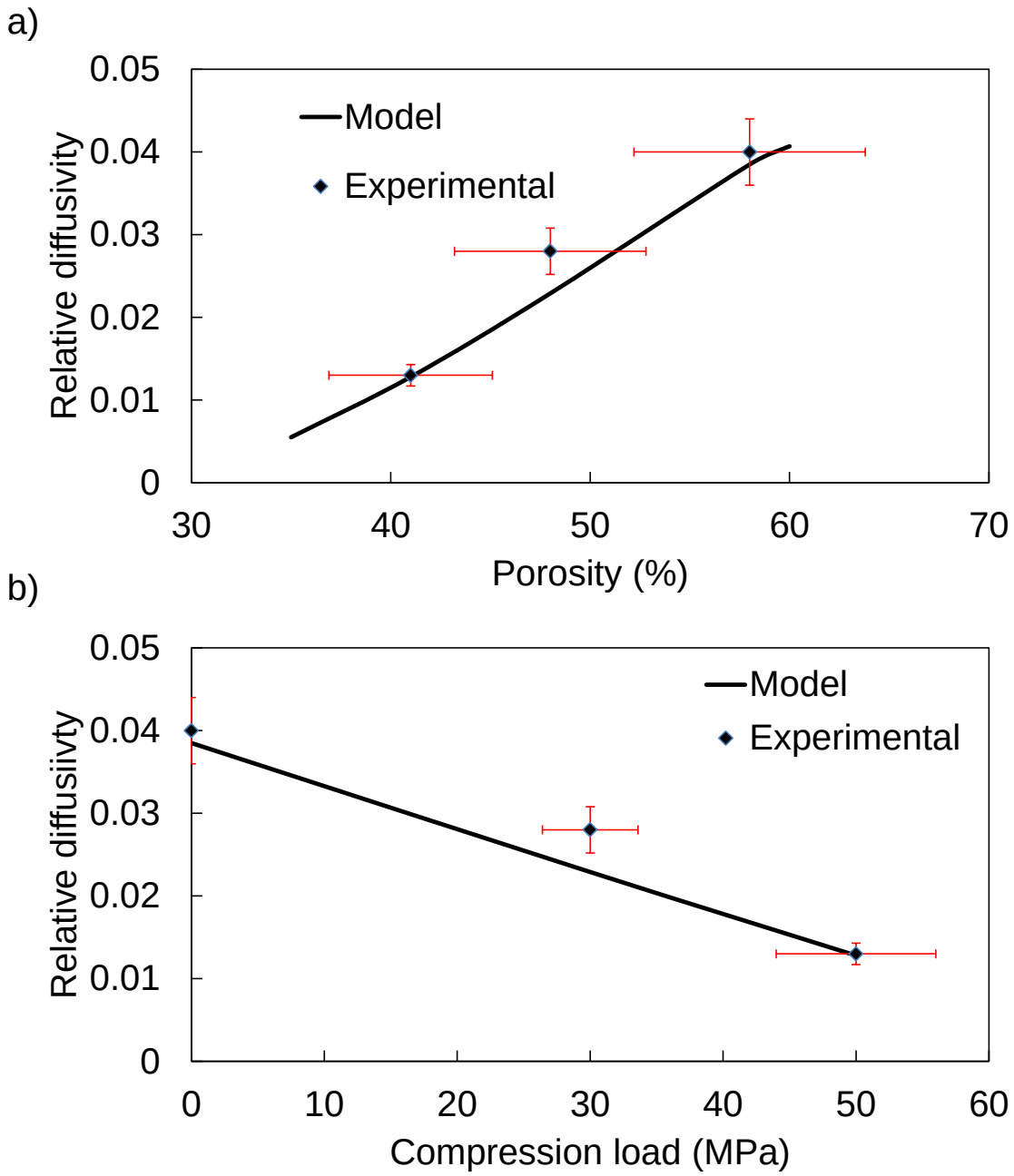

Figure 7.4 **a) The relative diffusivity versus porosity for the CL design #4 (l/C= 1.1, no dry milling, and T_d=50 ˚C). The change in porosity was due to compressive load. b) The relative diffusivity of the CL design #4 (l/C= 1.1, no dry milling, and T_d=50 ˚C) versus compressive load.**

7.3. Operating humidity and water content

7.3.1. Operating humidity

The RH values more than zero cause ionomer inside the CL to swell. Many researchers have studied the ionomer swell under humid condition (detailed review can be found in Ref. [128]). Most of these studies focused on membranes. However, the ionomer inside CL acts somehow different from the membrane. Therefore, they are categorized as ionomer thin film. The relationship between Nafion membrane swell and ionomer thin film (also Nafion) swell can be extracted from Ref. [137]. Kusoglu et al. showed that for the Nafion ionomer thin film swelling is less than for the Nafion membrane under the same humidity [137]. Here, the ionomer used in the CL was Aquivion 850. Unfortunately, the number of studies on Aquivion ionomer is far less than the ones on Nafion ionomer in the literature. Zhao and Benziger [131] studied the water content and swell of Aquivion 850 and Nafion 1100 membranes under the humid condition and soaked them in liquid water. The water content values of both membranes were almost the same, and the difference in swell was originated from the different EW numbers for each membrane. Assuming that the difference in swelling between Aquivion ionomer thin film and Aquivion membrane is the same as Nafion ionomer thin film and Nafion membrane, the response of swelling of Aquivion ionomer thin film to humidity and liquid water was calculated based on the Aquivion membrane response (There is no available data on the swelling behavior of Aquvion thin film under humid condition to our knowledge). The Aquivion 850 membrane water content versus humidity plot was generated using data presented in Ref. [131] and is presented in Figure 7.5. The same water content ratios between Nafion 1100 membrane and Nafion 1100 ionomer thin film water content calculated from Ref. [137] was used to calculate the ionomer thin film water content versus humidity and liquid water plots (Eq. 124) presented Figure 7.5. Using Eq. 68 the ionomer thin film swell was calculated (Figure 7.5).

$$\lambda_{\text{Aquivion thin film}} = \lambda_{\text{Aquivion membrane}} \times \frac{\lambda_{\text{Nafion thin film}}}{\lambda_{\text{Nafion membrane}}}$$

Eq. 124

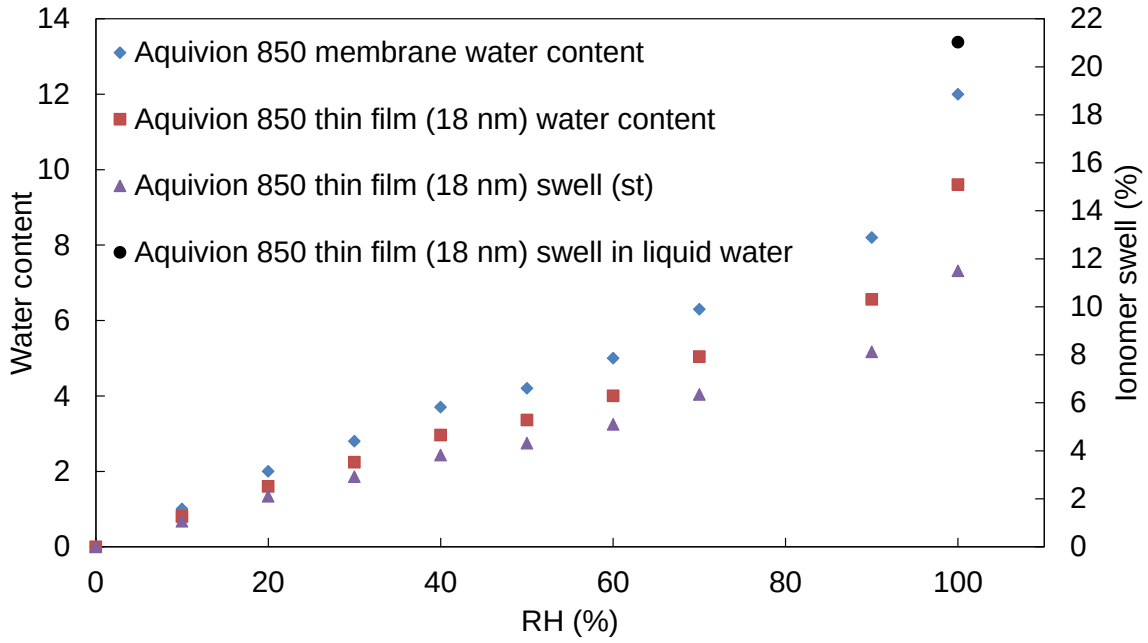

Figure 7.5 Aquivion membrane water content form Ref. [131]**, ionomer thin film water content, and swell versus RH**

The water content of Aquivion ionomer thin film was implemented in the model to calculate the effect of humidity on the CL PSD and relative diffusivity. Figure 7.6 shows how the CL (design #4) PSD changes due to ionomer swelling.

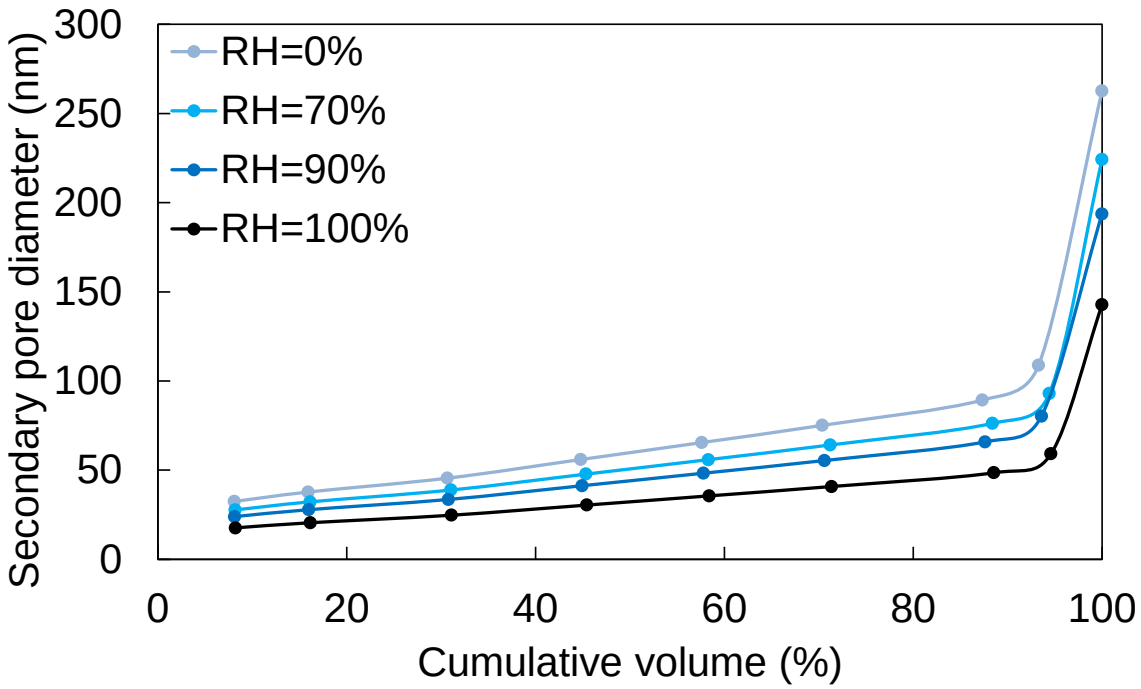

Figure 7.6 Calculated secondary PSD of the CL design #4 (I/C= 1.1, no dry milling, and T_d=50 ˚C) under different RHs

The results show that the CL PSD barely changed for RHs <70%. For RH=90%, the largest secondary pore diameter reduced about 25% (having the thickest ionomer film around the associated agglomerates), and the change in the rest of the secondary pore diameters was not significant (which are about 95% of the pore volume). Because of the mentioned fact, changing the operating RH from 0 to 90% did not change the CL relative diffusivity much (Figure 7.7). The modeling results showed the same trend. Unfortunately, reaching the absolute 100% RH was not possible due to limitations of the test bed humidifier.

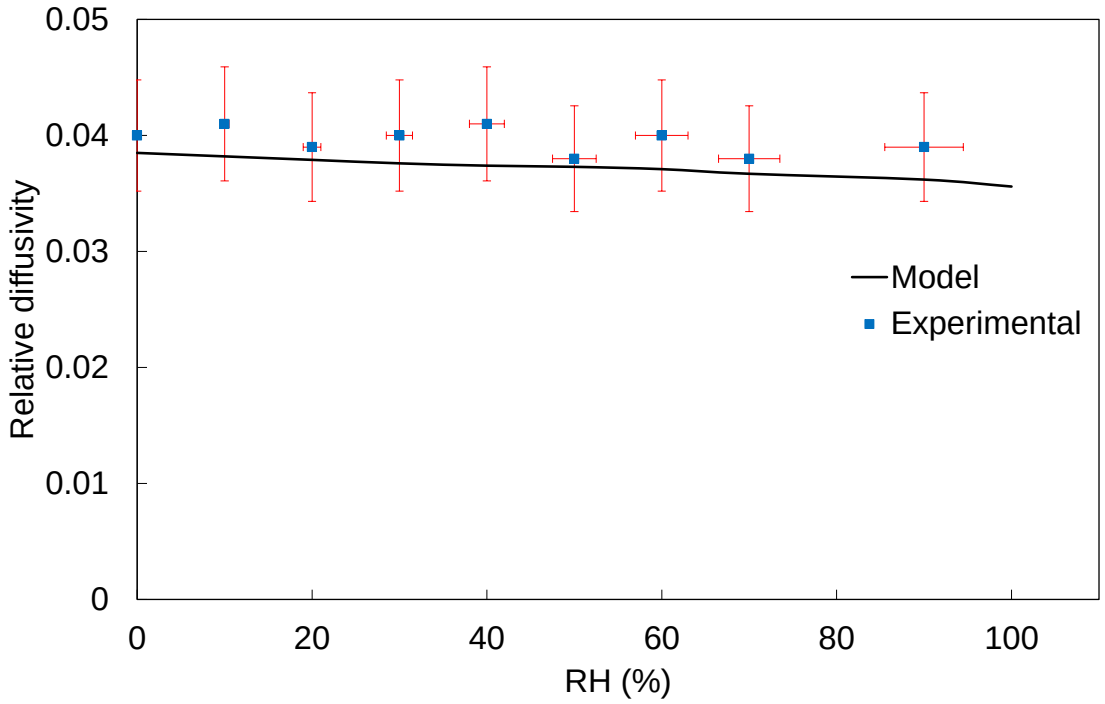

Figure 7.7 The measured and modeled relative diffusivities for the CL design #4 (I/C= 1.1, no dry milling, and T_d=50 ˚C) under different operating RHs

7.3.2. Water content

Figure 7.8 shows the measured and modeled relative diffusivity values of the CL design #4 (I/C= 1.1, no dry milling, and T_d=50 ˚C) containing different amount of liquid water. Due to the hydrophobic nature of the CL and the filter PTFE substrate, no more than 25% water could be introduced to the CL. As results suggest, the changes in the relative diffusivity of the CL was detectable here unlike working under humid condition because, here CL exposed to the liquid water, and the ionomer swell due to contact with liquid water is higher than the swell under humid conditions. Moreover, water fills part of the pores inside the CL and blocks part of the gas path. As a result, 25% water gain reduced the relative diffusivity of the CL by about 20%.

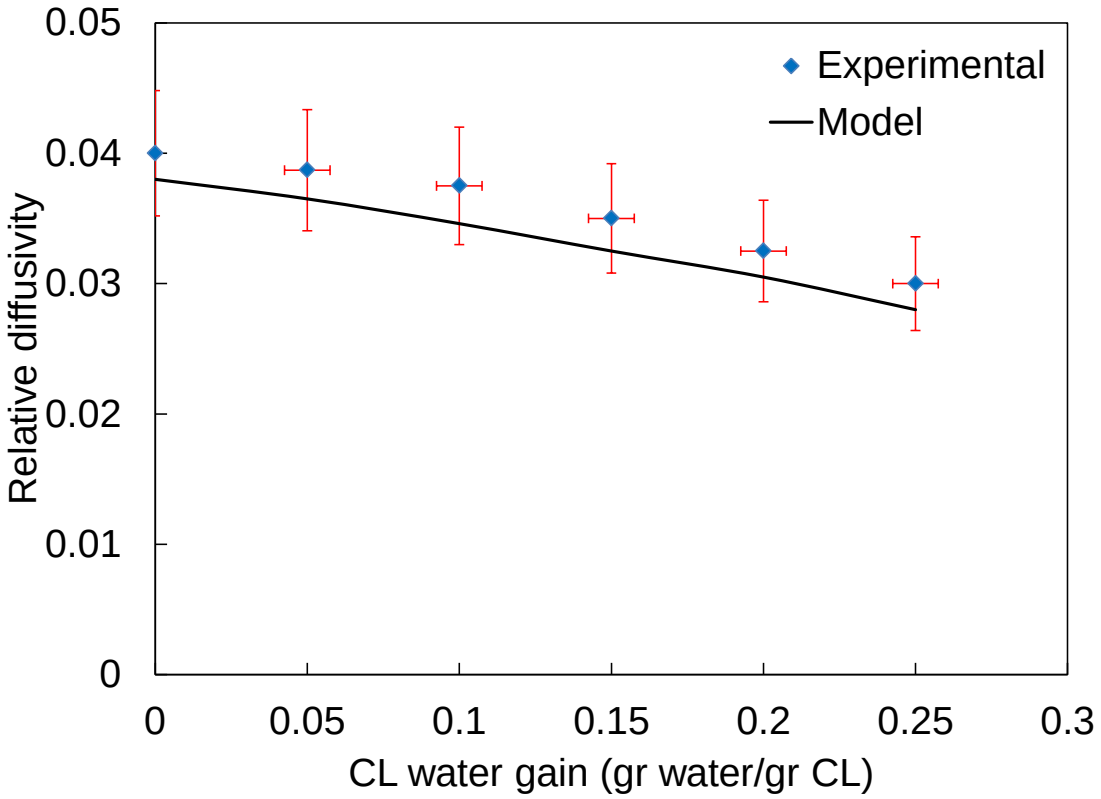

Figure 7.8 **Measured and modeled relative diffusivity values of the CL design #4 (I/C= 1.1, no dry milling, and T_d=50 ˚C) containing different amount of liquid water**

Chapter 8. Conclusion and future work

8.1. Thesis Conclusion

8.1.1. Challenges

Sample preparation. For gas diffusion measurements, there were specific demands with respect to the porosity, surface type, and thickness of the substrate and very limited options. After thorough investigation, a substrate was selected with sufficient mechanical strength for Mayer bar coating, low gas diffusion resistance (< E-8 s/m) relative to thin CL layers, i.e., the required high porosity and low thickness, and a hydrophobic surface to minimize the ink penetration. It was challenging to handle ultrathin (<50 µm) porous substrates without damaging them. The research required labour intensive production of a large number of uniform CL samples with a range of different compositions and processing procedures. Given the expensive substrates and catalyst powder, the sample production had to be extremely efficient. The AFCC coating facilities and training provided by AFCC technical staff was essential to this work.

Sample structural characterization. The measurement procedures for determining the thickness, porosity, and PSD of CL samples were systematically optimized and their accuracy evaluated. Accurate CL thickness measurements were needed for the analysis of gas diffusion. Initial thickness measurements required a half-day working with an SEM microscope. A faster technique (20 samples/day) was developed and verified with SEM measurements in which sample thickness was extrapolated from compression curves acquired with the custom-built instrument (TUC-RUC) described in Chapter 3. Porosity and PSD measurements were lengthy procedures, requiring two to three days for each sample run.

Gas diffusion measurement. At the start of this project, there was limited published data on ex-situ CL gas diffusivity measurements and a wide range of reported values in the literature. The ex-situ gas diffusion measurement procedure for CL under different operating conditions, especially under compression and saturated with water, were not established and had to be developed for the first time. Moreover, acquisition of

a sufficiently sensitive and accurate modified Loschmidt cell apparatus for gas diffusion measurements was a time consuming process (three years).

Model. There were number of complex structural models for CL in the literature. While reconstructing the geometry of CL based on images obtained by FIB-SEM or nano X-ray computed tomography or stochastic modeling is extremely helpful to understand the transport mechanisms in CL, the complexity of these techniques limits their use in the performance prediction models. The accuracy of the available simple analytical models, e.g. effective medium theory or percolation theory based models, for performance prediction was under question for CL. Moreover, the CL structure and gas diffusivity model should have inputs that are easy to measure or calculate. For example, use of agglomerate sizes as an input in the model creates a challenge, as measuring the agglomerate sizes in CL is an extremely challenging task itself.

Method developments and selections In this thesis, an MLC was used to measure relative diffusivity of the CL of PEMFC. The porous support substrate (Fluoropore FHUP04700, EMD Millipore), the coating method (Mayer bar), and a sample preparation method were chosen/devised proper for the through-plane gas diffusion measurements. Different thickness, porosity, and PSD measurement methods for the CL were evaluated, and the appropriate ones were chosen (Thickness measurement by TUC-RUC, porosity based on theoretical relationships between thickness and porosity, and PSD measurement by N_2 adsorption). The structure of the CL was modeled through considering a packed-sphere model for carbon particles within agglomerates, and a network of overlapped spherical agglomerates forming the CL. The gas diffusion problem was solved for the developed structure considering both molecular and Knudsen mechanisms. Effect of the compressive load, gas humidity and the water content were integrated into the model by considering the structural changes that the CL undergo in these conditions. The developed model used the catalyst composition, material properties, porosity, and PSD to calculate the gas diffusivity.

8.1.2. Conclusion

Twelve different CL designs were prepared, and the thickness, porosity, PSD, and gas diffusion measurements were performed under different conditions to evaluate effects of the composition, production procedure, and operating conditions on the CL

diffusivity. The model was validated with the measurement results, and following conclusions were reached:

- Increasing ionomer content of the CL caused a drop in porosity, a shift toward smaller pore diameters, and a drop in relative diffusivity of the CL.
- Dry milling the catalyst powders led to drops in the porosity, shifts of pore diameters toward smaller ones, introducing narrower necks for pores, and drops in the relative diffusivities of CLs.
- Drying CLs at elevated temperature after coating led to larger pore diameters and higher relative diffusivities.
- The CL effective diffusivity was higher at higher operating temperature; however, as the increase rate of effective diffusivity was less than the one for binary diffusion, the CL relative diffusivity decreased in higher operating temperatures.
- The CL porosity decreased under compressive load, and, as a result, the relative diffusivity dropped as well. However, in the compression ranges for the fuel cell operation (<5 MPa), the changes were negligible.
- The gas humidity caused the CL ionomer to swell. However, as the swell amount was not significant, changes in the relative diffusivity of the CL were almost negligible.
- Unlike the gas humidity, the liquid water effect on the ionomer swell was detectable. The ionomer swell due to liquid water and the pore-filling effect of liquid water led to a detectable drop in relative diffusivity of the CL.

In short, the CL processing and composition parameters had a considerable effect on its gas diffusivity, while operating conditions showed less importance, except for the water content of CL. Between the different parameters studied here, design processing ones were less studied in the literature, while they could affect the CL gas diffusivity the most, and, as a result, they could play a major role on optimizing CL performance. Also, this work showed for CL, compressing the membrane assembly more than the regular values (<2 MPa) but less than 10 MPa would not change the gas diffusivity of CL significantly, which could be of interest as higher compressive loads could improve other transport properties.

8.2. Future work

The following are additional research that can be done to further study the gas diffusivity in the CL:

- Measuring gas diffusivity of CL for different gas pairs e.g. H_2 and O_2 can shed more light on the Knudsen diffusion effect in CL, by de-convoluting Knudsen and molecular gas diffusivities.
- While the structural model was validated for gas diffusion, the effectiveness of the model could go beyond gas diffusion. It could be used for thermal, electrical, and ionic conductivity. However, especially for ionic conductivity, some aspect of the structural model should be validated including:
    - Agglomerate size distribution, e.g., by comparison with a reconstructed geometry based on FIB-SEM for the CL samples prepared in the same way as in this study.
    - Ionomer thickness distribution, e.g., by comparison with a reconstructed geometry based on FIB-SEM for the CL samples prepared in the same way as in this study.
    - Ionomer coverage, e.g., through experimentally determination by double layer capacitance.
- The composition and production parameters are not limited to those evaluated here. Samples of different CL designs could be produced, and the effects of more parameters could be assessed on the gas diffusivity of the CL, including:
    - Carbon support type
    - C/Pt ratio
    - Catalyst ink viscosity
    - Catalyst ink solvent parameters
    - Catalyst ink mixing time
- Adding the gas diffusion through water and ionomer to the model, the gas diffusivity value that delivers oxygen molecules to the reaction sites could be calculated. The result should be validated with the in-situ gas diffusivity measurements by limiting current method. Then, the model could be integrated into the performance prediction models of the fuel cell.

References

[1] Salari S, McCague C, Tam M, Saha MS, Stumper J, Bahrami M. Accurate ex-situ measurements of PEM fuel cells catalyst layer dry diffusivity. ECS Trans., vol. 69, 2015. doi:10.1149/06917.0419ecst.

[2] LaManna JM, Kandlikar SG. Determination of effective water vapor diffusion coefficient in pemfc gas diffusion layers. Int J Hydrogen Energy 2011;36:5021–9. doi:10.1016/j.ijhydene.2011.01.036.

[3] Carter D, Ryan M, Winf J. The Fuel Cell Industry Review 2012. Royston: 2012.

[4] Kandlikar SG, See EJ, Koz M, Gopalan P, Banerjee R. Two-phase flow in GDL and reactant channels of a proton exchange membrane fuel cell. Int J Hydrogen Energy 2014;39:6620–36. doi:http://dx.doi.org/10.1016/j.ijhydene.2014.02.045.

[5] Shen J, Zhou J, Astrath NGC, Navessin T, Liu Z-S (Simon), Lei C, et al. Measurement of effective gas diffusion coefficients of catalyst layers of PEM fuel cells with a Loschmidt diffusion cell. J Power Sources 2011;196:674–8. doi:http://dx.doi.org/10.1016/j.jpowsour.2010.07.086.

[6] Holdcroft S. Fuel cell catalyst layers: A polymer science perspective. Chem Mater 2014;26:381–93. doi:10.1021/cm401445h.

[7] Sadeghifar H, Djilali N, Bahrami M. Thermal conductivity of a graphite bipolar plate (BPP) and its thermal contact resistance with fuel cell gas diffusion layers: Effect of compression, PTFE, micro porous layer (MPL), BPP out-of-flatness and cyclic load. J Power Sources 2015;273:96–104. doi:http://dx.doi.org/10.1016/j.jpowsour.2014.09.062.

[8] Sadeghifar H, Djilali N, Bahrami M. Effect of Polytetrafluoroethylene (PTFE) and micro porous layer (MPL) on thermal conductivity of fuel cell gas diffusion layers: Modeling and experiments. J Power Sources 2014;248:632–41. doi:10.1016/j.jpowsour.2013.09.136.

[9] Mulone V, Karan K. Analysis of capillary flow driven model for water transport in PEFC cathode catalyst layer: Consideration of mixed wettability and pore size distribution. Int J Hydrogen Energy 2013;38:558–69. doi:10.1016/j.ijhydene.2012.07.107.

[10] Das PK, Li X, Liu ZS. Effective transport coefficients in PEM fuel cell catalyst and gas diffusion layers: Beyond Bruggeman approximation. Appl Energy

2010;87:2785–96. doi:10.1016/j.apenergy.2009.05.006.

[11] Glavatskiy K, Pharoah JG, Kjelstrup S. Thermal phenomena associated with water transport across a fuel cell membrane: Soret and Dufour effects. J Memb Sci 2013;431:96–104. doi:10.1016/j.memsci.2012.12.023.

[12] Norouzifard V, Bahrami M. Deformation of PEM fuel cell gas diffusion layers under compressive loading: An analytical approach. J Power Sources 2014;264:92–9. doi:10.1016/j.jpowsour.2014.04.057.

[13] Ohma A, Mashio T, Sato K, Iden H, Ono Y, Sakai K, et al. Analysis of proton exchange membrane fuel cell catalyst layers for reduction of platinum loading at Nissan. Electrochim Acta 2011;56:10832–41. doi:10.1016/j.electacta.2011.04.058.

[14] Zhang J, Lima FHB, Shao MH, Sasaki K, Wang JX, Hanson J, et al. Platinum monolayer on non-noble metal - noble metal core-shell nanoparticles electrocatalysts for O 2 reduction. J Phys Chem B 2005;109:11973. doi:10.1021/jp055634c.

[15] Sobolyeva T. On the microstructure of PEM fuel cell. Simon Fraser University, 2010.

[16] Kinoshita K. Carbon: electrochemical and physicochemical properties. 1988.

[17] Kinoshita K, Bett JAS. Potentiodynamic analysis of surface oxides on carbon blacks. Carbon N Y 1973;11:403–11. doi:http://dx.doi.org/10.1016/0008-6223(73)90080-8.

[18] Uchida M, Aoyama Y, Eda N, Ohta A. Investigation of the microstructure in the catalyst layer and effects of both perfluorosulfonate ionomer and PTFE-Loaded carbon on the catalyst layer of polymer electrolyte fuel cells. J Electrochem Soc 1995;142:4143–9. doi:10.1149/1.2048477.

[19] Uchida M. Effects of Microstructure of Carbon Support in the Catalyst Layer on the Performance of Polymer-Electrolyte Fuel Cells. J Electrochem Soc 1996;143:2245. doi:10.1149/1.1836988.

[20] Soboleva T, Zhao X, Malek K, Xie Z, Navessin T, Holdcroft S. On the micro-, meso-, and macroporous structures of polymer electrolyte membrane fuel cell catalyst layers. ACS Appl Mater Interfaces 2010;2:375–84. doi:10.1021/am900600y.

[21] Marrero TR, Mason EA. Gaseous diffusion coefficients. J Phys Chem Ref Data 1972;1:3.

[22] Okolo GN, Everson RC, Neomagus HWJP, Roberts MJ, Sakurovs R. Comparing the porosity and surface areas of coal as measured by gas adsorption, mercury intrusion and SAXS techniques. Fuel 2015;141:293–304. doi:10.1016/j.fuel.2014.10.046.

[23] Andisheh-Tadbir M, El Hannach M, Kjeang E, Bahrami M. An analytical relationship for calculating the effective diffusivity of micro-porous layers. Int J Hydrogen Energy 2015;40:10242–50. doi:10.1016/j.ijhydene.2015.06.067.

[24] Bruggeman DAG. Berechnung verschiedener physikalischer Konstanten von heterogenen Substanzen. I. Dielektrizitätskonstanten und Leitfähigkeiten der Mischkörper aus isotropen Substanzen. Ann Phys 1935;416:665–79.

[25] Wippermann K, Klafki K, Kulikovsky AA. In situ measurement of the oxygen diffusion coefficient in the cathode catalyst layer of a direct methanol fuel cell. Electrochim Acta 2014;141:212–5. doi:10.1016/j.electacta.2014.06.164.

[26] Kulikovsky AA. A simple equation for in situ measurement of the catalyst layer oxygen diffusivity in PEM fuel cell. J Electroanal Chem 2014;720–721:47–51. doi:10.1016/j.jelechem.2014.03.005.

[27] Sambandam S, Parrondo J, Ramani V. Estimation of electrode ionomer oxygen permeability and ionomer-phase oxygen transport resistance in polymer electrolyte fuel cells. Phys Chem Chem Phys 2013;15:14994–5002. doi:10.1039/c3cp51450a.

[28] Liu H, Epting WK, Litster S. Gas transport resistance in polymer electrolyte thin films on oxygen reduction reaction catalysts. Langmuir 2015;31:9853–8. doi:10.1021/acs.langmuir.5b02487.

[29] Hwang GS, Weber AZ. Effective-diffusivity measurement of partially-saturated fuel-cell gas-diffusion layers. J Electrochem Soc 2012;159:F683–92. doi:10.1149/2.024211jes.

[30] Baker DR, Caulk D a., Neyerlin KC, Murphy MW. Measurement of oxygen transport resistance in PEM fuel cells by limiting current methods. J Electrochem Soc 2009;156:B991–1003. doi:10.1149/1.3152226.

[31] He W, Zou J, Wang B, Vilayurganapathy S, Zhou M, Lin X, et al. Gas transport in porous electrodes of solid oxide fuel cells: A review on diffusion and diffusivity measurement. J Power Sources 2013;237:64–73. doi:http://dx.doi.org/10.1016/j.jpowsour.2013.02.089.

[32] Novitski D, Holdcroft S. Determination of O2 mass transport at the Pt | PFSA

ionomer interface under reduced relative humidity. ACS Appl Mater Interfaces 2015;7:27314–23. doi:10.1021/acsami.5b08720.

[33] Utaka Y, Tasaki Y, Wang S, Ishiji T, Uchikoshi S. Method of measuring oxygen diffusivity in microporous media. Int J Heat Mass Transf 2009;52:3685–92. doi:10.1016/j.ijheatmasstransfer.2009.02.032.

[34] Flückiger R, Freunberger SA, Kramer D, Wokaun A, Scherer GG, Büchi FN. Anisotropic, effective diffusivity of porous gas diffusion layer materials for PEFC. Electrochim Acta 2008;54:551–9. doi:10.1016/j.electacta.2008.07.034.

[35] Rashapov R, Imami F, Gostick JT. A method for measuring in-plane effective diffusivity in thin porous media. Int J Heat Mass Transf 2015;85:367–74. doi:10.1016/j.ijheatmasstransfer.2015.01.101.

[36] Quick C, Ritzinger D, Lehnert W, Hartnig C. Characterization of water transport in gas diffusion media. J Power Sources 2009;190:110–20. doi:10.1016/j.jpowsour.2008.07.093.

[37] Wicke E, Kallenbach R. Die oberächen diffusion von kohlendioxyd in aktiven kohlen. Kolloid Zeitschrift 1941;97:135–51.

[38] Zhang F, Hayes RE, Kolaczkowski ST. A new technique to measure the effective diffusivity in a catalytic monolith washcoat. Chem Eng Res Des 2004;82:481–9. doi:10.1205/026387604323050191.

[39] Stary T, Solcova O, Schneider P, Marek M. Effective diffusivities and pore-transport characteristics of washcoated ceramic monolith for automotive catalytic converter. Chem Eng Sci 2006;61:5934–43. doi:10.1016/j.ces.2006.05.014.

[40] Inoue G, Yokoyama K, Ooyama J, Terao T, Tokunaga T, Kubo N, et al. Theoretical examination of effective oxygen diffusion coefficient and electrical conductivity of polymer electrolyte fuel cell porous components. J Power Sources 2016;327:610–21. doi:10.1016/j.jpowsour.2016.07.107.

[41] Pant LM, Mitra SK, Secanell M. Absolute permeability and Knudsen diffusivity measurements in PEMFC gas diffusion layers and micro porous layers. J Power Sources 2012;206:153–60. doi:10.1016/j.jpowsour.2012.01.099.

[42] Yu Z, Carter RN. Measurement of effective oxygen diffusivity in electrodes for proton exchange membrane fuel cells. J Power Sources 2010;195:1079–84. doi:10.1016/j.jpowsour.2009.08.065.

[43] Soukup K, Schneider P, Šolcová O. Wicke-Kallenbach and Graham's diffusion cells: Limits of application for low surface area porous solids. Chem Eng Sci

2008;63:4490–3. doi:10.1016/j.ces.2008.06.020.

[44] Dong L. Accuracy Improvement for Measurement of Gas Diffusivity through Thin Porous Media. The University of Waterloo, 2012.

[45] Zamel N, Astrath NGC, Li X, Shen J, Zhou J, Astrath FBG, et al. Experimental measurements of effective diffusion coefficient of oxygen-nitrogen mixture in PEM fuel cell diffusion media. Chem Eng Sci 2010;65:931–7. doi:10.1016/j.ces.2009.09.044.

[46] Unsworth G, Dong L, Li X. Improved experimental method for measuring gas diffusivity through thin porous media. AIChE J 2012;59:1409–19.

[47] Siddique NA, Liu F. Process based reconstruction and simulation of a three-dimensional fuel cell catalyst layer. Electrochim Acta 2010;55:5357–66. doi:10.1016/j.electacta.2010.04.059.

[48] Neale GH, Nader WK. Prediction of transport processes within porous media: Diffusive flow processes within an homogeneous swarm of spherical particles. AIChe J 2004;19:112–9. doi:10.1002/aic.690190116.

[49] Eikerling M. Water management in cathode catalyst layers of PEM fuel cells. A structure-based model. J Electrochem Soc 2006;153:E58–70. doi:10.1149/1.2160435.

[50] Liu J, Eikerling M. Model of cathode catalyst layers for polymer electrolyte fuel cells : The role of porous structure and water accumulation 2008;53:4435–46. doi:10.1016/j.electacta.2008.01.033.

[51] Laudone GM, Matthews GP, Gane PAC. Modelling diffusion from simulated porous structures. Chem Eng Sci 2008;63:1987–96. doi:10.1016/j.ces.2007.12.031.

[52] Piri M, Blunt MJ. Three-dimensional mixed-wet random pore-scale network modeling of two- And three-phase flow in porous media. I. Model description. Phys Rev E - Stat Nonlinear, Soft Matter Phys 2005;71:1–30. doi:10.1103/PhysRevE.71.026301.

[53] Prat M. Recent advances in pore-scale models for drying of porous media. Chem Eng J 2002;86:153–64. doi:10.1016/S1385-8947(01)00283-2.

[54] Inoue G, Matsukuma Y, Minemoto M. Evaluation of Gas Diffusion Performance in Wet GDL with 3D Pore Network Model. ECS Trans 2009;25:1519–27. doi:10.1017/CBO9781107415324.004.

[55] El Hannach M, Prat M, Pauchet J. Pore network model of the cathode catalyst

layer of proton exchange membrane fuel cells: Analysis of water management and electrical performance. Int J Hydrogen Energy 2012;37:18996–9006. doi:10.1016/j.ijhydene.2012.09.139.

[56] Zamel N, Li X, Shen J. Correlation for the effective gas diffusion coefficient in carbon paper diffusion media. Energy and Fuels 2009;23:6070–8. doi:10.1021/ef900653x.

[57] Jiang F, Sousa ACM. Smoothed particle hydrodynamics modeling of transverse flow in randomly aligned fibrous porous media. Transp Porous Media 2008;75:17–33. doi:10.1007/s11242-008-9206-z.

[58] Rosen T, Eller J, Kang J, Prasianakis NI, Mantzaras J, Buchi FN. Saturation Dependent Effective Transport Properties of PEFC Gas Diffusion Layers. J Electrochem Soc 2012;159:F536–44. doi:10.1149/2.005209jes.

[59] El Hannach M, Kjeang E. Stochastic Microstructural Modeling of PEFC Gas Diffusion Media. J Electrochem Soc 2014;161:F951–60. doi:10.1149/2.1141409jes.

[60] Wang G, Mukherjee PP, Wang CY. Direct numerical simulation (DNS) modeling of PEFC electrodes: Part I. Regular microstructure. Electrochim Acta 2006;51:3139–50. doi:10.1016/j.electacta.2005.09.002.

[61] Zils S, Timpel M, Arlt T, Wolz A, Manke I, Roth C. 3D visualisation of PEMFC electrode structures using FIB nanotomography. Fuel Cells 2010;10:966–72. doi:10.1002/fuce.201000133.

[62] Ostadi H, Rama P, Liu Y, Chen R, Zhang XX, Jiang K. 3D reconstruction of a gas diffusion layer and a microporous layer. J Memb Sci 2010;351:69–74. doi:10.1016/j.memsci.2010.01.031.

[63] Berson A, Choi HW, Pharoah JG. Determination of the effective gas diffusivity of a porous composite medium from the three-dimensional reconstruction of its microstructure. Phys Rev E - Stat Nonlinear, Soft Matter Phys 2011;83:1–12. doi:10.1103/PhysRevE.83.026310.

[64] Bertei A, Nucci B, Nicolella C. Microstructural modeling for prediction of transport properties and electrochemical performance in SOFC composite electrodes. Chem Eng Sci 2013;101:175–90. doi:10.1016/j.ces.2013.06.032.

[65] Bertei A, Nicolella C. Percolation theory in SOFC composite electrodes: Effects of porosity and particle size distribution on effective properties. J Power Sources 2011;196:9429–36. doi:10.1016/j.jpowsour.2011.06.087.

[66] Wargo EA, Kotaka T, Tabuchi Y, Kumbur EC. Comparison of focused ion beam versus nano-scale X-ray computed tomography for resolving 3-D microstructures of porous fuel cell materials. J Power Sources 2013;241:608–18. doi:10.1016/j.jpowsour.2013.04.153.

[67] Thiele S, Zengerle R, Ziegler C. Nano-morphology of a polymer electrolyte fuel cell catalyst layer-imaging, reconstruction and analysis. Nano Res 2011;4:849–60. doi:10.1007/s12274-011-0141-x.

[68] Sadeghifar H, Bahrami M, Djilali N. A statistically-based thermal conductivity model for fuel cell Gas Diffusion Layers. J Power Sources 2013;233:369–79. doi:10.1016/j.jpowsour.2013.01.086.

[69] Wang Q, Eikerling M, Song D, Liu Z. Structure and performance of different types of agglomerates in cathode catalyst layers of PEM fuel cells. J Electroanal Chem 2004;573:61–9. doi:10.1016/j.jelechem.2004.06.022.

[70] Sadeghi E, Putz A, Eikerling M. Hierarchical Model of Reaction Rate Distributions and Effectiveness Factors in Catalyst Layers of Polymer Electrolyte Fuel Cells. J Electrochem Soc 2013;160:F1159–69. doi:10.1149/2.090310jes.

[71] Lange K, Sui P, Djilali N. Pore scale simulation of transport and electrochemical reactions in reconstructed PEMFC catalyst layers. J Electrochem Soc 2010;157:B1434. doi:10.1149/1.3478207.

[72] Hattori T, Suzuki A, Sahnoun R, Koyama M, Tsuboi H, Hatakeyama N, et al. Development of the overpotential simulator for polymer electrolyte fuel cells and application for optimization of cathode structure. Appl Surf Sci 2008;254:7929–32. doi:10.1016/j.apsusc.2008.03.165.

[73] Wang Q, Song D, Navessin T, Holdcroft S, Liu Z. A mathematical model and optimization of the cathode catalyst layer structure in PEM fuel cells. Electrochim Acta 2004;50:725–30. doi:10.1016/j.electacta.2004.01.113.

[74] Sun W, Peppley BA, Karan K. An improved two-dimensional agglomerate cathode model to study the influence of catalyst layer structural parameters. Electrochim Acta 2005;50:3359–74. doi:10.1016/j.electacta.2004.12.009.

[75] Suzuki T, Kudo K, Morimoto Y. Model for investigation of oxygen transport limitation in a polymer electrolyte fuel cell. J Power Sources 2013;222:379–89. doi:10.1016/jjpowsour.2012.08.068.

[76] Kamarajugadda S, Mazumder S. Generalized flooded agglomerate model for the cathode catalyst layer of a polymer electrolyte membrane fuel cell. J Power

Sources 2012;208:328–39. doi:10.1016/j.jpowsour.2012.02.063.

[77] Cetinbas FC, Advani SG, Prasad AK. A Modified Agglomerate Model with Discrete Catalyst Particles for the PEM Fuel Cell Catalyst Layer. J Electrochem Soc 2013;160:F750–6. doi:Doi 10.1149/2.017308jes.

[78] Cheng B, Ni P, Jin C, Li Z, Zhang D, Dong P, et al. More direct evidence of the fcc arrangement for artificial opal. Opt Commun 1999;170:41–6. doi:10.1016/S0030-4018(99)00434-4.

[79] Inoue G, Kawase M. Effect of porous structure of catalyst layer on effective oxygen diffusion coefficient in polymer electrolyte fuel cell. J Power Sources 2016;327:1–10. doi:10.1016/j.jpowsour.2016.07.037.

[80] Litster S, Epting WK, Wargo EA, Kalidindi SR, Kumbur EC. Morphological analyses of polymer electrolyte fuel cell electrodes with nano-scale computed tomography imaging. Fuel Cells 2013;13:935–45. doi:10.1002/fuce.201300008.

[81] Epting WK, Gelb J, Litster S. Resolving the three-dimensional microstructure of polymer electrolyte fuel cell electrodes using nanometer-scale X-ray computed tomography. Adv Funct Mater 2012;22:555–60. doi:10.1002/adfm.201101525.

[82] Sabharwal M, Pant LM, Putz A, Susac D, Jankovic J, Secanell M. Analysis of catalyst layer microstructures: from imaging to performance. Fuel Cells 2016:734–53. doi:10.1002/fuce.201600008.

[83] Gao Y, Zhang X. Geometrical structures of catalyst layer and their impact on oxygen reduction in proton exchange membrane fuel cell. Electrochim Acta 2016;218:101–9. doi:10.1016/j.electacta.2016.09.100.

[84] Soboleva T, Malek K, Xie Z, Navessin T, Holdcroft S. PEMFC catalyst layers: The role of micropores and mesopores on water sorption and fuel cell activity. ACS Appl Mater Interfaces 2011;3:1827–37. doi:10.1021/am200590w.

[85] Yu Z, Carter RN, Zhang J. Measurements of pore size distribution, porosity, effective oxygen diffusivity, and tortuosity of PEM fuel cell electrodes. Fuel Cells 2012;12:557–65. doi:10.1002/fuce.201200017.

[86] Dim PE, Fletcher RS, Rigby SP. Improving the accuracy of catalyst pore size distributions from mercury porosimetry using mercury thermoporometry. Chem Eng Sci 2016;140:291–8. doi:10.1016/j.ces.2015.10.023.

[87] Morishige K. Hysteresis critical point of nitrogen in porous glass: occurrence of sample spanning transition in capillary condensation. Langmuir 2009;25:6221–6. doi:10.1021/la900022s.

[88] Morishige K, Tarui N. Capillary Condensation of Nitrogen in Ordered Mesoporous Silica with Bicontinuous Gyroid Structure. J Phys Chem C 2007;111:280–5. doi:10.1021/jp064946s.

[89] Kruk M, Jaroniec M, Sayari A. Application of large pore MCM-41 molecular sieves to improve pore size analysis using nitrogen adsorption measurements. Langmuir 1997;13:6267–73. doi:10.1021/la970776m.

[90] Quantachrome Instruments. Autosorb iQ and ASiQwin gas sorption system. 2013.

[91] De Lange MF, Vlugt TJH, Gascon J, Kapteijn F. Adsorptive characterization of porous solids: Error analysis guides the way. Microporous Mesoporous Mater 2014;200:199–215. doi:10.1016/j.micromeso.2014.08.048.

[92] Kowalczyk P, Gauden PA, Furmaniak S, Terzyk AP, Ilnicka A, Jerzy Ł, et al. Morphologically disordered pore model for characterization of micro-mesoporous carbons. Carbon N Y 2017;111:358–70. doi:10.1016/j.carbon.2016.09.070.

[93] Neimark A V, Lin Y, Ravikovitch PI, Thommes M. Quenched solid density functional theory and pore size analysis of micro-mesoporous carbons. Carbon N Y 2009;47:1617–28. doi:10.1016/j.carbon.2009.01.050.

[94] Groen JC, Peffer LAA, Pérez-Ramírez J. Pore size determination in modified micro- and mesoporous materials. Pitfalls and limitations in gas adsorption data analysis. Microporous Mesoporous Mater 2003;60:1–17. doi:10.1016/S1387-1811(03)00339-1.

[95] Britton B, Holdcroft S. The control and effect of pore size distribution in AEMFC catalyst layers. J Electrochem Soc 2016;163:F353–8. doi:10.1149/2.0421605jes.

[96] Chisaka M, Matsuoka E, Daiguji H. Effect of organic solvents on the pore structure of catalyst layers in polymer electrolyte membrane fuel cells. J Electrochem Soc 2010;157:B1218. doi:10.1149/1.3439617.

[97] Peron J, Edwards D, Besson A, Shi Z, Holdcroft S. Microstructure–Performance Relationships of sPEEK-Based Catalyst Layers. J Electrochem Soc 2010;157:B1230. doi:10.1149/1.3454735.

[98] Ye L, Gao Y, Zhu S, Zheng J, Li P. Short Communication A Pt content and pore structure gradient distributed catalyst layer to improve the PEMFC performance. Int J Hydrogen Energy 2017;42:1–5. doi:10.1016/j.ijhydene.2016.11.002.

[99] Zhao G, Zhao TS, Xu J, Lin Z, Yan X. Impact of pore size of ordered mesoporous carbon FDU-15-supported platinum catalysts on oxygen reduction reaction. Int J Hydrogen Energy 2017;42:3325–34. doi:10.1016/j.ijhydene.2016.11.089.

[100] Kim SH, Pitsch H. Reconstruction and effective transport properties of the catalyst layer in PEM fuel cells. J Electrochem Soc 2009;156:B673. doi:10.1149/1.3106136.

[101] Kang J, Moriyama K, Kim SH. An extended stochastic reconstruction method for catalyst layers in proton exchange membrane fuel cells. J Power Sources 2016;325:752–61. doi:10.1016/j.jpowsour.2016.06.083.

[102] Park Y, Tokiwa H, Kakinuma K, Watanabe M, Uchida M. Effects of carbon supports on Pt distribution , ionomer coverage and cathode performance for polymer electrolyte fuel cells. J Power Sources 2016;315:179–91. doi:10.1016/j.jpowsour.2016.02.091.

[103] Uchida M, Fukuoka Y, Sugawara Y, Eda N, Ohta A. Effects of microstructure of carbon support in the catalyst layer on the performance of polymer-electrolyte fuel cells. J Electrochem Soc 1996;143:2245–52. doi:10.1149/1.1836988.

[104] Takahashi K, Kakinuma K, Uchida M. Improvement of Cell Performance in Low-Pt-Loading PEFC Cathode Catalyst Layers Prepared by the Electrospray Method 2016;163:1182–8. doi:10.1149/2.0611610jes.

[105] Zhao J, Shahgaldi S, Alaefour I, Yang S, Li X. Pore structure and effective diffusion coefficient of catalyzed electrodes in polymer electrolyte membrane fuel cells. Int J Hydrogen Energy 2018;43:3776–85. doi:10.1016/j.ijhydene.2018.01.019.

[106] Radzig AA. Handbook of physical quantities. Boca Raton: CRC Press; 1996.

[107] Rossman RP, Smith WR. Density of carbon black by helium displacement. Ind Eng Chem 1943;35:972–6. doi:10.1021/ie50405a008.

[108] Zook LA, Leddy J. Density and solubility of nafion: recast, annealed, and commercial films. Anal Chem 1996;68:3793–6. doi:10.1021/ac960604e.

[109] Webb PA. An Introduction To The Physical Characterization of Materials by Mercury Intrusion Porosimetry with Emphasis On Reduction And Presentation of Experimental Data. Norcross, Georgia: 2001.

[110] Barrett EP, Joyner LG, Halenda PP. The Determination of Pore Volume and Area Distributions in Porous Substances. I. Computations from Nitrogen Isotherms. J Am Chem Soc 1951;73:373–80. doi:10.1021/ja01145a126.

[111] Ravikovitch PI, Haller GL, Neimark A V. Density functional theory model for calculating pore size distributions : pore structure of nanoporous catalysts 1998:203–26.

[112] Volfkovich YM, Bagotzky VS, Sosenkin VE, Blinov IA. The standard contact porosimetry. Colloids Surfaces A Physicochem Eng Asp 2001;187–188:349–65. doi:10.1016/S0927-7757(01)00650-1.

[113] Kleemann J. Einflüsse der Gasdiffusionslage auf Leistungsdichte und Kosten der PEM-Brennstoffzelle. Ulm, 2012.

[114] Wakeham WA, Nagashima A, Sengers J V. Measurement of the transport properties of fluids. Blackwell Scientific Publications; 1991.

[115] Waterloo Technical Instrument. Symmetrical Modified Loschmidt Cell Operator ' s Manual. 2017.

[116] Marrero T MEG. No Title. J Phys Chem Ref Data 1972;1:3–118.

[117] Mench M. Introduction to Fuel Cells. Fuel Cell Engines, Wiley-Blackwell; 2008. doi:10.1002/9780470209769.ch1.

[118] Cheng X, Yi B, Han M, Zhang J, Qiao Y, Yu J. Investigation of platinum utilization and morphology in catalyst layer of polymer electrolyte fuel cells 1999:75–81.

[119] Kim SH. The Effects of Catalyst Layer Microstructure and Water Saturation on the Effective Diffusivity in PEMFC 2018;165:468–78. doi:10.1149/2.0711807jes.

[120] Lavakumar A. Concepts in Physical Metallurgy. Morgan & Claypool Publishers; 2017. doi:10.1088/978-1-6817-4473-5.

[121] B. Ellis A, Geselbracht MJ, Johnson BJ, Lisensky GC, Robinson WR. Teaching general chemistry: A materials science companion. 1st ed. American Chemical Society Publication; 1993.

[122] Uchida M, Aoyama Y, Eda N, Ohta A. New preparation method for pPolymer-electrolyte fuel-cells. J Electrochem Soc 1995;142:463–8. doi:10.1149/1.2044068.

[123] Ihonen J, Jaouen F, Lindbergh G, Lundblad A, Sundholm G. Investigation of mass-transport limitations in the solid polymer fuel cell cathode. J Electrochem Soc 2002;149:A448. doi:10.1149/1.1456917.

[124] Andreaus B, Eikerling M. Catalyst layer operation in PEM fuel cells: from structural pictures to tractable models. Top Appl Phys 2009;113. doi:10.1007/978-0-387-78691-9.

[125] Malek K, Eikerling M, Wang Q, Navessin T, Liu Z. Self-organization in catalyst layers of polymer electrolyte fuel cells. J Phys Chem C 2007;111:13627–34. doi:10.1021/jp072692k.

[126] Bahrami M, Yovanovich MM, Culham JR. Pressure drop of fully-developed, laminar flow in microchannels of arbitrary cross-section. J Fluids Eng

2006;128:1036. doi:10.1115/1.2234786.

[127] Malekian A. Mechanical Properties of Thin Porous Catalyst Layers of PEM Fuel Cells. Simon Fraser University, 2018.

[128] Kusoglu A, Weber AZ. New Insights into Per fl uorinated Sulfonic-Acid Ionomers. Chem Rev 2017. doi:10.1021/acs.chemrev.6b00159.

[129] Springer TE, Zawodzinski TA, Gottesfeld S. Polymer Electrolyte Fuel Cell Model 1991;138:2334–42.

[130] Inc. S. Aquivion PFSA, Solid , Perfluorinated Superacid Catalysts. n.d.

[131] Zhao Q, Benziger J. Mechanical Properties of Perfluoro Sulfonated Acids : The Role of Temperature and Solute Activity. J Polym Sci Part B Polym Phys 2013:915–25. doi:10.1002/polb.23284.

[132] Pollard WG, Present RD. On gaseous self-diffusion in long capillary tubes. PhD Propos 1948;73:762–774.

[133] ANSYS. ANSYS Fluent Release 14.0 user manual. 2011.

[134] Wu W, Jiang F. Microstructure reconstruction and characterization of PEMFC electrodes. Int J Hydrogen Energy 2014;39:15894–906. doi:10.1016/j.ijhydene.2014.03.074.

[135] Voet A, Aboytes P. Porosity of carbon blacks. Carbon N Y 1971;9:135–8. doi:http://dx.doi.org/10.1016/0008-6223(71)90126-6.

[136] Ishikawa H, Sugawara Y, Inoue G, Kawase M. E ff ects of Pt and ionomer ratios on the structure of catalyst layer : A theoretical model for polymer electrolyte fuel cells. J Power Sources 2018;374:196–204. doi:10.1016/j.jpowsour.2017.11.026.

[137] Kusoglu A, Kushner D, Paul DK, Karan K, Hickner MA, Weber AZ. Impact of Substrate and Processing on Confi nement of Nafi on Thin Films 2014:4763–74. doi:10.1002/adfm.201304311.

Appendix A.

Measured experimental data

To measure gas diffusivity of each CL design and each operating condition, the oxygen concentration vs time measurements were done mostly for three different stacks of CL samples of the same design, and at least ten repetitions per stack. A sample of these measurements for CL design #1 presented in the Table A 1.

Table A 1 oxygen concentration versus time measurements by MLC for CL design #1. The instrument also read the operating conditions.

Design #1, T=20 ˚C, RH=0, compressive load=0, water content=0								
t (s)	C[17] (%)	C[28] (%)	T1[9] (˚C)	T2[10] (˚C)	P1[11] (kPa)	P2[12] (kPa)	RH1[13] (%)	RH2[14] (%)
0.000	2.041	4.177	19.927	19.896	101.159	101.156	1.196	1.892
0.500	4.826	5.477	19.896	19.927	101.164	101.153	1.222	1.892
1.000	7.625	6.851	19.896	19.927	101.159	101.153	1.222	1.892
1.500	9.805	8.561	19.866	19.927	101.167	101.167	1.170	1.918
2.000	11.369	10.161	19.866	19.927	101.164	101.144	1.170	1.918
2.500	12.585	11.442	19.896	19.927	101.164	101.167	1.170	1.892
3.000	13.785	12.554	19.896	19.927	101.164	101.159	1.170	1.892
3.500	14.978	13.581	19.896	19.927	101.159	101.156	1.196	1.892
4.000	16.064	14.566	19.896	19.927	101.162	101.167	1.196	1.892
4.500	17.033	15.513	19.927	19.927	101.167	101.164	1.196	1.918
5.000	17.921	16.345	19.927	19.927	101.159	101.162	1.196	1.918

[7] Oxygen concentration reading of probe 1 located at 5 mm away from the valve between the chambers in nitrogen chamber

[8] Oxygen concentration reading of probe 2 located at 10 mm away from the valve between the chambers in nitrogen chamber

[9] Temperature of the nitrogen chamber

[10] Temperature of the oxygen chamber

[11] Pressure of the nitrogen chamber

[12] Pressure of the oxygen chamber

[13] RH of the nitrogen chamber

[14] RH of the oxygen chamber

5.500	18.733	17.137	19.896	19.927	101.167	101.164	1.170	1.892
6.000	19.505	17.886	19.896	19.927	101.167	101.156	1.170	1.892
6.500	20.211	18.565	19.896	19.927	101.153	101.162	1.170	1.892
7.000	20.877	19.242	19.896	19.927	101.164	101.159	1.170	1.892
7.500	21.519	19.827	19.896	19.927	101.150	101.164	1.170	1.866
8.000	22.080	20.411	19.896	19.927	101.159	101.159	1.170	1.866
8.500	22.666	20.978	19.896	19.927	101.162	101.162	1.196	1.866
9.001	23.159	21.485	19.896	19.927	101.162	101.156	1.196	1.866
9.501	23.668	21.994	19.896	19.958	101.153	101.164	1.170	1.866
10.001	24.137	22.437	19.896	19.958	101.162	101.164	1.170	1.866
10.501	24.578	22.880	19.896	19.927	101.159	101.159	1.196	1.866
11.001	24.980	23.310	19.896	19.927	101.153	101.170	1.196	1.866
11.501	25.394	23.721	19.896	19.896	101.164	101.164	1.170	1.866
12.001	25.780	24.109	19.896	19.896	101.153	101.164	1.170	1.866
12.501	26.157	24.485	19.866	19.927	101.150	101.150	1.145	1.892
13.001	26.517	24.833	19.866	19.927	101.159	101.156	1.145	1.892
13.501	26.792	25.196	19.896	19.927	101.162	101.156	1.196	1.866
14.001	27.145	25.528	19.896	19.927	101.144	101.159	1.196	1.866
14.501	27.484	25.809	19.896	19.927	101.153	101.162	1.196	1.841
15.001	27.765	26.122	19.896	19.927	101.159	101.150	1.196	1.841
15.501	28.047	26.402	19.896	19.927	101.156	101.153	1.170	1.892
16.001	28.336	26.738	19.896	19.927	101.162	101.159	1.170	1.892
16.502	28.586	26.987	19.896	19.927	101.153	101.159	1.196	1.892
17.001	28.858	27.253	19.896	19.927	101.167	101.153	1.196	1.892
17.501	29.102	27.478	19.896	19.927	101.164	101.156	1.196	1.841
18.001	29.331	27.742	19.896	19.927	101.162	101.167	1.196	1.841
18.501	29.583	27.994	19.896	19.958	101.167	101.159	1.170	1.866
19.001	29.810	28.251	19.896	19.958	101.167	101.164	1.170	1.866
19.501	30.027	28.435	19.896	19.958	101.156	101.159	1.196	1.841
20.001	30.233	28.674	19.896	19.958	101.150	101.156	1.196	1.841
0.000	2.041	4.177	19.927	19.896	101.159	101.156	1.196	1.892
0.500	4.826	5.477	19.896	19.927	101.164	101.153	1.222	1.892
1.000	7.625	6.851	19.896	19.927	101.159	101.153	1.222	1.892
1.500	9.805	8.561	19.866	19.927	101.167	101.167	1.170	1.918
2.000	11.369	10.161	19.866	19.927	101.164	101.144	1.170	1.918
2.500	12.585	11.442	19.896	19.927	101.164	101.167	1.170	1.892
3.000	13.785	12.554	19.896	19.927	101.164	101.159	1.170	1.892
3.500	14.978	13.581	19.896	19.927	101.159	101.156	1.196	1.892
4.000	16.064	14.566	19.896	19.927	101.162	101.167	1.196	1.892
4.500	17.033	15.513	19.927	19.927	101.167	101.164	1.196	1.918
5.000	17.921	16.345	19.927	19.927	101.159	101.162	1.196	1.918
5.500	18.733	17.137	19.896	19.927	101.167	101.164	1.170	1.892

6.000	19.505	17.886	19.896	19.927	101.167	101.156	1.170	1.892
6.500	20.211	18.565	19.896	19.927	101.153	101.162	1.170	1.892
7.000	20.877	19.242	19.896	19.927	101.164	101.159	1.170	1.892
7.500	21.519	19.827	19.896	19.927	101.150	101.164	1.170	1.866
8.000	22.080	20.411	19.896	19.927	101.159	101.159	1.170	1.866
8.500	22.666	20.978	19.896	19.927	101.162	101.162	1.196	1.866
9.001	23.159	21.485	19.896	19.927	101.162	101.156	1.196	1.866
9.501	23.668	21.994	19.896	19.958	101.153	101.164	1.170	1.866
10.001	24.137	22.437	19.896	19.958	101.162	101.164	1.170	1.866
10.501	24.578	22.880	19.896	19.927	101.159	101.159	1.196	1.866
11.001	24.980	23.310	19.896	19.927	101.153	101.170	1.196	1.866
11.501	25.394	23.721	19.896	19.896	101.164	101.164	1.170	1.866
12.001	25.780	24.109	19.896	19.896	101.153	101.164	1.170	1.866
12.501	26.157	24.485	19.866	19.927	101.150	101.150	1.145	1.892
13.001	26.517	24.833	19.866	19.927	101.159	101.156	1.145	1.892
13.501	26.792	25.196	19.896	19.927	101.162	101.156	1.196	1.866
14.001	27.145	25.528	19.896	19.927	101.144	101.159	1.196	1.866
14.501	27.484	25.809	19.896	19.927	101.153	101.162	1.196	1.841
15.001	27.765	26.122	19.896	19.927	101.159	101.150	1.196	1.841
15.501	28.047	26.402	19.896	19.927	101.156	101.153	1.170	1.892
16.001	28.336	26.738	19.896	19.927	101.162	101.159	1.170	1.892
16.502	28.586	26.987	19.896	19.927	101.153	101.159	1.196	1.892
17.001	28.858	27.253	19.896	19.927	101.167	101.153	1.196	1.892
17.501	29.102	27.478	19.896	19.927	101.164	101.156	1.196	1.841
18.001	29.331	27.742	19.896	19.927	101.162	101.167	1.196	1.841
18.501	29.583	27.994	19.896	19.958	101.167	101.159	1.170	1.866
19.001	29.810	28.251	19.896	19.958	101.167	101.164	1.170	1.866
19.501	30.027	28.435	19.896	19.958	101.156	101.159	1.196	1.841
20.001	30.233	28.674	19.896	19.958	101.150	101.156	1.196	1.841
20.501	30.441	28.888	19.896	19.958	101.162	101.164	1.170	1.866
21.001	30.628	29.042	19.896	19.958	101.153	101.156	1.170	1.866
21.501	30.810	29.313	19.896	19.896	101.156	101.156	1.196	1.866
22.001	31.010	29.494	19.896	19.896	101.159	101.164	1.196	1.866
22.501	31.195	29.671	19.896	19.927	101.159	101.147	1.170	1.866
23.001	31.355	29.883	19.896	19.927	101.156	101.150	1.170	1.866
23.501	31.539	30.041	19.896	19.927	101.162	101.162	1.170	1.841
24.001	31.688	30.208	19.896	19.927	101.159	101.162	1.170	1.841
24.501	31.864	30.396	19.866	19.927	101.162	101.159	1.196	1.841
25.001	32.032	30.548	19.866	19.927	101.164	101.150	1.196	1.841
25.501	32.181	30.707	19.896	19.927	101.156	101.164	1.196	1.841
26.001	32.347	30.890	19.896	19.927	101.164	101.150	1.196	1.841
26.502	32.497	31.060	19.896	19.896	101.167	101.159	1.196	1.841

27.002	32.621	31.196	19.896	19.896	101.156	101.162	1.196	1.841
27.502	32.769	31.338	19.927	19.927	101.147	101.156	1.222	1.866
28.002	32.897	31.493	19.927	19.927	101.162	101.147	1.222	1.866
28.502	33.012	31.649	19.927	19.896	101.156	101.164	1.170	1.841
29.002	33.159	31.762	19.927	19.896	101.153	101.162	1.170	1.841
29.502	33.286	31.901	19.866	19.927	101.159	101.159	1.196	1.815
30.002	33.417	32.042	19.866	19.927	101.170	101.150	1.196	1.815
30.502	33.548	32.111	19.896	19.927	101.162	101.150	1.196	1.841
31.002	33.659	32.255	19.896	19.927	101.162	101.150	1.196	1.841
31.502	33.799	32.391	19.896	19.958	101.150	101.156	1.170	1.815
32.002	33.910	32.516	19.896	19.958	101.141	101.153	1.170	1.815
32.502	34.019	32.632	19.896	19.927	101.153	101.156	1.170	1.841
33.002	34.095	32.749	19.896	19.927	101.164	101.159	1.170	1.841
33.502	34.226	32.850	19.896	19.958	101.153	101.162	1.196	1.815
34.002	34.347	33.002	19.896	19.958	101.156	101.159	1.196	1.815
34.501	34.431	33.101	19.927	19.927	101.159	101.150	1.170	1.841
35.001	34.523	33.254	19.927	19.927	101.153	101.150	1.170	1.841
35.501	34.642	33.361	19.896	19.958	101.159	101.162	1.170	1.841
36.001	34.705	33.421	19.896	19.958	101.156	101.159	1.170	1.841
36.501	34.816	33.481	19.896	19.927	101.159	101.150	1.170	1.892
37.001	34.925	33.645	19.896	19.927	101.164	101.162	1.170	1.892
37.501	35.019	33.699	19.896	19.927	101.153	101.162	1.196	1.866
38.001	35.109	33.840	19.896	19.927	101.156	101.156	1.196	1.866
38.501	35.192	33.939	19.896	19.927	101.159	101.153	1.196	1.841
39.001	35.298	34.032	19.896	19.927	101.156	101.156	1.196	1.841
39.501	35.397	34.068	19.866	19.896	101.159	101.150	1.170	1.841
40.001	35.492	34.232	19.866	19.896	101.156	101.159	1.170	1.841
40.501	35.576	34.278	19.896	19.927	101.162	101.159	1.196	1.841
41.001	35.653	34.369	19.896	19.927	101.164	101.159	1.196	1.841
41.501	35.703	34.447	19.896	19.927	101.162	101.153	1.170	1.841
42.001	35.784	34.598	19.896	19.927	101.159	101.156	1.170	1.841
42.501	35.857	34.591	19.927	19.958	101.156	101.159	1.196	1.841
43.001	35.939	34.696	19.927	19.958	101.164	101.162	1.196	1.841
43.501	36.013	34.792	19.927	19.927	101.162	101.156	1.170	1.841
44.002	36.079	34.825	19.927	19.927	101.162	101.164	1.170	1.841
44.502	36.145	34.901	19.896	19.927	101.150	101.159	1.196	1.866
45.002	36.247	35.025	19.896	19.927	101.159	101.147	1.196	1.866
45.502	36.298	35.061	19.896	19.927	101.159	101.164	1.170	1.841
46.002	36.389	35.162	19.896	19.927	101.159	101.159	1.170	1.841
46.502	36.468	35.269	19.896	19.927	101.162	101.159	1.196	1.841
47.002	36.515	35.319	19.896	19.927	101.156	101.156	1.196	1.841
47.502	36.606	35.451	19.866	19.927	101.167	101.162	1.196	1.841

48.002	36.650	35.451	19.866	19.927	101.159	101.159	1.196	1.841
48.502	36.706	35.519	19.896	19.927	101.159	101.147	1.222	1.866
49.002	36.797	35.638	19.896	19.927	101.159	101.150	1.222	1.866
49.502	36.813	35.685	19.896	19.927	101.162	101.159	1.170	1.841
50.002	36.918	35.767	19.896	19.927	101.167	101.147	1.170	1.841
50.502	36.966	35.825	19.866	19.927	101.159	101.164	1.170	1.841
51.002	37.006	35.860	19.866	19.927	101.150	101.159	1.170	1.841
51.502	37.063	35.932	19.896	19.927	101.164	101.159	1.196	1.815
52.001	37.176	36.001	19.896	19.927	101.162	101.164	1.196	1.815
52.501	37.184	36.032	19.896	19.927	101.156	101.150	1.170	1.866
53.001	37.269	36.118	19.896	19.927	101.153	101.156	1.170	1.866
53.501	37.322	36.135	19.927	19.896	101.156	101.156	1.196	1.866
54.001	37.416	36.177	19.927	19.896	101.167	101.153	1.196	1.866
54.501	37.420	36.299	19.927	19.896	101.167	101.164	1.170	1.841
55.001	37.485	36.403	19.927	19.896	101.164	101.153	1.170	1.841
55.501	37.534	36.449	19.896	19.927	101.153	101.156	1.170	1.841
56.001	37.608	36.445	19.896	19.927	101.159	101.162	1.170	1.841
56.501	37.629	36.536	19.896	19.958	101.164	101.164	1.196	1.841
57.001	37.703	36.613	19.896	19.958	101.159	101.156	1.196	1.841
57.501	37.790	36.663	19.896	19.958	101.156	101.170	1.222	1.815
58.001	37.819	36.680	19.896	19.958	101.159	101.153	1.222	1.815
58.501	37.856	36.808	19.866	19.927	101.162	101.156	1.196	1.841
59.001	37.881	36.836	19.866	19.927	101.164	101.150	1.196	1.841
59.501	37.972	36.871	19.896	19.927	101.150	101.164	1.170	1.866
60.001	38.026	36.946	19.896	19.927	101.156	101.159	1.170	1.866
60.501	38.051	37.014	19.896	19.927	101.162	101.159	1.196	1.841
61.001	38.139	37.035	19.896	19.927	101.150	101.150	1.196	1.841
61.502	38.152	37.071	19.927	19.927	101.159	101.159	1.196	1.841
62.002	38.240	37.103	19.927	19.927	101.159	101.153	1.196	1.841
62.502	38.244	37.189	19.866	19.958	101.153	101.159	1.170	1.841
63.002	38.303	37.175	19.866	19.958	101.153	101.159	1.170	1.841
63.502	38.340	37.232	19.896	19.958	101.150	101.162	1.170	1.866
64.002	38.370	37.300	19.896	19.958	101.159	101.153	1.170	1.866
64.502	38.437	37.300	19.896	19.896	101.162	101.162	1.170	1.866
65.002	38.463	37.333	19.896	19.896	101.156	101.153	1.170	1.866
65.502	38.497	37.380	19.896	19.958	101.159	101.159	1.170	1.841
66.002	38.552	37.488	19.896	19.958	101.159	101.164	1.170	1.841
66.502	38.599	37.524	19.896	19.927	101.159	101.167	1.196	1.841
67.002	38.633	37.597	19.896	19.927	101.150	101.167	1.196	1.841
67.502	38.692	37.637	19.896	19.927	101.159	101.162	1.196	1.841
68.002	38.756	37.644	19.896	19.927	101.153	101.159	1.196	1.841
68.502	38.782	37.728	19.896	19.927	101.159	101.156	1.170	1.841

69.002	38.777	37.776	19.896	19.927	101.164	101.156	1.170	1.841
69.501	38.876	37.845	19.927	19.896	101.156	101.156	1.222	1.866
70.001	38.854	37.871	19.927	19.896	101.156	101.162	1.222	1.866
70.501	38.902	37.882	19.896	19.927	101.153	101.162	1.145	1.841
71.001	38.949	37.919	19.896	19.927	101.164	101.162	1.145	1.841
71.501	38.966	37.974	19.896	19.927	101.156	101.159	1.170	1.841
72.001	39.000	38.066	19.896	19.927	101.159	101.162	1.170	1.841
72.501	39.039	38.051	19.896	19.958	101.167	101.164	1.196	1.866
73.001	39.065	38.121	19.896	19.958	101.173	101.159	1.196	1.866
73.501	39.104	38.129	19.896	19.958	101.150	101.159	1.170	1.866
74.001	39.147	38.195	19.896	19.958	101.162	101.153	1.170	1.866
74.501	39.190	38.210	19.866	19.958	101.156	101.167	1.170	1.841
75.001	39.229	38.255	19.866	19.958	101.164	101.156	1.170	1.841
75.501	39.260	38.281	19.896	19.958	101.162	101.167	1.170	1.866
76.001	39.290	38.344	19.896	19.958	101.167	101.164	1.170	1.866
76.501	39.338	38.348	19.896	19.958	101.153	101.162	1.170	1.841
77.001	39.364	38.441	19.896	19.958	101.170	101.156	1.170	1.841
77.501	39.412	38.404	19.896	19.927	101.159	101.159	1.196	1.866
78.001	39.460	38.400	19.896	19.927	101.164	101.159	1.196	1.866
78.501	39.473	38.467	19.896	19.958	101.162	101.170	1.196	1.866
79.002	39.513	38.546	19.896	19.958	101.159	101.159	1.196	1.866
79.502	39.543	38.572	19.896	19.958	101.167	101.170	1.196	1.841
80.002	39.578	38.606	19.896	19.958	101.159	101.156	1.196	1.841
80.502	39.627	38.602	19.866	19.958	101.156	101.156	1.196	1.841
81.002	39.631	38.734	19.866	19.958	101.156	101.170	1.196	1.841
81.502	39.653	38.719	19.896	19.896	101.162	101.156	1.196	1.841
82.002	39.724	38.738	19.896	19.896	101.159	101.156	1.196	1.841
82.502	39.732	38.787	19.896	19.927	101.167	101.162	1.196	1.841
83.002	39.768	38.772	19.896	19.927	101.162	101.156	1.196	1.841
83.502	39.803	38.783	19.866	19.927	101.150	101.156	1.170	1.841
84.002	39.843	38.912	19.866	19.927	101.167	101.167	1.170	1.841
84.502	39.847	38.855	19.866	19.927	101.153	101.162	1.196	1.841
85.002	39.918	38.885	19.866	19.927	101.159	101.162	1.196	1.841
85.502	39.949	38.961	19.896	19.958	101.156	101.156	1.170	1.866
86.002	39.976	39.007	19.896	19.958	101.159	101.156	1.170	1.866
86.502	39.980	39.014	19.896	19.927	101.159	101.164	1.196	1.841
87.001	39.998	39.029	19.896	19.927	101.167	101.156	1.196	1.841
87.501	40.016	39.029	19.896	19.927	101.156	101.156	1.196	1.841
88.001	40.047	39.067	19.896	19.927	101.167	101.156	1.196	1.841
88.501	40.100	39.056	19.896	19.958	101.170	101.159	1.196	1.866
89.001	40.105	39.083	19.896	19.958	101.156	101.167	1.196	1.866
89.501	40.167	39.155	19.866	19.927	101.167	101.164	1.170	1.866

90.001	40.158	39.197	19.866	19.927	101.159	101.156	1.170	1.866
90.501	40.194	39.194	19.896	19.927	101.164	101.167	1.196	1.866
91.001	40.257	39.255	19.896	19.927	101.162	101.167	1.196	1.866
91.501	40.243	39.297	19.866	19.927	101.156	101.162	1.170	1.866
92.001	40.306	39.335	19.866	19.927	101.170	101.162	1.170	1.866
92.501	40.293	39.389	19.866	19.927	101.164	101.167	1.196	1.841
93.001	40.338	39.420	19.866	19.927	101.167	101.156	1.196	1.841
93.501	40.396	39.447	19.896	19.927	101.156	101.164	1.196	1.866
94.001	40.360	39.501	19.896	19.927	101.164	101.170	1.196	1.866
94.501	40.396	39.497	19.896	19.927	101.164	101.153	1.196	1.841
95.001	40.441	39.505	19.896	19.927	101.164	101.167	1.196	1.841
95.501	40.473	39.563	19.866	19.927	101.173	101.159	1.196	1.841
96.001	40.486	39.575	19.866	19.927	101.156	101.162	1.196	1.841
96.502	40.486	39.641	19.896	19.927	101.159	101.162	1.170	1.866
97.002	40.509	39.629	19.896	19.927	101.164	101.156	1.170	1.866
97.502	40.532	39.703	19.866	19.927	101.170	101.170	1.170	1.866
98.002	40.595	39.656	19.866	19.927	101.153	101.164	1.170	1.866
98.502	40.609	39.804	19.896	19.927	101.162	101.162	1.170	1.892
99.002	40.595	39.753	19.896	19.927	101.156	101.159	1.170	1.892
99.502	40.645	39.796	19.896	19.958	101.159	101.162	1.196	1.866
100.002	40.672	39.808	19.896	19.958	101.156	101.162	1.196	1.866
100.502	40.677	39.863	19.896	19.927	101.162	101.159	1.196	1.841
101.002	40.708	39.828	19.896	19.927	101.159	101.164	1.196	1.841
101.502	40.736	39.886	19.896	19.958	101.162	101.159	1.170	1.866
102.002	40.749	39.941	19.896	19.958	101.156	101.162	1.170	1.866
102.502	40.822	39.949	19.866	19.927	101.150	101.167	1.196	1.866
103.002	40.795	40.008	19.866	19.927	101.164	101.167	1.196	1.866
103.502	40.873	40.000	19.896	19.958	101.170	101.162	1.170	1.866
104.002	40.841	40.071	19.896	19.958	101.156	101.162	1.170	1.866
104.501	40.868	40.027	19.866	19.927	101.164	101.159	1.196	1.841
105.001	40.937	40.098	19.866	19.927	101.164	101.153	1.196	1.841
105.501	40.918	40.134	19.896	19.958	101.156	101.162	1.196	1.866
106.001	40.928	40.130	19.896	19.958	101.156	101.164	1.196	1.866
106.501	40.918	40.110	19.866	19.927	101.167	101.173	1.170	1.841
107.001	40.960	40.090	19.866	19.927	101.167	101.167	1.170	1.841
107.501	40.996	40.197	19.896	19.896	101.162	101.156	1.196	1.866
108.001	41.028	40.161	19.896	19.896	101.167	101.162	1.196	1.866
108.501	41.028	40.220	19.927	19.927	101.162	101.162	1.196	1.866
109.001	41.065	40.193	19.927	19.927	101.162	101.153	1.196	1.866
109.501	41.042	40.280	19.927	19.927	101.162	101.167	1.196	1.866
110.001	41.065	40.284	19.927	19.927	101.162	101.167	1.196	1.866
110.501	41.125	40.272	19.896	19.927	101.164	101.162	1.145	1.892

111.001	41.107	40.312	19.896	19.927	101.164	101.159	1.145	1.892
111.501	41.157	40.292	19.896	19.927	101.156	101.156	1.170	1.866
112.001	41.171	40.347	19.896	19.927	101.167	101.156	1.170	1.866
112.501	41.162	40.351	19.896	19.927	101.156	101.162	1.196	1.866
113.001	41.217	40.363	19.896	19.927	101.167	101.156	1.196	1.866
113.501	41.236	40.419	19.866	19.958	101.162	101.153	1.170	1.866
114.002	41.254	40.391	19.866	19.958	101.167	101.162	1.170	1.866
114.502	41.287	40.423	19.896	19.958	101.162	101.162	1.170	1.892
115.002	41.305	40.447	19.896	19.958	101.153	101.147	1.170	1.892
115.502	41.296	40.463	19.896	19.958	101.159	101.150	1.196	1.866
116.002	41.342	40.498	19.896	19.958	101.164	101.167	1.196	1.866
116.502	41.384	40.502	19.866	19.927	101.170	101.159	1.196	1.866
117.002	41.366	40.522	19.866	19.927	101.156	101.156	1.196	1.866
117.502	41.421	40.510	19.866	19.958	101.156	101.153	1.170	1.866
118.002	41.435	40.526	19.866	19.958	101.162	101.162	1.170	1.866
118.502	41.459	40.590	19.896	19.958	101.156	101.162	1.170	1.866
119.002	41.487	40.618	19.896	19.958	101.159	101.156	1.170	1.866
119.502	41.496	40.594	19.927	19.927	101.167	101.159	1.170	1.892
120.002	41.510	40.662	19.927	19.927	101.147	101.153	1.170	1.892
120.502	41.533	40.638	19.866	19.927	101.156	101.150	1.196	1.866
121.002	41.557	40.630	19.866	19.927	101.156	101.164	1.196	1.866
121.502	41.552	40.718	19.896	19.896	101.162	101.164	1.222	1.866
122.001	41.575	40.714	19.896	19.896	101.164	101.156	1.222	1.866
122.501	41.627	40.755	19.866	19.958	101.153	101.164	1.222	1.841
123.001	41.617	40.803	19.866	19.958	101.156	101.162	1.222	1.841
123.501	41.664	40.747	19.866	19.958	101.156	101.167	1.170	1.866
124.001	41.636	40.747	19.866	19.958	101.164	101.162	1.170	1.866
124.501	41.711	40.767	19.866	19.927	101.156	101.156	1.170	1.866
125.001	41.720	40.827	19.866	19.927	101.162	101.167	1.170	1.866
125.501	41.702	40.787	19.896	19.896	101.164	101.156	1.196	1.866
126.001	41.730	40.900	19.896	19.896	101.164	101.162	1.196	1.866
126.501	41.739	40.863	19.896	19.927	101.167	101.167	1.196	1.892
127.001	41.767	40.908	19.896	19.927	101.167	101.156	1.196	1.892
127.501	41.772	40.843	19.927	19.927	101.162	101.153	1.196	1.918
128.001	41.796	40.871	19.927	19.927	101.167	101.156	1.196	1.918
128.501	41.819	40.944	19.896	19.927	101.162	101.156	1.196	1.866
129.001	41.847	40.904	19.896	19.927	101.156	101.162	1.196	1.866
129.501	41.819	40.952	19.866	19.958	101.170	101.167	1.196	1.866
130.001	41.881	40.993	19.866	19.958	101.162	101.164	1.196	1.866
130.501	41.932	40.989	19.896	19.927	101.170	101.153	1.222	1.866
131.001	41.899	41.013	19.896	19.927	101.156	101.156	1.222	1.866
131.502	41.909	40.993	19.927	19.927	101.162	101.164	1.170	1.892

132.002	41.942	41.074	19.927	19.927	101.164	101.156	1.170	1.892
132.502	41.947	41.090	19.896	19.958	101.164	101.153	1.222	1.866
133.002	41.975	41.074	19.896	19.958	101.164	101.156	1.222	1.866
133.502	41.961	41.114	19.896	19.927	101.162	101.167	1.196	1.892
134.002	41.956	41.110	19.896	19.927	101.162	101.153	1.196	1.892
134.502	42.022	41.135	19.866	19.958	101.156	101.164	1.222	1.892
135.002	41.980	41.094	19.866	19.958	101.162	101.162	1.222	1.892
135.502	42.018	41.118	19.896	19.927	101.159	101.153	1.170	1.892
136.002	42.022	41.200	19.896	19.927	101.167	101.153	1.170	1.892
136.502	42.027	41.245	19.896	19.958	101.159	101.162	1.145	1.866
137.002	42.008	41.265	19.896	19.958	101.156	101.156	1.145	1.866
137.502	42.075	41.269	19.896	19.927	101.156	101.167	1.170	1.866
138.002	42.075	41.310	19.896	19.927	101.167	101.170	1.170	1.866
138.502	42.065	41.281	19.896	19.927	101.164	101.167	1.170	1.892
139.002	42.089	41.253	19.896	19.927	101.167	101.173	1.170	1.892
139.501	42.113	41.281	19.866	19.927	101.167	101.164	1.196	1.866
140.001	42.108	41.290	19.866	19.927	101.167	101.159	1.196	1.866
140.501	42.151	41.302	19.896	19.927	101.162	101.156	1.222	1.892
141.001	42.136	41.347	19.896	19.927	101.159	101.167	1.222	1.892
141.501	42.132	41.384	19.866	19.927	101.167	101.170	1.222	1.866
142.001	42.151	41.404	19.866	19.927	101.162	101.162	1.222	1.866
142.501	42.151	41.478	19.866	19.927	101.159	101.162	1.222	1.866
143.001	42.174	41.453	19.866	19.927	101.164	101.162	1.222	1.866
143.501	42.222	41.494	19.896	19.958	101.159	101.167	1.196	1.892
144.001	42.222	41.449	19.896	19.958	101.167	101.159	1.196	1.892
144.501	42.217	41.494	19.896	19.927	101.156	101.156	1.196	1.892
145.001	42.217	41.482	19.896	19.927	101.162	101.153	1.196	1.892
145.501	42.260	41.507	19.866	19.927	101.159	101.159	1.222	1.866
146.001	42.298	41.503	19.866	19.927	101.164	101.162	1.222	1.866
146.501	42.289	41.503	19.896	19.958	101.164	101.162	1.222	1.866
147.001	42.308	41.527	19.896	19.958	101.167	101.159	1.222	1.866
147.501	42.303	41.585	19.896	19.958	101.156	101.159	1.196	1.892
148.001	42.337	41.540	19.896	19.958	101.159	101.150	1.196	1.892
148.501	42.356	41.585	19.927	19.927	101.150	101.159	1.196	1.892
149.002	42.346	41.606	19.927	19.927	101.164	101.167	1.196	1.892
149.502	42.404	41.622	19.896	19.958	101.162	101.156	1.196	1.892
150.002	42.365	41.643	19.896	19.958	101.156	101.156	1.196	1.892
150.502	42.408	41.668	19.866	19.958	101.159	101.167	1.196	1.892
151.002	42.428	41.663	19.866	19.958	101.159	101.153	1.196	1.892
151.502	42.447	41.676	19.866	19.927	101.167	101.162	1.196	1.892
152.002	42.476	41.746	19.866	19.927	101.164	101.156	1.196	1.892
152.502	42.485	41.746	19.896	19.958	101.164	101.156	1.222	1.892

153.002	42.485	41.738	19.896	19.958	101.167	101.153	1.222	1.892
153.502	42.582	41.755	19.896	19.958	101.164	101.156	1.196	1.866
154.002	42.524	41.771	19.896	19.958	101.150	101.159	1.196	1.866
154.502	42.514	41.742	19.896	19.927	101.159	101.159	1.222	1.866
155.002	42.553	41.746	19.896	19.927	101.167	101.164	1.222	1.866
155.502	42.553	41.800	19.866	19.927	101.159	101.156	1.222	1.892
156.002	42.577	41.792	19.866	19.927	101.159	101.162	1.222	1.892
156.502	42.635	41.833	19.896	19.927	101.164	101.162	1.196	1.866
157.001	42.601	41.854	19.896	19.927	101.167	101.162	1.196	1.866
157.501	42.635	41.867	19.896	19.958	101.153	101.156	1.196	1.866
158.001	42.630	41.900	19.896	19.958	101.156	101.159	1.196	1.866
158.501	42.649	41.896	19.896	19.896	101.162	101.164	1.222	1.892
159.001	42.668	41.971	19.896	19.896	101.162	101.156	1.222	1.892
159.501	42.659	41.967	19.896	19.927	101.162	101.167	1.222	1.892
160.001	42.678	41.958	19.896	19.927	101.162	101.164	1.222	1.892
160.501	42.702	41.946	19.896	19.927	101.159	101.167	1.222	1.892
161.001	42.678	41.942	19.896	19.927	101.159	101.167	1.222	1.892
161.501	42.678	41.929	19.927	19.896	101.164	101.156	1.196	1.892
162.001	42.712	42.008	19.927	19.896	101.162	101.159	1.196	1.892
162.501	42.727	42.008	19.927	19.927	101.170	101.150	1.196	1.892
163.001	42.731	42.008	19.927	19.927	101.162	101.173	1.196	1.892
163.501	42.727	42.029	19.927	19.927	101.162	101.162	1.196	1.892
164.001	42.770	42.058	19.927	19.927	101.162	101.176	1.196	1.892
164.501	42.741	42.096	19.896	19.927	101.164	101.156	1.196	1.918
165.001	42.741	42.100	19.896	19.927	101.167	101.162	1.196	1.918
165.501	42.809	42.117	19.896	19.927	101.156	101.170	1.222	1.866
166.001	42.804	42.025	19.896	19.927	101.167	101.179	1.222	1.866
166.502	42.794	42.104	19.896	19.927	101.173	101.156	1.196	1.866
167.002	42.804	42.130	19.896	19.927	101.159	101.167	1.196	1.866
167.502	42.814	42.084	19.896	19.927	101.173	101.167	1.222	1.892
168.002	42.799	42.134	19.896	19.927	101.153	101.173	1.222	1.892
168.502	42.794	42.155	19.896	19.958	101.167	101.167	1.196	1.892
169.002	42.838	42.146	19.896	19.958	101.167	101.173	1.196	1.892
169.502	42.843	42.180	19.927	19.927	101.162	101.164	1.222	1.892
170.002	42.843	42.243	19.927	19.927	101.164	101.159	1.222	1.892
170.502	42.848	42.197	19.896	19.927	101.167	101.162	1.196	1.918
171.002	42.887	42.159	19.896	19.927	101.164	101.159	1.196	1.918
171.502	42.887	42.201	19.896	19.927	101.164	101.164	1.170	1.866
172.002	42.926	42.277	19.896	19.927	101.159	101.156	1.170	1.866
172.502	42.896	42.230	19.835	19.927	101.162	101.164	1.196	1.866
173.002	42.887	42.239	19.835	19.927	101.162	101.164	1.196	1.866
173.502	42.940	42.285	19.896	19.927	101.173	101.159	1.196	1.892

174.002	42.906	42.306	19.896	19.927	101.167	101.164	1.196	1.892
174.501	42.926	42.327	19.927	19.927	101.167	101.167	1.222	1.892
175.001	42.945	42.277	19.927	19.927	101.167	101.162	1.222	1.892
175.501	42.945	42.306	19.927	19.958	101.159	101.164	1.222	1.918
176.001	42.974	42.251	19.927	19.958	101.159	101.167	1.222	1.918
176.501	42.979	42.323	19.927	19.927	101.173	101.167	1.222	1.892
177.001	42.955	42.357	19.927	19.927	101.167	101.164	1.222	1.892
177.501	43.033	42.378	19.896	19.958	101.164	101.164	1.170	1.866
178.001	43.004	42.382	19.896	19.958	101.159	101.170	1.170	1.866
178.501	43.053	42.298	19.866	19.958	101.156	101.170	1.196	1.892
179.001	43.023	42.344	19.866	19.958	101.164	101.167	1.196	1.892
179.501	43.062	42.395	19.896	19.927	101.167	101.167	1.196	1.892
180.001	43.077	42.357	19.896	19.927	101.162	101.167	1.196	1.892

The oxygen concentration readings for stacks of catalyst-coated filter PTFEs and stacks of filter PTFEs were processed to gas diffusion resistances and the using Eq. 18 to gas diffusivity of CL. These resistances and diffusivities are presented in %% to %% for different designs and operating conditions. It should be mentioned that for each design and operating condition usually three different stacks (of the same design) were tested; however, as the results were consistent, here just one stack result is presented.

Table A 2 Measured effective lengths of stack of catalyst-coated filter PTFEs and stack of filter PTFEs, CL stack thickness, and resulted relative diffusivities for different operating conditions and designs

Specifications	l_{eff} (m) CL-PTFE stack	l_{eff} (m) PTFE stack	t (m) CL stack	D^* CL
	0.019332	0.015109	0.000121	0.014163
	0.020319	0.014938	0.000121	0.011149
Design #1	0.019708	0.014970	0.000121	0.012643
T=20 ˚C	0.020233	0.014980	0.000121	0.011417
RH=0%	0.019778	0.014965	0.000121	0.012449
Compressive load=0 MPa	0.020212	0.015049	0.000121	0.011615
Probe #1	0.019783	0.014981	0.000121	0.012478
	0.019931	0.015031	0.000121	0.012229
	0.019829	0.015028	0.000121	0.012480
	0.019980	0.015017	0.000121	0.012076
Average	**0.019910**	**0.015007**	**0.000121**	**0.012221**
	0.011656	0.011292	0.000018	0.024500
	0.011791	0.011358	0.000018	0.020594
	0.011706	0.011214	0.000018	0.018196
Design #2	0.011620	0.011242	0.000018	0.023557
T=20 ˚C	0.011634	0.011297	0.000018	0.026369
RH=0%	0.011681	0.011196	0.000018	0.018444
Compressive load=0 MPa	0.011884	0.011541	0.000018	0.025874
Probe #1	0.011836	0.011260	0.000018	0.015592
	0.011574	0.011112	0.000018	0.019319
	0.011964	0.011323	0.000018	0.014032
Average	**0.011735**	**0.011283**	**0.000018**	**0.019812**

Specifications	l_{eff} (m) CL-PTFE stack	l_{eff} (m) PTFE stack	t (m) CL stack	D^* CL
	0.012183	0.011292	0.000058	0.031760
	0.012112	0.011358	0.000058	0.037292
	0.012020	0.011214	0.000058	0.034975
Design #3	0.012025	0.011242	0.000058	0.035985
T=20 ˚C	0.012115	0.011297	0.000058	0.034501
RH=0% Compressive load=0 MPa	0.012050	0.011196	0.000058	0.033063
Probe #1	0.012214	0.011541	0.000058	0.041585
	0.012242	0.011260	0.000058	0.028880
	0.012162	0.011112	0.000058	0.027073
	0.012268	0.011323	0.000058	0.029992
Average	**0.012139**	**0.011283**	**0.000058**	**0.033018**
	0.012011	0.011292	0.000062	0.041290
	0.012113	0.011358	0.000062	0.039383
	0.011954	0.011214	0.000062	0.040118
Design #4	0.011868	0.011242	0.000062	0.047075
T=20 ˚C	0.011941	0.011197	0.000062	0.039919
RH=0% Compressive load=0 MPa	0.011979	0.011261	0.000062	0.041307
Probe #1	0.012624	0.011911	0.000062	0.041622
	0.011996	0.011232	0.000062	0.038968
	0.011944	0.011201	0.000062	0.039978
	0.012064	0.011341	0.000062	0.041031
Average	**0.012048**	**0.011323**	**0.000062**	**0.040957**

Specifications	l_{eff} (m) CL-PTFE stack	l_{eff} (m) PTFE stack	t (m) CL stack	D* CL
	0.016356	0.015323	0.000083	0.038786
	0.016285	0.015380	0.000083	0.044043
	0.016315	0.015300	0.000083	0.039443
Design #5	0.016319	0.015216	0.000083	0.036419
T=20 ˚C	0.016570	0.015338	0.000083	0.032739
RH=0% Compressive load=0 MPa	0.016346	0.015533	0.000083	0.048800
Probe #2	0.016392	0.015309	0.000083	0.037063
	0.016300	0.015500	0.000083	0.049524
	0.016431	0.015370	0.000083	0.037833
	0.016449	0.015288	0.000083	0.034669
Average	**0.016376**	**0.015356**	**0.000083**	**0.039249**
	0.013498	0.011292	0.000034	0.007566
	0.013386	0.011358	0.000034	0.008222
	0.013394	0.011214	0.000034	0.007656
Design #6	0.013365	0.011242	0.000034	0.007858
T=20 ˚C	0.013340	0.011297	0.000034	0.008164
RH=0% Compressive load=0 MPa	0.013371	0.011196	0.000034	0.007674
Probe #1	0.013807	0.011541	0.000034	0.007367
	0.013448	0.011260	0.000034	0.007627
	0.013219	0.011112	0.000034	0.007918
	0.013475	0.011323	0.000034	0.007754
Average	**0.013430**	**0.011283**	**0.000034**	**0.007772**

Specifications	l_{eff} (m) CL-PTFE stack	l_{eff} (m) PTFE stack	t (m) CL stack	D^* CL
	0.011704	0.011292	0.000017	0.020553
	0.011770	0.011358	0.000017	0.020520
	0.011742	0.011214	0.000017	0.016080
Design #7	0.011673	0.011242	0.000017	0.019657
T=20 ˚C	0.011617	0.011197	0.000017	0.020153
RH=0% Compressive load=0 MPa	0.011770	0.011261	0.000017	0.016690
Probe #1	0.011952	0.011679	0.000017	0.030679
	0.011979	0.011687	0.000017	0.028709
	0.011970	0.011548	0.000017	0.020044
	0.011903	0.011609	0.000017	0.028555
Average	**0.011808**	**0.011409**	**0.000017**	**0.021172**
	0.013498	0.011292	0.000034	0.007566
	0.013386	0.011358	0.000034	0.008222
	0.013394	0.011214	0.000034	0.007656
Design #8	0.013365	0.011242	0.000034	0.007858
T=20 ˚C	0.013340	0.011297	0.000034	0.008164
RH=0% Compressive load=0 MPa	0.013371	0.011196	0.000034	0.007674
Probe #1	0.013807	0.011541	0.000034	0.007367
	0.013448	0.011260	0.000034	0.007627
	0.013219	0.011112	0.000034	0.007918
	0.013475	0.011323	0.000034	0.007754
Average	**0.013430**	**0.011283**	**0.000034**	**0.007772**

Specifications	l_{eff} (m) CL-PTFE stack	l_{eff} (m) PTFE stack	t (m) CL stack	D^* CL
	0.015866	0.015109	0.000084	0.052423
	0.015718	0.014938	0.000084	0.050913
	0.015743	0.014970	0.000084	0.051416
Design #9	0.015739	0.014980	0.000084	0.052293
T=20 ˚C	0.015758	0.014965	0.000084	0.050204
RH=0% Compressive load=0 MPa	0.015809	0.015049	0.000084	0.052235
Probe #2	0.015751	0.014981	0.000084	0.051594
	0.015819	0.015031	0.000084	0.050440
	0.015783	0.015028	0.000084	0.052567
	0.015779	0.015017	0.000084	0.052119
Average	**0.015777**	**0.015007**	**0.000084**	**0.051608**
	0.011779	0.011466	0.000022	0.034584
	0.011750	0.011364	0.000022	0.028136
	0.011843	0.011541	0.000022	0.035773
Design #10	0.011810	0.011429	0.000022	0.028507
T=20 ˚C	0.011802	0.011278	0.000022	0.020936
RH=0% Compressive load=0 MPa	0.011954	0.011614	0.000022	0.031882
Probe #1	0.011952	0.011534	0.000022	0.026095
	0.011845	0.011600	0.000022	0.043750
	0.011980	0.011690	0.000022	0.037152
	0.011822	0.011403	0.000022	0.026042
Average	**0.011854**	**0.011492**	**0.000022**	**0.030020**

Specifications	l_{eff} (m) CL-PTFE stack	l_{eff} (m) PTFE stack	t (m) CL stack	D^* CL
	0.015405	0.015109	0.000037	0.058216
	0.015269	0.014938	0.000037	0.052247
	0.015435	0.014970	0.000037	0.037796
Design #11	0.015290	0.014980	0.000037	0.055601
T=20 ˚C	0.015333	0.014965	0.000037	0.047341
RH=0% Compressive load=0 MPa	0.015374	0.015049	0.000037	0.053115
Probe #2	0.015341	0.014981	0.000037	0.048352
	0.015265	0.015031	0.000037	0.072191
	0.015414	0.015028	0.000037	0.045194
	0.015300	0.015017	0.000037	0.060571
Average	**0.015343**	**0.015007**	**0.000037**	**0.051578**
	0.015962	0.015109	0.000121	0.06402
	0.015830	0.014938	0.000121	0.063653
	0.015751	0.014970	0.000121	0.072073
Design #12	0.015884	0.014980	0.000121	0.062901
T=20 ˚C	0.015855	0.014965	0.000121	0.063828
RH=0% Compressive load=0 MPa	0.016178	0.015049	0.000121	0.051006
Probe #2	0.015880	0.014981	0.000121	0.063245
	0.015860	0.015031	0.000121	0.068171
	0.015971	0.015028	0.000121	0.060494
	0.015817	0.015017	0.000121	0.070459
Average	**0.015899**	**0.015007**	**0.000121**	**0.063686**

Specifications	l_{eff} (m) CL-PTFE stack	l_{eff} (m) PTFE stack	t (m) CL stack	D^* CL
	0.011813	0.010941	0.000062	0.034250
	0.011627	0.010935	0.000062	0.042800
	0.011689	0.010965	0.000062	0.041020
Design #4	0.011697	0.010953	0.000062	0.039924
T=20 ˚C	0.011825	0.011121	0.000062	0.042114
RH=0% Compressive load=0 MPa	0.011614	0.010950	0.000062	0.044558
Probe #1	0.011798	0.010966	0.000062	0.035877
	0.011706	0.011044	0.000062	0.044657
	0.011697	0.010998	0.000062	0.042419
	0.011762	0.010967	0.000062	0.037516
Average	**0.011723**	**0.010984**	**0.000062**	**0.040214**
	0.011726	0.010723	0.000062	0.029940
	0.011636	0.010709	0.000062	0.032313
	0.011610	0.010738	0.000062	0.034292
Design #4	0.011547	0.010839	0.000062	0.041853
T=68 ˚C	0.011550	0.010779	0.000062	0.038605
RH=0% Compressive load=0 MPa	0.011526	0.010723	0.000062	0.037137
Probe #1	0.011551	0.010719	0.000062	0.035882
	0.011507	0.010714	0.000062	0.037572
	0.011608	0.010907	0.000062	0.042319
	0.011527	0.010798	0.000062	0.040737
Average	**0.011579**	**0.010761**	**0.000062**	**0.036487**

Specifications	l_{eff} **(m) CL-PTFE stack**	l_{eff} **(m) PTFE stack**	t **(m) CL stack**	D^* **CL**
	0.012186	0.011460	0.000062	0.040869
	0.012219	0.011564	0.000062	0.045151
	0.012216	0.011453	0.000062	0.038993
Design #4	0.012332	0.011599	0.000062	0.040500
T=20 ˚C	0.012246	0.011499	0.000062	0.039792
RH=50% Compressive load=0 MPa	0.012254	0.011582	0.000062	0.044054
Probe #1	0.012287	0.011440	0.000062	0.035262
	0.012312	0.011580	0.000062	0.040543
	0.012294	0.011511	0.000062	0.038019
	0.012301	0.011456	0.000062	0.035323
Average	**0.012186**	**0.011460**	**0.000062**	**0.040869**
	0.012387	0.011591	0.000062	0.037431
	0.012337	0.011607	0.000062	0.040690
	0.012328	0.011627	0.000062	0.042292
Design #4	0.012273	0.011612	0.000062	0.044699
T=20 ˚C	0.012511	0.011603	0.000062	0.032970
RH=85% Compressive load=0 MPa	0.012328	0.011625	0.000062	0.042209
Probe #1	0.012312	0.011606	0.000062	0.041990
	0.012493	0.011555	0.000062	0.031957
	0.012360	0.011622	0.000062	0.040278
	0.012346	0.011644	0.000062	0.042282
Average	**0.012370**	**0.011605**	**0.000062**	**0.038916**

Specifications	l_{eff} (m) CL-PTFE stack	l_{eff} (m) PTFE stack	t (m) CL stack	D^* CL
	0.026255	0.024996	0.000094	0.036001
	0.026141	0.025054	0.000094	0.041449
Design #4	0.026290	0.025142	0.000094	0.039342
T=20 ˚C	0.026230	0.025284	0.000094	0.047343
RH=0% **Compressive load=0 MPa**	0.026060	0.025048	0.000094	0.044406
Probe #2	0.026091	0.024917	0.000094	0.038498
Compression sample holder	0.026185	0.025199	0.000094	0.045519
	0.026125	0.025027	0.000094	0.041049
	0.026558	0.025311	0.000094	0.036342
	0.026271	0.025219	0.000094	0.042739
Average	**0.026220**	**0.025120**	**0.000094**	**0.040953**
	0.039011	0.037985	0.000076	0.035717
	0.039238	0.037903	0.000076	0.027669
Design #4	0.039151	0.037737	0.000076	0.026177
T=20 ˚C	0.038869	0.037741	0.000076	0.032603
RH=0% **Compressive load=30 MPa**	0.038847	0.037625	0.000076	0.030151
Probe #2	0.039174	0.037669	0.000076	0.024629
Compression sample holder	0.039212	0.037969	0.000076	0.029654
	0.039028	0.037759	0.000076	0.029082
	0.039285	0.037817	0.000076	0.025224
	0.039072	0.037781	0.000076	0.028598
Average	**0.039011**	**0.037985**	**0.000076**	**0.035717**
Design #4	0.043067	0.040798	0.000067	0.014545
T=20 ˚C	0.043282	0.040467	0.000067	0.011763
RH=0% **Compressive load=50 MPa**	0.043044	0.040802	0.000067	0.014724

Probe #2	0.043087	0.040424	0.000067	0.012420
	0.043278	0.040587	0.000067	0.012298
Compression sample holder	0.043073	0.040924	0.000067	0.015348
	0.043105	0.040494	0.000067	0.012669
	0.043297	0.040756	0.000067	0.013015
	0.043179	0.040363	0.000067	0.011753
	0.043187	0.040580	0.000067	0.012687
Average	**0.043160**	**0.040620**	**0.000067**	**0.013015**

Table A 3 Measured effective lengths of stack of catalyst-coated filter PTFEs (design #4) and stack of filter PTFEs, CL stack thickness, and resulted relative diffusivities for different water content of CL at T=20 ˚C and RH=85%.

Water gain of CL (g Water / g CL)	***l*$_{eff}$ (m) CL-PTFE stack**	***l*$_{eff}$ (m) PTFE stack**	***t* (m) CL stack**	***D** CL**
0.25	0.026255	0.024996	0.000094	0.036001
0.20	0.026141	0.025054	0.000094	0.041449
0.15	0.026290	0.025142	0.000094	0.039342
0.10	0.026230	0.025284	0.000094	0.047343
0.05	0.026060	0.025048	0.000094	0.044406
0	0.026091	0.024917	0.000094	0.038498
0	0.026185	0.025199	0.000094	0.045519
0	0.026125	0.025027	0.000094	0.041049
0	0.026558	0.025311	0.000094	0.036342
0	0.026271	0.025219	0.000094	0.042739
0	0.033146	0.021219	0.000738	0.030000
0	0.031978	0.020997	0.000738	0.032500
0	0.031243	0.021072	0.000738	0.035000

0	0.030346	0.020878	0.000738	0.037500
0	0.030137	0.020974	0.000738	0.038700
0	0.029964	0.021111	0.000738	0.040000
0	0.030142	0.020941	0.000738	0.038548
0	0.028919	0.021037	0.000738	0.044712
0	0.030149	0.020746	0.000738	0.037748
0	0.029426	0.021088	0.000738	0.042368
0	0.030062	0.020981	0.000738	0.039036

Appendix B.

The developed code for CL structure and gas diffusion

```
%diffusivityfinal finds out non dimensional diffusivity (D),
diameter of
%agglomerates and percentage of them in form of two arrays
(d_agg,p_agg)
%d_agg is array of agglomerates diameter form large to small
%inputs are:
%psd is the pore size distribution from big to small psd(1,1) is
the d and
%psd(1,2) is the percentage
%e is porosity of the CL
%T is temperature
%st_check =1 if ionomer swell is considered, =0 if not
%w_wt is ratio of water weight to CL, e.g. 0.3

function
[D,f_inside_agg,xes,i_coverage]=Diffusivityfinal(psd,e,ic,w_ptc,d
_primary_pore,T,st_check,w_wt)

%-Kn_inclusion: this one check the pore diameter to see if Kn is
%important and if it is it includes Kn diffusivity
%-D_unitcell_cal calculate diffusivity of a unit cell with carbon
support
%size and one big d
%-F_inside_agg_cal which calculates the ratio of effective
diffusivity to binary
%-geometry parameters calculate the unit cell size a and
overlapping parameter which is xes
%-Psd_corrector it checks to see if the psd is not from big to
small
%sort it that way

%density and porosity values
[ro_c,ro_ionomer,ro_pt,M,f_FCC,e_carbon,e_FCC]=Materialproperties
();
e_carbon=e_c;

% changing I/C from weight to volume ratio:
ic=ic*ro_c/ro_ionomer;

%considers Knudsen
kn_check=1;
```

```
%binary diffusion
Db=1.13/1000/1000/1000*T^1.724;
%*************************************************************
**********
%                                GEOMETRY
%*************************************************************
**********

%it checks to make PSD from big to small, and check to make sure
it is in
%meter
psd=Psd_corrector(psd);

%PSD percent checker is a code that make sure the second column
of the PSD
%is in the right format (sum of all is 1)

psd=PSD_percent_check(psd);

e_agg=Porosityagglomerates(ro_c,ro_ionomer,ro_pt,e_carbon,e_FCC,w
_ptc,ic);
e_agg_filled=e_agg;

%priimary pore diameter in nm
d_primary_pore=d_primary_pore/1000000000;

%p_primary_pore is the volume percentage of primary pores, and
%d_primary_effective is the effective primary pore
%psd_icf is psd without primary pores
[psd_icf,d_primary_effective,p_primary_pore]=PSD_gen_without_prim
ary_pores(psd,d_primary_pore);
i_coverage=Ionomer_coverage_cal(p_primary_pore,e,e_agg)

nm=size(psd_icf);
n=nm(1,1);

xes=Find_zero_bisection(e,e_agg);
vi=V_ionomer(i_coverage,ro_c,ro_ionomer,ro_pt,e_FCC,w_ptc,ic)

%overlap parameter without ionomer
xesi=Find_zero_bisection_xesi(xes,vi);
if abs(xesi)<1
    xesi=((1-vi)*(4.5*xes^2-2*xes^3-1.5))^(1/3);
end
tav=0;
for i=1:n
    a(i)=Cell_dimension_cal(xes,psd_icf(i,1));
    t_i(i)=(xes-xesi)*a(i);
    r(i)=a(i)*xes;
    tav=tav+t_i(i)*psd_icf(i,2);
end
```

```
%*************************************************************************
**********
%                                  Water content
%*************************************************************************
**********
if (st_check==1)

   %saturated weight
    w_CL=0.25;

    st=0.21*0.93-.93*.21*(w_CL-w_wt)/w_CL;
    % for Ew=850.

    tav=tav*(1+st);
    i_coverages=i_coverage*(1+st)^2;
    if(i_coverages>1)
        i_coverages=1;
        for i=1:n
            t_is(i)=t_i(i)*(1+st)^3*i_coverage;
        end
    else
        for i=1:n
            t_is(i)=t_i(i)*(1+st);
        end
    end
    for i=1:n
        xess(i)=xes+(t_is(i)-t_i(i))/a(i);
    end

    psds=PSD_maker_s(psd_icf,a,xess);
    es=Porosity_s(e,xes,ro_ionomer,ro_pt,ro_c,ic,e_FCC,st);
    v_pptp=(1-e)*e_agg/(1-e_agg)/e;
    v_sptp=1-v_pptp;
    v_sptap=1-p_primary_pore;

    gama=((1+st)^3-1)*Ew/ro_ionomer/18;
    Mw_i=18*gama/Ew*ic/(1+ic+w_ptc)


ro_CL=(1+ic+w_ptc)/((ro_pt*ic/ro_ionomer/(ro_pt+ro_c*w_ptc)+1/ro_
c)*
      (1+ro_c*w_ptc/ro_pt));
    vapptp=v_pptp*(1-i_coverage);
    Mw_pp=ro_CL*e*vapptp
    v_sptp_s=(e*v_sptp+es-e)/es;
    v_f_sptsp_sat=(w_CL-Mw_i-Mw_pp)*ro_CL/(es*v_sptp_s);
    if(v_f_sptsp_sat<0)
        v_f_sptsp_sat=0;
    end
    v_we=(1-w_wt/w_CL)
```

```
end

if (st_check==0)
    psds=psd_icf;
    v_we=1;
    v_f_sptsp_sat=0;
    nm=size(psd_icf);
    n=nm(1,1);
    for i=1:n
        xess(i)=xes;
    end
end

%*****************************************************************
**********
%                                Diffusivity
%*****************************************************************
**********
%f_FCC is the diffusivity ratio for f_inside_agg_cal packed bed
without considering Dkn
%f_inside_agg is the non-dimensional diffusivity of
f_inside_agg_cal (agglomerate)
if (st_check==1)

f_inside_agg=F_inside_agg_cal(T,M,d_primary_effective,f_FCC,Db);
    f_inside_agg=f_inside_agg*(1-i_coverage);
    f_inside_agg=0.07*f_inside_agg+0.93*f_inside_agg*(w_CL-
w_wt)/w_CL;
else

f_inside_agg=F_inside_agg_cal(T,M,d_primary_effective,f_FCC,Db);
    f_inside_agg=f_inside_agg*(1-i_coverage);
end

sz=size(psd_icf);
n=sz(1);


%D_binary_and_Kn is diffusivity of the secondary pore considering
kn and binary effects together
%Here we keep the ratio of diffusivity inside and outside
agglomerates
%right, because Kn diffusivity is different inside and outside
%agglomerates

for i=1:n
    f_binary_and_Kn=Kn_inclusion(1,psds(i,1),T,M,Db,kn_check);

f_unitcelli=D_unitcell_cal(xess(i),f_inside_agg/f_binary_and_Kn);
    f_unitcell(i)=f_unitcelli*f_binary_and_Kn;
end
```

```
psd_icf(:,1)
f=Av(f_unitcell,psds(:,2),1-v_f_sptsp_sat,v_we);
D=f;

% If we needed the ionomer and agglomerate size distribution,
this part should be uncommented
% m=r'*10^9/xes*(4.5*xes^2-2*xes^3-1.5)^(1/3)

% for i=1:n(1,1)
%     e_agg_eq=e_agg*p_primary_pore+e_agg_filled*(1-
p_primary_pore);
%     [a,kes]=Geometryparameters(e,e_agg_filled,psd_icf(i,1));
%
thickness=thickness+thickness_function(e_FCC,e_carbon,ic,a/kes,a,
kes)*psd_icf(i,2);
%     d_agg(i)=a*(1.5*(3*kes^2-4/3*kes^3-1))^(1/3);
%     p_agg(i)=psd_icf(i,2);
% end


function f=Av(fs,pr,w_coef,w_e)
% pr is the distribution

sz=size(fs);
n=sz(1,2)
s=0;
sp=0;
%s is the summation
%sp is the probability counter

w_coef
if (w_coef==1)
    for i=1:n
        s=s+fs(i)*pr(i);
        sp=sp+pr(i);
    end
    f=s/sp;
else
    i=1;
    sum=pr(1);
    while (w_e>sum && i<=n)
        s=s+fs(i)*pr(i);
        i=i+1;
        if (i<=n)
            sum=sum+pr(i);
        end
    end
    if (i<n)
        s=s+fs(i)*(sum-w_e)*w_coef+(pr(i)-sum+w_e)*fs(i);
        for j=i+1:n
            s=s+fs(j)*pr(j)*w_coef;
```

```
            sum=sum+pr(j);
        end
    end
    f=s/sum;
end

function a=Cell_dimension_cal(xes,dg)
%fi is overlapped angle

fi=acos(1/xes);
a=dg/2/(1+(fi-pi/4)*xes^2-tan(fi))^0.5;
end

function Dst=D_unitcell_cal(xes,f)
%1 geometryparameters: calculates the unit cell parameters which
is
%[a,xes]a is unit cell size (for the cube)and xes is the
overlapped
%parameter d/2a
%2 Rcal: calculates nondimensional diffusivity resistance
%fst is ratio of the unit cell diffusivity to binary without Dkn
%dg is d pore
%dc is d base carbon
%gp is the unit cell parameters which is [a,xes]a is unit cell
size (for the cube)
%and xes is the overlapped parameter d/2a

R=Rcal(xes,f);
%Rsn is diffusivity resistance non dimensionized with a and Db
Dst=1/R;
end

function Dkn=Dkn_cal(T,M,d)

Dkn=4/3*d*(8.314*T/(2*pi*M))^0.5;
end

function
f_inside_agg=F_inside_agg_cal(T,M,d_primary_effective,f_FCC,Db)
%f_inside_agg is the diffusivity of FCC considering geometry and
KN
%1 Dkncal is calculator for Dkn which need T p M and diameter of
pore
%Dfcc is the effective diffusivity (of arrangement (FCC) without
Kn effect

Dkn=Dkn_cal(T,M,d_primary_effective);
D=(1/Dkn+1/Db/f_FCC)^-1;
f_inside_agg=D/Db;
end
```

```
function re=F_xes(xr,e,e_agg)
%re is the resedual

re=e-1+(3.14159*(1-e_agg)/6)*(4.5*xr^2-2*xr^3-1.5);
end

function re=F_xesi(vi,xes,xesi)

m=4.5*xes^2-2*xes^3-1.5;
re=4.5*xesi^2-2*xesi^3-1.5-(1-vi)*m;
end

function xes=Find_zero_bisection(e,e_agg)
%F_xes: is the function relates porosiy (e) and overlapping
parameter xes

xl=1;
xu=1.4;
xr=1.2;
for i=1:9
    if F_xes(xl,e,e_agg)*F_xes(xr,e,e_agg)<0
        xu=xr;
    elseif F_xes(xl,e,e_agg)*F_xes(xr,e,e_agg)>0
       xl=xr;
    else
        i=10;
    end
    xr=xl/2+xu/2;
end
xes=xr;

function xesi=Find_zero_bisection_xesi(xes,vi)

if (F_xesi(vi,xes,1)>0)
    xr=0.5;
else
xl=1;
xu=xes;
xr=xes/2;
for i=1:19
    if F_xesi(vi,xes,xl)*F_xesi(vi,xes,xr)<0
        xu=xr;
    elseif F_xesi(vi,xes,xl)*F_xesi(vi,xes,xr)>0
       xl=xr;
    else
        i=20;
    end
    xr=xl/2+xu/2;
end
end
xesi=xr;
```

```
function ans=Fun_integral_Rl1(x,xes,f)
% refer to the lower bound R1

xes_e=(xes^2-(tan(x))^2)^0.5;
fi=acos(1/xes_e);
n=1+(tan(x))^2;
m=((pi-4*fi)*xes_e^2+4*tan(fi))*(f-1)+4;
ans=n/m;
end

function ans=Fun_integral_Rl1(x,xes,f)
% refer to the lower bound R1

xes_e=(xes^2-(tan(x))^2)^0.5;
fi=acos(1/xes_e);
n=1+(tan(x))^2;
m=((pi-4*fi)*xes_e^2+4*tan(fi))*(f-1)+4;
ans=n/m;
end

function ans=Fun_integral_Rl1f(x,xes)

n=1/cos(x)/cos(x);
xese=(xes^2-tan(x)*tan(x))^0.5;
fie=acos(1/xese);
m=4-4*(tan(fie)+(xese^2)*(pi/4-fie));
ans=n/m;
end

function ans=Fun_integral_Rl2(x,xes,f)
% refer to the lower bound R2

n=xes*cos(x);
m=4-(1-f)*pi*(xes*cos(x))^2;
ans=n/m;
end

function ans=Fun_integral_Rl2f(x,xes)

n=xes*cos(x);
m=4-pi*xes*xes*cos(x)*cos(x);
ans=n/m;
end

function ans=Fun_integral_Ru2(x,xes,f)
% refer to the lower bound R2

n=f*pi*x*xes^2;
m=xes*(1-f)*(1-x^2)^0.5+f;
ans=n/m;
```

```
end

function [a,xes]=Geometryparameters(e,e_agg,dg)

xes=Find_zero_bisection(e,e_agg);
a=Cell_dimension_cal(xes,dg);
end

function sum=IntegralnumRl1(b1,b2,xes,f)
%1 funingRl1 it is the function inside the integral for R1low
%n is number of intervals

n=1000;
dx=(b2-b1)/n;
sum=0;
for i=1:n
    sum=sum+dx*Fun_integral_Rl1(b1+i*dx/2,xes,f);
end
end

function sum=IntegralnumRl1f(b1,b2,xes)

n=1000;
dx=(b2-b1)/n;
sum=0;
for i=1:n-1
    sum=sum+dx*Fun_integral_Rl1f(b1+i*dx,xes);
end
sum=sum+dx*0.5*(Fun_integral_Rl1f(b1,xes)+Fun_integral_Rl1f(b2,xe
s));
end

function sum=IntegralnumRl2(b1,b2,xes,f)

n=1000;
dx=(b2-b1)/n;
sum=0;
for i=1:n
    sum=sum+dx*Fun_integral_Rl2(b1+i*dx/2,xes,f);
end
end

function sum=integralnumRl2f(b1,b2,xes)

n=1000;
dx=(b2-b1)/n;
sum=0;
for i=1:n-1
    sum=sum+dx*Fun_integral_Rl2f(b1+i*dx,xes);
end
```

```
sum=sum+dx*0.5*(Fun_integral_Rl2f(b1,xes)+Fun_integral_Rl2f(b2,xe
s));
end

function sum=IntegralnumRu2(b1,b2,xes,f)

n=1000;
dx=(b2-b1)/n;
sum=0;
for i=1:n-1
    sum=sum+dx*Fun_integral_Ru2(b1+i*dx,xes,f);
end
sum=sum+dx*0.5*(Fun_integral_Ru2(b1,xes,f)+Fun_integral_Ru2(b2,xe
s,f));

function i_coverage=Ionomer_coverage_cal(p_primary_pore,e,e_agg)

v_pptp=(1-e)*e_agg/(e*(1-e_agg));
i_coverage=(v_pptp-p_primary_pore)/(v_pptp*(1-p_primary_pore));
end

function f=Kn_inclusion(f1,d,T,M,Db,knc)

f=f1;
knn=63/273000000000*T;
kn=knn/d;
if kn>=knc
    Dkn=Dkn_cal(T,M,d);
    fkn=Dkn/Db;
    f=1/(1/fkn+1/f1);
end
end

function
[ro_c,ro_ionomer,ro_pt,M,f_FCC,e_carbon,e_FCC]=Materialproperties
()
%density carbon particles, ionomer, and platinum gr/cm3

ro_c=2;
ro_ionomer=1.9;
ro_pt=21.45;
%oxygen molecular weight
M=32;
%relative diffusivity FCC
f_FCC=0.12;
%porosity carbon particles
e_carbon=0.287;
%porosity FCC
e_FCC=0.26;

function
```

```
p_pores_not_filled_agg=P_pores_not_filled_agg_cal(p_primary_pore,
e,e_agg)
%rp is the ratio of primary pores to total pore volume
rp=e_agg*(1-e)/e/(1-e_agg);
p_pores_not_filled_agg=p_primary_pore/rp;

end

function

[d_primary_effective,pr]=Percentfinder_of_d_primary_pore(psd,d_pr
imary_pore)
n=size(psd);
pr=0;
d_primary_effective=0;
for i=1:n(1,1)
    if psd(i,1)<=d_primary_pore
        pr=pr+psd(i,2);
        d_primary_effective=psd(i,1)*psd(i,2);
    end
end
d_primary_effective=d_primary_effective/pr;

function es=Porosity_s(e,xes,ro_i,ro_pt,ro_c,ic,e_FCC,st)

n=pi*(4.5*xes^2-2*xes^3-1.5)*((1+st)^3-1);
m=ro_i*(ro_pt+ro_c*ic)/(1-e_FCC)/ro_pt/ro_c/ic+1;
es=e*(1-n/6/m);
end

function
e_agg=Porosityagglomerates(ro_c,ro_ionomer,ro_pt,e_carbon,e_FCC,w
_ptc,ic)
part1=ro_pt*ro_ionomer*e_carbon*(1-e_FCC);
part2=ro_ionomer*e_FCC*(ro_pt+ro_c*w_ptc);
part3=ro_ionomer*(ro_pt+ro_c*w_ptc);
part4=ro_pt*ro_c*ic*(1-e_FCC);
e_agg=(part1+part2)/(part3+part4);

function dpp=PSD1(dpt,ep,e,dbpl)
%this function gets the PSD and output would be the PSD1 for non-
filled
%agglomerates
%dpt is PSD, first column is the diameter and the second one is
percentage
%from large to small
%ep is porosity within non-filled agglomerates (FCC)
%e is CL porosity
%dbpl is the limit for base pores, pores smaller than this one
are primary
```

```
%pr is the percentage of volume of base pores for non-filled agg
%Prr is the real percentage of base pores
%fpr2 is the percentage of each pores goes into the filled pore
category
%the first element is the base pore, the second element is the
factor of
%big pores goes into the filled agglomerates

pr=ep*(1-e)/e/(1-ep);
n=size(dpt);
i=n(1,1);
d=0;
while dpt(i,1)<dbpl
    d=d+dpt(i,1)*dpt(i,2);
    Prr=Prr+dpt(i,2);
    i=i-1;
end
d=d/Prr;
fpr2=1-Prr*(1-pr)/pr;

for j=2:i
    dpp(j,1)=dpt(j-1,1);
    dpp(j,2)=dpt(j-1,2);
end
dpp(1,1)=d;
dpp(1,2)=fpr2;

function psdc=Psd_corrector(psd)
if psd(1,1)<psd(2,1)
    n=size(psd);
    for i=1:n(1,1)
        psdc(i,1)=psd(n(1,1)+1-i,1);
        psdc(i,2)=psd(n(1,1)+1-i,2);
    end
else
    psdc=psd;
end
if psdc(1,1)>0.001
    disp 'dimater unit correction from nanometer to meter'
    psdc(:,1)=psdc(:,1)/10^9;
end

function
[psd_ic,d,pr]=PSD_gen_without_primary_pores(psd,d_primary_pore)
%it gets the psd finds out primary pore (averaged) and then put
it as the first element then put the rest of diameter in the new
psd

n=size(psd);
pr=0;
d=0;
```

```
j=0;
for i=n(1,1):-1:1
    if psd(i,1)<=d_primary_pore
        pr=pr+psd(i,2);
        d=d+psd(i,2)*psd(i,1);
        j=j+1;
    end
end
if pr>0
    d=d/pr;
end

for i=1:n(1,1)-j
    psd_ic(i,1)=psd(i,1);
    psd_ic(i,2)=psd(i,2);
end
end

function psds=PSD_maker_s(psd,a,xess)

nm=size(psd);
n=nm(1,1)
for i=1:n
    fi=acos(1/xess(i));
    psds(i,1)=2*a(i)*(1+(fi-pi/4)*xess(i)^2-tan(fi))^0.5;
    psds(i,2)=psd(i,2);
end

function psd_checked=PSD_percent_check(psd)
sum=0;
n=size(psd);
for i=1:n(1,1)
    sum=sum+psd(i,2);
end
psd(:,2)=psd(:,2)/sum;
psd_checked=psd;
end

function [PSDs1,PSDlsm]=PSDVa(dcv,dd)
%dcv is a matrix which first column is pore diameter and the
second one is
%the volume of the pore cumulative from zero to the final value
%dd is the matrix of pore distribution we need. For example if we
want 0-10
%and 10-50 dd would be dd=[0;10;50]
%prv is the volume percentage
%_s is source _t is target
%PSDsl is PSD small to large
%PSDlsm is PSD large to small without zeros for diffusivity model
dd=dd';
%dcv=[dcv1,dcv2];
```

```
%the values are in nm but PSDlsm for model is in meter
nn=size(dcv);
n=nn(1,1)
mm=size(dd);
m=mm(1,2);
mf=m;
%prv_s is the volume percentage for diameter
prv_s(1)=dcv(1,2)/dcv(n,2);
for i=2:n
    prv_s(i)=(dcv(i,2)-dcv(i-1,2))/dcv(n,2);
end
for i=1:m-1
    PSDsl(i,1)=0;
    PSDsl(i,2)=0;
end

if dcv(1,1)<dcv(2,1)
    j=1;
    for i=1:m-1
        sd=0;
        sp=0;
        while dcv(j,1)<dd(i+1)
            sd=sd+dcv(j,1)*prv_s(j)
            sp=sp+prv_s(j)
            if j==n
                dcv(j,1)=dd(m)+1;
                ii=i;
                i=m-1;
            else
                j=j+1
            end

        end
        if sd==0
            PSDsl(i,1)=0;
            PSDsl(i,2)=0;
        else
            if i==m
                PSDsl(ii,1)=sd/sp;
                PSDsl(ii,2)=sp;
            else
                PSDsl(i,1)=sd/sp;
                PSDsl(i,2)=sp;
            end
        end
    end
else
    j=n;
    for i=1:m
        sd=0;
        sp=0;
```

```
        while dcv(j,1)<dd(i)
            sd=sd+dcv(j,1)*prv_s(j);
            sp=sp+prv_s(j);
            j=j-1;
        end
        PSDsl(i,1)=sd/sp;
        PSDsl(i,2)=sp;
    end
end
hh=size(PSDsl)
h=hh(1,1);
while(PSDsl(h,2)==0)
    h=h-1;
end
for i=1:h
    PSDs1(i,1)=PSDsl(i,1);
    PSDs1(i,2)=PSDsl(i,2);
    PSDls(i,1)=PSDsl(h+1-i,1);
    PSDls(i,2)=PSDsl(h+1-i,2);
end
s=0;
for i=1:h
    if PSDls(i,2)==0
        s=s+1
    else
        PSDlsm(i-s,1)=PSDls(i,1)/10^9;
        PSDlsm(i-s,2)=PSDls(i,2);
    end
end

function Rl1=R1low(xes,f)
%1 intgralnumRl1 is numerical integral for Rl1

integral_first_bound=0;
integral_second_bound=acos(1/xes);
Rl1=2*IntegralnumRl1(integral_first_bound,integral_second_bound,x
es,f);
end

function Rl1=R1lowf(xes,f)
%1 intgralnumRl1 is numerical integral for Rl1

integral_first_bound=0;
integral_second_bound=acos(1/xes);
Rl1=2*IntegralnumRl1f(integral_first_bound,integral_second_bound,
xes);
end

function Rl2=R2low(xes,f)
%1 ansintgralfunctionRl2 is the function answer to the integral
for Rl2
```

```
integral_first_bound=acos(1/xes);
integral_second_bound=pi/2-acos(1/xes);
Rl2=2*IntegralnumRl2(integral_first_bound,integral_second_bound,x
es,f);
end

function Rl2=R2lowf(xes)
%1 ansintgralfunctionRl2 is the function answer to the integral
for Rl2

integral_first_bound=acos(1/xes);
integral_second_bound=pi/2-acos(1/xes);
Rl2=2*IntegralnumRl2f(integral_first_bound,integral_second_bound,
xes);
end

function R=Rcal(xes,f)

R=Rlow(xes,f);
end

function Rsn=Rcalf(xes,f)

Rsn=Rlowf(xes);
end

function Rl=Rlow(xes,f)
%1 R1low calculates the first region resistance in lower bound
%2 R2low calculates the second region resistance in lower bound
%%%%%%%%%%


Rl1=R1low(xes,f);
Rl2=R2low(xes,f);
Rl=Rl1+Rl2;
end

function Rl=Rlowf(xes)
%1 R1low calculates the first region resistance in lower bound
%2 R2low calculates the second region resistance in lower bound
%%%%%%%%%%


Rl1=R1lowf(xes);
Rl2=R2lowf(xes);
Rl=Rl1+Rl2;
end

function
```

```
thickness=thickness_function(eps_FCC,eps_carbon,phi_IC,r_agglomer
ate,a,xes)

V_agglomerate=4/3*pi*a^3*(4.5*xes^2-2*xes^3-1.5);
V_carbon=V_agglomerate*(1-eps_FCC)*(1-eps_carbon);
V_ionomer=V_carbon*phi_IC;
A_agglomerate=4*pi*r_agglomerate^2-
12*pi*r_agglomerate*(r_agglomerate-a);

thickness=V_ionomer/A_agglomerate;

end

function
vi=V_ionomer(i_coverage,ro_c,ro_ionomer,ro_pt,e_FCC,w_ptc,ic)

part1=ro_pt*ro_c*ic;
part2=ro_ionomer*(ro_pt+ro_c*w_ptc)/(1-e_FCC);
vi=part1/(part2+part1);
end

function re=Xesi_finder(vi,xes,xesi)

m=4.5*xes^2-2*xes^3-1.5;
re=4.5*xesi^2-2*xesi^3-1.5-(1-vi)*m==0,x));
end
```